# Investigation of Stimuli-Responsive Polymer Nanocomposites for Dye Treatment in Aqueous Solution

A Thesis Submitted to the College of Graduate and
Postdoctoral Studies in Partial Fulfillment of
The Requirements for the Degree of

**Doctor of Philosophy**

In the Department of Chemistry
University of Saskatchewan
Saskatoon

By

Asghar Dolatkhah

# Permission to use

In presenting this thesis in partial fulfillment of the requirements for a Postgraduate degree from the University of Saskatchewan, I agree that the Libraries of this University may make it freely available for inspection. I further agree that permission for copying of this thesis in any manner, in whole or in part, for scholarly purposes may be granted by the professors who supervised my thesis work or, in their absence, by the Head of the Department or the Dean of the College in which my thesis work was done. It is understood that any copying or publication or use of this thesis or parts thereof for financial gain shall not be allowed without my written permission. It is also understood that due recognition shall be given to me and to the University of Saskatchewan in any scholarly use which may be made of any material in my thesis.

Requests for permission to copy or to make other uses of materials in this thesis/dissertation in whole or part should be addressed to:

Head of the Department of Chemistry
University of Saskatchewan
Saskatoon, Saskatchewan
S7N 5C9, Canada

OR

Dean
College of Graduate and Postdoctoral Studies
University of Saskatchewan
107 Administration Place
Saskatoon, Saskatchewan S7N 5A2
Canada

# Abstract

Currently, environmental pollution associated with dyes has become an issue of global concern that is gaining significant attention. Developing inexpensive nanocomposites via combination of functional properties of dissimilar materials is of increasing interest for dye treatment in aqueous solution. Chitosan is a natural, low-cost, biocompatible and biodegradable polymer that is widely researched and applied in advanced water treatment. π-conjugated polyaniline is a notable polymer for adsorption purposes due to the relatively low cost of the monomer precursor, environmental stability, ease of doping/de-doping chemistry and its relatively high nitrogen content. Among conductive polymers, polyaniline is one of the most highly studied. Unfortunately, there are some technical limitations associated with each respective polymer system, chitosan and polyaniline. Therefore, the application of *as-prepared* chitosan and PANI for adsorption processes and catalytic treatment of dyes is somewhat limited since single component polymer systems possess limited adsorption sites and low surface area, especially without further post synthetic modification.

This thesis investigates various approaches for dye removal from aqueous solution via development of chitosan and polyaniline-based, stimuli-responsive, nanocomposite materials. These approaches continue to be of great interest since they combine functional properties of dissimilar materials to design multifunctional nanocomposites with enhanced properties. The major aim of this thesis is the development of nanocomposite materials for treatment of model dye pollutants from aqueous solution.

In the first section of this thesis, to overcome the limited physicochemical properties of chitosan, synthetic modification was carried out to develop pH-responsive polymer brush nano adsorbents for controlled adsorption of methylene blue. By grafting poly anion functional groups onto the chitosan backbone, and integrating such a system onto iron oxide nanocrystalline

materials, significant enhancement was observed for methylene blue adsorption. This effect was achieved through electrostatic interactions and creation of osmotic pressure within polymer side chains, where the regeneration of the nanocomposite was facilitated with stimuli-responsiveness and magnetic separation.

In the second section, redox-responsive catalyst systems were developed and utilized towards reduction of 4-nitrophenol with sodium borohydride. Single component precursor (Ag nanoparticles, chitosan and polyaniline) materials were observed to display poor catalytic reduction with 4-nitrophenol. By interfacing a stimuli-responsive polymer with silver nanoparticles, greater catalytic activity was demonstrated for the enhanced reduction of 4-nitrophenol with respect to the single component precursors. Nanocomposites of this type present a new and efficient approach for conversion of 4-nitrophenol to 4-aminophenol.

Following on the research of methylene blue adsorption, polyaniline/chitosan magnetic nanocomposites were synthesized and used for removal of methylene blue via adsorption in aqueous media. Molecular selective adsorption of methylene blue and methyl orange was measured to bring insight into the adsorption properties of polyaniline nanostructures. In addition, the interaction of polyaniline with NaCl was investigated as a path to further explore dye adsorption onto PANI in a de-doped state. During this project, it was discovered that polyaniline interacts with salt, which resulted in weakening of the intramolecular hydrogen bonding as confirmed by dynamic light scattering and Raman spectroscopy. The salt-responsive behavior of the nanocomposites and the preferential adsorption of a cationic dye over an anionic dye proved that methylene blue likely associates with de-doped polyaniline in a similar fashion as $Na^+$ ions via cation-dipole interactions.

To better understand the observed experimental results of salt and dye interaction with polyaniline, nitrogen containing self-healing materials were encapsulated inside polyaniline macroparticles (size of ca. 500 nm) and their release upon exposure to salt was monitored. Therefore, a versatile-activation type of delivery systems was developed. The kinetics of release further unraveled the details of methylene blue adsorption and disintegration of polyaniline upon interaction with salt. The results demonstrated that such interactions and disintegration of polyaniline is the result of a combination of factors (such as osmotic pressure within polymer shell, polymer permeability, polymer flexibility and dynamic motion) that work in a cooperative fashion. In particular, the role of anion hydration according to the Hofmeister series plays a key role in stabilizing the salt-doped form of the polyaniline-$M^+$ complex.

# Acknowledgements

First and foremost, I would like to extend my sincere gratitude to my advisor, Dr. Lee D. Wilson for his immense support and guidance over the five years I have spent in his group. His balanced leadership provided an environment where I was able to develop as a researcher and I also learned many non-scientific lessons from him. He was a wonderful mentor who played a significant role in my intellectual growth. Indeed, it has been a privilege to be mentored by such an amazing person who made it easy for me to attain my goals.

I would like to thank the members of my advisory committee Dr. Richard K. Bowles, Dr. Jian Wang and Dr. Jafar Soltan for their helpful feedbacks and support along the way. A big thank you goes to the Dr. Wilson group members, past and present for the wonderful times and the support they have provided me. In particular, Dr. Mohamed H. Mohamed for his help and great support on the first year of my program.

I would like to express my appreciation to my mother, father and brothers for their unconditional love and support. You have been always a source of inspiration and encouragement for me. I love you all.

Above all, I cannot express enough gratitude to my dear wife Shabnam for her love and support and the big role that she has played along the way, you will always be the most significant person in my life.

I would like to thank University of Saskatchewan for the financial support through the Graduate Teaching Fellowship (GTF) program. I am thankful for the financial supports from the Government of Canada through the Natural Sciences and Engineering Research Council of Canada (NSERC), (Discovery Grant Number: RGPIN 2016-06197) and the Government of Saskatchewan through the Agriculture Development Fund (Project no.: 20110162).

Finally, I am grateful for the Graduate Research Fellowship award by the University of Saskatchewan and Gerhard Herzberg Doctoral Promotion Award funded by Dr. Herzberg, the Herzberg family, Dr. G. Russel Walker, and by friends and colleagues of Dr. Herzberg.

*To my parents, and my supervisor*

# Table of contents

Permission to use.....i

Abstract. .....ii

Acknowledgements .....v

Table of contents ..... vii

List of Figures ..... xii

List of Schemes .....xx

List of Tables.....xxi

List of Abbreviations..... xxii

CHAPTER 1. Introduction.....1

1.1. Need for organic dye removal ..... 1

1.2. Adsorption ..... 2

1.3. Chitosan ..... 3

1.3.1. Structure and properties ..... 3

1.3.1. Chitosan crystallinity ..... 4

1.3.2. Disadvantages of chitosan as adsorbent..... 5

1.3.3. Modification of chitosan for adsorption ..... 5

1.3.3.1. Physical modification..... 6

1.3.3.2. Chemical modification..... 6

1.4. Polyaniline ..... 8

1.4.1. Synthesis and history ..... 8

1.4.2. Conductivity in conjugated polymers ..... 9

1.4.3. Concept of doping and conductivity in PANI ..... 10
1.4.4. Stimuli-responsiveness ..... 13
1.4.5. PANI based adsorbents ..... 14
1.4.5.1. Adsorption of metal ions ..... 14
1.4.5.2. Adsorption of organic dyes ..... 16
1.5. Catalytic reduction of dyes ..... 17
1.5.1. Noble metal nanocatalyst ..... 18
1.6. Thesis scope ..... 19
1.6.1. Objectives of the project ..... 19
1.6.2. Connection between chapters ..... 20
1.7. References ..... 22
CHAPTER 2 ..... 31
Magnetite/polymer Brush Nanocomposites with Switchable Uptake Behavior toward Methylene Blue ..... 31
2.1. Abstract ..... 32
2.2. Introduction ..... 32
2.3. Experimental section ..... 35
2.3.1. Materials ..... 35
2.3.2. Synthesis of PIA and PAA grafted chitosan brushes (PAAgCHI and PIAgCHI) ..... 36
2.3.3. Synthesis of MNPs, $Fe_3O_4$-PAAgCHI and $Fe_3O_4$-PAAgCHI nanohybrids ..... 36
2.3.4. Characterization ..... 37
2.3.5. Adsorption-desorption and pH-responsive experiments ..... 38
2.3.6. Adsorption Kinetics ..... 40
2.4. Results and discussion ..... 40
2.4.1. Preparation of materials ..... 40

2.4.2. Characterization of the chitosan brushes and nanohybrids ..... 41
2.4.3. Cation dye sorption mechanism and molecular recognition ..... 50
2.4.4. Adsorption isotherms ..... 53
2.4.5. Desorption and pH-responsive behavior of adsorbents ..... 57
2.4.6. pH-dependent morphology changes of polymer brush nanohybrids ..... 57
2.4.7. Adsorption kinetics ..... 63
2.5. Conclusion ..... 64
2.7. References ..... 66
CHAPTER 3 ..... 72
Redox-responsive Polymer Template as an Advanced Multifunctional Catalyst Support for Silver Nanoparticles ..... 72
3.1 Abstract ..... 73
3.2. Introduction ..... 73
3.3. Experimental section ..... 76
3.3.1. Materials ..... 76
3.3.2. Synthesis of catalysts ..... 76
3.3.3. Catalytic activity of nanocomposites ..... 77
3.3.4. Measurements and characterization ..... 78
3.4. Results and discussion ..... 79
3.5. Conclusion ..... 93
3.7. References ..... 95
CHAPTER 4 ..... 100
Salt-Responsive $Fe_3O_4$ Nanocomposites and Phase Behavior in Water ..... 100
4.1. Abstract ..... 101

4.2. Introduction ..... 101
4.3. Experimental section ..... 104
4.3.1. Materials ..... 104
4.3.4. Characterization ..... 104
4.3.2. Surface functionalized particles ..... 106
4.3.3. Assembly of composites ..... 106
4.3.4. Selective affinity and ionic dye recognition experiments ..... 107
4.3.5. Adsorption isotherms: ..... 107
4.4. Results and discussion ..... 108
4.4.1. Design and assembly into responsive biphasic hybrid particles ..... 108
4.4.2. Structural characterization of NC hetero-structures ..... 110
4.4.3. Phase characterization of NCs ..... 112
4.4.4. Salt-stimulated disassembly and size/phase transition in solution ..... 120
4.5. Conclusion ..... 129
4.7. References ..... 130
CHAPTER 5 ..... 137
Activated Release of Self-Healing Materials from Hydrogen Bonding-Gated Stimuli-Responsive Polyaniline Microparticles ..... 137
5.1. Abstract ..... 138
5.2. Introduction ..... 138
5.3. Experimental section ..... 140
5.3.1. Materials ..... 140
5.3.2. Synthesis of particles and materials loading ..... 140
5.3.3. Release experiments ..... 141
5.3.4. Characterization and general techniques ..... 141

5.4. Results and discussion ..... 143
5.5. Conclusion ..... 153
5.7. References ..... 155
CHAPTER 6 ..... 158
6.1. Integrated discussion of manuscript chapters ..... 158
6.2. Summary ..... 163
6.3. Future work ..... 170
6.3.1. 4-NPh removal ..... 171
6.3.1.1. 4-NPh adsorption ..... 171
6.3.1.2. Preliminary results on 4-NPh adsorption ..... 172
6.3.2. MB removal ..... 173
6.3.2.1. MB reduction ..... 173
6.3.2.2. Preliminary results on MB reduction ..... 174
6.4. References ..... 176
Appendix: Supporting Tables and Figures ..... 181

# List of Figures

**Figure 1.1**. Illustration of (a) absorption and (b) adsorption phenomena. Reproduced from reference[2] with permission from The Royal Society of Chemistry. (c) The chemical structure of some of organic dyes studied in this thesis, from top to bottom: methylene blue (MB), methyl orange (MO) and 4-nitrophenol (4-NPh). ..... 2

**Figure 1.2.** The chemical structure of chitosan. R represents H or acetyl groups depending on the level of deacetylation. ..... 3

**Figure 1.3.** (a) Scheme showing hierarchical organization in chitosan powder and its plasticized structure with reduced crystallinity. (b) PXRD patterns of natural chitosan powder and its plasticized forms with variable compositions of lactic acid and glycerol, where the inset labels give sample conditions: A. Original chitosan, and plasticized chitosan with different plasticization compositions of B. with equivalent amount of lactic acid, C. 3g of glycerol, D. 6g of glycerol, E. 3g of glycerol and 3g of water, and F. 18g of water. Reprinted with permission from reference[20] © 2014 American Chemical Society. ..... 5

**Figure 1.4.** (a) Scheme showing the cross-linked chitosan with glutaraldehyde and epichlorohydrin. Reprinted with permission from reference[19] © 2014 Taylor & Francis. (b) Chemical structure of poly itaconic acid grafted chitosan cross-linked with glutaraldehyde for metal ions adsorption. Reprinted with permission from reference[29] © 2014 American Chemical Society. ..... 7

**Figure 1.5.** Schematic representation of molecular orbitals in ethylene, highest occupied molecular orbital (HOMO), lowest unoccupied molecular orbital (LUMO) and evolution of band structures with extension of conjugation from butadiene to polyacetylene as the simplest π-conjugated system. Adapted from reference[24]. ..... 10

**Figure 1.6.** Doping PANI with acids and internal oxidation (the same number of electrons). Formation of positive polarons and bipolaron charge carriers with doping of 2 equivalents of acid. Reprinted from reference[54] with permission from The Royal Society of Chemistry. ..... 12

**Figure 1.7.** Band theory in conducting polymers. (a) Formation of positive polaron at lower doping level, bipolarons at moderate doping level and bipolaron bands at high doping level (p-doping). (b) Formation of negative polaron at lower doping level, bipolarons at moderate doping level and bipolaron bands at high doping level (n-doping).[56] CB: Conduction band, VB: Valence band. (c) UV-vis spectra of the silica-PANI core-shell nanoparticles at different proton doping levels. (d) Photograph of the PANI containing nanoparticles at different doping

levels. Adapted and reprinted from reference[52] with permission from The Royal Society of Chemistry. ..... 13

**Figure 1.8.** (a) Schematic representation of modified PANI nanofibers and their switchable doping/de-doping chemistry accompanied by catch and release of mercury. **Note**: release experiments were carried out under oxidation potentials, therefore reduction of $Hg^{2+}$ to $Hg^{+}$ or $Hg^{0}$ form does not occur. (b) Recyclability of functionalized PANI for catch and release of mercury ions from solution. Release by achieved applying a fixed oxidation potential. (c) selective adsorption of mercury by PANI towards various cations. Adapted and reprinted with permission from reference[11] © 2018 American Chemical Society. ..... 15

**Figure 1.9.** (a) Chemical formulae and adsorption sites of PANII nanofibers doped with Cl and phytic acid under different pH conditions for adsorption of $Cu^{2+}$ ions. (b) comparison of $Cu^{2+}$ adsorption to PANI nanofibers doped with Cl (Cl-PAni NFs) and phytic acid (Ph-PAni NFs). Adapted and reprinted with permission from reference[65] © 2017 American Chemical Society. ..... 16

**Figure 2.1.** FTIR spectra of (a) PIAgCHI (iii), itaconic acid (ii) and pristine chitosan (i); (b) PIAgCHI modified MNPs (i), PIAgCHI modified MNPs (ii) as-prepared MNPs (iii) and pristine chitosan (iv); and (c) illustration of the grafted bridging bidentate interaction in hybrid nanostructures. ..... 44

**Figure 2.2.** Chemical structure and $^{1}H$ NMR (500 MHz) spectra of CHI, PIAgCHI, and PAAgCHI polymer brushes. (inset) $^{1}H$ NMR spectra of itaconic acid (a) and acrylic acid (b) in $D_2O$/HCl (10% v/v), where n denotes the degree of polymerization of the pendant groups for the polymer brushes. ..... 45

**Figure 2.3.** TGA and DTG profiles of PIAgCHI brush (a), MNPs (b), and $Fe_3O_4$-PAAgCHI (c). ..... 47

**Figure 2.4.** PXRD patterns of $Fe_3O_4$ and polymer brush MNCs. ..... 49

**Figure 2.5.** TEM micrographs of (a) magnetite NPs; (b) $Fe_3O_4$-PIAgCHI; (c) $Fe_3O_4$-PAAgCHI; and (d) $Fe_3O_4$-PIAgCHI particles. (inset) HRTEM of $Fe_3O_4$-PIAgCHI nanoparticles. ..... 50

**Figure 2.6.** (a) Chemical structures of PIA-chitosan brush and MB; (b) photographs of MB before (i) and after sorption (ii) by PIAgCHI polymer brush where $C_0$ (MB) = 0.2 mM; (c) images of MB before (i) and after sorption by $Fe_3O_4$-PIAgCHI (ii) $Fe_3O_4$-PAAgCHI and (iii) MNCs (after applying magnetic field) where $C_0$ (MB) = 0.6 mM. ..... 53

**Figure 2.7.** Isotherm sorption results for MB with various sorbent materials: (a) CHI and PIAgCHI and (b) $Fe_3O_4$-PAAgCHI composites. ..... 56

**Figure 2.8.** pH-dependent solution behavior of polymer brush MNCs; (a) Changes in mean hydrodynamic radius (solid lines) of $Fe_3O_4$-PIAgCHI (▼) and $Fe_3O_4$-PAAgCHI (■) samples and PDI (dash lines) in response to pH changes according to DLS. The mean $R_h$ distributions of PAAgCHI MNCs at pH of 7 (b), 6 (c), and 2 (d)..... 59

**Figure 2.9.** (a-e) TEM results and an illustration of the self-assembly for MNCs. TEM images of $Fe_3O_4$-PIAgCHI (top) and $Fe_3O_4$-PAAgCHI (bottom) from vacuum-dried water solutions with variable pH on copper grids: (a, c) pH 6; (b, d) pH 2; and (e) schematic illustration of pH-responsive aggregation behavior and the MB release process of MNCs. ..... 61

**Figure 2.10.** Reversible pH-controlled MB adsorption/desorption; and color changes of solutions (C0 = 0.3 mmol $L^{-1}$ ) containing (a) PIA grafted polymer brushes after settling, (b) $Fe_3O_4$-PIAgCHI MNCs and magnetic separation of adsorbents, (c) PIA grafted polymer brushes before settling, and (d) $Fe_3O_4$-PAAgCHI MNC sorbents and magnetic separation of adsorbents. ..... 62

**Figure 2.11.** Adsorption-desorption cycles of PIAgCHI (orange bar), $Fe_3O_4$-PIAgCHI (green bar), and $Fe_3O_4$-PAAgCHI (purple bar) for MB systems ..... 63

**Figure 2.12.** Adsorption kinetic profiles of MB on PIAgCHI (red ▼), $Fe_3O_4$-PAAgCHI (green ●), and $Fe_3O_4$-PIAgCHI (blue ■). Experimental conditions: adsorbent dose = 20 mg; initial MB concentration = 0.09 mM. V(solution) = 120 mL. The solid line is PSO fit to the experimental data. ..... 64

**Figure 3.1.** (a) PXRD spectra of materials. Inset curves are expanded spectra in the range 2θ = (10-55). TEM images of (b, d) AgNP-CP50, (c, e) AgNP-CP75 and; evidence for well dispersed metal NPs on the surface of the active polymer matrix. Insets (b, c): corresponding size distribution of supported Ag NPs based on N=100 NPs. ..... 81

**Figure 3.2**. UV-vis spectra recorded during catalytic reaction which shows gradual reduction of 4-NPh to 4-APh at variable conditions: (a) unsupported Ag NPs (b) AgNP-CP25. Red arrow shows residual 4-NPh after 30 min (c) AgNP-CP50 and (d) AgNP-CP75 at 295 K. Insets: (a) catalytic reaction over PMix, (c) Typical optical images before and after catalysis reduction by AgNP-CP50 and UV-vis spectra of the sample after reduction without dilution, (d) Typical optical images before and after catalysis of the AgNP-CP75; Conditions: [4-NPh] = $1.1\times10^{-3}$ M, 10 mL, [$NaBH_4$]= 0.053M, 20 mg and amount of catalyst: 10 mg. ..... 83

**Figure 3.3.** (a) Plot of $\ln(C_t/C_0)$ versus time for reduction of 4-NPh using PMix, Ag NPs and different catalysts. (b) Residual fraction of 4-NPh in solution *vs.* reaction time upon treatment with unsupported Ag NPs and different catalysts or PMix

(inset). (c) Schematic illustration of the Fermi alignment and charge injection at the interface of AgNPs-CP composites. In parallel, the polymer is reduced as electrons are added to the $\pi^*$ band and holes injected into metal NPs contact region, and (d) Schematic illustration of Ag NPs stabilization by PG/LE. ..... 85

**Figure 3.4.** (a) XPS survey**,** (b, c) High resolution Ag 3*d* XPS spectra obtained from the AgNPs-CP nanocomposites..... 89

**Figure 3.5**. (a) N 1s XPS spectra of the PMix and catalysts. (b) The Arrhenius plot for the reaction catalyzed by different catalysts..... 90

**Figure 3.6.** Reusability of the AgNPs-CP catalysts for the reduction of 4-NPh; Reaction conditions: 50 mL [4-NPh] = $1.1\times10^{-3}$ M, 25 °C, t=30 min, and 50 mg catalyst loading. ..... 92

**Figure 4.1.** (a) Schematic representation of the PIONcx synthesis and representative images of samples prepared at each stage. Synthetic preparation involves two steps: *i*. surface treatment of IONPs and self- assembly, and *ii*. Self-assembled polymer particles generated through surface initialized seeded nucleation polymerization. (b) FT-IR spectra of (1) acrylic acid adsorbed IONPs, (2) PIONCc3, (3) IOPNc5, (4) PIONc7 samples. Image (c) shows absorbance spectra of hetero particles ($\lambda_{max}$ = 330 and 620 nm) dispersed in NMP solutions. (d) PXRD patterns for (1) IONPs and PIONcx nanostructures; (2) x=7, (3) x=5, (4) x=3, where the band observed ca. $2\theta$ = 25 relates to PANI domains. (e) Illustration of self-assembly and polymer growth onto the IONPs surface. ..... 111

**Figure 4.2.** (a-b-c) show the TEM images of IOPNc3 nanohybrids and inset (a) a schematic representation of dimple-shaped particles formed in NCs. In inset b, the selected area of the electron diffraction pattern where the beam focused on larger particles and inset c the selected area of electron diffraction pattern related to the magnetite phase (from image in inset 2c bottom) in NC materials. (d) Size distribution histograms PIONc3 particles consisting of a bimodal size population ($d_{av.}$ ~ 18 and 220 nm). (e) Proposed four-step formation of dimple-shaped aggregates: seeded-nucleation, formation of porous-like spheres (yellow spheres represent trapped solvent), coalescence, and breaking bubble due to high *surface-to-volume*. (Particles are from different images) and size histogram of PIONc3 composites obtained from TEM. (f) The corresponding EDX mapping lines collected from small-sized domains and (g) larger particles (from different images). (♦) indicates Fe band position. Shown in (h) bimodal intensity-average hydrodynamic diameter distribution $f(D_h)$ of PIONc3 hetero particles measured by DLS compared to *as prepared* parent IONPs..... 114

**Figure 4.3.** (a) TEM bright-field micrographs of heteroparticles of the magnetic/PANI domain that are well tuned with variable CHI content (3%, 5%, and 7%). (b) Bimodal intensity size distribution of heteroparticle hybrids with variable CHI

content obtained by DLS relate to the TEM images presented above. (c) Schematic size-tuning of PANI domains. The inset in (b) shows the dispersion of aqueous NC (x = 5%). Note the presence of free magnetite particles. ..... 119

**Figure 4.4.** (a) TEM micrograph of PIONc0 particles synthesized without initial CHI; the scale bar is 100 nm. (Inset) DLS characterization of IONPs and PIONc0 showing the change in size distribution of particles in composite. (b) Histograms of size distribution of PIONc0. (c) Size and phase transitions of PANI components in PIONcx prepared in variable stabilizer %. (d) Size transition of PANI domains in NCs plotted as function of CHI % as measured by DLS and TEM (inset). (e) Magnetic response of PIONc5 as function of time in NMP under magnetic field (non-uniform). ..... 122

**Figure 4.5.** (a) TGA/DTG profiles of PIONcx NCs measured under nitrogen flow over range of 25-900 ˚C and their comparison with pure PANI and PANI/IONPs with IONPs loading of 20 % prepared by physical mixture at a temperature ramp of 5˚ C $min^{-1}$. (b, c) DLS characterization of the salt-doped PIONc5 NC at variable $C_{NaCl}$ and following micro-phase behavior in water. (d) Following phase transformation and salt effects on the polymer components using Raman spectroscopy ($\lambda$ = 514.5 nm excitation) for dispersed samples in aqueous dispersion, from top to bottom are from PIONc3 composite and different levels of NaCl with $C_{NaCl}$ = 0.1, 0.5, 0.8, and 1.8 M, respectively. (e) Schematic hydrogen bonding regulated disassembly of PANI aggregates at the magnetite surface and disrupting inter-/intra-chain hydrogen bonding in the presence of ions. Insets (b) and (c) show the images of PIONc5 samples in dimethyl sulfoxide (DMSO) after de-doping and doping with salt (2.0 M)..... 126

**Figure 4.6.** (a) Langmuir adsorption isotherms (Eq. 4.2) of MB and MO on PIONc5. $C_e$ (mmol/L): equilibrium concentration of dyes. $q_e$ ($mmolg^{-1}$): the amount of dye adsorbed at equilibrium. Insets: the chemical structures of MB and MO (b) DLS measurements monitoring the evolution of PIONc5 average size in the aqueous solution with successive salt addition from $C_{NaCl}$ = 0.1 to 1.8 M (c) Photographs of MB/MO mixture before (left) and after (right) treated with PIONc5. Initial concentrations approximately 0.013 and 0.037 mM respectively (*cf*. Figure A.17). (d) Peak DLS particle $<D_h>$ recorded at alternated 1.8 M salt and washing/centrifuging in consecutive doping runs. Photograph images of NaCl doped/de-doped sample in DMSO..... 128

**Figure 5.1.** Nanocontainers consist of distinct core/shell structure and hollow nanocapsules morphology. TEM micrographs of the stimuli-responsive PANI nanocapsules (a) loaded with MBT materials (c,e) MBI (b,d,f) and BTA (g,h,i). The insets in the upper left-hand corners, a schematic depiction of nanocontainer with

payload and without payload and schematic of core/shell morphology. (j-l) size histograms of particles. 145

**Figure 5.2.** $^{1}$H NMR spectra recorded (500 MHz, 293 K) for (a) PANI and particles loaded with guest materials (in DMSO-$d_6$) with DMT as internal standard for quantification of payloads (b) Internal standard and load materials (in DMSO-$d_6$). 147

**Figure 5.3.** Salt concentration-activated release profiles and % release of payloads from microcapsule constructs when exposed to 20 mL 0.5 M aqueous NaCl. (a) MBI and (b) BTA. In normal conditions and without salt there is no leakage observed for the materials (control sample); however, materials release is activated upon change in environment. From qNMR measurements, the amount of guest in capsules were 3% wt. for MBT and BTA. The data points represent the average value of 3 measurements and the error bars reflect standard deviations from three experiments. 150

**Figure 5.4.** Stimuli-induced release profiles and % release of payloads from microcapsule constructs with and without salt exposure for (a) MBT. The concentration of guest in capsules was 2% wt. (b) summary and comparison of release with and without salt vs. loading efficiency. 151

**Figure 6.1.** Outline of four projects in this thesis for chemical and physical MB and 4-NPh dyes treatment in aqueous solution by fabrication of stimuli-responsive nanocomposites. a) Design of magnetite/chitosan polymer brush nanocomposites ($Fe_3O_4$-PAAgCHI and $Fe_3O_4$-PAIgCHI) for MB adsorption. Reprinted with permission from reference[8] © 2016 American Chemical Society. b) 4-NPh catalytic reduction in the presence of $NaBH_4$ by designing PANI/Ag nanocomposites (AgNP-CP75). Reprinted with permission from reference[9] © 2018 American Chemical Society. c) Design of PANI/MNP nanocomposites (PIONc3) with higher surface area and easy manipulation for selective MB adsorption. Reprinted with permission from reference[7] © 2017 American Chemical Society. d) Mechanistic understanding of MB adsorption on PANI and its interaction with salt by designing PANI containers for salt triggered release of MBT, MBI and BTA guest molecules as function of salt and interaction with cation. 162

**Figure 6.2.** Equilibrium adsorption isotherms of 4-NPh on PANI/Ag nanocatalysts, where the solid lines are the best-fits according to the Sips and Langmuir adsorption isotherms 172

**Figure 6.3.** a) Successive UV-vis spectra of MB aqueous solution containing $NaBH_4$ and PANI/Ag nanocatalysts as a function of reaction time. [MB] = 0.1mM, [$BH_4^-$] = 40 mg in 500 μL water, catalyst solution = 10 mg in 1 ml. b) corresponding color changes of MB before and after reduction. 175

**Figure A.1.** FT-IR spectra of the PAAgCHI polymer brush (i) and pristine chitosan (ii) (a), CHI, PAAgCHI, PIAgCHI, $Fe_3O_4$-PIAgCHI and $Fe_3O_4$-PAAgCHI in the range of carbonyl groups (b,c,d) and symmetric/asymmetric stretching vibrations for $COO^-$ groups (e,f,g,h). ..... 183

**Figure A.2.** TGA and DTG profile of $Fe_3O_4$-PIAgCHI assemblies. ..... 183

**Figure A.3.** PXRD patterns for PIAgCHI (a), and PAAgCHI (b) brushes. ..... 184

**Figure A.4.** Effect of pH of solution on MB adsorption at 298 K: (a) PIAgCHI; (b) $Fe_3O_4$-PIAgCHI (●) and $Fe_3O_4$-PAAgCHI (■). Experiment conditions: graph (a): m = 10 mg, t = 20 min, $C_0$ (MB) = 0.01 mM, V = 3 ml. graph (b): m = 10 mg, t = 20 min, $C_0$ (MB) =0.06 mM, V= 3 ml. ..... 184

**Figure A.5.** Isotherm sorption results for $Fe_3O_4$-PIAgCHI composite system with MB. ..... 185

**Figure A.6.** Dependence of MB desorption from PIAgCHI brush (a) and PIAgCHI polymer brush- containing nano hybrids (●) and PAAgCHI polymer brush nano hybrid at variable pH conditions (▲) (b). ..... 185

**Figure A.7.** Adsorption kinetics of MB on PIAgCHI (●) $Fe_3O_4$-PAAgCHI (■) and $Fe_3O_4$-PIAgCHI (*) MNCs. The solid line is the PSO best-fit to the experiment data. ..... 186

**Figure A.8.** The mean hydrodynamic diameter distributions of $Fe_3O_4$-PIAgCHI particles at pH of 8 (a); $Fe_3O_4$-PAAgCHI at pH 10 (b), and pH 8 (c). ..... 186

**Figure A.9.** Calibration curve for optical absorbance of MB (λ=664 nm) versus concentration. ..... 187

**Figure A.10.** Size and catalytic activity as a function of PANI fraction. ..... 187

**Figure A.11.** Calibration curve for 4-NPh, optical absorbance (λ=400 nm) versus dye concentration. ..... 188

**Figure A.12.** TEM image of *as-prepared* Ag-NPs and particle size histogram. ..... 188

**Figure A.13.** (a) TEM micrograph of as-prepared IONPs and (inset) size distribution obtained from counting 100 particles in the TEM image using the ImageJ software. (b) DLS hydrodynamic diameter distribution of IONPs. ..... 189

**Figure A.14.** Additional TEM micrographs of the PIONcx structures. ..... 189

**Figure A.15.** Expanded TGA profiles of PIONcx nanocomposites, IONPs and PMix measured under nitrogen flow. ..... 190

**Figure A.16.** TEM characterization of PIONc3 samples prepared after addition of salt and their phase transition behavior: a) 1.4 M , b) 1.6 M, c) 1.8 M, d) 1 M (bars: a,b,d = 500 nm, c = 100 nm). ..... 190

**Figure A.17.** (a) UV-vis spectra of MO/MB mixture before and after adsorption by PIONc5; MB ($\lambda_{max}$ = 664 nm) and MO ($\lambda_{max}$ = 462 nm); V = 15 mL, t = 5 h,

m= 150 mg. (b) Calibration curve for MB ($\lambda_{max}$ = 664 nm) and MO ($\lambda_{max}$ = 462 nm). The experiment was carried out to further investigate ion recognition ability of the NCs..... 191

**Figure A.18.** $^{1}$HNMR spectra of BTA loaded in capsules vs. DMT. ..... 192

**Figure A.19.** $^{1}$HNMR spectra of MBT loaded in capsules vs. DMT..... 193

**Figure A.20.** $^{1}$HNMR spectra of MBI loaded in capsules vs. DMT..... 194

**Figure A.21.** Standard UV-vis curves used to quantify released self-healing agents..... 195

# List of Schemes

**Scheme 1.1.** Reaction scheme for preparation of 50% doped/oxidized polyaniline.[14, 49] ..... 8

**Scheme 2.1.** Two-step synthetic route for polymer brush nanocomposites containing magnetite ($Fe_3O_4$-PIAgCHI). **Note:** -NHR; where R = acetyl group or H depending on the degree of deacetylation. ..... 35

**Scheme 3.1.** a) Scheme showing the relative reduction potential for PANI, Ag, $NaBH_4$ and 4-NPh with respect to NHE, indicating the thermodynamic feasibility of $e^-$ transfer from $BH_4^-$ to both PG and 4-NPh species.* Value converted from data referred to the Ag/AgCl/3M NaCl electrode from ref.[5] b) Top: reduction process during synthesis and Bottom: oxidation process and receiving $H^-$ at interface during catalysis performance. ..... 87

**Scheme 5.1.** a) Polymeric capsules were prepared using o/w miniemulsion and droplets interface as template. Illustration of salt-gated molecular transport through release into aqueous sodium chloride solution dialysis. b) Interchangeable PANI structure and emeraldine salt formation. c) Optical images of polymer particles dispersed in water and the color change, d) Solutions of MBT dissolved in NMP before (green) and after stimuli exposure (blue) in a dialysis bag (e). ..... 144

**Scheme 6.1.** Organization of the PhD Thesis objectives into four research themes and five chapters. ..... 159

**Scheme 6.2.** Illustration of salt-sensitive transformation and *salting-in* interactions in PANI domains leads to intensified screening of intermolecular hydrogen bonding in an aggregate-like arrangement (right) and intramolecular hydrogen bonding induced assembly (left). ..... 168

**Scheme 6.3.** Oxidized and reduced forms of MB ..... 174

# List of Tables

**Table 2.1.** Isotherm parameters for the adsorption of MB with various sorbent materials. *The adsorption data are plotted using a MB concentration in mmol $L^{-1}$, but for the purpose of comparison, the $q_{max}$ values were calculated using a dye concentration in mg $g^{-1}$ ..... 56

**Table 2.2.** Adsorption kinetic parameters at 295 K in aqueous solution at ambient conditions. ..... 64

**Table 3.1.** Corresponding apparent rate constants $k_{app}$ ($s^{-1}$) for catalysts. Activity factors, the ratio of rate constant $k_{app}$ to the total mass of the catalyst ($s^{-1}$ $g^{-1}$) were calculated and a comparison of values with literature is presented in Table 6.2. $^{*}k_{app}$ for PMix: $2.6\times10^{-6}$ $s^{-1}$. ..... 84

**Table 3.2.** Proportion (%) of N species in catalysts. ..... 91

**Table 6.1.** Literature comparison of adsorption capacities of various adsorbent materials toward MB in aqueous solution. ..... 164

**Table 6.2.** Comparison of the catalytic activity of the related Ag nanocomposite catalysts reported in literature for the reduction of 4-NPh by $NaBH_4$. ..... 166

**Table A.1.** PFO and PSO adsorption kinetics. ..... 196

**Table A.2.** Summary of TGA results of polymer brushes and the corresponding MNCs. ..... 197

**Table A.3.** Rate constant values as a function of variable temperature. ..... 197

**Table A.4.** Langmuir adsorption isotherm parameters. ..... 197

# List of Abbreviations

| | |
|---|---|
| 4-APh | 4-Aminophenol |
| 4-NPh | 4-Nitrophenol |
| AIONP | Acrylic acid functionalized iron oxide nanoparticle |
| APS | Ammonium peroxydisulfate |
| *B* | Benzenoid |
| BE | Binding energy |
| BTA | Benzotriazole |
| CB | Conduction band |
| CHI | Chitosan |
| COF | Covalent organic framework |
| CP | Chitosan polyaniline |
| $D_h$ | Mean hydrodynamic diameter |
| DLS | Dynamic light scattering |
| DMSO | Dimethyl sulfoxide |
| DMT | Dimethyl terephthalate |
| DRIFT | Diffuse reflectance infrared Fourier transform |
| DTG | Derivative thermal gravimetry |
| EB | Emeraldine base |
| EDX | Energy dispersive X-ray |
| ES | Emeraldine Salt |
| FTIR | Fourier transform infrared |
| HOMO | Highest occupied molecular orbital |
| IONP | Iron oxide nanoparticle |
| LE | Leucoemeraldine |
| LMB | Leucomethylene blue |
| LUMO | Lowest unoccupied molecular orbital |
| MB | Methylene blue |
| MBI | 2-Mercaptobenzimidazole |
| MBT | 2-Mercaptobenzothiazole |

| | |
|---|---|
| MNC | Magnetic nanocomposite |
| MNP | Magnetite nanoparticles |
| MO | Methyl orange |
| NC | Nanocomposite |
| NMP | N-Methyl-2-pyrrolidone |
| NMR | Nuclear magnetic resonance |
| NP | Nanoparticle |
| PAA | Poly(acrylic acid) |
| PANI | Polyaniline |
| PDI | Polydispersity index |
| PFO | Pseudo first order |
| PG | Pernigraniline |
| PIA | Poly(itaconic acid) |
| PIONc | PANI/Iron oxide nanocomposite |
| PMix | Physical mixture of PANI/CHI |
| PSO | Pseudo second order |
| PXRD | Powder X-ray diffraction |
| *Q* | Quinoid |
| qNMR | Quantitative nuclear magnetic resonance |
| $R_h$ | Mean hydrodynamic radius |
| SAED | Selected area electron diffraction |
| TEM | Transmission electron microscope |
| TGA | Thermogravimetric analysis |
| UV-vis | Ultra-violet and visible light |
| VB | Valence band |
| XPS | X-ray photoelectron spectroscopy |

# CHAPTER 1. Introduction

## 1.1. Need for organic dye removal

Water is continuously being polluted by industrial effluents, human activities, underground water leakages, agricultural runoff, oil spills etc. when these contaminants are released into aquatic environments. Pollutants from surface water supplies make their way down into groundwater and lead to ground water contamination. Population expansion and continuous growth of industrialization causes severe water pollution.[1] In addition, global water shortage requires urgent technologies and adsorbents to remove toxic agents from water.[2] Dyes are among the common classes of pollutants that are considered as toxic chemical compounds with considerable structural diversity and complexity.[3]

The chemical structure of dyes comprise two key components: a chromophore unit that is responsible for dye production and an auxochrome group that makes dye soluble in water that may also supplement the chromophore by modifying the photophysical properties via the intensity and wavelength of light absorption (*cf.* Figure 1.1c herein).[4] Dye molecules are toxic compounds and their complex aromatic structure renders such compounds resistant against light degradation, biodegradation, and conventional chemical oxidation. Organic dyes have been extensively used in textile, paper, leather, food processing, pharmaceuticals, pesticides and dye manufacturing industries.[3] The total dye consumption by textile industry worldwide is estimated to be over 10,000 tonnes per year and estimates indicate that approximately 100 tonnes are discharged into the global environment annually.[4] Therefore, uncontrolled discharge into water streams pose significant amount of pollution to water resources that cause serious concern over environmental contamination.[5]

## 1.2. Adsorption

There have been various methods such as adsorption, membrane separation, oxidation, ion exchange and coagulation to remove pollutants from wastewater.[5] Adsorption as a separation method is one of the most efficient methods for the removal of organic, inorganic and biological contaminants (e.g., heavy metals, organic dyes, bacteria pollutants) from contaminated water.[1-2, 6] It is considered as the most convenient, cost effective, facile and practical method[7] with high adsorption capacity,[8-10] recyclability,[8, 10-11] high selectivity[8-9, 12-13] and relatively fast kinetics[12] of uptake. Adsorption is the accumulation of a gas or liquid solute (adsorbate) on the surface of a solid or liquid, known as the adsorbent through physical or chemical interactions to form a molecular or atomic film (Figure 1.1b). On the other hand, absorption processes often involve an adsorbate that permeates or dissolves into a liquid or solid adsorbent (Figure 1.1a). A combination of these two phenomena are collectively referred to as sorption.[14]

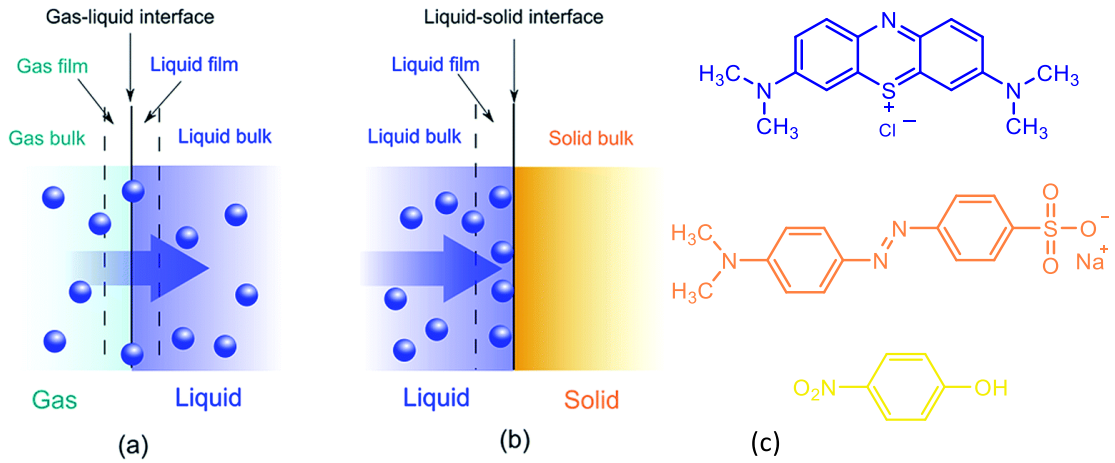


**Figure 1.1**. Illustration of (a) absorption and (b) adsorption phenomena. Reproduced from reference[2] with permission from The Royal Society of Chemistry. (c) The chemical structure of some of organic dyes studied in this thesis, from top to bottom: methylene blue (MB), methyl orange (MO) and 4-nitrophenol (4-NPh).

# 1.3. Chitosan

## 1.3.1. Structure and properties

Chitosan (CHI) is the second most abundant polysaccharide next to cellulose, the most abundant biopolymer in nature.[15-16] CHI is available in variable degrees depending on the amount of deacetylation. Chitosan is usually prepared from alkaline deacetylation of chitin that is widely distributed in naturally occurring sources such as fungi, shrimps, prawn, insects, marine diatoms, algae, crab shells and yeasts.[16] Chitosan is nontoxic, biodegradable, and an abundant resource with high biocompatibility. The inherent biocompatibility of chitosan makes it potentially amenable for areas of biomedicine, hydrogels, drug delivery systems, biosorption and water treatment.[16-17] Chitosan has numerous reactive amine and hydroxyl groups on its backbone which can be used for further chemical modifications (Figure 1.2).

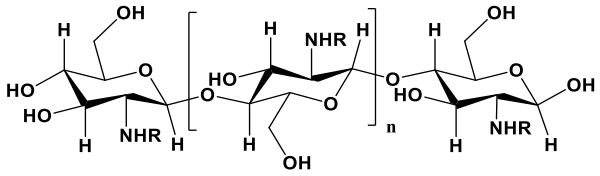


**Figure 1.2.** The chemical structure of chitosan. R represents H or acetyl groups depending on the level of deacetylation.

The presence of these functional groups in chitosan also makes it promising as an environmentally friendly material for adsorption-based applications. Chitosan has a relatively high adsorption capacity due to favorable adsorption interaction of its functional groups and outstanding chelation capacities with water pollutants such as metal ions.[18-19]

### 1.3.1. Chitosan crystallinity

Chitosan is believed to possess a hierarchical structure with different levels of crystalline domains due to the formation of intra- and intermolecular hydrogen bonding.[20] The degree of crystallinity also affects adsorption capacity of chitosan as it limits accessibility of amino and internal adsorption sites for the adsorbate.[21] For example, Meng et al.[20] have used a thermomechanical method to prepare plasticized chitosan with lactic acid and glycerol. They were able to reduce the level of crystallinity of the original chitosan sample from 63.7% to almost zero using variable concentrations of plasticizer such as glycerol and lactic acid (Figure 1.3). Addition of plasticizers leads to the formation of linkage networks between sheets, where the plasticizer component infiltrates the chitosan microfibers. Salt linkages between the chitosan and lactic acid fraction results in expansion of the chitosan sheets, while glycerol and water molecules further separate the sheets from each other. Consequently, no diffraction peaks were observed in the powder X-ray diffraction (PXRD) spectral patterns for plasticized chitosan with water and glycerol, where almost zero crystallinity was achieved (*cf.* pattern F in Figure 1.3).[20]

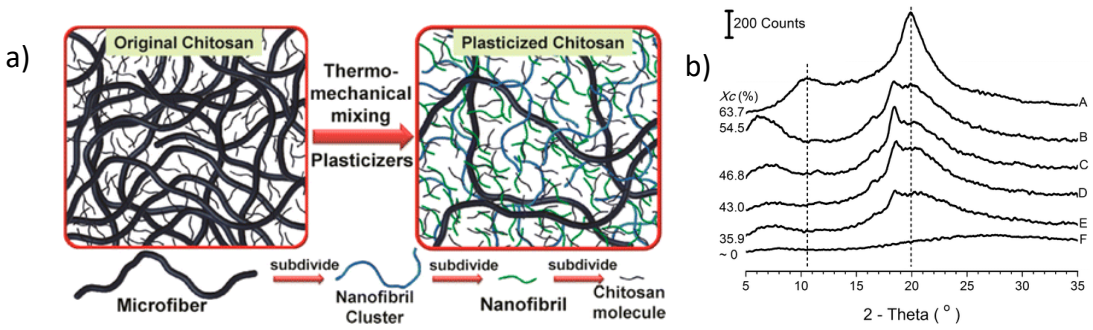


**Figure 1.3.** (a) Scheme showing hierarchical organization in chitosan powder and its plasticized structure with reduced crystallinity. (b) PXRD patterns of natural chitosan powder and its plasticized forms with variable compositions of lactic acid and glycerol, where the inset labels give sample conditions: A. Original chitosan, and plasticized chitosan with different plasticization compositions of B. with equivalent amount of lactic acid, C. 3g of glycerol, D. 6g of glycerol, E. 3g of glycerol and 3g of water, and F. 18g of water. Reprinted with permission from reference[20] © 2014 American Chemical Society.

## 1.3.2. Disadvantages of chitosan as adsorbent

The adsorption performance of an adsorbent is described by characteristics such as high affinity toward target pollutant species, high adsorption capacity, selectivity, kinetic rate of adsorption and the possibility of adsorbent regeneration. All these characteristics are affected by several physical and chemical factors such as adsorbent-adsorbate interaction,[10] surface area and particle size of adsorbent,[10] surface accessible active sites of the adsorbent,[22] pH of solution,[22] temperature and contact time.[10, 22] Chitosan in its unmodified form still has some drawbacks such as crystallinity and low adsorption capacity, low specific surface area, instability in acidic media, non-selectivity, difficult to recycle due to its irregular particle shape, and limited favorable adsorption sites for ionized organic dyes. The above disadvantages limit the widespread use of chitosan in adsorption-based applications.

## 1.3.3. Modification of chitosan for adsorption

In order to improve the adsorption capacity of chitosan for various adsorbates, physical or chemical modifications is often necessary. To modify and improve adsorption performance of

chitosan, adsorption mechanisms need be identified, and proper modification strategies must be developed. As mentioned in section 1.3.2, the adsorption capacity of chitosan mainly depends on its crystallinity, surface functionality, accessibility of its functional groups and surface area. Chitosan adsorbents could be altered by different approaches of physical and/or chemical modification. Such types of modification will alter the physicochemical properties of chitosan and further enhance its adsorption performance to expand its utility for practical applications.

#### 1.3.3.1. Physical modification

Commercial chitosan is offered in flake or powder form with variable degree of deacetylation, low specific surface area, resistance to mass transfer and limited pore structure which is not suitable for practical applications. The physical state of chitosan significantly affects its adsorptive performance and kinetics of adsorption.[23] Physical modification of chitosan includes conversion of powder into its forms with a higher specific surface area, more porosity and smaller size to allow for greater access to internal adsorption sites and reduced crystallinity.[21, 24] Deaceylation of CHI results in an increase in the number -$NH_2$ groups per unit area and presence of more active functional groups for interaction with the solvent and adsorbate. For example, chitosan adsorbents in various forms have been reported with reduced crystallinity[21] such as fibers,[25] sponges,[26-27] gels, films, nanoparticles, beads and microspheres.[28] These chitosan materials with different morphology have enabled a wider field of application, in contrast to conventional systems in powder form.

#### 1.3.3.2. Chemical modification

The chemical modification of chitosan includes approaches such as cross-linking[29-33] and grafting.[29] The presence of abundant -OH and -$NH_2$ active groups on the chitosan backbone allows for its chemical modification through various chemical reactions such as amide formation,[31]

esterification,[31] Schiff base reaction[29-30, 33-36] and etherification.[37] Chemical modification of chitosan affords derivatives with enhanced adsorption capacity and chemical stability. Cross-linking has been used to lower the solubility of chitosan in acidic solution, where cross-linkers such as glutaraldehyde[30, 36, 38] and epichlorohydrin[36, 38-39] are two commonly used systems (Figure 1.4a). Cross-linking at variable composition enables tuning of the adsorptive properties of chitosan through changes in the textural and surface properties. Cross-linkers serve as molecular links between polymers to form 3D network, hence improving its chemical stability against acidic media. In addition, cross-linkers can introduce new active functional groups to the adsorbent structure, resulting in changes to the solubility and hydrophile-lipophile profile. The degree of cross-linking can also tune the swelling level and water retention of the adsorbent.[33] Therefore, by judicious choice of cross-linker and composition, chitosan adsorbent materials can be obtained with modified textural (surface area and pore structure) and adsorption properties.[36, 38, 40]

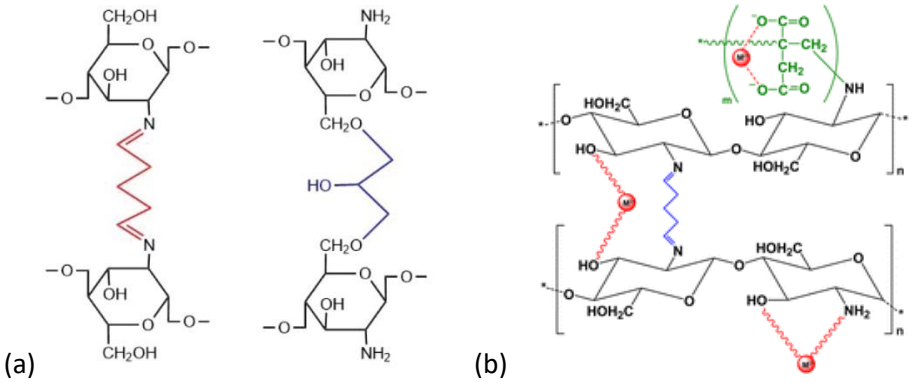


**Figure 1.4.** (a) Scheme showing the cross-linked chitosan with glutaraldehyde and epichlorohydrin. Reprinted with permission from reference[19] © 2014 Taylor & Francis. (b) Chemical structure of poly itaconic acid grafted chitosan cross-linked with glutaraldehyde for metal ions adsorption. Reprinted with permission from reference[29] © 2014 American Chemical Society.

Grafting differs from cross-linking wherein small molecules such as monomers or pre-polymers are covalently bonded onto the polymer backbone. Some of the disadvantages of

chitosan such as low potential for hydrogen bond formation with an adsorbate due to strong competitive intermolecular interactions between CHI chains, limited electrostatic interactions, low hydrodynamic volume and low adsorption capacity can be circumvented by grafting long and flexible polymers onto the polymer backbone.[22, 29, 41] Graft copolymerization is an important technique that allows for increasing the number of surface functional groups on a polymer adsorbent. In this method, monomers must be capable of polymerization and possess reactive functional groups that are suitable for adsorption. Various kinds of monomers containing vinyl groups such as acrylamide,[42] acrylic acid,[43] and itaconic acid[29] (Figure 1.4b) have been used for grafting where such materials possessed enhanced adsorption performance and improved properties, as compared with the unmodified polymers.

# 1.4. Polyaniline

## 1.4.1. Synthesis and history

Polyaniline (PANI) is an intrinsically conducting polymer which has been known for over 150 years. This so-called "aniline black" was originally prepared by Runge in 1835.[44] PANI can be prepared by electrochemical oxidation of aniline on various electrodes, or direct chemical oxidative polymerization of aniline in the presence of oxidizing agents such as ammonium persulfate (APS) with APS/aniline ratio of 1.25.[45-48] This yields PANI in the form of emeraldine salt (ES) form where 50% of polymer is oxidized or protonated (Scheme 1.1).

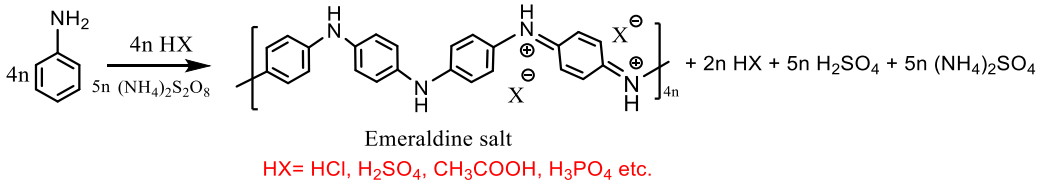


**Scheme 1.1.** Reaction scheme for preparation of 50% doped/oxidized polyaniline.[14, 49]

PANI has attracted significant attention based on its excellent properties, low cost, ease of synthesis, high environmental stability, acid doping/de-doping capacity, and reversible conductivity upon alteration of its oxidation state. As well, PANI has promising material-based applications as an adsorbent, supercapacitor, sensor, battery material, electronic device and so on.[48]

## 1.4.2. Conductivity in conjugated polymers

Conjugated polymers are those that consist of repeating units that contain alternating double and single bonds. Conductivity in conjugated polymers result from the delocalization of π-electrons in an extended π-system. Polyethylene is an example of one of the simplest conjugated π-system with hybridized $sp^2$ carbon orbitals that overlap to create a polymer backbone. The remaining $2p_z$ orbitals perpendicular to the plane of the $sp^2$ orbitals overlap with the adjacent carbon atoms to form bonding (π) and antibonding (π*) molecular orbitals. As the π-conjugation is extended in a conjugated polymer, the energy levels of the π and π* orbitals further split to energy levels with a very small spacing and in a very highly extended conjugation, energy bands are close enough to form continuous energy levels known as valence band (VB) for π bonding orbitals and conduction band (CB) for π* antibonding orbitals (Figure 1.5). Conductivity in semiconductors is based on charge carrier mobility because of electrons in the conduction band and electron holes in the valence band. In the case of intrinsic semiconductors, the number of holes and electrons in valence band and conduction band are the same and often depend on whether the material conducts holes or electrons more easily, intrinsic semiconductors are classified as either p-type or n-type.

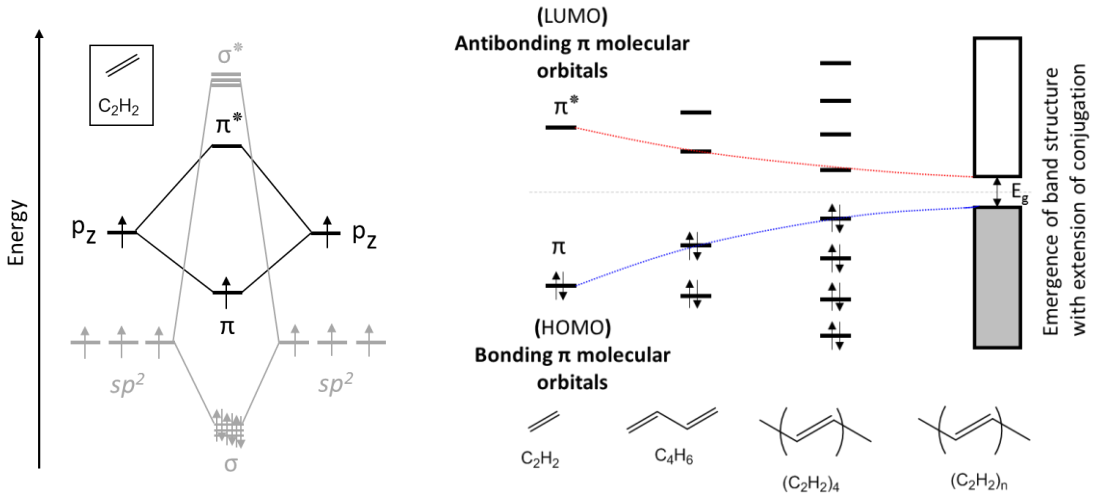


**Figure 1.5.** Schematic representation of molecular orbitals in ethylene, highest occupied molecular orbital (HOMO), lowest unoccupied molecular orbital (LUMO) and evolution of band structures with extension of conjugation from butadiene to polyacetylene as the simplest π-conjugated system. Adapted from reference[24].

## 1.4.3. Concept of doping and conductivity in PANI

Although polyaniline has been known for more than 150 years, the mechanism of its conductivity was not researched until the 1980's when A. Heeger, G. MacDiarmid, and H. Shirakawa realized that the conductivity of π-conjugated polymer materials such as polyacetylene significantly increased by oxidative doping with halogens. After that, electrically conducting polymers were born which was recognized by the Nobel Prize in Chemistry in 2000 *"for the discovery and development of conductive polymers"*.[53] After that time, the research area related to electronic conducting polymers was initiated that gained considerable attraction for many potential applications.

In semiconductors, the addition of suitable impurities (dopant) to material is known as doping. A dopant is introduced into a semiconductor and leads to an increase in the number of free charge carriers, which are either electrons or holes. Depending on the type of dopant, the resultant extrinsic semiconductor could be identified as p-type or n-type. If an electron is transferred from

the polymer backbone to a dopant, the polymer undergoes internal oxidation to leave the polymer positively charged. This type of electron transfer is known as p-doping. On the other hand, if an electron is transferred from the dopant to a polymer, the polymer backbone is reduced and creates a negative charge carrier which is known as n-doping. Polyaniline is a p-type intrinsic semiconductor,[50] where it has the highest conductivity in its doped state. The notable increase in the electrical conductivity after the proton doping process is attributed to the creation of polarons and bipolarons through an internal redox reaction (Figure 1.6).

Therefore, dopants can result in the formation of two new lower intraband transitions and consequently new charge carriers, radical ions (polarons and bipolarons) are formed. The creation of these mid-gap levels in doped polymers greatly affects their conductivity as electronic transitions become dominated by two lower energy sub-gap transitions from the VB to the bipolaronic bands (indicated as $E_{b1}$ and $E_{b2}$ in Figure 1.7a,b). Further doping (oxidation or reduction) leads to the formation of bipolaron defects (coupled cations or dication species) and as the polymer is further doped, bipolaron energy states overlap to create bipolaronic band structures as presented in Figure 1.7a,b.[51-52] This leads to the development of lower energy absorptions and enhanced polymer conductivity. Depending on the type of doping (p- or n- for oxidation or reduction) and the charge introduced into polymer, polarons can be either positive or negative.

Therefore, the dopant can result in the formation of a new band by acting as electron acceptor or donor which allows new electronic transitions at lower energies to become possible and leads to variations in the conductivity level.[53] Figure 1.7d shows that the color of PANI solution at pH values of 8 and 12 shifted from green to blue and violet. This blue shift upon PANI de-doping is due to the disappearance of the polaron bands as the absorption band of low bipolaronic and bipolaronic transitions appear at lower energies.

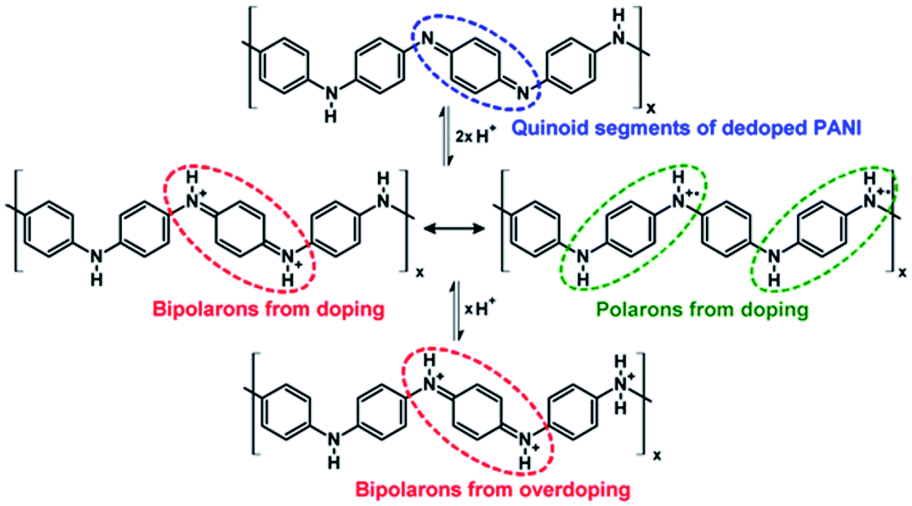


**Figure 1.6.** Doping PANI with acids and internal oxidation (the same number of electrons). Formation of positive polarons and bipolaron charge carriers with doping of 2 equivalents of acid. Reprinted from reference[54] with permission from The Royal Society of Chemistry.

Figure 1.7c shows the ultra violet and visible light (UV-vis) spectra of PANI nanomaterials with increasing proton doping (p doping) levels at variable pH. As expected, PANI exists in a doped state at pH 3, as indicated by the appearance of polaron band transitions around 420 nm and 800 to 1000 nm. However, at pH 12, PANI completely transformed into the emeraldine base (EB) de-doped state, where the polaron bands at 420 nm and 800-1000 nm disappeared.[52] The polaron absorption band around 420 nm is found only for pH values below pH 7, where PANI is doped.[55] At higher levels of doping, an overlap between bipolaron states result in the formation of two wide bipolaron bands within the intrinsic band gap of the polymer. For example, the doping of polypyrrole (33 mol %) results in the overlap of bipolaron states and the formation of bipolaron bands. This led to an increase in the polymer band gap from 3.2 to 3.6 eV in 33 mol% doping.[51] The increase in band gap is due to the fact that upon doping, bipolaron electrons are removed from VB and CB. Consequently, the bipolaron bands that are generated within the gap are taken from the VB and CB, where the Fermi level shifts accordingly due to formation of electron holes.

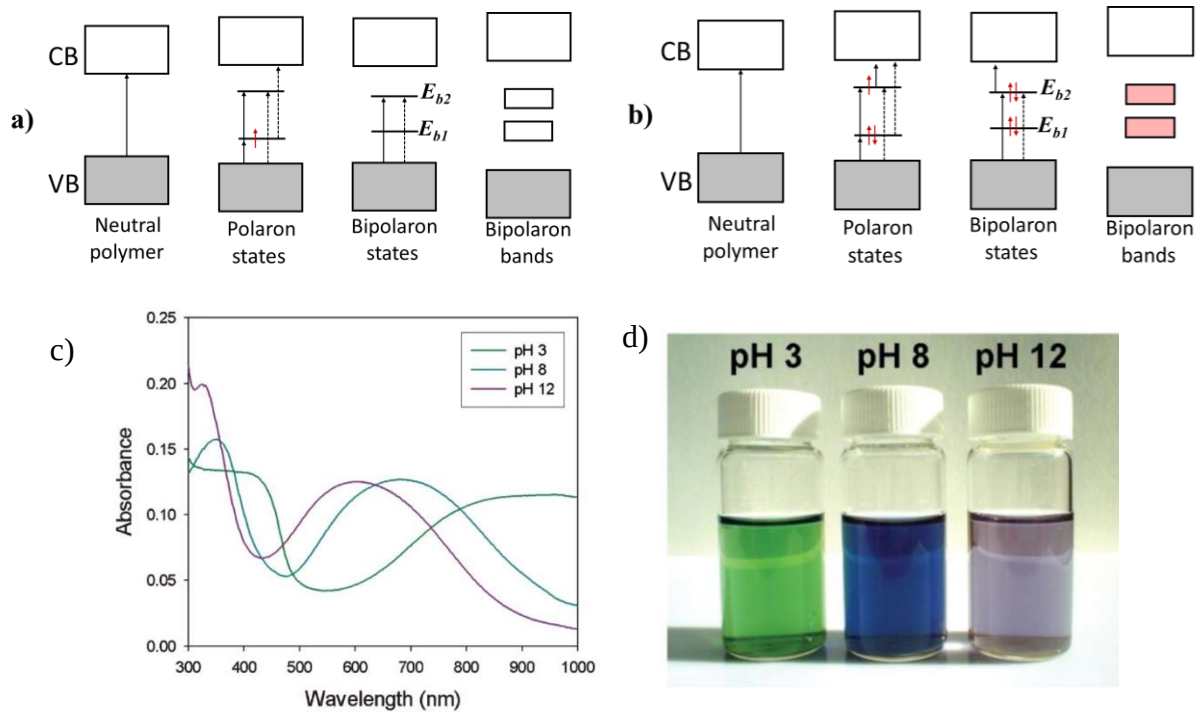


**Figure 1.7.** Band theory in conducting polymers. (a) Formation of positive polaron at lower doping level, bipolarons at moderate doping level and bipolaron bands at high doping level (p-doping). (b) Formation of negative polaron at lower doping level, bipolarons at moderate doping level and bipolaron bands at high doping level (n-doping).[56] CB: Conduction band, VB: Valence band. (c) UV-vis spectra of the silica-PANI core-shell nanoparticles at different proton doping levels. (d) Photograph of the PANI containing nanoparticles at different doping levels. Adapted and reprinted from reference[52] with permission from The Royal Society of Chemistry.

## 1.4.4. Stimuli-responsiveness

Stimuli-responsive polymers are a class of materials that respond to change in their environment by altering their physicochemical properties.[57] These polymers can respond to change in a variety of stimuli such as pH, temperature, ionic strength, light, magnetic field, reduction/oxidation, $CO_2/N_2$[58] and small molecules or chemical species.[59] In other words, these materials can adopt to changes in their surrounding environment.[57, 60] These types of polymers have found widespread applications in many fields that include drug delivery, adsorption and separation,[58] controlled- release,[61] sensors, fuel cells, tissue engineering etc.[57, 62] PANI has interesting multi-stimuli responsiveness since it can respond to pH, oxidation, reduction and

electric field.[61, 63] In chapter 4 of this thesis, it will be shown that PANI also can respond to salinity which extends its applicability beyond normal interaction with acids dopants by the formation of bipolarons and also affect the intermolecular packing structure.

## 1.4.5. PANI based adsorbents

### 1.4.5.1. Adsorption of metal ions

PANI materials have aroused considerable attention for applications in many areas especially for the adsorption of metal ions due to the low cost of the monomer, facile synthesis, and technical advantages, such as environmental stability, reversible doping/de-doping chemistry.[14] Polyaniline by itself or in a composite forms has been shown to have an incredible potential for removal of heavy metal ions such as Pb (II),[64] Cu (II),[64-65] Hg (II),[66] Cd (II),[64, 67] Cr (VI),[64, 68-69] Eu (III), Cs (I), Sr (II)[46] from water due to numerous amine (-NH-) and imine (-N=) functional groups. Adsorption occurs by the formation of complexes with accessible sites such as amine, imine, or other functional groups of PANI in its modified forms.[11, 70] Redox-active PANI nanofibers that serve as working electrodes have been designed by Kim et al. for reversible and selective adsorption of $Hg^{2+}$ ions from water (Figure 1.8a,b).[11] Due to their simple doping/de-doping chemistry, the materials can yield electrochemically switchable and reusable adsorbents (Figure 1.8a). In its de-doped state, PANI is anticipated to capture metal ions. However, upon oxidization electrochemically, it becomes doped with positively charged nitrogen site that result in the release of cations as a result of electrostatic repulsion with the adsorbent surface.

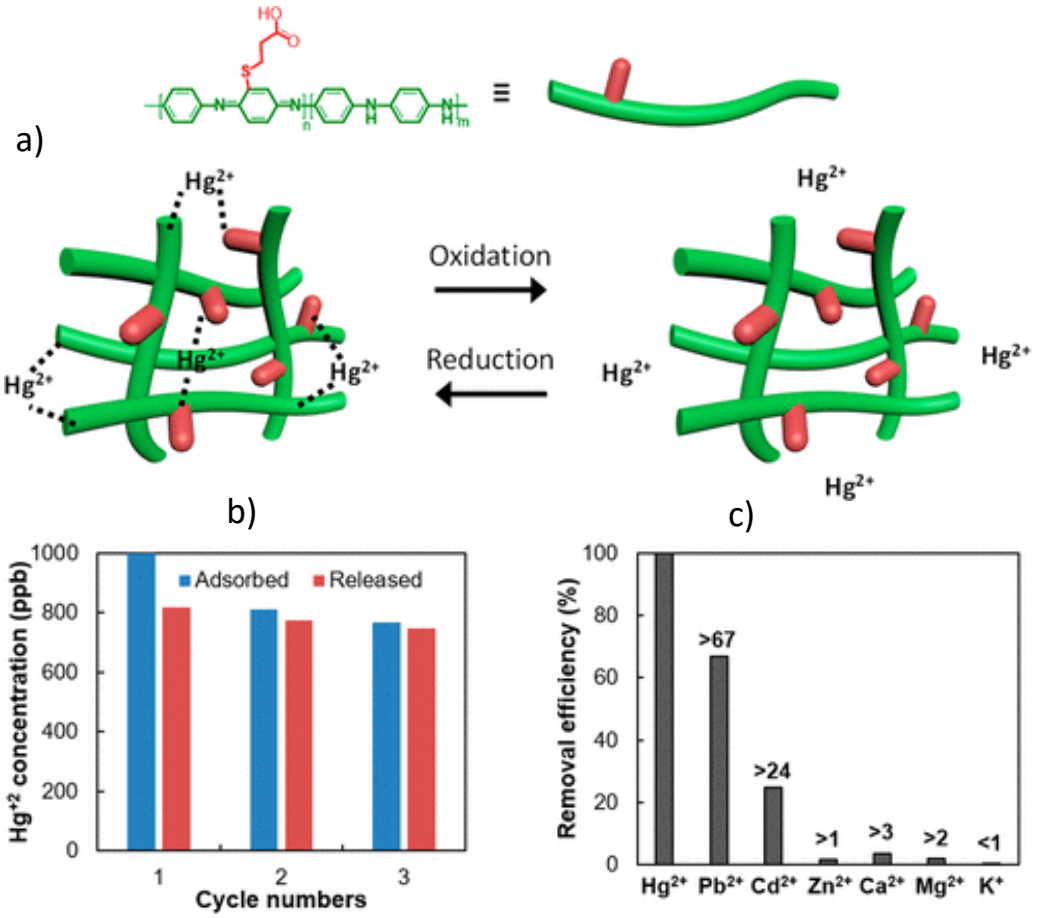


**Figure 1.8.** (a) Schematic representation of modified PANI nanofibers and their switchable doping/de-doping chemistry accompanied by catch and release of mercury. **Note**: release experiments were carried out under oxidation potentials, therefore reduction of $Hg^{2+}$ to $Hg^{+}$ or $Hg^{0}$ form does not occur. (b) Recyclability of functionalized PANI for catch and release of mercury ions from solution. Release by achieved applying a fixed oxidation potential. (c) selective adsorption of mercury by PANI towards various cations. Adapted and reprinted with permission from reference[11] © 2018 American Chemical Society.

The relatively low adsorption capacity of PANI and its limited functional groups for the removal of metal ions can be circumvented by modification of PANI due to its simple doping/de-doping and electrochemical modulation. Doping PANI with phytic acid has been reported to remove Cu (II) ions from solution with markedly improved adsorption capacity in comparison to undoped PANI (Figure 1.9a,b). Doping PANI with phytic acid leads to functionalization of PANI with phosphate functional groups which have high ionic attraction to copper ions (Figure 1.9a).[65]

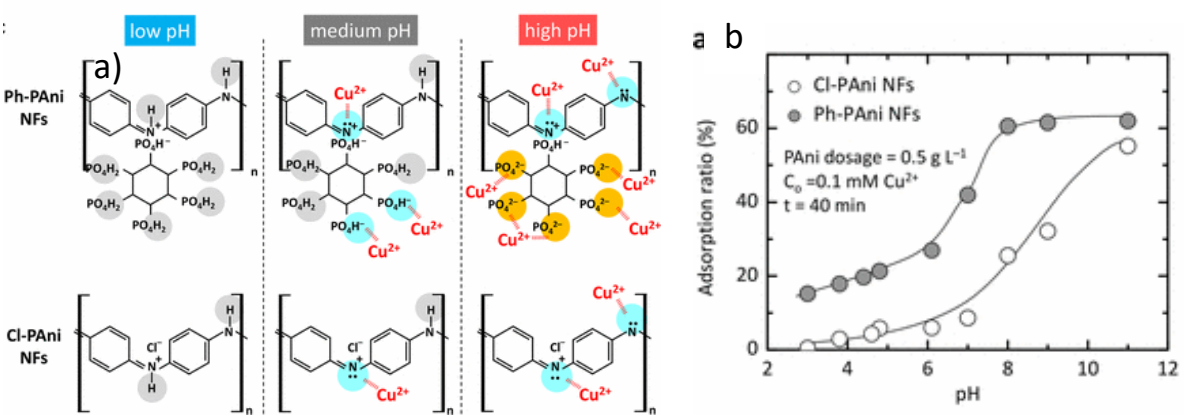


**Figure 1.9.** (a) Chemical formulae and adsorption sites of PANII nanofibers doped with Cl and phytic acid under different pH conditions for adsorption of $Cu^{2+}$ ions. (b) comparison of $Cu^{2+}$ adsorption to PANI nanofibers doped with Cl (Cl-PAni NFs) and phytic acid (Ph-PAni NFs). Adapted and reprinted with permission from reference[65] © 2017 American Chemical Society.

### 1.4.5.2. Adsorption of organic dyes

PANI in various composites forms, in a de-doped and doped form has been used for adsorption of cationic and anionic dyes.[47, 70-74] Doping/de-doping affords tunability of PANI that allows for its applicability in the removal of both cationic and anionic dyes from aqueous solution. PANI doped with various acids exists as the emeraldine salt form, carrying positive charges on its backbone (protonated quinoid sites) which provide favorable interaction sites for anionic dyes such as congo red, acid green 25 and acid red 18.[74-75] Increasing pH of the solution, leads to the conversion of the emeraldine salt into the undoped PANI base and depletion of the polaron/bipolaron adsorption sites. As a result, active adsorption sites are depleted and adsorption of anionic dyes are retarded due to repulsive electrostatic interactions.[75-77] PANI in its undoped form has been used for adsorption of cationic dyes such as MB and brilliant green.[47, 73, 78-79] MB is a typical cationic dye, where the adsorption onto PANI (emeraldine base form) occurs via hydrogen bonding, dipole-dipole interactions, and π-π interactions. However, for anionic dyes in a doped form additional electrostatic attractions may also play a crucial role in the adsorption process.[1]

Although PANI in its pure form was reported as an effective adsorbent for various organic dyes, organic-inorganic PANI hybrid nanomaterials have received a wide range of interest for adsorption-based applications. This is due to their multifunctional characteristics, synergistic effects and enhanced adsorption performance. Polyaniline nanocomposites (NCs) with inorganic materials such as Polyaniline-silica,[74] Polyaniline-zirconium,[72] Polyaniline-silver[79] and Polyaniline-iron oxide materials[80] showed higher adsorption capacity for removal of organic dyes, in comparison to PANI in its pure form.

## 1.5. Catalytic reduction of dyes

Among current technologies that can be used to remove dyes, chemical reduction of dyes is another alternative approach.[81] Reduction of organic dyes such as MB and 4-NPh is crucial because these compounds are widely used in various industries. MB is a toxic cationic dye with a bright and intense blue color.[82] 4-NPh is considered as priority water pollutant. Reduction of these dyes yield by-products that can be used as useful intermediates in many fields and applications.[82-83] The reduced forms of these dye-based compounds, leucomethylene blue (LMB) and 4-aminophenol (4-APh), are not only less hazardous compared to original oxidized dyes, they are also considered as important synthetic precursors for various industrial applications.[81-83] For example, the bright color of MB can block photosynthesis and affect the growth of plants in aqueous environments by reducing sunlight penetration in contaminated water environments. However, the blue color rapidly disappears in reduced form i.e. LMB ($\lambda_{max}$ = 256 nm). The reduction and oxidation of MB to LMB also have found to be a useful process in many applications. For example, in industrial applications reduction and oxidation of MB establishes the colorimetric oxygen indicators by accepting or donating hydronium ions.[82] The reduced form of

4-NPh (i.e. 4-APh) has many applications in photography, oxidation inhibition, and in chemical synthesis as a precursor for the synthesis of paracetamol.[82]

However, these dyes are not reduced easily in aqueous solution using $NaBH_4$ because the reaction is not kinetically favoured under conventional conditions. For this transition, electrons are needed to undergo transfer from $BH_4^-$ to the dye species. Further, both dye species, the borohydride ions are needed to attach onto the surface to have an efficient interaction for electron transfer. Noble metal nanoparticles with high surface area and efficient catalytic activity have been frequently used for this purpose as a catalyst.

### 1.5.1. Noble metal nanocatalyst

Heterogeneous catalysis based on noble metal nanostructures such as Au, Ag, Pd and Pt is a promising strategy for hydrogenation and reduction reactions, especially for dye removal and wastewater treatment.[84] Generally, noble metals are expensive, and catalysis is a surface phenomenon. Therefore, to lower the cost of a potential catalyst and improve its atom efficiency, the high surface area of metallic catalysts is of central importance. However, utilization of bare metal nanoparticles has disadvantages due to aggregation of particles due to their high surface energies.[84] Nanoparticles are also difficult to be isolated from the reaction solution. Due to these limitations, the efforts to design efficient catalysts systems and catalyst supports are necessary. Polymer supports not only mitigate nanocatalyst agglomeration, but also facilitate more effective phase separation from solution for the regeneration and utilization for consecutive processing cycles. Furthermore, hybridization of noble metal nanoparticles with suitable supports result in the emergence of new functional properties and synergistic effects arise from the respective components and their combinatorial effects.[85] Immobilizing metal nanoparticles onto a supporting material has another major advantage related to greater ease of separation by conventional

filtration of centrifugation. As noble metals are expensive, their regeneration is another strategy to further reduce the cost of the catalyst.[84]

Various organic and inorganic support materials have been used to design catalyst systems for reduction processes and water treatment. Biopolymers such as chitosan,[86-87] cellulose[84, 87-89] and starch[90] have been successfully used as supports for metal nanocatalyst systems. These biomass derived polymer supports have advantages such as availability, low cost, non-toxicity, biocompatibility and high adsorption affinity and adsorption capacity towards metal ions which provide unique opportunities to design catalysts with high performance for reduction of dyes.[84] In this thesis, PANI/chitosan composites were employed as supports for silver nanoparticles to make use of the aforementioned advantages of PANI for reduction of 4-NPh in aqueous solution. The catalytic reduction of 4-NPh serves as part of an overall strategy for dye treatment in this thesis.

# 1.6. Thesis scope

## 1.6.1. Objectives of the project

The overall objective of this thesis relates to the removal of dye species in aqueous solution by design and fabrication of high performance and multifunctional stimuli-responsive polymer nanocomposites. To accomplish this goal, two distinct approaches of adsorption and catalytic reduction of dyes was investigated, where the results are reported in chapters 2-5. Therefore, in chapter 2 and 4, PANI- and chitosan-based adsorbent materials with high adsorption capacity are described for dye adsorption-based applications. The chemical-based approach focuses on design of stimuli-responsive nanocomposites with high catalytic activity for dye reduction which is reported in chapter 3. Chapter 5 specifically focuses on the mechanism of dye adsorption on PANI adsorbents and hydrogen bonding as function of ionic dye and salt concentration. Over the course of four projects in this thesis, this thesis describes design of nanocomposites for dye removal and

the molecular mechanism of dye removal. Each of these individual chapters contributes toward the overall objective, with the theme of dye removal from aqueous solution.

## 1.6.2. Connection between chapters

As mentioned in section 1.6.1., two approaches of adsorption and catalytic reduction were explored towards dye removal from aqueous solution in order to achieve overall goal. In this section the logical transition between chapters and their contribution to overall objective of thesis is described.

In chapter 2, chitosan was modified to design pH-responsive polymer nanocomposites for adsorption of a cationic dye (methylene blue; MB). In this chapter, the design, characterization of the dye adsorption performance and adsorption mechanism were explored in detail. The goal of this project was to design nano-based adsorbents with superior and exceptional adsorption behavior for MB. This project investigates the development of chitosan based adsorbent materials for the removal of methylene blue from aqueous solution. Chitosan in its native form suffers from a relatively low surface area, lack of surface charge and adsorption sites for cationic dye adsorption. Grafting polyacids onto the backbone of chitosan and incorporating onto magnetite nanocrystals results in the design of polymer nanocomposites with stimuli-responsive properties with superior adsorption performance for cationic dye. An increase in the adsorption efficiency of MB was achieved according to the synthesis of pH-responsive polymer brush nanocomposites.

In chapter 3, the catalytic reduction approach was used to remove 4-NPh from aqueous solution. Therefore, an efficient nanocatalyst based on Ag and PANI were designed by hybridization and interfacing two components which resulted in higher catalytic activity towards reduction of 4-NPh to 4-APh. In this chapter, to achieve an increase in the catalytic activity of silver nanoparticles, polyaniline was used as a support to develop redox responsive catalyst

systems with remarkably increased catalytic behavior toward reduction of 4-nitrophenol to 4-aminophenol.

Chapter 4 will elaborate upon the design and adsorption properties of PANI/magnetite nanocomposites for the removal of MB and MO dyes. Selective adsorption of MB over MO by PANI nanocomposites led us to investigate dye adsorption mechanism by exposing nanocomposites to NaCl and to monitor their phase behavior and physical properties. The results indicated that salt interaction with PANI resulted in the formation of polarons and bipolarons that provided further details on the mechanism of cationic dye adsorption. In this chapter, polyaniline magnetite nanocomposites were prepared for selective adsorption of mixtures that contain methylene blue and methyl orange. While investigating the mechanism of dye adsorption in PANI nanocomposites, salt-responsive behavior was discovered, and the mechanism of salt interaction contributed to the overall project as a path to carry out systematic studies on the mechanism of dye adsorption.

In order to gain further details on dye adsorption on PANI and intermolecular hydrogen bonding, self-healing materials capable of forming hydrogen bonding were encapsulated inside PANI and mechanism of release of these materials as function of time when exposed to salt was investigated. The results confirmed that salt interaction with PANI and disruption of hydrogen bonding is a combination of several factors that are triggered by salt mediated processes. In this chapter, salt-responsive PANI capsules were prepared and self-healing molecular species were entrapped physically within the capsular materials. Then their salt-responsive release behavior was studied. The mechanism of salt-induced release contributed to the overall project as a means to study the mechanism of dye and salt interactions.

# 1.7. References


1. Nasar, A.; Mashkoor, F., Application of Polyaniline-Based Adsorbents for Dye Removal from Water and Wastewater-A Review. *Environ. Sci. Pollut. R* **2019**, *26*, 5333-5356.

2. Huang, Y.; Li, J.; Chen, X.; Wang, X., Applications of Conjugated Polymer Based Composites in Wastewater Purification. *RSC Adv.* **2014**, *4*, 62160-62178.

3. Sen, T. K.; Afroze, S.; Ang, H. M., Equilibrium, Kinetics and Mechanism of Removal of Methylene Blue from Aqueous Solution by Adsorption onto Pine Cone Biomass of Pinus radiata. *Water Air Soil Pollut.* **2010**, *218*, 499-515.

4. Yagub, M. T.; Sen, T. K.; Afroze, S.; Ang, H. M., Dye and its Removal from Aqueous Solution by Adsorption: A review. *Adv. Colloid Interface Sci.* **2014**, *209*, 172-184.

5. Banat, I. M.; Nigam, P.; Singh, D.; Marchant, R., Microbial Decolorization of Textile-Dye-Containing Effluents: A Review. *Bioresour. Technol.* **1996**, *58*, 217-227.

6. Ali, I., New Generation Adsorbents for Water Treatment. *Chem. Rev.* **2012**, *112*, 5073-5091.

7. Yu, J.-G.; Yue, B.-Y.; Wu, X.-W.; Liu, Q.; Jiao, F.-P.; Jiang, X.-Y.; Chen, X.-Q., Removal of Mercury by Adsorption: A Review. *Environ. Sci. Pollut. Res.* **2015**, *23*, 5056-5076.

8. Huang, N.; Zhai, L.; Xu, H.; Jiang, D., Stable Covalent Organic Frameworks for Exceptional Mercury Removal from Aqueous Solutions. *J. Am. Chem. Soc.* **2017**, *139*, 2428-2434.

9. Ma, L.; Wang, Q.; Islam, S. M.; Liu, Y.; Ma, S.; Kanatzidis, M. G., Highly Selective and Efficient Removal of Heavy Metals by Layered Double Hydroxide Intercalated with the $MoS_4^{2-}$ Ion. *J. Am. Chem. Soc.* **2016**, *138*, 2858-2866.

10. Huang, P.; Xia, D.; Kazlauciunas, A.; Thornton, P.; Lin, L.; Menzel, R., Dye-Mediated Interactions in Chitosan-Based Polyelectrolyte/Organoclay Hybrids for Enhanced Adsorption of Industrial Dyes. *ACS Appl. Mater. Interfaces* **2019**, *11*, 11961-11969.

11. Kim, Y.; Lin, Z.; Jeon, I.; Van Voorhis, T.; Swager, T. M., Polyaniline Nanofiber Electrodes for Reversible Capture and Release of Mercury(II) from Water. *J. Am. Chem. Soc.* **2018**, *140*, 14413-14420.

12. Sun, D. T.; Peng, L.; Reeder, W. S.; Moosavi, S. M.; Tiana, D.; Britt, D. K.; Oveisi, E.; Queen, W. L., Rapid, Selective Heavy Metal Removal from Water by a Metal–Organic Framework/Polydopamine Composite. *ACS Cent. Sci.* **2018**, *4*, 349-356.

13. Wei, W.; Lu, R.; Xie, H.; Zhang, Y.; Bai, X.; Gu, L.; Da, R.; Liu, X., Selective Adsorption and Separation of Dyes From an Aqueous Solution on Organic–Inorganic Hybrid Cyclomatrix Polyphosphazene Submicro-Spheres. *J. Mater. Chem. A* **2015**, *3*, 4314-4322.

14. Trey, S.; Jafarzadeh, S.; Johansson, M., In situ Polymerization of Polyaniline in Wood Veneers. *ACS Appl. Mater. Interfaces* **2012**, *4*, 1760-1769.

15. Dash, M.; Chiellini, F.; Ottenbrite, R. M.; Chiellini, E., Chitosan-A Versatile Semi-Synthetic Polymer in Biomedical Applications. *Prog. Polym. Sci.* **2011**, *36*, 981-1014.

16. Honarkar, H.; Barikani, M., Applications of Biopolymers I: Chitosan. *Monatsh. Chem.* **2009**, *140*, 1403-1420.

17. Giri, T. K.; Thakur, A.; Alexander, A.; Ajazuddin; Badwaik, H.; Tripathi, D. K., Modified Chitosan Hydrogels as Drug Delivery and Tissue Engineering Systems: Present Status and Applications. *Acta Pharmacol. Sin. B* **2012**, *2*, 439-449.

18. Kyzas, G.; Bikiaris, D., Recent Modifications of Chitosan for Adsorption Applications: A Critical and Systematic Review. *Mar. Drugs* **2015**, *13*, 312-337.

19. Wang, J.; Zhuang, S., Removal of Various Pollutants from Water and Wastewater by Modified Chitosan Adsorbents. *Crit. Rev. Env. Sci. Technol.* **2018**, *47*, 2331-2386.

20. Meng, Q.; Heuzey, M.-C.; Carreau, P. J., Hierarchical Structure and Physicochemical Properties of Plasticized Chitosan. *Biomacromolecules* **2014**, *15*, 1216-1224.

21. Trung, T. S.; Ng, C. H.; Stevens, W. F., Characterization of Decrystallized Chitosan and its Application in Biosorption of Textile Dyes. *Biotechnol. Lett.* **2003**, *25*, 1185-1190.

22. Ghorai, S.; Sarkar, A.; Raoufi, M.; Panda, A. B.; Schönherr, H.; Pal, S., Enhanced Removal of Methylene Blue and Methyl Violet Dyes from Aqueous Solution Using a Nanocomposite of Hydrolyzed Polyacrylamide Grafted Xanthan Gum and Incorporated Nanosilica. *ACS Appl. Mater. Interfaces* **2014**, *6*, 4766-4777.

23. Wang, J.; Chen, C., Chitosan-Based Biosorbents: Modification and Application for Biosorption of Heavy Metals and Radionuclides. *Bioresour. Technol.* **2014**, *160*, 129-141.

24. Stalder, R., Organic Semiconducting Molecules and Polymers for Solution Processed Organic Electronics. PhD Thesis; University of Florida, **2015**, 1-50.

25. Habiba, U.; Afifi, A. M.; Salleh, A.; Ang, B. C., Chitosan/(Polyvinyl Alcohol)/Zeolite Electrospun Composite Nanofibrous Membrane for Adsorption of $Cr^{6+}$, $Fe^{3+}$ and $Ni^{2+}$. *J. Hazard. Mater.* **2017**, *322*, 182-194.

26. Wu, S.-J.; Liou, T.-H.; Yeh, C.-H.; Mi, F.-L.; Lin, T.-K., Preparation and Characterization of Porous Chitosan-Tripolyphosphate Beads for Copper(II) ion Adsorption. *J. Appl. Polym. Sci.* **2013**, *127*, 4573-4580.

27. Vincent, C.; Barre, Y.; Vincent, T.; Taulemesse, J. M.; Robitzer, M.; Guibal, E., Chitin-Prussian Blue Sponges for Cs(I) Recovery: From Synthesis to Application in the Treatment of Accidental Dumping of Metal-Bearing Solutions. *J. Hazard. Mater.* **2015**, *287*, 171-179.

28. Zhang, H.; Dang, Q.; Liu, C.; Cha, D.; Yu, Z.; Zhu, W.; Fan, B., Uptake of Pb(II) and Cd(II) on Chitosan Microsphere Surface Successively Grafted by Methyl Acrylate and Diethylenetriamine. *ACS Appl. Mater. Interfaces* **2017**, *9*, 11144-11155.

29. Kyzas, G. Z.; Siafaka, P. I.; Lambropoulou, D. A.; Lazaridis, N. K.; Bikiaris, D. N., Poly(itaconic acid)-Grafted Chitosan Adsorbents with Different Cross-Linking for Pb(II) and Cd(II) Uptake. *Langmuir* **2014**, *30*, 120-131.

30. Mohamed, M. H.; Udoetok, I. A.; Wilson, L. D.; Headley, J. V., Fractionation of Carboxylate Anions from Aqueous Solution Using Chitosan Cross-Linked Sorbent Materials. *RSC Adv.* **2015**, *5* (100), 82065-82077.

31. Ayoub, A.; Venditti, R. A.; Pawlak, J. J.; Salam, A.; Hubbe, M. A., Novel Hemicellulose–Chitosan Biosorbent for Water Desalination and Heavy Metal Removal. *ACS Sustainable Chem. Eng.* **2013**, *1*, 1102-1109.

32. Wang, Y.; Dang, Q.; Liu, C.; Yu, D.; Pu, X.; Wang, Q.; Gao, H.; Zhang, B.; Cha, D., Selective Adsorption toward Hg(II) and Inhibitory Effect on Bacterial Growth Occurring on Thiosemicarbazide-Functionalized Chitosan Microsphere Surface. *ACS Appl. Mater. Interfaces* **2018**, *10*, 40302-40316.

33. Timur, M.; Paşa, A., Synthesis, Characterization, Swelling, and Metal Uptake Studies of Aryl Cross-Linked Chitosan Hydrogels. *ACS Omega* **2018**, *3*, 17416-17424.

34. Elwakeel, K. Z.; El-Bindary, A. A.; Ismail, A.; Morshidy, A. M., Magnetic Chitosan Grafted with Polymerized Thiourea for Remazol Brilliant Blue R Recovery: Effects of Uptake Conditions. *J. Dispersion Sci. Technol.* **2016**, *38*, 943-952.

35. Udoetok, I. A.; Wilson, L. D.; Headley, J. V., Self-Assembled and Cross-Linked Animal and Plant-Based Polysaccharides: Chitosan–Cellulose Composites and Their Anion Uptake Properties. *ACS Appl. Mater. Interfaces* **2016**, *8*, 33197-33209.

36. Mahaninia, M. H.; Wilson, L. D., Modular Cross-Linked Chitosan Beads with Calcium Doping for Enhanced Adsorptive Uptake of Organophosphate Anions. *Ind. Eng. Chem. Res.* **2016**, *55*, 11706-11715.

37. Ge, H.-C.; Luo, D.-K., Preparation of Carboxymethyl Chitosan in Aqueous Solution Under Microwave Irradiation. *Carbohydr. Res.* **2005**, *340*, 1351-1356.

38. Mahaninia, M. H.; Wilson, L. D., Phosphate Uptake Studies of Cross-Linked Chitosan Bead Materials. *J. Colloi. Interface Sci.* **2017**, *485*, 201-212.

39. Chen, A.-H.; Liu, S.-C.; Chen, C.-Y.; Chen, C.-Y., Comparative Adsorption of Cu(II), Zn(II), and Pb(II) Ions in Aqueous Solution on the Crosslinked Chitosan with Epichlorohydrin. *J. Hazard. Mater.* **2008**, *154*, 184-191.

40. Mahaninia, M. H.; Wilson, L. D., Cross-Linked Chitosan Beads for Phosphate Removal From Aqueous Solution. *J. Appl. Polym. Sci.* **2016**, *133*, 42949- 42959.

41. Bhattacharya, A., Grafting: a Versatile Means to Modify Polymers: Techniques, Factors and Applications. *Prog. Polym. Sci.* **2004**, *29*, 767-814.

42. Li, N.; Bai, R., Development of Chitosan-Based Granular Adsorbents for Enhanced and Selective Adsorption Performance in Heavy Metal Removal. *Water Sci. Technol.* **2006**, *54*, 103-113.

43. Benamer, S.; Mahlous, M.; Tahtat, D.; Nacer-Khodja, A.; Arabi, M.; Lounici, H.; Mameri, N., Radiation Synthesis of Chitosan Beads Grafted with Acrylic Acid for mMetal Ions Sorption. *Radiat. Phys. Chem.* **2011**, *80*, 1391-1397.

44. Genies, E. M.; Boyle, A.; Lapkowski, M.; Tsintavis, C., Polyaniline: a Historical Survey. *Synth. Met.* **1990**, *36*, 139-182.

45. Shimano, J. Y.; MacDiarmid, A. G., Polyaniline, a Dynamic Block Copolymer: Key to Attaining its Intrinsic Conductivity? *Synth. Met.* **2001**, *123* (2), 251-262.

46. Sun, Y. B.; Shao, D. D.; Chen, C. L.; Yang, S. B.; Wang, X. K., Highly Efficient Enrichment of Radionuclides on Graphene Oxide-Supported Polyaniline. *Environ. Sci. Technol.* **2013**, *47*, 9904-9910.

47. Mohamed, M. H.; Dolatkhah, A.; Aboumourad, T.; Dehabadi, L.; Wilson, L. D., Investigation of Templated and Supported Polyaniline Adsorbent Materials. *RSC Adv.* **2015**, *5* (9), 6976-6984.

48. Li, D.; Huang, J.; Kaner, R. B., Polyaniline Nanofibers: A Unique Polymer Nanostructure for Versatile Applications. *Acc. Chem. Res.* **2009**, *42*, 135-145.

49. Abu-Thabit, N. Y., Chemical Oxidative Polymerization of Polyaniline: A Practical Approach for Preparation of Smart Conductive Textiles. *J. Chem. Educ.* **2016**, *93*, 1606-1611.

50. Yakuphanoglu, F.; Şenkal, B. F., Electronic and Thermoelectric Properties of Polyaniline Organic Semiconductor and Electrical Characterization of Al/PANI MIS Diode. *J. Phys. Chem. C* **2007**, *111*, 1840-1846.

51. Bredas, J. L.; Street, G. B., Polarons, Bipolarons, and Solitons in Conducting Polymers. *Acc. Chem. Res.* **2002**, *18*, 309-315.

52. Jang, J.; Ha, J.; Lim, B., Synthesis and Characterization of Monodisperse Silica–Polyaniline Core–Shell Nanoparticles. *Chem. Commun.* **2006**, 1622-1624.

53. Heeger, A. J., Semiconducting and Metallic Polymers: The Fourth Generation of Polymeric Materials (Nobel lecture). *Angew. Chem. Int. Ed.* **2001**, *40*, 2591-2611.

54. Silva, C. H. B.; Ferreira, A. M. D.; Constantino, V. R. L.; Temperini, M. L. A., Hybrid Materials of Polyaniline and Acidic Hexaniobate Nanoscrolls: High Polaron Formation and Improved Thermal Properties. *J. Mater. Chem. A* **2014**, *2*, 8205-8214.

55. Stejskal, J.; Kratochvíl, P.; Radhakrishnan, N., Polyaniline Dispersions 2. UV-Vis Absorption Spectra. *Synth. Met.* **1993**, *61*, 225-231.

56. Beverina, L.; Pagani, G. A.; Sassi, M., Multichromophoric Electrochromic Polymers: Colour Tuning of Conjugated Polymers Through the Side Chain Functionalization Approach. *Chem. Commun.* **2014**, *50*, 5413-5430.

57. Stuart, M. A. C.; Huck, W. T. S.; Genzer, J.; Müller, M.; Ober, C.; Stamm, M.; Sukhorukov, G. B.; Szleifer, I.; Tsukruk, V. V.; Urban, M.; Winnik, F.; Zauscher, S.; Luzinov, I.; Minko, S., Emerging Applications of Stimuli-Responsive Polymer Materials. *Nat. Mater.* **2010**, *9*, 101-113.

58. Li, Y.; Zhu, L.; Grishkewich, N.; Tam, K. C.; Yuan, J.; Mao, Z.; Sui, X., CO2-Responsive Cellulose Nanofibers Aerogels for Switchable Oil–Water Separation. *ACS Appl. Mater. Interfaces* **2019**, *11*, 9367-9373.

59. Gao, Y.; Wei, M.; Li, X.; Xu, W.; Ahiabu, A.; Perdiz, J.; Liu, Z.; Serpe, M. J., Stimuli-Responsive Polymers: Fundamental Considerations and Applications. *Macromol. Res.* **2017**, *25*, 513-527.

60. Karoyo, A. H.; Wilson, L. D., Preparation and Characterization of a Polymer-Based "Molecular Accordion". *Langmuir* **2016**, *32*, 3066-3078.

61. Zhao, Y.; Lv, L.-P.; Jiang, S.; Landfester, K.; Crespy, D., Advanced Stimuli-Responsive Polymer Nanocapsules with Enhanced Capabilities for Payloads Delivery. *Polym. Chem.* **2015**, *6*, 4197-4205.

62. Wei, M.; Gao, Y.; Li, X.; Serpe, M. J., Stimuli-Responsive Polymers and their Applications. *Poly. Chem.* **2017**, *8*, 127-143.

63. Kolosnjaj-Tabi, J.; Gibot, L.; Fourquaux, I.; Golzio, M.; Rols, M.-P., Electric Field-Responsive Nanoparticles and Electric Fields: Physical, Chemical, Biological Mechanisms and Therapeutic Prospects. *Adv. Drug Delivery Rev.* **2019**, *138*, 56-67.

64. Alcaraz-Espinoza, J. J.; Chávez-Guajardo, A. E.; Medina-Llamas, J. C.; Andrade, C. A. S.; de Melo, C. P., Hierarchical Composite Polyaniline-(Electrospun Polystyrene) Fibers Applied to Heavy Metal Remediation. *ACS Appl. Mater. Interfaces* **2015**, *7*, 7231-7240.

65. Kim, H. J.; Im, S.; Kim, J. C.; Hong, W. G.; Shin, K.; Jeong, H. Y.; Hong, Y. J., Phytic Acid Doped Polyaniline Nanofibers for Enhanced Aqueous Copper(II) Adsorption Capability. *ACS Sustainable Chem. Eng.* **2017**, *5*, 6654-6664.

66. Gupta, R. K.; Singh, R. A.; Dubey, S. S., Removal of Mercury Ions From Aqueous Solutions by Composite of Polyaniline With Polystyrene. *Sep. Purif. Technol.* **2004**, *38*, 225-232.

67. Mansour, M. S.; Ossman, M. E.; Farag, H. A., Removal of Cd (II) Ion From Waste Water by Adsorption onto Polyaniline Coated on Sawdust. *Desalin.* **2011**, *272*, 301-305.

68. Ding, J.; Pu, L. T.; Wang, Y. F.; Wu, B. D.; Yu, A. Q.; Zhang, X. L.; Pan, B. C.; Zhang, Q. X.; Gao, G. D., Adsorption and Reduction of Cr(VI) Together with Cr(III) Sequestration by Polyaniline Confined in Pores of Polystyrene Beads. *Environ. Sci. Technol.* **2018**, *52*, 12602-12611.

69. Zhu, K.; Gao, Y.; Tan, X.; Chen, C., Polyaniline-Modified Mg/Al Layered Double Hydroxide Composites and Their Application in Efficient Removal of Cr(VI). *ACS Sustainable Chem. Eng.* **2016**, *4*, 4361-4369.

70. Das, S.; Chakraborty, P.; Ghosh, R.; Paul, S.; Mondal, S.; Panja, A.; Nandi, A. K., Folic Acid-Polyaniline Hybrid Hydrogel for Adsorption/Reduction of Chromium(VI) and Selective Adsorption of Anionic Dye from Water. *ACS Sustainable Chem. Eng.* **2017**, *5*, 9325-9337.

71. Patra, B. N.; Majhi, D., Removal of Anionic Dyes from Water by Potash Alum Doped Polyaniline: Investigation of Kinetics and Thermodynamic Parameters of Adsorption. *J. Phys. Chem. B* **2015**, *119*, 8154-8164.

72. Wang, L.; Wu, X.-L.; Xu, W.-H.; Huang, X.-J.; Liu, J.-H.; Xu, A.-W., Stable Organic–Inorganic Hybrid of Polyaniline/α-Zirconium Phosphate for Efficient Removal of Organic Pollutants in Water Environment. *ACS Appl. Mater. Interfaces* **2012**, *4*, 2686-2692.

73. Ayad, M. M.; El-Nasr, A. A., Adsorption of Cationic Dye (Methylene Blue) from Water Using Polyaniline Nanotubes Base. *J. Phys. Chem. C* **2010**, *114*, 14377-14383.

74. Ayad, M. M.; El-Nasr, A., Anionic dye (acid green 25) Adsorption from Water by Using Polyaniline Nanotubes Salt/Silica Composite. *J. . Nanostruct. Chem.* **2012**, *3*, 3.

75. Salem, M. A., The Role of Polyaniline Salts in the Removal of Direct Blue 78 from Aqueous Solution: A kinetic study. *React. Funct. Polym.* **2010**, *70*, 707-714.

76. Han, R.; Ding, D.; Xu, Y.; Zou, W.; Wang, Y.; Li, Y.; Zou, L., Use of Rice Husk for the Adsorption of Congo Red from Aqueous Solution in Column Mode. *Bioresour. Technol.* **2008**, *99*, 2938-2946.

77. Shabandokht, M.; Binaeian, E.; Tayebi, H.-A., Adsorption of Food Dye Acid Red 18 onto Polyaniline-Modified Rice Husk Composite: Isotherm and Kinetic Analysis. *Desalin. Water Treat.* **2016**, *57*, 27638-27650.

78. Mu, B.; Tang, J.; Zhang, L.; Wang, A., Preparation, Characterization and Application on Dye Adsorption of a Well-Defined Two-Dimensional Superparamagnetic Clay/Polyaniline/$Fe_3O_4$ Nanocomposite. *Appl. Clay Sci.* **2016**, *132-133*, 7-16.

79. Salem, M. A.; Elsharkawy, R. G.; Hablas, M. F., Adsorption of Brilliant Green Dye by Polyaniline/Silver Nanocomposite: Kinetic, Equilibrium, and Thermodynamic Studies. *Eur. Polym. J.* **2016**, *75*, 577-590.

80. Usmani, M.; Khan, I.; Bhat, A.; Pillai, R.; Ahmad, N.; Haafiz, M.; Oves, M., Current Trend in the Application of Nanoparticles for Waste Water Treatment and Purification: A Review. *Curr. Org. Synth.* **2017**, *14*, 206-226.

81. Zhao, P.; Feng, X.; Huang, D.; Yang, G.; Astruc, D., Basic Concepts and Recent Advances in Nitrophenol Reduction by Gold- and other Transition Metal Nanoparticles. *Coord. Chem. Rev.* **2015**, *287*, 114-136.

82. Sohrabnezhad, S., Study of Catalytic Reduction and Photodegradation of Methylene Blue by Heterogeneous Catalyst. *Spectrochim. Acta, Part A* **2011**, *81*, 228-235.

83. Naseem, K.; Farooqi, Z. H.; Begum, R.; Irfan, A., Removal of Congo Red Dye from Aqueous Medium by its Catalytic Reduction Using Sodium Borohydride in the Presence of Various Inorganic Nano-Catalysts: A Review. *J. Cleaner Prod.* **2018**, *187*, 296-307.

84. Wu, X.; Shi, Z.; Fu, S.; Chen, J.; Berry, R. M.; Tam, K. C., Strategy for Synthesizing Porous Cellulose Nanocrystal Supported Metal Nanocatalysts. *ACS Sustainable Chem. Eng.* **2016**, *4*, 5929-5935.

85. Liang, M.; Su, R.; Huang, R.; Qi, W.; Yu, Y.; Wang, L.; He, Z., Facile in Situ Synthesis of Silver Nanoparticles on Procyanidin-Grafted Eggshell Membrane and Their Catalytic Properties. *ACS Appl. Mater. Interfaces* **2014**, *6*, 4638-4649.

86. Xue, Z.; Sun, X.; Li, Z.; Mu, T., CO2 as a Regulator for the Controllable Preparation of Highly Dispersed Chitosan-Supported Pd Catalysts in Ionic Liquids. *Chem. Commun.* **2015**, *51*, 10811-10814.

87. Kamal, T.; Khan, S. B.; Asiri, A. M., Nickel Nanoparticles-Chitosan Composite Coated Cellulose Filter Paper: An Efficient and Easily Recoverable Dip-Catalyst for Pollutants Degradation. *Environ. Pollut.* **2016**, *218*, 625-633.

88. Lin, X.; Wu, M.; Wu, D.; Kuga, S.; Endo, T.; Huang, Y., Platinum Nanoparticles Using Wood Nanomaterials: Eco-Friendly Synthesis, Shape Control and Catalytic Activity for p-Nitrophenol Reduction. *Green Chem.* **2011**, *13*, 283-287.

89. Han, Y.; Wu, X.; Zhang, X.; Zhou, Z.; Lu, C., Reductant-Free Synthesis of Silver Nanoparticles-Doped Cellulose Microgels for Catalyzing and Product Separation. *ACS Sustainable Chem. Eng.* **2016**, *4*, 6322-6331.

90. Budarin, V. L.; Clark, J. H.; Luque, R.; Macquarrie, D. J.; White, R. J., Palladium Nanoparticles on Polysaccharide-Derived Mesoporous Materials and their Catalytic Performance in C–C Coupling Reactions. *Green Chem.* **2008**, *10*, 382-387.

# CHAPTER 2

# Magnetite/polymer Brush Nanocomposites with Switchable Uptake Behavior toward Methylene Blue*

*Reprinted with permission from Dolatkhah, A. and Wilson, L. D. *ACS Appl. Mater. Interfaces*, 2016, 8, 5595–5607.  DOI: 10.1021/acsami.5b11599. A.D. performed all experimental work and wrote the first draft of the manuscript. L.D.W. directed the study and revised the manuscript prior to publication.

## 2.1. Abstract

The *grafting from* approach was used to prepare pH-responsive polyacid brushes using poly (itaconic acid) (PIA) and poly(acrylic acid) (PAA) at the amine functional groups of chitosan. Hybrid materials consisting of polymer brushes and magnetite nanoparticles (MNPs) were also prepared. The products were structurally characterized and displayed reversible pH-responsive behavior and controlled adsorption/desorption of methylene blue. Switchable binding of MB involves cooperative effects due to conformational changes of brushes and swelling phenomena in solution which arise from response to changes in pH. Above the p$K_a$, magnetite nanocomposites (MNCs) are deprotonated and display enhanced electrostatic interactions with high MB removal efficiency (>99%). Below the p$K_a$, MNCs undergo self-assembly and release the cationic dye. The switchable binding of MB and the structure of the polymer brush between collapsed and extended forms relate to changes in osmotic pressure due to reversible ionization of acid groups at variable pH. Reversible adsorption-desorption with variable binding affinity and regeneration ability was demonstrated after five cycles.

## 2.2. Introduction

Stimuli-responsive polymer brushes represent a class of materials with "smart" surface and interfacial properties due to reversible dynamic changes in their physicochemical properties triggered by external stimuli such as pH, light, or temperature.[1,2] The pH-responsiveness alters the charge density along the polymer brush at variable pH, along with the polymer conformation and osmotic balance of ionizable groups in solution. Magnetite nanocomposites have been developed for diverse applications owing to their unique magnetic responsiveness at room temperature to external stimuli and biocompatibility.[3,4] Magnetic nanoparticles (MNP) are nontoxic which afford their use in biomedicine,[5] drug delivery,[6,7] environmental remediation,[8] and wastewater

treatment.[9-12] Methylene blue is a well-known cationic dye, which is widely used in various applications such as printing, textile, cosmetics, and pharmaceuticals.

The development of modified adsorbent containing chitosan[13,14] are suitable for the removal of toxic species such as Cu, Pb, Hg, As, Cd, Ni, Cd, Cr, etc., from water.[14-22] The polar functional groups (OH, and NHR; where R = acetyl or H) with Lewis base character can facilitate adsorption of metal ion species due to chelation.[23] Fewer studies have been reported that use chitosan based adsorbents for removal of cationic dyes.[24-26] Further, these engineered chitosan materials for cationic dyes have either low specific surface area or poor adsorption capacity, which may require significant energy for regeneration. Thus, there is a need to develop advanced sorbents materials with low-cost, improved adsorption, and regeneration properties toward waterborne contaminants. Polymer brushes offer several advantages over monolayer modified materials because of the greater surface accessibility of functional groups, textural properties, and stimuli responsive properties.[27-29] Polymer brushes are unique and possess abundant surface functional groups that may facilitate binding with cation or anion waterborne contaminants.[30] The design of polymer brushes can be achieved by three main strategies: (i) "grafting through", (ii) "grafting to", and (iii) "grafting from" methods. Method i involves the polymerization of various monomers with functionality capable of initiating polymerization. Method ii involves the reaction between a prepolymer with active functional groups on each monomer in combination with an end-functionalized prepolymer. Method iii starts with polymerization of monomers on the surface of a polymer backbone. Such polymers are comprised of monomer units with functionalities to initiate polymerization of a secondary monomer species on the surface of the backbone. Each grafting method contributes different structural parameters of brushes such as the chemical composition, grafting density, and degree of polymerization of side chains.[27] Farrukh et al. reported the

preparation of MNCs containing polymer brushes for removal of mercury (II) ions from water.[31] They observed that polymer brushes decorated with metal nanoparticles have greater adsorption capacity than similar monolayer functionalized magnetite. Polymer nanocomposites of this type are generally expensive and involve complicated multistep synthesis to anchor polymer brushes at the surface of MNPs.[10,32] Embedding MNPs into responsive polymer brush structures offers a new class of "smart" hybrid nanocomposites with reversible and controlled sorption behavior with rapid recovery from aqueous solution.[33-35]

Herein, the fabrication of pH-responsive adsorption/release polymer nanohybrid systems containing MNPs and polymer brushes for the controlled uptake of MB was reported. The resulting MNCs were prepared using a modular synthetic strategy, as follows: (1) PIA and PAA units were grafted onto chitosan backbone using a grafting from approach and (2) MNCs containing pH responsive polymer brushes and MNPs were prepared by anchoring brushes onto the surface of MNPs through covalent linking with the polymer brush scaffold (*cf.* Scheme 2.1). Taking the advantage of the high *surface-to-volume* ratio and abundant polymer brush adsorption sites, notable adsorption capacities were observed for $Fe_3O_4$-PIAgCHI (470.2 mg $g^{-1}$) and $Fe_3O_4$-PAAgCHI (421.2 mg $g^{-1}$) nanocomposites. These materials afford the controlled and reversible adsorption and release of MB due to the pH dependent ionization behavior. The objective of this study involved the design of pH responsive CHI brush nanohybrid adsorbents and composites containing iron oxide for the sorption of methylene blue. Herein, a first example of such materials using a green and facile strategy was reported where dye loaded composite nanostructures can be readily regenerated by changing the pH of solution, combined with fast magnetic field-assisted separation, which makes these materials highly cost-effective for wastewater treatment processes.

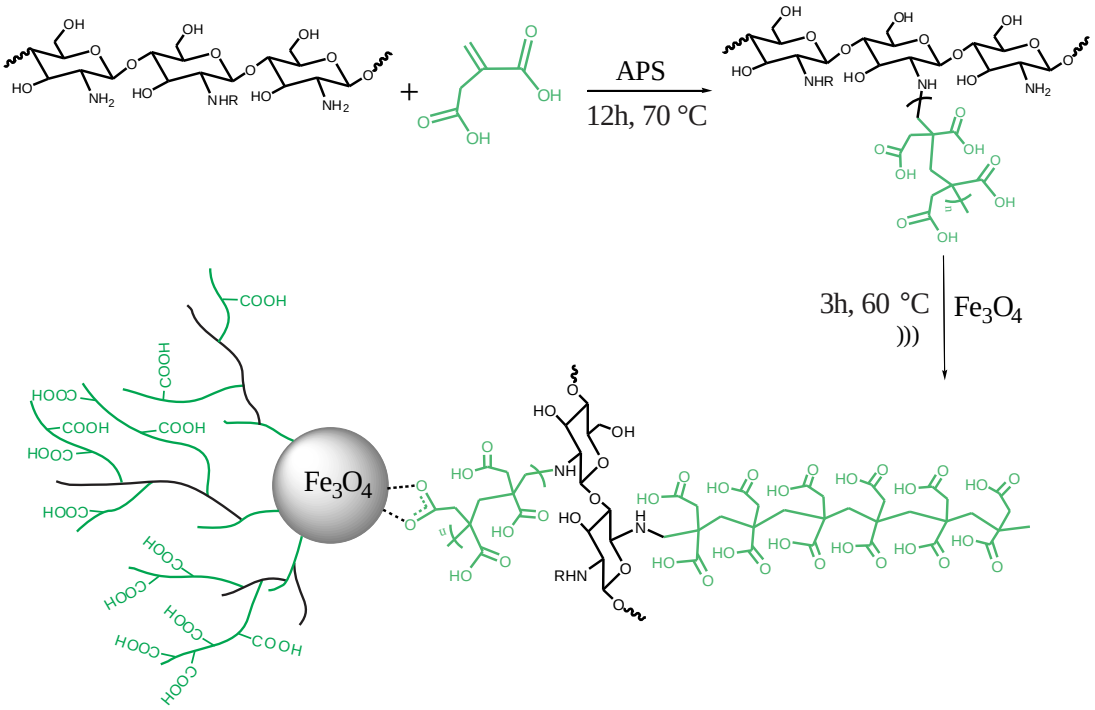


**Scheme 2.1.** Two-step synthetic route for polymer brush nanocomposites containing magnetite ($Fe_3O_4$-PIAgCHI). **Note:** -NHR; where R = acetyl group or H depending on the degree of deacetylation.

# 2.3. Experimental section

## 2.3.1. Materials

Ferrous chloride (purity ≥99.0%), ferric chloride (purity ≥99.0%), acrylic acid (99% purity), itaconic acid (purity ≥99.0%), chitosan powder with 75-85% deacetylation (CHI, 190 kDa based on viscosity), ammonium persulfate (98% purity), methanol, and semi-permeable dialysis tubing was obtained from Sigma-Aldrich Canada Ltd. Methylene blue was provided by Alfa Aesar, Canada. All materials were used without further purification and Milli-Q ultrapure water (18.2 MΩ.cm) was used for the preparation of aqueous solutions herein.

## 2.3.2. Synthesis of PIA and PAA grafted chitosan brushes (PAAgCHI and PIAgCHI)

The poly (itaconic acid) (PIA) and poly (acrylic acid) (PAA) grafted chitosan polymer brushes were prepared by the method described by Edgefield et al[36] with slight modification. Briefly, a solution of 1% CHI in aqueous acetic acid (1%; w/v) solution was prepared by dissolving powdered chitosan overnight with stirring in a three-neck round-bottom flask equipped with a rubber septum. The solution was purged with nitrogen for 10 min. followed by the addition of APS solution (1% w/v) to the chitosan solution with stirring for 20 min. A solution of monomer (5% w/v itaconic acid or acrylic acid) was added to the chitosan solution (as above) drop-wise over a 20 min interval under constant nitrogen gas flow. The resulting concentrations were 2.5% and 0.5% of monomer and initiator, respectively. The mixture was heated at 60°C for 12 h where the resulting clear solution was cooled and neutralized to pH 7 using 1 M NaOH solution to yield chitosan grafted materials as a precipitate. The product was washed with Millipore water several times and dried in a vacuum oven. The PAA grafted chitosan materials were completely soluble in water and the polymer brushes were precipitated in methanol twice to remove side products and low molecular weight unreacted acrylic acid. The precipitate was dissolved in Millipore water and was dialyzed with water (3 × 2 L changes) for 72 h to remove unreacted APS. The final product obtained by removal of water with drying in a vacuum oven at 60 °C.

## 2.3.3. Synthesis of MNPs, $Fe_3O_4$-PAAgCHI and $Fe_3O_4$-PAAgCHI nanohybrids

In a typical procedure, 13 g $FeCl_3.6H_2O$ (0.05 mol) and 5 g $FeCl_2 \cdot 4H_2O$ (0.025 mol) were dissolved in 200 mL Millipore water in a three-neck round-bottom flask. The reaction was done at 80 °C in an oil bath under a nitrogen atmosphere. After 10 min, 100 mL of NaOH solution was

added drop-wise over 20 min. The solution rapidly turned black, indicating the formation of MNPs. The reaction was stirred for 40 min at 80 °C after which the product was collected and purified by five washing cycles with water and magnetic separation to yield magnetic nanoparticles ($Fe_3O_4$). To prepare polymer brush/magnetic particles, an aqueous sol of ultrafine MNPs was prepared by sonicating 1 g of MNPs in 100 mL Millipore water for 30 min. Then an aqueous solution of PAAgCHI at pH 5 was added drop-wise under $N_2$ gas. PIAgCHI brush was solubilized in 1% acetic acid overnight and then filtrated to obtain clear PIAgCHI solution. The mixture was sonicated for 1 h at 70 °C. The product was washed with Millipore water and separated magnetically with a permanent magnet to yield PAAgCHI and PIAgCHI modified MNPs as $Fe_3O_4$-PAAgCHI and $Fe_3O_4$-PIAgCHI nanohybrids.

## 2.3.4. Characterization

Fourier transform infrared (FTIR) spectra of samples were obtained with a Bio-RAD FTS-40 spectrophotometer where samples were analyzed in reflectance mode. All of the samples were prepared by mixing materials (about 6 mg) with pure spectroscopic grade KBr (60 mg) in a mortar and pestle. The diffuse reflectance infrared Fourier transform (DRIFT) spectra were obtained with a resolution of 4 $cm^{-1}$ and scanning in the range of 400-4500 $cm^{-1}$. Multiple scans were acquired in reflectance mode and all spectra presented here were baseline corrected relative to spectroscopic grade KBr. Nuclear magnetic resonance (NMR) spectra of various samples were recorded at 500 MHz on Bruker Advance 600 or 500 MHz spectrometers at room temperature with tetramethylsilane as the internal standard and using either deuterated water or 1% $HCl/D_2O$ as the solvent system. NMR spectra were acquired using standard solvent suppression. Thermogravimetric analysis (TGA) was performed with a TA Instruments (TGA Q500). Samples were placed in an aluminum pan and heated at a scanning rate of 5°C/min under a nitrogen flow

(90 mL/min). PXRD patterns of the magnetic products were obtained on a PANalytical Empyrean diffractometer using monochromatic Co-$K_1$ radiation (1.79 Å) with a 2θ scan rate of 3.2° $min^{-1}$ from 14° to 80° (2θ). Transmission electron microscope (TEM) images of samples were obtained using a Hitachi HT-7700 microscope at voltage 100 kV. Samples were prepared by depositing a drop of colloidal suspension in ethanol onto a carbon-coated copper TEM grid. The pH-induced sizes of the nanocomposites were performed on a dynamic light scattering spectrometer from (DynaPro) equipment. The measurements were performed at 20 °C and a 90° scattering angle.

## 2.3.5. Adsorption-desorption and pH-responsive experiments

The uptake capacity of PIAgCHI polymer brush and MNCs was evaluated by using fixed amounts of adsorbent in sealed 5 mL glass vials. The adsorption isotherms were obtained in batch mode by dosing 10 mg adsorbent to 3 mL of MB solutions (pH = 7) at variable initial [MB] (0.1–5 mM) with mixing on a horizontal shaker (SCILOGEX SK-O330-Pro) at 293 K for 24 h to ensure equilibrium. The adsorption isotherms of chitosan with medium molecular weight and bare MNPs were carried out for comparison. Stock solutions of MB were prepared by dissolving 3 g of MB powder in 1 L of water (3% w/v) with appropriate dilution. A linear calibration curve for MB absorbance at 664 nm vs [MB] (up to 5 mM) was obtained with a slope of 66.16 = $Abs_{664nm}$/[MB] (Figure A.9). After 24 h, the sample powders were directly separated from the solution either by centrifuge or using a permanent magnet and the residual [MB] was measured with UV–vis spectroscopy (Varian Cary 100 Scan UV–vis spectrophotometer) at 664 nm (wavelength absorption maximum of MB). The equilibrium uptake of MB was calculated using Eq. 2.1.

$$q_e = \frac{(C_0 - C_e) \times V}{m} \tag{2.1}$$

Where $q_e$ (mmol $g^{-1}$) is the MB adsorbed per unit mass of adsorbent, $C_0$ (mM) is the initial dye concentration, $C_e$ (mM) is the residual amount of MB, $V$ (L) is the volume of the MB solution, and $m$ (g) is the weight of the adsorbent. Solutions with variable pH (pH 2–12) were obtained using 0.1 M HCl or 0.1 M NaOH to reach final pH values. The removal efficiency (%$R$) of dyes in aqueous solution was obtained by Eq. 2.2.

$$\%R = \frac{C_0 - C_e}{C_0} \times 100 \tag{2.2}$$

$C_0$ and $C_e$ are defined as in Eq. 2.1. The reuse of adsorbent during adsorption/desorption cycles, where adsorption was performed at optimum pH conditions ($pH_{ads}$ = 7, 7, and 9 for PIAgCHI, $Fe_3O_4$-PIAgCHI, and $Fe_3O_4$-PIAgCHI, respectively) and $t_{ads}$ = 24 h. Next, the dye loaded adsorbent materials were separated from the solution and followed by multiple washing to neutral pH. Desorption of MB from the adsorbent materials was performed in 12 mL aqueous solutions at variable pH (2-11) to illustrate the pH-based desorption. The adsorption-desorption of materials was measured by reversible switching of the pH of solutions with adsorbent materials between pH 2 (collapsed state) and pH 9 (swollen state). The above procedure was repeated for 5 consecutive cycles of regeneration without separating dye loaded/stripped sorbents from its original solution throughout cycles to avoid loss of adsorbent via filtration. At pH 2, an external magnet was used to separate stripped sorbents from solution where desorption (%) was calculated using Eq. 2.3.

$$Desorption\ (\%) = \frac{concentration\ of\ dye desorbed (mM)}{concentration\ of\ dye adsorbed (mM)} \times 100\% \tag{2.3}$$

### 2.3.6. Adsorption Kinetics

Kinetics studies were performed isothermally at 298 K using the "one-pot" method with an adsorbent confined in a semipermeable barrier with ex-situ sampling, which recently have been developed in our laboratory for heterogeneous adsorption processes of nanomaterial sorbents.[37] Dialysis tube was applied as the semipermeable membrane barrier for MNCs. A 20 mg portion of sorbent was placed in dialysis tube and after closure with a polypropylene clip followed by immersion in a 120 mL MB solution. A 200 μL portion of sample was continuously taken at fixed time intervals (0 to 190 min) and diluted with Millipore water for UV–vis analysis. The adsorbed amount of MB was estimated at λ = 664 nm using Beer's law. The adsorption capacity at variable time (*t*) for the sorbent materials was calculated analogously to Eq. 2.1., $q_t = V(C_0 - C_t)/m$, where $V$ is the solution volume, $C_0$ is the initial MB concentration, $C_t$ is the MB concentration in the solution at variable $t$, and $m$ is the weight of adsorbent. The available adsorption sites present on the surface of the adsorbent exceed the MB concentration. The adsorption process follows a pseudo first order (PFO) or pseudo second (PSO) order kinetic profile described in Table A.1. The amount of adsorbed dye at any time ($q_t$) can be related to MB concentration at any time $C_t$ as expressed in Table A.1.[38,39] Nonlinear least-squares fitting of the results used theoretical models to determine the "best-fit" kinetic parameters ($k_i$ and $q_e$).

## 2.4. Results and discussion

### 2.4.1. Preparation of materials

Unlike classical grafting from and grafting to approaches which require synthesis of a macro initiator, free radical graft polymerization is a simple, inexpensive, and versatile method that eliminates the step required for functionalizing the polymer backbone to produce a macro initiator

prior to grafting. Pal et al.[40] used the grafting from mechanism by applying surface initiated and controlled radical polymerization method to polymerize acrylic acid onto a glycogen backbone. However, the preparation is costly and includes two steps. Grafting initiation by persulfate initiator such as APS generates free sulfate radical ($SO_4^{-\bullet}$) which results in polymerization via the amino groups, according to the proposed grafting from mechanism.[36] After grafting CHI with PAA, the product was water-soluble due to the PAA grafts, in contrast to water insoluble chitosan. Polyacrylamide grafted CHI displayed similar water solubility characteristics as the CHI-PAA system reported by Hall-Edgefield et al.[36] The CHI-PAA system was solubilized in methanol and stirred vigorously to remove unreacted acrylic acid and unwanted side products of PAA. To remove unreacted persulfate, the product was dissolved in water and dialyzed for 72 h against Millipore water. The PIA grafted polymer brush was obtained as a precipitate upon neutralizing the solution to pH 7 at ambient conditions.

## 2.4.2. Characterization of the chitosan brushes and nanohybrids

Comparison of the FTIR spectra of neat CHI, monomer units (itaconic acid and acrylic acid), and CHI-graft polymer brushes reveal that the polymers were successfully grafted onto the chitosan backbone. As shown in Figure 2.1a, the FTIR spectrum of chitosan is characterized by adsorption bands at 1659 $cm^{-1}$; amide I υ(C═O), 1593; amide II δ (N–H), 3000–3500 $cm^{-1}$; υ(N–H of primary amine and O–H), 1000–1100 $cm^{-1}$; υ(C–O–C of skeletal and C–N of amine) bands and at 2870 $cm^{-1}$; υ(aliphatic C–H of backbone). The IR spectra of the grafted materials differed from the spectra of CHI and the monomer units. The polymer brushes reveal signatures in the fingerprint region for the polysaccharide backbone of chitosan and a peak at 1660 $cm^{-1}$ corresponding to amide carbonyl group (Figure A.1 in Appendix). After grafting, characteristic bands at 850–970, 1630, and 3060 $cm^{-1}$for monomers are assigned to various modes such as =C–

H bending and C═C stretching, while after grafting, the stretching bands of vinyl groups are absent. As shown in Figures 2.1a. and A.1a, the greater intensity of C–H stretching bands at 2870 $cm^{-1}$ for the polymer brush support that polymerization of monomers occurs on the surface of CHI. As well, there are shoulder-like bands at 1718 $cm^{-1}$ for itaconic acid and 1715 $cm^{-1}$ for acrylic acid that indicate the incorporation of the carboxyl groups (Figure A.1 in Appendix). Another noteworthy observation is a broad peak ca. 3400–3600 $cm^{-1}$ for polymer brushes are more pronounced due to overlap with the O–H stretching and intermolecular hydrogen bonded O–H groups of -COOH/-NHR groups of the chitosan backbone. The IR spectrum for $Fe_3O_4$ nanoparticles exhibit a broad absorption band at ~580 $cm^{-1}$ that is characteristic of the Fe–O bond vibration (Figure 2.1b). As expected, in the polymer brush MNCs, a new signal was observed around 580 $cm^{-1}$ that indicates Fe–O lattice vibrations and magnetite loading. The presence of residual free carboxylic groups is evidenced by a band at 1723 $cm^{-1}$ and a shoulder-like peak at 1715 $cm^{-1}$ for PIA and PAA magnetite materials, respectively (*cf.* Figure A.1). For carboxylate ions within the polymer brush materials, there are two peaks assigned for the asymmetric ($\upsilon_a$) and symmetric ($\upsilon_s$) bands resulting from stretching of $CO_2^-$ bonds at ca. 1650–1510 and 1450–1400 $cm^{-1}$, respectively. The signatures for the grafted materials appeared at $\upsilon_s$(1407 $cm^{-1}$) and $\upsilon_a$(1550 $cm^{-1}$) for PIA grafted polymer brushes and $\upsilon_s$(1409 $cm^{-1}$) and $\upsilon_a$(1560 $cm^{-1}$) for PAA grafted polymers (Figure 2.1a and A.1a and the expanded region of Figure A.1e,f). The mode of coordination of the carboxylate ligand on the MNPs surface can be readily deduced from the magnitude of the splitting ($\Delta$) for asymmetric and symmetric bands ($\Delta = \upsilon_a - \upsilon_s$) before and after coordination. When $\Delta$ is greater ($\Delta$ = 200–300 $cm^{-1}$), monodentate incorporation, when $\Delta$ is close to that value of free ligand ($\Delta$ = 110–200 $cm^{-1}$) supports bridging bidentate or ionic interactions occur. The carboxylate ion behaves like a chelating bidentate ligand when $\Delta$ is smaller

($\Delta < 110$ $cm^{-1}$) relative to the free carboxylate ion. MNCs formation result in incorporation of MNPs onto the polymer brush surface where IR bands appear ca. $\upsilon_s$(1406 $cm^{-1}$) and $\upsilon_a$(1575 $cm^{-1}$) for PAA and $\upsilon_s$(1390 $cm^{-1}$) and $\upsilon_a$(1536 $cm^{-1}$) for PIA MNCs (*cf.* Figure 2.1b and the expanded region of Figures A.1g,h). For $Fe_3O_4$–PIAgCHI MNCs, the symmetric ($\upsilon_s$) stretching of $CO_2^-$ is difficult to locate due to overlap with the other bands at 1300–1450 $cm^{-1}$ due to the C–N stretching vibration of amine and amide groups $\upsilon$(amide III) of chitosan. However, the small band ca.1400 $cm^{-1}$ is assigned to the $\upsilon_s$ mode. Herein, $\Delta$ is calculated as 159 (PAA) and 146 $cm^{-1}$ (PIA) polymer brush MNCs which lie close to the values for initial polymer brushes (151 and 143 $cm^{-1}$), suggesting that carboxyl groups behave like bridging bidentate ligands (Figure 2.1c) and interact with the electron deficient orbitals of the Fe species on the surface of the $Fe_3O_4$ NPs. The above are in agreement with previous results.[41,42]

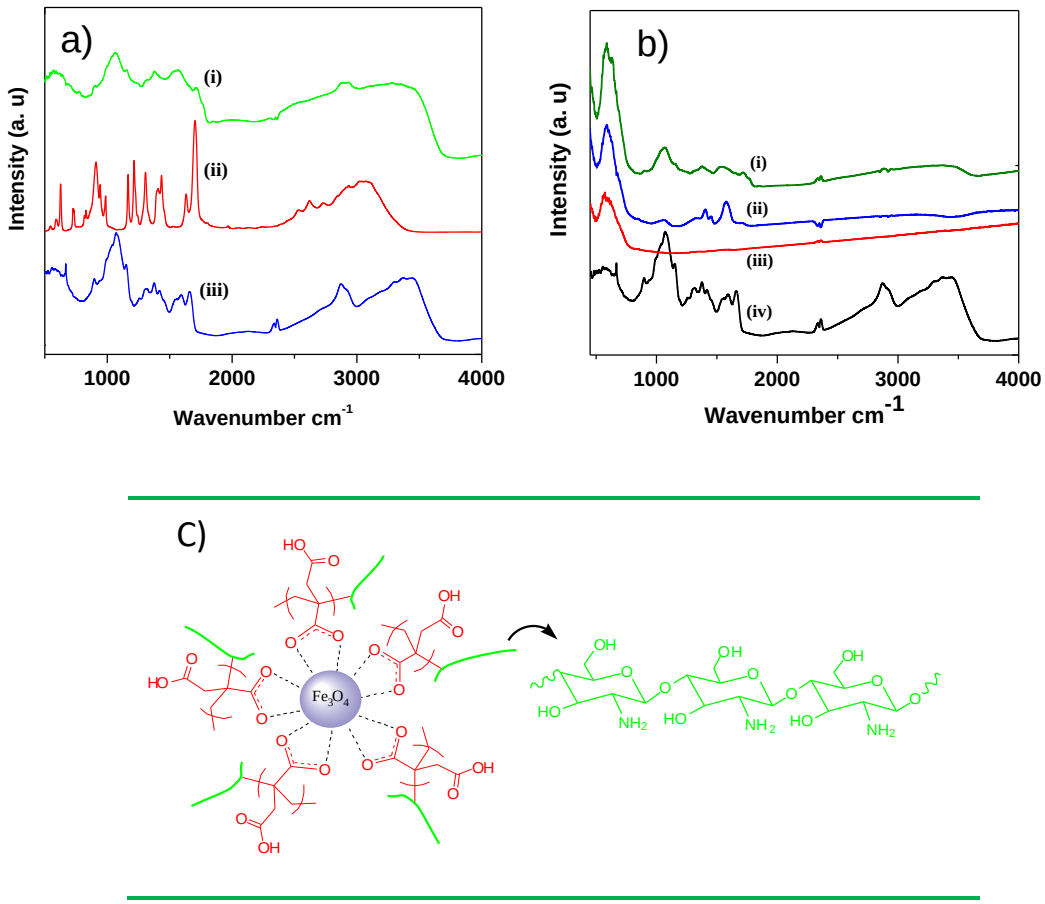


**Figure 2.1.** FTIR spectra of (a) PIAgCHI (iii), itaconic acid (ii) and pristine chitosan (i); (b) PIAgCHI modified MNPs (i), PIAgCHI modified MNPs (ii) as-prepared MNPs (iii) and pristine chitosan (iv); and (c) illustration of the grafted bridging bidentate interaction in hybrid nanostructures.

The chemical structure and $^{1}H$ NMR spectra of CHI and grafted polymers are shown in Figure 2.2. In the $^{1}H$ NMR spectral lines of CHI in the region of 1.9 ppm was assigned to acetyl group, while broad signatures at 3.5–4 and 3 ppm correspond to the chitosan backbone H atoms and the -NH group of chitosan. In the $^{1}H$ NMR spectra of the chitosan brushes, the structure of grafted materials was confirmed by the presence of several spectral lines (2.6, 3.1 and 1.5, 2.5, 3.5 ppm) that correspond to the methylene groups of the PIA and PAA. The $^{1}H$ signals at 2.6, 3.1 and

1.5, 2.5, 3.5 ppm correspond to the methylene groups of PIA and PAA, in agreement with other $^{1}H$ NMR results.[40]

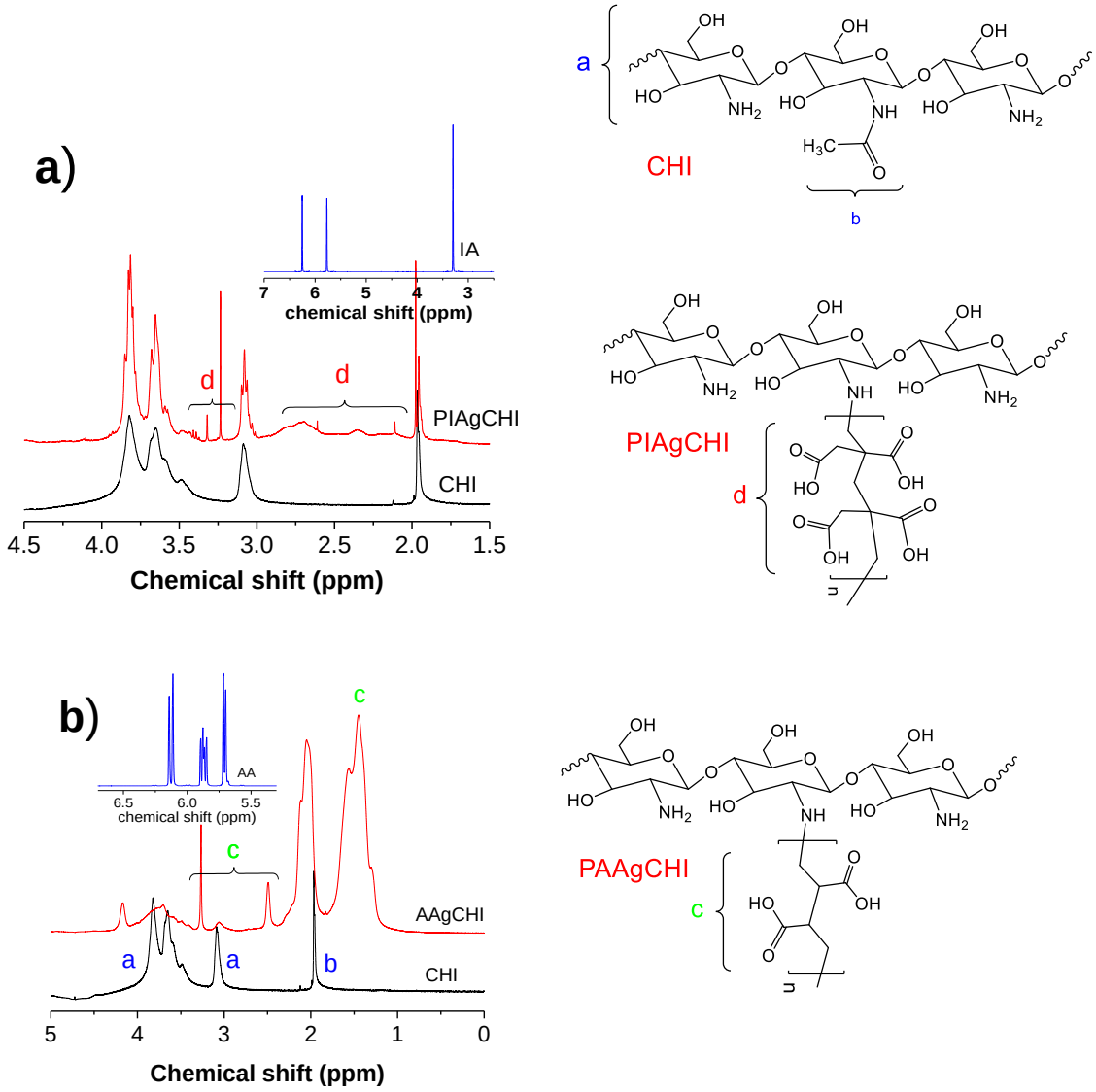


**Figure 2.2.** Chemical structure and $^{1}H$ NMR (500 MHz) spectra of CHI, PIAgCHI, and PAAgCHI polymer brushes. (inset) $^{1}H$ NMR spectra of itaconic acid (a) and acrylic acid (b) in $D_2O$/HCl (10% v/v), where n denotes the degree of polymerization of the pendant groups for the polymer brushes.

The TGA results in Figure 2.3a for the PIA graft polymer reveal three key weight loss events. The first occurs at 40–140 °C (derivative thermal gravimetry (DTG) peak at 79 °C) with a mass loss of 5.6% due to the loss of free or bound water. The second event occurs between 150 and 280

°C (DTG peak at 253 °C) due to the decomposition of CHI. The third event relates to the degradation of grafted polymer (PIA) at 280–460 °C (DTG peak at 309 °C) which overlaps with the weight loss associated with deacetylation[16] of chitosan and contributes to a 57.2% weight loss overall. MNPs were found to have a negligible weight loss (≈1%) between 30 and 500 °C (*cf.* in Figure 2.3b). The weight loss event of MNCs occur from 40 to 150 °C (Figure 2.3c and A.2 in Appendix) and relate to the loss of solvent from the CHI backbone and grafted side chains that contain hydrophilic groups (COOH and NHR; where R = H and acetyl). The second decomposition event (150 to 350 °C) is characteristic of the degradation of CHI and the grafted side chains. $Fe_3O_4$–PAAgCHI presented further weight loss (≈4.6%) between 350 and 450 °C (DTG peak at 400 °C) was ascribed to the cleavage of the Fe–OOCR bond and release of $CO_2$.[42] The PIAgCHI MNC system does not show this thermal event. However, a process at 267–350 °C which is related to the gradual decomposition of the ligands due to decomposition of weakly bound iron in PIA brushes was observed. The mass fraction of inorganic component within nanocomposites was 93.4% and 87.3% for $Fe_3O_4$–PIAgCHI and $Fe_3O_4$–PAAgCHI, respectively, which occurs upon heating to the upper temperature limit (500 °C). The weight loss (%) and DTG results of the polymer brushes and corresponding magnetite nanohybrid assemblies are listed in Table A.2.

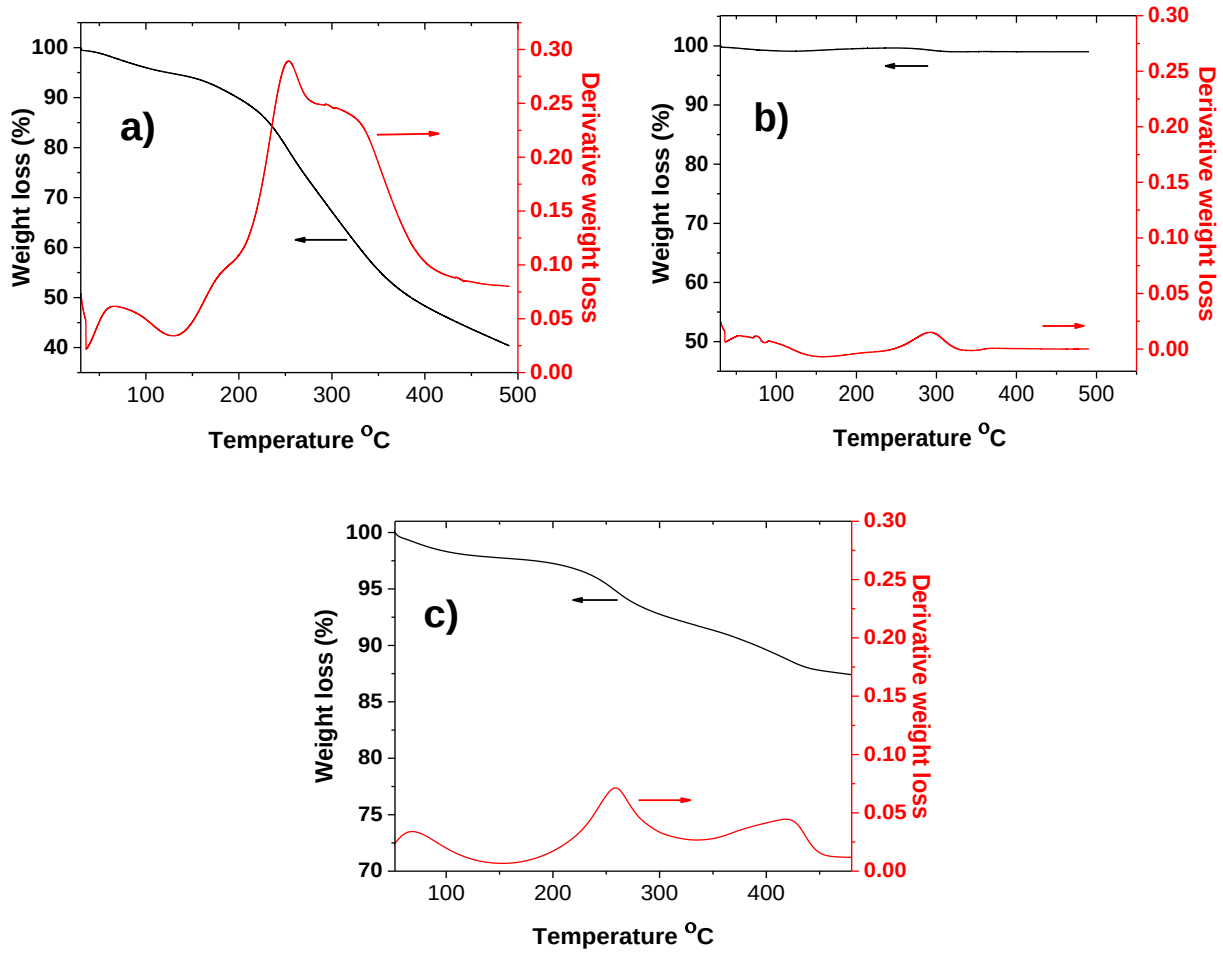


**Figure 2.3.** TGA and DTG profiles of PIAgCHI brush (a), MNPs (b), and $Fe_3O_4$-PAAgCHI (c).

The PXRD patterns of $Fe_3O_4$ MNPs and the polymer loaded $Fe_3O_4$ MNCs are shown in Figure 2.4. Several diffraction peaks are seen for the MNPs which correspond to the primary diffraction of the (440), (511), (422), (400), (311), (220), and (111) planes of the iron oxide, respectively. The main diffraction lines of the magnetite-loaded MNCs are similar to $Fe_3O_4$, implying that the crystal phases of iron oxide were maintained after formation of the MNC.[9,34,43] The PXRD signatures that correspond to the chitosan fraction of the $Fe_3O_4$–PAAgCHI material were not observed.[9,34,43] The latter is attributed to the relatively thin coating of polymer material on the magnetite surface and significant change in morphology of chitosan grafted with

PAA, relative to the more crystalline form of unmodified chitosan. A similar type of thin layer organic polymer formation was reported for PANI/α-ZrP organic/inorganic nanocomposites, where the absence of an organic phase diffraction peak was observed.[44] HRTEM results for the $Fe_3O_4$-PAAgCHI MNC reveal evidence of black domains attributed to inorganic MNPs. Clearly, the disorder of the polymer brushes occur as the interchain hydrogen bonding between the hydroxyl and amino groups along the chitosan backbone become weakened due to steric hindrance effects due to the PAA side chains.[45] However, the broad and relatively intense PXRD peak for $Fe_3O_4$-PIAgCHI centered at about $2\theta = 24.5°$ is observed. A similar signature is evident for the PXRD patterns of PIA grafted CHI brushes (*cf.* Figure A.3a,b). The broad feature relates to the amorphous PIA grafted CHI layers associated with the magnetite surface, in agreement with the TEM images of $Fe_3O_4$–PIAgCHI MNC. These results are supported from a study of silica polymers functionalized MNPs[46] that have similarly broad PXRD features due to the formation of amorphous silica polymers on the MNP surface.

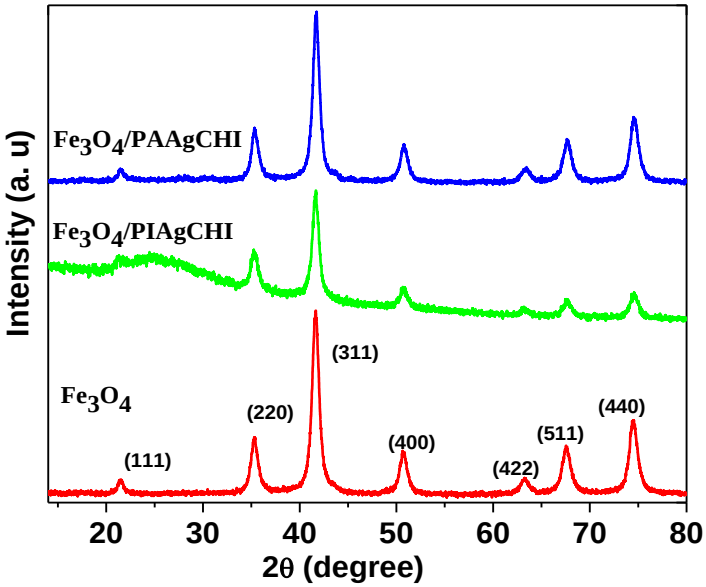


**Figure 2.4.** PXRD patterns of $Fe_3O_4$ and polymer brush MNCs.

Next, the morphology of synthesized $Fe_3O_4$ and MNCs was analyzed by TEM. Typical TEM results for the naked and polymer brush MNCs are depicted in Figure 2.5. Accordingly, the as-prepared ultrafine MNPs in Figure 2.5a have pseudo spherical morphology that appear as aggregates with a variable size range (12 to 30 nm) with an average diameter of 20 nm. After modification, the size-distribution of the MNCs does not change significantly. Comparable diameters are observed as follows; $Fe_3O_4$–PIAgCHI (11–37 nm) and $Fe_3O_4$–PAAgCHI (13–26 nm) where the mean diameter of the MNCs do not change significantly.[9] The results for $Fe_3O_4$–PIAgCHI (25 nm) and $Fe_3O_4$–PAAgCHI (20 nm) systems are shown in Figure 2.5. A noteworthy observation is that the TEM images of the MNCs reveal that they are more highly dispersed than naked MNPs, as evidenced by the reduced agglomeration due to the polymer brush stabilization (Figures 2.5b-d). The inset images are shown with high magnification for the $Fe_3O_4$–PIAgCHI MNCs, where it appears that the $Fe_3O_4$ nanospheres (black region) are partially coated by an outer polymer layer (shadow region). The results in Figures 2.5b,d (see inset) indicate successful surface

modification of the MNPs. It was speculated that the thin layer of polymer coating for the $Fe_3O_4$–PAAgCHI system may be difficult to resolve using TEM due to the low contrast between polymer phase and background.[47] Supporting evidence is provided by the above FT-IR and TGA results.

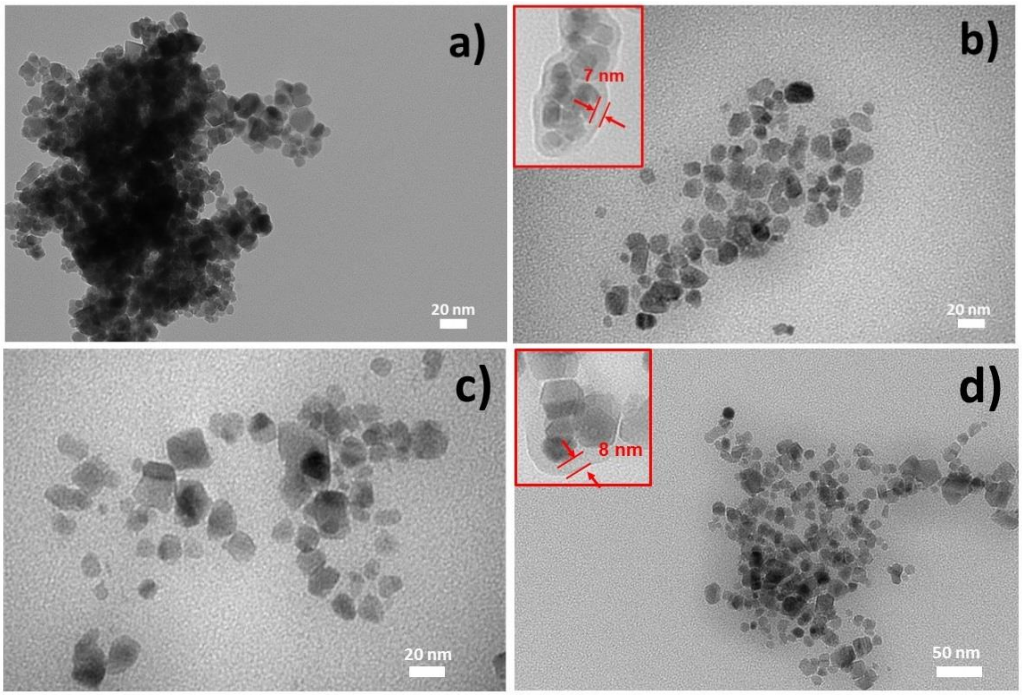


**Figure 2.5.** TEM micrographs of (a) magnetite NPs; (b) $Fe_3O_4$-PIAgCHI; (c) $Fe_3O_4$-PAAgCHI; and (d) $Fe_3O_4$-PIAgCHI particles. (inset) HRTEM of $Fe_3O_4$-PIAgCHI nanoparticles.

## 2.4.3. Cation dye sorption mechanism and molecular recognition

The adsorption properties of the PIAgCHI and related MNPs were examined using MB as a model cationic dye. Chitosan shows negligible adsorption for MB (results not shown), while PIAgCHI brush materials exhibit greater uptake of MB relative to pristine chitosan (*cf.* Figure 2.6b). Thus, there is a strong binding interaction between the cationic dye and the chitosan brush material, especially with materials possessing higher density of negatively charged grafted side chains. MB is a cationic ($S^+$) dye (Figure 2.6a) which displays favorable binding with

the grafted chitosan material while the polymer brush materials also show enhanced adsorption performance after modification with $Fe_3O_4$. The effect is principally attributed to the nature of the polymer interface and hydrophilic property of the MNCs in aqueous solution. Typically, a dosage of 10 mg of PIAgCHI and $Fe_3O_4$-PIAgCHI remove about 96% ($C_0$ = 0.2 mM) and 100% ($C_0$ = 0.6 mM) of the MB dye from aqueous solution. In Figure 2.6b, a dye solution of MB ($C_0$ = 0.2 mM) which initially appears dark-blue in color (vial i) undergoes a vivid and rapid decolorization after dosage of 10 mg PIAgCHI powder (vial ii). Figure 2.6c similarly shows an initial stock solution of MB ($C_0$ = 0.6 mM) which decolorizes after addition of 10 mg of $Fe_3O_4$-PIAgCHI powder (vial ii) and $Fe_3O_4$-PAAgCHI (vial iii) at equilibrium conditions. The polymer-modified MNCs could be magnetically separated within seconds after the adsorption process. Modified magnetite NPs are well-dispersed in aqueous phase which affords a relatively large *surface-to-volume* ratio with the aqueous phase for effective removal of MB, as compared with the chitosan brush material. Enhanced dispersion of the MNCs in water will increase the available adsorption sites and the uptake efficiency.

Unlike strong polyacid brushes where the number of charged monomers are fixed, weakly acidic or basic polyelectrolytes respond to changes in solution pH due to the presence of ionizable groups along the polymer brush backbone. The pH of the solution is a key factor affecting the adsorption properties of weak polyelectrolyte brushes by altering the charges on the brush according to the p$K_a$. Ionization leads to changes in electrostatic force and osmotic balance of the brush structure. This effect consequently controls the associated uptake or release of water and cationic dye species.[48,49] In the case of brush modified nanocomposites, these materials display highly responsive pH-dependent morphology and dye adsorption/release via self-assembly in aqueous solution (vide infra). The influence of pH on the removal efficiency of polymer brushes

and MNCs were investigated over a pH range (2–12), while the other parameters were fixed. In Figure A.4a, a maximum removal (%) of MB was observed for PIAgCHI at pH 7 (94.8%) where it remained constant up to pH 10. As the pH increases above 2 above the p$K_a$ of the brushes, further ionization occurs. In Figure A.4b, the adsorption efficiency of MB for the MNCs increased sharply up to 99%. As the pH increases from 2 to 6, a maximum removal (%) occurs at pH 7 for $Fe_3O_4$-PIAgCHI (ca. 99.5%). Similar uptake behavior was observed for $Fe_3O_4$-PAAgCHI MNCs where the removal efficiency increased to a maximum value at pH = 9 (99.2%). Further increase of the pH (up to 12) led to a significant decrease of MB adsorption for all three sorbents. The effect was attributed to counterion binding of excess hydroxide species and the relative stability of MB at alkaline pH.[50] This trend in removal (%) for these adsorbents could be related to the formation of stable hydroxyl-MB complexes[50] which attenuate the interaction of MB with the brushes. The results indicate that the removal of MB is greatly influenced by the initial pH value of the polymer brush in solution through its effect on the hydration and ionization of the adsorbent materials. As well, the competition between cationic dye and competitor ions ($OH^-/H^+$) present in the dye solution affect the removal of MB. In Figure A.4a,b reduced adsorption efficiency is observed at reduced pH due to an excess amount of $H^+$ on the surface of the brushes which compete with the positively charged dye and attenuate adsorption efficiency. At elevated pH (pH > p$K_a$ of polymer brush), greater adsorption occurs owing to the increased number of ionized -COOH groups of the polymer brush. At higher pH values, greater electrostatic repulsion among densely grafted polymer brushes occurs which increase the availability of the active sites for MB adsorption.[51] Hence, the formation of ionic complexes between MB dye molecules and the anion sites of the adsorbents are the key factor for the higher adsorption capacity. The pH dependent and cooperative adsorptive behavior of polyelectrolyte brushes may have several contributing factors: (1) The -COOH groups

are ionized (pH > p$K_a$) which yield favorable adsorption sites due to electrostatic interactions between the MB cation and the carboxylate anions. (2) At pH values above the p$K_a$ of the polymer brush, electrostatic repulsive force between neighboring ionized carboxyl groups increase due to ionization. The repulsive interactions are decreased by brush side chains that adopt an extended conformation. Increased repulsion forces between side chains and greater osmotic pressure results in further adsorption of solvent and MB species onto the brush surface.[48,49,51] According to section 2.4.6., increased density of negative charges enhance the dispersion of MNPs and minimize unwanted aggregation through electrostatic and steric stabilization of the polymer brush MNCs. The foregoing enhances their adsorption properties and accessible surface area, while Incorporation of CHI brushes onto MNPs yield MNCs with notably greater adsorption capacity.

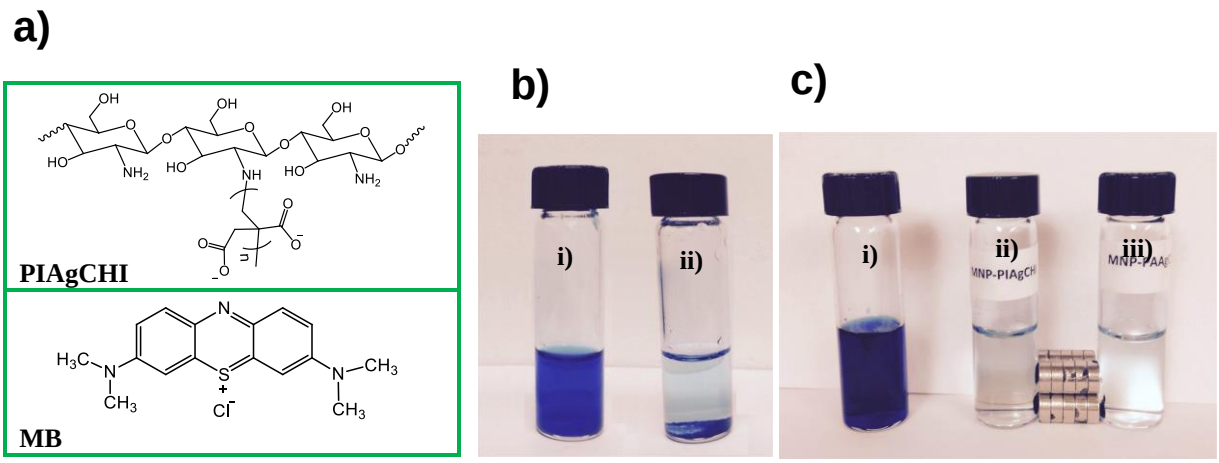


**Figure 2.6.** (a) Chemical structures of PIA-chitosan brush and MB; (b) photographs of MB before (i) and after sorption (ii) by PIAgCHI polymer brush where $C_0$ (MB) = 0.2 mM; (c) images of MB before (i) and after sorption by $Fe_3O_4$-PIAgCHI (ii) $Fe_3O_4$-PAAgCHI and (iii) MNCs (after applying magnetic field) where $C_0$ (MB) = 0.6 mM.

## 2.4.4. Adsorption isotherms

Figures 2.7 and A.5 illustrate the isotherm results for the sorption of MB from aqueous solution onto various sorbent materials (CHI, PIAgCHI, $Fe_3O_4$-PAAgCHI, and $Fe_3O_4$-PIAgCHI MNCs).

To optimize the usage of adsorbent, the isotherm uptake parameters obtained from the models (Langmuir, Freundlich, and Sips) were used to analyze the MB adsorption results. The Langmuir model describes homogeneous monolayer adsorption by Eq. 2.4.[45,52]

$$q_e = \frac{q_m K_L C_e}{1 + K_L C_e} \tag{2.4}$$

$C_e$ is the equilibrium MB concentration, $q_e$ is the amount of MB adsorbed per unit mass of the adsorbent at equilibrium (mmol $g^{-1}$), $q_m$ is the monolayer adsorption capacity (mmol $g^{-1}$) and $K_L$ (L $mmol^{-1}$) is the Langmuir affinity constant for the adsorption process. The occurrence of favorable adsorption may be quantified by terms of a dimensionless factor called separation factor, also known as the equilibrium parameter ($R_L$) according to the Langmuir isotherm, defined by Eq. 2.5.

$$R_L = \frac{1}{1 + K_L C_0} \tag{2.5}$$

$K_L$ is the Langmuir constant (L $mmol^{-1}$) and $C_0$ is the initial MB concentration. The value of $R_L$ determines the occurrence of favorable uptake; unfavorable ($R_L > 1$), linear ($R_L = 1$), irreversible ($R_L = 0$), or favorable ($0 < R_L < 1$). The Freundlich isotherm describes heterogeneous adsorption processes onto surfaces with variable adsorption sites, according to Eq. 2.6.[16,53]

$$q_e = K_F C_e^{1/n} \tag{2.6}$$

$C_e$ (mmol $L^{-1}$), $q_m$ (mmol $g^{-1}$), and $q_e$ (mmol $g^{-1}$) are defined above, and $K_F$ (L $g^{-1}$) is the Freundlich constant that relates to the adsorption capacity. The exponent term ($n$) is an isotherm constant which refers to nature and intensity of the adsorption, where $0.1 < 1/n < 1.0$ denotes highly

favorable adsorption, whereas; $1/n > 2$ indicates unfavorable adsorption. The Sips model shares attributes of the Langmuir and Freundlich models, and is defined by Eq. 2.7.

$$q_e = \frac{q_m K_S C_e^{\,n_s}}{1 + K_S C_e^{\,n_s}} \tag{2.7}$$

$K_s$ is the Sips isotherm constant that relates to the energy of adsorption and $n_s$ denotes the sorbent surface heterogeneity parameter. If the value of $n_s$ is unity, the Sips model describes Langmuir adsorption behavior. Alternatively, as the value of $C_e$ or $K_S$ approaches zero, the Sips isotherm describes Freundlich isotherm behavior. The adsorption isotherms for MB onto PIAgCHI, $Fe_3O_4$-PIAgCHI, and $Fe_3O_4$-PAAgCHI, as shown in Figures 2.7 and A.5 are well described by Eq. 2.4, 2.6, and 2.7. In Table 2.1, the isotherm parameters are listed for the adsorption of MB. CHI, polymer brushes, and MNCs reveal best-fit results according to the Sips model, according to favorable correlation coefficients ($R^2$), where $0.977 \leq R^2 \leq 0.993$. The results are described by monolayer adsorption onto homogeneous adsorption sites of the sorbent surface, as evidenced by a value of $n_s$ close to unity ($n_s = 0.98$) for densely surface grafted polymer brushes (PIAgCHI). The monolayer adsorption capacity ($q_m$) of MB, according to the Sips model in parentheses; $Fe_3O_4$-PAAgCHI (421.3 mg $g^{-1}$) and $Fe_3O_4$-PIAgCHI MNCs (470.2 mg $g^{-1}$) and exceed the $q_m$ values of pristine CHI and chitosan polymer brush materials. The $q_m$ value of polymer brushes increased by 70-fold for $Fe_3O_4$-PIAgCHI and 122-fold relative to unmodified CHI, reflecting the superior adsorption properties of these polymer brush MNCs. The results reveal that higher $q_m$ values may be due to several effects. (i) The higher density of surface functional groups of polymer brushes provides greater density of negatively charged adsorption sites, and (ii) improved dispersion of MNCs coated with hydrophilic polymer brushes favor the interactions for the sorbent-MB dye system. An improved dispersion of the MNCs result in greater surface area

and accessibility of the adsorption sites, which favor the uptake of MB. The calculated, $R_L$ values (Eq. 2.5) for adsorption of MB onto polymer brushes and MNCs with MB at variable $C_0$ (32-1600 mg $L^{-1}$) display a range of values; 0.421-0.014 (PIAgCHI), 0.0454–0.00095 ($Fe_3O_4$-PIAgCHI), and 0.352–0.011 ($Fe_3O_4$-PAAgCHI). The results reveal that favorable adsorption occurs for these adsorbents, in agreement with the exponent parameter $1/n_s$ obtained from Eq 2.6., where $1/n < 1$ for all three sorbents.

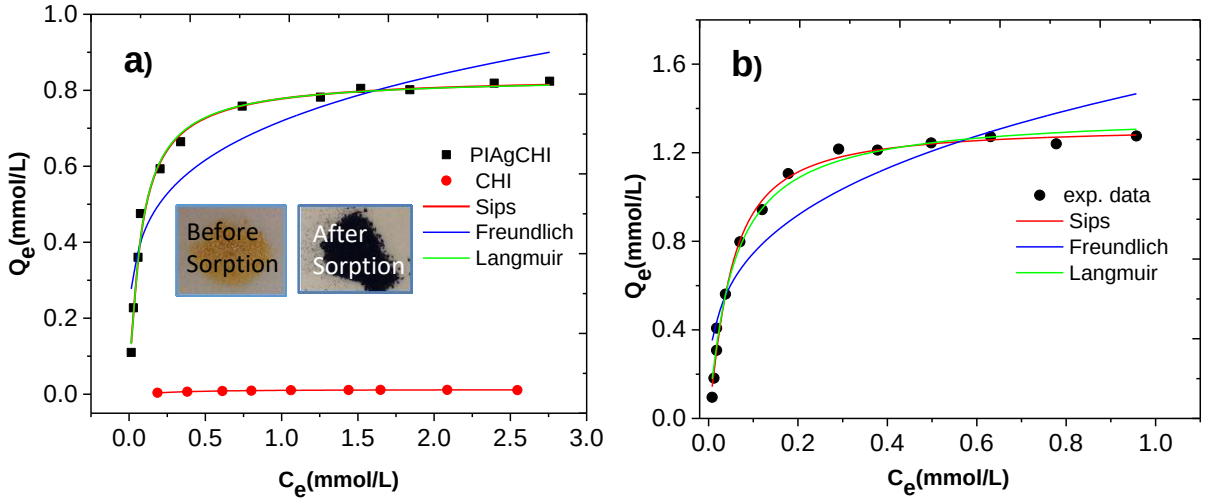


**Figure 2.7.** Isotherm sorption results for MB with various sorbent materials: (a) CHI and PIAgCHI and (b) $Fe_3O_4$-PAAgCHI composites.

**Table 2.1.** Isotherm parameters for the adsorption of MB with various sorbent materials. *The adsorption data are plotted using a MB concentration in mmol $L^{-1}$, but for the purpose of comparison, the $q_{max}$ values were calculated using a dye concentration in mg $g^{-1}$

| | **Langmuir isotherm*** | | | **Freundlich isotherm** | | | **Sips isotherm*** | | |
|---|---|---|---|---|---|---|---|---|---|
| **Sample** | $q_{max}$ (mg $g^{-1}$) | $K_L$ (L $mmol^{-1}$) | $R_L^2$ | $K_F$ (L $mmol^{-1}$) | $1/n_F$ | $R_F^2$ | $q_{max}$ (mg $g^{-1}$) | $n_s$ | $R_S^2$ |
| CHI | - | - | - | - | - | - | 3.84 | 1.52 | 0.977 |
| PIAgCHI | 267.04 | 13.72 | 0.993 | 0.72 | 0.22 | 0.887 | 267.99 | 0.98 | 0.993 |
| $Fe_3O_4$-PIAgCHI | 469.09 | 209.88 | 0.972 | 5.14 | 0.36 | 0.834 | 470.18 | 1.45 | 0.990 |
| $Fe_3O_4$-AAgCHI | 441.58 | 18.38 | 0.990 | 1.49 | 0.30 | 0.875 | 421.21 | 1.18 | 0.993 |

## 2.4.5. Desorption and pH-responsive behavior of adsorbents

To investigate the pH-dependence of the adsorption–desorption properties for MB, various adsorbent-MB dye systems were exposed to aqueous solutions at variable pH. The pH-dependent MB release profiles of polymer brushes and MNCs are plotted in Figure A.6a,b. At pH 2, desorption from solution shows a fast and maximal amount of release, where 91% of the initially adsorbed dye is desorbed for all three systems. However, the level of desorption (%) decreases sharply as the solution pH reaches pH 4, while a minimum (ca. 2%) is observed at pH 8. As shown in Figure A.6b, pH dependent desorption behavior of polyacid brushes and MNCs originate from protonation/deprotonation equilibria of carboxyl groups. At low pH, the carboxylic groups are favorably protonated and the dye-polymer brush interactions are destabilized, where MB is released into solution.

## 2.4.6. pH-dependent morphology changes of polymer brush nanohybrids

Previous studies indicate that solvated brushes containing poly acids such as PAA can interconvert between swollen and collapsed states via changes of the solution pH. The pH responsive adsorption behavior of MNCs also affect the aggregation and self-assembly of the system. Dynamic light scattering (DLS) results were used to follow the change in the mean hydrodynamic radius ($R_h$) of the polymer MNCs at variable pH (Figure 2.8a). DLS results indicate that the $R_h$ value of the MNCs in aqueous solution decrease as the pH increases. The polydispersity index (PDI) values obtained from results in Figure 2.8 infer a narrow size-distribution, where the change in $R_h$ for the MNCs is related to the variation in hydrophile–lipophile balance of the MNCs with pH. Below the p$K_a$ (pH ≈ 2) of the polyacid, the COOH groups are nonionized and the polymer brush has sufficient lipophilic character to favor self-assembly. Above the p$K_a$ (pH ≈ 6), the COOH groups undergo ionization and the polymer brush attains more hydrophilic character.

The swelling due to hydration and steric repulsion between ionized groups occur due to the greater charge density of the polymer brush and variable hydrodynamic radii. The dehydrated mean diameter distribution of $Fe_3O_4$–PAAgCHI MNCs obtained from TEM results are generally smaller (∼20 nm) than $R_h$ values from DLS since nanocomposites are well hydrated at this pH (*cf.* Figure 2.8b at pH 7 (30.3 nm)). $R_h$ values for $Fe_3O_4$-PAAgCHI are ca. 32.3 nm at pH 6 (Figure 2.8c), where the average value at pH 2 varies dramatically, as seen by the presence of micron-sized aggregates in Figure 2.8d. The pH-dependent swelling and collapse of PAA brushes have been studied by AFM and ellipsometry.[54] Herein, the characterization of the sorbent morphology and the pH dependent dye adsorption/release behavior of MB was studied. Strong affinity of polymer brushes for MB at higher pH reveal favorable interactions and higher charge density of polymer brushes that lead to greater osmotic pressure due to the positively charged ions bound on the MNCs surface.[49] On the other hand, counterion binding and hydronium ions at acidic pH contribute to shrinkage of the polymer brushes that afford destabilization of the bound dye and its subsequent release.[48]

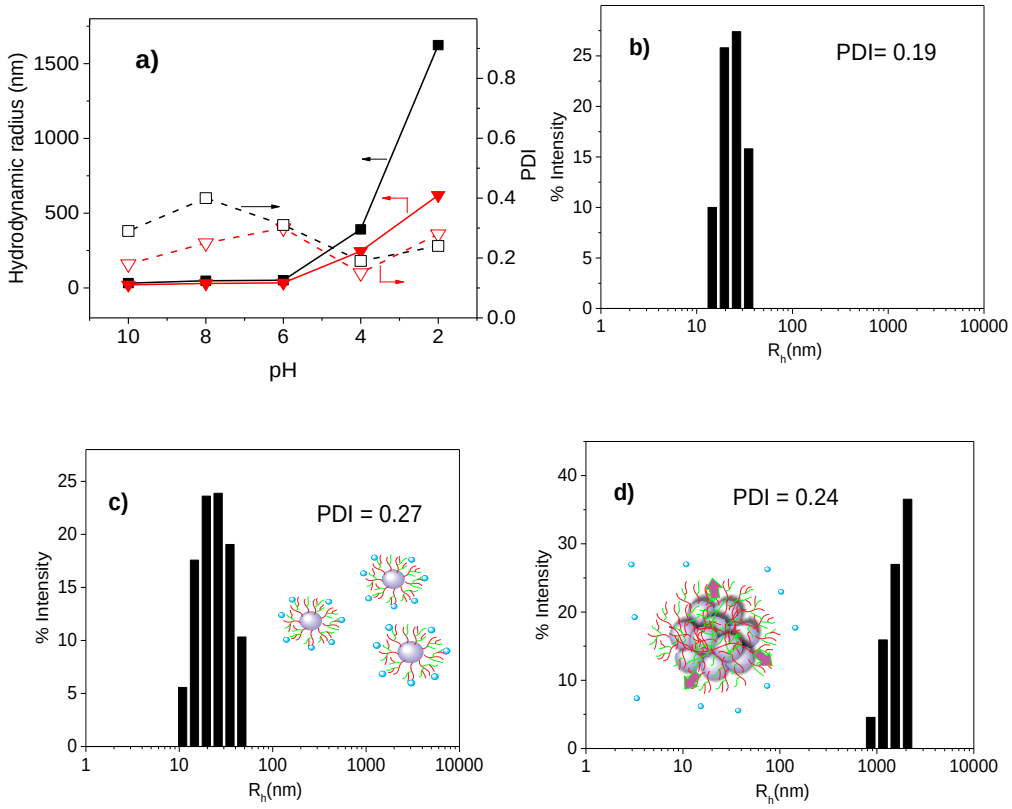


**Figure 2.8.** pH-dependent solution behavior of polymer brush MNCs; (a) Changes in mean hydrodynamic radius (solid lines) of $Fe_3O_4$-PIAgCHI (▼) and $Fe_3O_4$-PAAgCHI (■) samples and PDI (dash lines) in response to pH changes according to DLS. The mean $R_h$ distributions of PAAgCHI MNCs at pH of 7 (b), 6 (c), and 2 (d).

TEM results were used to further investigate the pH-dependent aggregation behavior and aqueous collapse of the brush-modified MNCs. The variation in morphology was investigated at pH values above and below the p$K_a$ of polymer brushes (pH 2 and 6). Representative TEM images of the MNCs are shown in Figure 2.9. At pH 2, there is notable aggregation for both MNCs (Figure 2.9b,d). At pH 6, the MNCs are uniform with a well-dispersed spherical morphology and no apparent aggregation (Figure 2.9a,c). As the pH is decreased, neutralization of charged monomers cause the polyelectrolyte brush to collapse due to decreased inter- and intrachain repulsive forces. The repulsive interactions between -$COO^-$ groups are overcome by hydrogen

bonding and hydrophobic effects due to changes in pH. In turn, this leads to brush-containing assemblies with reduced charge that undergoes aggregation with release of water and MB into the solution phase. The change in hydrophile-lipophile balance of the polymer results in enhanced aggregation (Figure 2.9b,d). The self-assembly of the MNCs contribute to dye release, as described above. As the pH increases, an opposite effect occurs since electrostatic repulsion among the -$COO^-$ groups attenuate aggregation. Thus, the dye adsorption/release process is a synergistic process of electrostatic interactions and morphological changes due to pH responsiveness and self-assembly in solution. An illustration of the proposed aggregation and dye release for the MNCs is depicted in Figure 2.9e. By comparison, Figure 2.10a-d reveal that the pH responsive behavior is fully reversible when the pH is varied between pH 2 (adsorption) and pH 6 (desorption). Approximately 91% release of bound MB occurs for polymer brushes and MNCs for these pH-switching conditions.

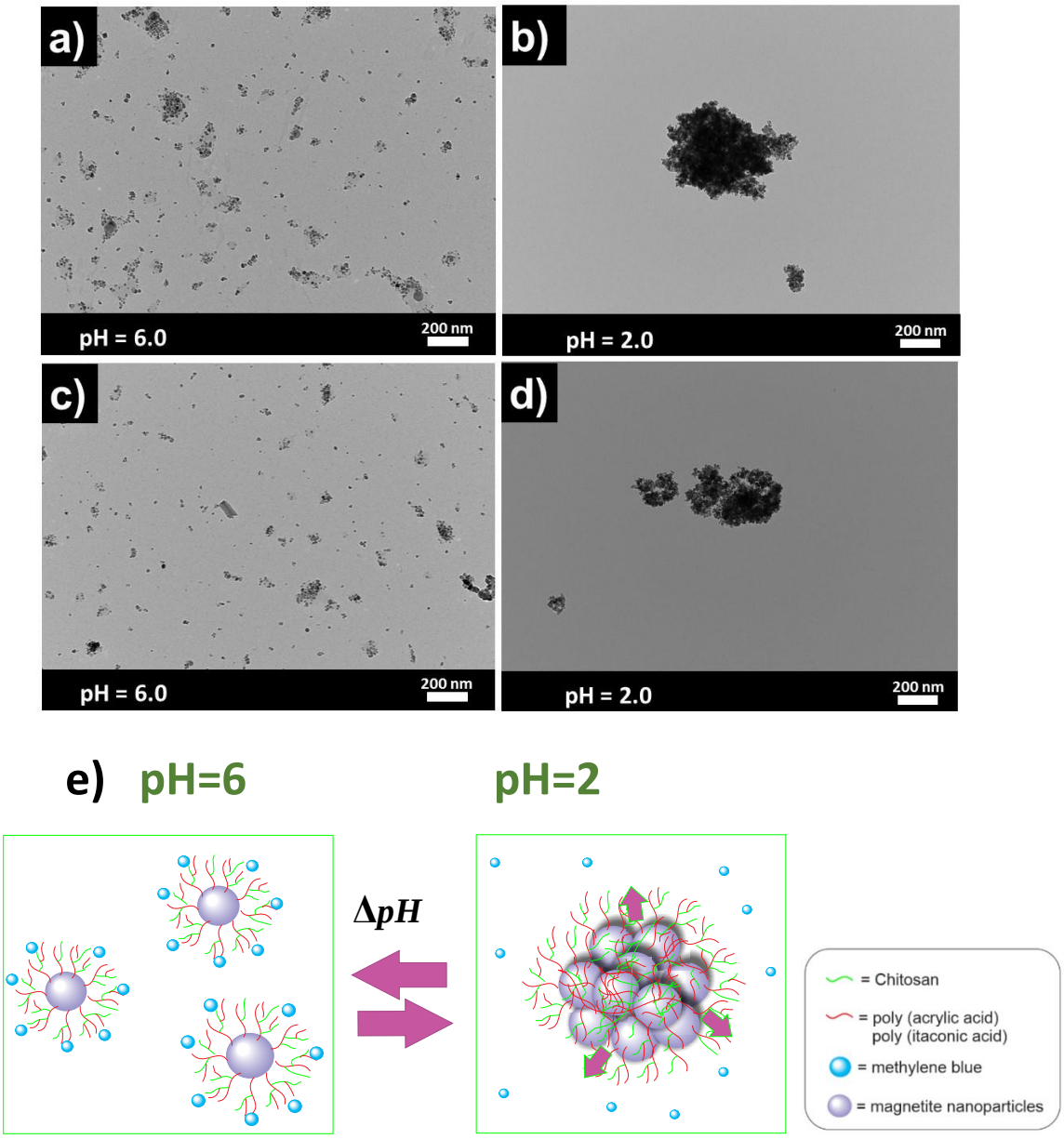


**Figure 2.9.** (a-e) TEM results and an illustration of the self-assembly for MNCs. TEM images of $Fe_3O_4$-PIAgCHI (top) and $Fe_3O_4$-PAAgCHI (bottom) from vacuum-dried water solutions with variable pH on copper grids: (a, c) pH 6; (b, d) pH 2; and (e) schematic illustration of pH-responsive aggregation behavior and the MB release process of MNCs.

The reuse and regeneration of an advanced adsorbent are important considerations for large-scale and industrial wastewater treatment applications. One challenge associated with conventional nanoscale adsorbent materials is the challenge concerning separation and regeneration because of the difficulty with phase separation, and potential loss of highly dispersed materials during each

cycle. Material losses may cause secondary problems by inadvertent release into the environment. Thus, an advantage of MNCs developed herein is their paramagnetic properties because it affords efficient separation and reuse over multiple cycles. The regeneration of the sorbents was studied by switching the solution pH between 2 and 9 to evaluate the MB removal (%) for five consecutive cycles. Across the first to the fifth cycle, the sorbent materials maintain high removal efficiency for MB with minor differences, as shown in Figure 2.11. After the fifth cycle, the MB removal (%) is preserved up to 84.3% for $Fe_3O_4$-PAAgHI, relative to the first cycle at 99.8%. Comparable performance was observed for PIAgCHI (82.6%) and $Fe_3O_4$-PIAgCHI (79.4%) up to the fifth cycle. The recovery process of the magnetic polymer brush materials is rapid within minutes upon switching the pH in the presence of an external magnetic field. The regeneration properties and the unique features of such MNCs demonstrate their utility for large-scale wastewater treatment of waterborne cationic dye contaminants.

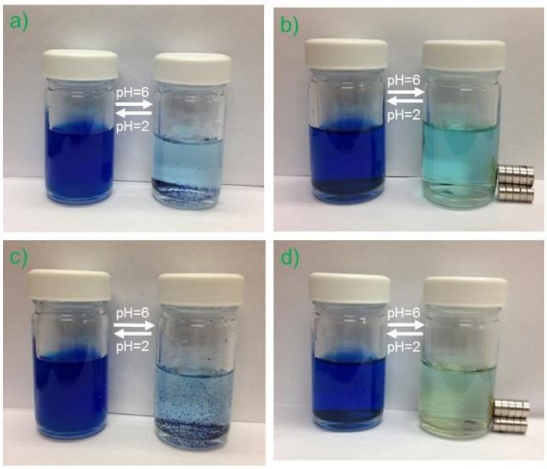


**Figure 2.10.** Reversible pH-controlled MB adsorption/desorption; and color changes of solutions (C0 = 0.3 mmol $L^{-1}$ ) containing (a) PIA grafted polymer brushes after settling, (b) $Fe_3O_4$-PIAgCHI MNCs and magnetic separation of adsorbents, (c) PIA grafted polymer brushes before settling, and (d) $Fe_3O_4$-PAAgCHI MNC sorbents and magnetic separation of adsorbents.

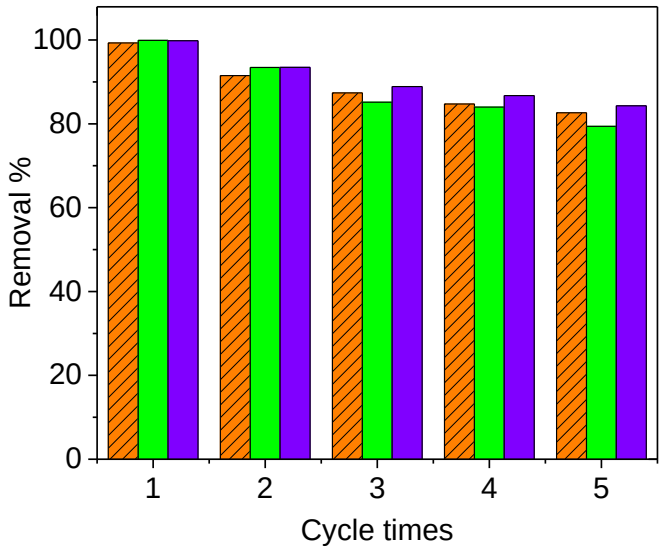


**Figure 2.11.** Adsorption-desorption cycles of PIAgCHI (orange bar), $Fe_3O_4$-PIAgCHI (green bar), and $Fe_3O_4$-PAAgCHI (purple bar) for MB systems

## 2.4.7. Adsorption kinetics

The adsorption kinetics were studied using a one-pot system.[37] The uptake behavior was followed using plots of $q_t$ at variable time ($t$) where the initial MB concentration (0.1 mM) is shown in Figure 2.12. The adsorption capacity of MB increased rapidly for the three adsorbents over the first 70 min and decreased thereafter. The initial rapid uptake of MB is related to the accessibility of the negatively charged adsorption sites on the adsorbent surface. The slower uptake relates to the occupancy of the adsorption sites and reduced osmotic pressure as the surface sites becomes saturated with MB. Therefore, initial adsorption of MB may limit the diffusion of other unbound species within the densely grafted brush structure, resulting in longer equilibrium times. The PFO and PSO kinetic models were used to determine the uptake kinetics where the best-fit results are shown in Figure 2.12 and Figure A.7 (Appendix). According to Table 2.2, the MNCs reveal greater uptake when compared against the polymer brush systems. The trends in uptake kinetic profiles for the three adsorbent materials complement the results for the $q_m$ values at

equilibrium. The PSO model provides a better description of the kinetic results relative to the PFO model, as evidenced by the best-fit results ($R^2$ values) in Table 2.2.

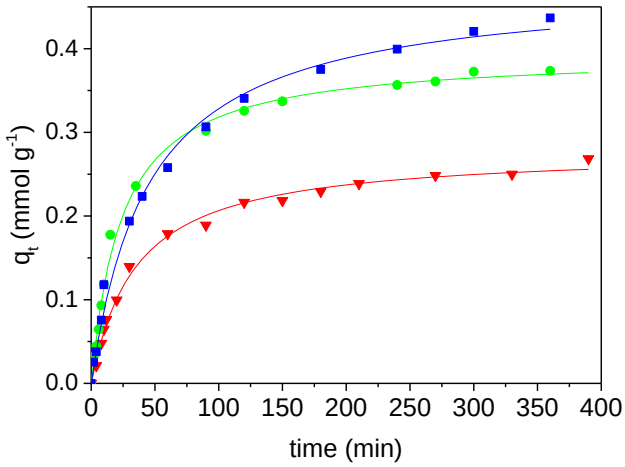


**Figure 2.12.** Adsorption kinetic profiles of MB on PIAgCHI (red ▼), $Fe_3O_4$-PAAgCHI (green ●), and $Fe_3O_4$-PIAgCHI (blue ■). Experimental conditions: adsorbent dose = 20 mg; initial MB concentration = 0.09 mM. V(solution) = 120 mL. The solid line is PSO fit to the experimental data.

**Table 2.2.** Adsorption kinetic parameters at 295 K in aqueous solution at ambient conditions.

| | **first-order kinetic model** | | | **second-order kinetic model** | | |
|---|---|---|---|---|---|---|
| **Sample** | $q_{max}$ (mmol g$^{-1}$) | $k_1$ (min$^{-1}$) | $R^2$ | $q_{max}$ (mmol g$^{-1}$) | $k_2$ (g/mmol.min) | $R^2$ |
| PIAgCHI | 0.240 | 0.025 | 0.978 | 0.279 | 0.103 | 0.995 |
| $Fe_3O_4$-PIAgCHI | 0.407 | 0.019 | 0.980 | 0.476 | 0.047 | 0.995 |
| $Fe_3O_4$-AAgCHI | 0.350 | 0.037 | 0.985 | 0.394 | 0.107 | 0.996 |

# 2.5. Conclusion

Polymer brushes and their iron oxide composites were prepared and characterized, along with the efficacy of MB removal from aqueous solution. These “smart” materials were designed by grafting PAA or PIA onto chitosan to yield pH-responsive polymer brushes and their composites containing iron oxide nanoparticles (IONPs). The MNCs are pH-responsive and magnetic adsorbents with switchable polymer morphology between swollen and collapsed states, along with

the controlled adsorption and desorption of MB. Switchable MB uptake is based on the pH driven molecular recognition and conformational changes of brushes. The adsorption capacity of the materials varies between 421.2 and 470.2 mg $g^{-1}$ with a removal efficiency of 99.2% ($Fe_3O_4$-PIAgCHI) and 99.5% ($Fe_3O_4$-PIAgCHI) for the MNCs. Sorbents can be recovered and efficiently regenerated by switching the pH of solution under an applied external field over five recycle steps. This work illustrates the potential utility of "smart" polymer brush systems for the remediation of cationic dye contaminants in wastewater. These eco-friendly sorbent materials possess excellent adsorption capacity, modular design, low cost, excellent regeneration, and rapid separation. Polymer brush nanocomposites are of immense interest for the future development of *smart materials* with tunable adsorption/release properties for advanced water treatment, nanomedicine, and drug delivery.

# 2.7. References


1. Mendes, P. M. Stimuli-Responsive Surfaces for Bio-Applications. *Chem. Soc. Rev.* **2008**, *37*, 2512-2529.

2. Liu, F.; Urban, M. W. Recent Advances and Challenges in Designing Stimuli-Responsive Polymers. *Prog. Polym. Sci.* **2010**, *35*, 3-23.

3. Lu, A. H.; Salabas, E. L.; Schuth, F. Magnetic Nanoparticles: Synthesis, Protection, Functionalization, and Application. *Angew. Chem. Int. Edit.* **2007**, *46*, 1222-1244.

4. Reddy, L. H.; Arias, J. L.; Nicolas, J.; Couvreur, P. Magnetic Nanoparticles: Design and Characterization, Toxicity and Biocompatibility, Pharmaceutical and Biomedical Applications. *Chem. Rev.* **2012**, *112*, 5818-5878.

5. Gao, J. H.; Gu, H. W.; Xu, B. Multifunctional Magnetic Nanoparticles: Design, Synthesis, and Biomedical Applications. *Acc. Chem. Res.* **2009**, *42*, 1097-1107.

6. Wang, S. Y.; Chen, K. M.; Xu, Y. S.; Yu, X. J.; Wang, W. H.; Li, L.; Guo, X. H. Protein Immobilization and Separation using Anionic/Cationic Spherical Polyelectrolyte Brushes Based on Charge Anisotropy. *Soft. Matter.* **2013**, *9*, 11276-11287.

7. Neuberger, T.; Schopf, B.; Hofmann, H.; Hofmann, M.; von Rechenberg, B. Superparamagnetic Nanoparticles for Biomedical Applications: Possibilities and Limitations of a New Drug Delivery System. *J. Magn. Magn. Mater.* **2005**, *293*, 483-496.

8. Li, L.; Fan, M. H.; Brown, R. C.; Van Leeuwen, J. H.; Wang, J. J.; Wang, W. H.; Song, Y. H.; Zhang, P. Y. Synthesis, Properties, and Environmental Applications of Nanoscale Iron-Based Materials: A Review. *Crit. Rev. Env. Sci. Technol.* **2006**, *36*, 405-431.

9. Chang, Y. C.; Chen, D. H. Preparation and Adsorption Properties of Monodisperse Chitosan-Bound $Fe_3O_4$ Magnetic Nanoparticles for Removal of Cu(II) Ions. *J. Colloid Interface Sci.* **2005**, *283*, 446-451.

10. Mittal, H.; Ballav, N.; Mishra, S. B. Gum Ghatti and $Fe_3O_4$ Magnetic Nanoparticles Based Nanocomposites for the Effective Adsorption of Methylene Blue from Aqueous Solution. *J. Ind. Eng. Chem.* **2014**, *20*, 2184-2192.

11. Wu, R. C.; Qu, J. H.; Chen, Y. S. Magnetic Powder MnO-$Fe_2O_3$ Composite - A Novel Material for the Removal of Azo-Dye from Water. *Water Res.* **2005**, *39*, 630-638.

12. Zhong, L. S.; Hu, J. S.; Liang, H. P.; Cao, A. M.; Song, W. G.; Wan, L. J. Self-Assembled 3D Flowerlike Iron Oxide Nanostructures and their Application in Water Treatment. *Adv. Mater.* **2006**, *18*, 2426-2431.

13. Pratt, D. Y.; Wilson, L. D.; Kozinski, J. A. Preparation and Sorption Studies of Glutaraldehyde Cross-Linked Chitosan Copolymers. *J. Colloid Interface Sci.* **2013**, *395*, 205-211.

14. Dragan, E. S.; Loghin, D. F. A.; Cocarta, A. I. Efficient Sorption of $Cu^{2+}$ by Composite Chelating Sorbents Based on Potato Starch-graft-Polyamidoxime Embedded in Chitosan Beads. *ACS Appl. Mater. Interfaces* **2014**, *6*, 16577-16592.

15. Kyzas, G. Z.; Kostoglou, M.; Lazaridis, N. K. Copper and Chromium(VI) Removal by Chitosan Derivatives-Equilibrium and Kinetic Studies. *Chem. Eng. J.* **2009**, *152*, 440-448.

16. Kyzas, G. Z.; Siafaka, P. I.; Lambropoulou, D. A.; Lazaridis, N. K.; Bikiaris, D. N. Poly(Itaconic acid)-Grafted Chitosan Adsorbents with Different Cross-Linking for Pb(II) and Cd(II) Uptake. *Langmuir* **2014**, *30*, 120-131.

17. Kyzas, G. Z.; Kostoglou, M.; Lazaridis, N. K.; Bikiaris, D. N. N-(2-Carboxybenzyl) Grafted Chitosan as Adsorptive Agent for Simultaneous Removal of Positively and Negatively Charged toxic Metal Ions. *J. Hazard. Mater.* **2013**, *244*, 29-38.

18. Guzman, J.; Saucedo, I.; Navarro, R.; Revilla, J.; Guibal, E. Vanadium Interactions with Chitosan: Influence of Polymer Protonation and Metal Speciation. *Langmuir* **2002**, *18*, 1567-1573.

19. Guibal, E. Interactions of Metal Ions with Chitosan-Based Sorbents: A Review. *Sep. Purif. Technol.* **2004**, *38*, 43-74.

20. Kandile, N. G.; Nasr, A. S. Environment Friendly Modified Chitosan Hydrogels as a Matrix for Adsorption of Metal Ions, Synthesis and Characterization. *Carbohyd. Polym.* **2009**, *78*, 753-759.

21. Muzzarelli, R. A. A.; Tanfani, F.; Emanuelli, M.; Mariotti, S. N-(Carboxymethylidene)Chitosans and N-(Carboxymethyl)-Chitosans - Novel Chelating Polyampholytes Obtained from Chitosan Glyoxylate. *Carbohyd. Res.* **1982**, *107*, 199-214.

22. Gerente, C.; Lee, V. K. C.; Le Cloirec, P.; McKay, G. Application of Chitosan for the Removal of Metals from Wastewaters by Adsorption - Mechanisms and Models Review. *Crit. Rev. Env. Sci. Technol.* **2007**, *37*, 41-127.

23. Muzzarelli, R. A. A.: Natural Chelating Polymers: Alginic Acid, Chitin, and Chitosan. *The University of Michigan*, Pergamon Press, 1973.

24. Cho, D. W.; Jeon, B. H.; Chon, C. M.; Schwartz, F. W.; Jeong, Y.; Song, H. Magnetic Chitosan Composite for Adsorption of Cationic and Anionic Dyes in Aqueous Solution. *J. Ind. Eng. Chem.* **2015**, *28*, 60-66.

25. Zeng, L. X.; Xie, M. J.; Zhang, Q. Y.; Kang, Y.; Guo, X. M.; Xiao, H. J.; Peng, Y. N.; Luo, J. W. Chitosan/Organic Rectorite Composite for the Magnetic Uptake of Methylene Blue and Methyl Orange. *Carbohyd. Polym.* **2015**, *123*, 89-98.

26. Fan, L. L.; Luo, C. N.; Sun, M.; Li, X. J.; Lu, F. G.; Qiu, H. M. Preparation of Novel Magnetic Chitosan/Graphene Oxide Composite as Effective Adsorbents Toward Methylene Blue. *Bioresour. Technol.* **2012**, *114*, 703-706.

27. Sheiko, S. S.; Sumerlin, B. S.; Matyjaszewski, K. Cylindrical Molecular Brushes: Synthesis, Characterization, and Properties. *Prog. Polym. Sci.* **2008**, *33*, 759-785.

28. Lee, H. I.; Pietrasik, J.; Sheiko, S. S.; Matyjaszewski, K. Stimuli-Responsive Molecular Brushes. *Prog. Polym. Sci.* **2010**, *35*, 24-44.

29. Stuart, M. A. C.; Huck, W. T. S.; Genzer, J.; Muller, M.; Ober, C.; Stamm, M.; Sukhorukov, G. B.; Szleifer, I.; Tsukruk, V. V.; Urban, M.; Winnik, F.; Zauscher, S.; Luzinov, I.; Minko, S. Emerging Applications of Stimuli-Responsive Polymer Materials. *Nat. Mater.* **2010**, *9*, 101-113.

30. Edmondson, S.; Osborne, V. L.; Huck, W. T. S. Polymer Brushes via Surface-Initiated Polymerizations. *Chem. Soc. Rev.* **2004**, *33*, 14-22.

31. Farrukh, A.; Akram, A.; Ghaffar, A.; Hanif, S.; Hamid, A.; Duran, H.; Yameen, B. Design of Polymer-Brush-Grafted Magnetic Nanoparticles for Highly Efficient Water Remediation. *ACS Appl. Mater. Interfaces* **2013**, *5*, 3784-3793.

32. Liu, X. W.; Hu, Q. Y.; Fang, Z.; Zhang, X. J.; Zhang, B. B. Magnetic Chitosan Nanocomposites: A Useful Recyclable Tool for Heavy Metal Ion Removal. *Langmuir* **2009**, *25*, 3-8.

33. Suh, S. K.; Yuet, K.; Hwang, D. K.; Bong, K. W.; Doyle, P. S.; Hatton, T. A. Synthesis of Nonspherical Superparamagnetic Particles: In Situ Coprecipitation of Magnetic Nanoparticles in Microgels Prepared by Stop-Flow Lithography. *J. Am. Chem. Soc.* **2012**, *134*, 7337-7343.

34. Ayad, M.; Salahuddin, N.; Fayed, A.; Bastakoti, B. P.; Suzuki, N.; Yamauchi, Y. Chemical Design of a Smart Chitosan-Polypyrrole-Magnetite Nanocomposite Toward Efficient Water Treatment. *Phys. Chem. Chem. Phys.* **2014**, *16*, 21812-21819.

35. Zhao, L. L.; Liu, H. R.; Wang, F. W.; Zeng, L. Design of Yolk-Shell $Fe_3O_4$@PMAA Composite Microspheres for Adsorption of Metal Ions and pH-Controlled Drug Delivery. *J. Mater. Chem. A* **2014**, *2*, 7065-7074.

36. Hall-Edgefield, D. L.; Shi, T.; Nguyen, K.; Sidorenko, A. Hybrid Molecular Brushes with Chitosan Backbone: Facile Synthesis and Surface Grafting. *ACS Appl. Mater. Interfaces* **2014**, *6*, 22026-22033.

37. Mohamed, M. H.; Wilson, L. D. Kinetic Uptake Studies of Powdered Materials in Solution. *Nanomaterials* **2015**, *5*, 969-980.

38. Ho, Y. S. Review of Second-Order Models for Adsorption Systems. *J. Hazard. Mater.* **2006**, *136*, 681-689.

39. Azizian, S. Kinetic Models of Sorption: A Theoretical Analysis. *J. Colloid Interface Sci.* **2004**, *276*, 47-52.

40. Pal, A.; Das, D.; Sarkar, A. K.; Ghorai, S.; Das, R.; Pal, S. Synthesis of Glycogen and Poly (Acrylic Aacid)-Based Graft Copolymers via ATRP and its Application for Selective Removal of $Pb^{2+}$ Ions from Aqueous Solution. *Eur. Polym. J.* **2015**, *66*, 33-46.

41. Odio, O. F.; Lartundo-Rojas, L.; Santiago-Jacinto, P.; Martinez, R.; Reguera, E. Sorption of Gold by Naked and Thiol-Capped Magnetite Nanoparticles: An XPS Approach. *J. Phys. Chem. C* **2014**, *118*, 2776-2791.

42. Palchoudhury, S.; An, W.; Xu, Y. L.; Qin, Y.; Zhang, Z. T.; Chopra, N.; Holler, R. A.; Turner, C. H.; Bao, Y. P. Synthesis and Growth Mechanism of Iron Oxide Nanowhiskers. *Nano Lett.* **2011**, *11*, 1141-1146.

43. Arias, J. L.; Reddy, L. H.; Couvreur, P. $Fe_3O_4$/Chitosan Nanocomposite for Magnetic Drug Targeting to Cancer. *J. Mater. Chem.* **2012**, *22*, 7622-7632.

44. Wang, L.; Wu, X. L.; Xu, W. H.; Huang, X. J.; Liu, J. H.; Xu, A. W. Stable Organic-Inorganic Hybrid of Polyaniline/alpha-Zirconium Phosphate for Efficient Removal of Organic Pollutants in Water Environment. *ACS Appl. Mater. Interfaces* **2012**, *4*, 2686-2692.

45. Kyzas, G. Z.; Bikiaris, D. N.; Seredych, M.; Bandosz, T. J.; Deliyanni, E. A. Removal of Dorzolamide from Biomedical Wastewaters with Adsorption onto Graphite Oxide/Poly(Acrylic Acid) Grafted Chitosan Nanocomposite. *Bioresour. Technol.* **2014**, *152*, 399-406.

46. He, H. B.; Li, B.; Dong, J. P.; Lei, Y. Y.; Wang, T. L.; Yu, Q. W.; Feng, Y. Q.; Sun, Y. B. Mesostructured Nanomagnetic Polyhedral Oligomeric Silsesquioxanes (POSS) Incorporated with Dithiol Organic Anchors for Multiple Pollutants Capturing in Wastewater. *ACS Appl. Mater. Interfaces* **2013**, *5*, 8058-8066.

47. Luo, B.; Song, X. J.; Zhang, F.; Xia, A.; Yang, W. L.; Hu, J. H.; Wang, C. C. Multi-Functional Thermosensitive Composite Microspheres with High Magnetic Susceptibility Based on Magnetite Colloidal Nanoparticle Clusters. *Langmuir* **2010**, *26*, 1674-1679.

48. Ballauff, M.; Borisov, O. Polyelectrolyte Brushes. *Curr. Opin. Colloid Interface Sci.* **2006**, *11*, 316-323.

49. Willott, J. D.; Humphreys, B. A.; Murdoch, T. J.; Edmondson, S.; Webber, G. B.; Wanless, E. J. Hydrophobic Effects Within the Dynamic pH-Response of Polybasic Tertiary Amine Methacrylate Brushes. *Phys. Chem. Chem. Phys.* **2015**, *17*, 3880-3890.

50. Samiey, B.; Ashoori, F. Adsorptive Removal of Methylene Blue by Agar: Effects of NaCl and Ethanol. *Chem. Cent. J.* **2012**, *6*, 68137-17133.

51. Alswieleh, A. M.; Cheng, N.; Canton, I.; Ustbas, B.; Xue, X.; Ladmiral, V.; Xia, S. J.; Ducker, R. E.; El Zubir, O.; Cartron, M. L.; Hunter, C. N.; Leggett, G. J.; Armes, S. P. Zwitterionic Poly(amino acid methacrylate) Brushes. *J. Am. Chem. Soc.* **2014**, *136*, 9404-9413.

52. Langmuir, I. The Constitution and Fundamental Properties of Solids and Liquids Part I Solids. *J. Am. Chem. Soc.* **1916**, *38*, 2221-2295.

53. Mohamed, M. H.; Wilson, L. D.; Headley, J. V.; Peru, K. M. Sequestration of Naphthenic Acids from Aqueous Solution using Beta-Cyclodextrin-Based Polyurethanes. *Phys. Chem. Chem. Phys.* **2011**, *13*, 1112-1122.

54. Amalvy, J. I.; Wanless, E. J.; Li, Y.; Michailidou, V.; Armes, S. P.; Duccini, Y. Synthesis and Characterization of Novel pH-Responsive Microgels Based on Tertiary Amine Methacrylates. *Langmuir* **2004**, *20*, 8992-8999.

# CHAPTER 3

# Redox-responsive Polymer Template as an Advanced Multifunctional Catalyst Support for Silver Nanoparticles*

*Reprinted with permission from Dolatkhah, A.; Jani, P.; Wilson, L. D. *Langmuir* **2018**, 34, 10560-10568. © 2018 American Chemical Society. DOI: 10.1021/acs.langmuir.8b02336. Permission was obtained from all co-authors to include this manuscript in the thesis. A.D. carried out all experimental work (except where noted below) and wrote the first draft of the manuscript. P.J. and A.D. performed an equal contribution to the catalytic reduction experiments. L.D.W. directed the study and revised the manuscript prior to publication.

## 3.1 Abstract

Hybridization of metal NPs with redox-switchable polymer supports not only mitigates their aggregation, but also introduces interfacial electron pathways desirable for catalysis and numerous other applications. The large surface area and surface accessible atoms for noble metal nanoparticles (e.g., Ag, Au, Pt) offer promising opportunities to address challenges in catalysis and environmental remediation. Herein, Ag NPs were supported onto redox-switchable polyaniline that acts as an advanced multifunctional conducting template for enhanced catalytic activity. At the initial stage of reduction of $Ag^{+}$, leucoemeraldine (LE) is oxidized *in-situ* to pernigraniline (PG) which acts as interfacial pathway between NPs for electron transport. With the contribution of $BH_4^{-}$, PG acts as an electron-acceptor site which creates interfacial electron-hole pairs, serving as additional active catalytic reduction sites. The use of a redox-responsive composite system as a template enhances catalyst performance through adjustable charge injection across interfacial sites, along with catalyst reusability for the reduction of 4-NPh. Strikingly, from XPS results it was observed that *in-situ* reduction of $Ag^{+}$ onto the conductive polymer alters the electronic character of the catalyst. The unique multi-electronic effects of such Ag supported NPs enrich the scope of such catalytic systems via a tunable interface, diversified catalytic activity, fast kinetics, minimization of Ag NPs aggregation, and maintenance of high stability under multiple reaction cycles.

## 3.2. Introduction

Conducting polymeric materials have gained considerable attention,[1-3] especially in the case of PANI where it plays a pivotal role in environmental remediation, energy transport[4,5] and catalysis[6,7] because of its high stability,[5] pH/redox-responsiveness,[5] high conductivity[6,8] and facile synthesis. Owing to their unusual properties that differ from their bulk counterparts, noble metal

nanoparticles (NPs)[9] such as Au, Pt and Ag are of special interest due to their unique optical and electronic properties.[10,11] These properties lead to widespread utility of such NPs in energy storage,[4,12] antibacterial agents,[13] catalysis,[6,7,9,11,14,15] environmental remediation,[12,15] and SERS detection.[10,11,16,17] However, the practical use of NPs as catalysts is offset as the surface must be passivated with ligands to minimize aggregation and maintain stability. In passivated NPs, ligands may cause steric effects at the NPs surface active sites which may adversely affect catalytic activity.[18] Besides, from a catalysis point-of-view, sluggish kinetics and limited active sites for reactants may pose limitations when Ag NPs are used for catalytic reactions. Such shortcomings present challenges for use of NPs in catalytic reactions. The combination of componential and structural properties of dissimilar functional materials and metal NPs with the intention of modifying their properties in a synergistic manner is an attractive strategy to yield materials with diverse and integrated applications.[4,6,7,11,14,16,17,19-23] In the case of noble metal NPs, this strategy can lower the cost of Ag or Au and to also widen the scope of properties for ameliorated catalytic efficiency and stability of integrated systems.

In this context, researchers have put significant effort on the development and structural design of nanocomposites for catalytic reduction of model systems such as 4-NPh. A previous report[14] indicated that extraordinary catalytic activity of Ag NPs was attainable via hybridization of NPs with various polymers and functional supports. For example Liang et al. [19] found that the use of Cu/CuO-Ag nanocatalyst for reduction of 4-NPh outperformed those for Cu/CuO and Ag NPs.[19] Lu et al.[16] produced a covalent organic framework (COF), COF-templated catalysts containing ultrafine metal NPs for efficient reduction of 4-NPh. While the COF material does not display any notable catalytic activity, it plays critical role in catalysis stability, well-defined particle size and excellent catalytic activity. Liu et al.[17] reported on the *in-situ* synthesis of metal NPs in chalcogel

support networks, where the substrate favours dispersion, high surface area, and catalyst recyclability. Eggshell membrane biotemplate[14] was used for *in-situ* reduction of Ag NPs to add stability to the integrated catalyst for 4-NPh reduction. In another study,[23] Ag NPs were passivated with PAA which can be exchanged with proteins and biomolecules to achieve catalyst with high colloidal stability and adjustable activity.

These examples provide support that judicious choice of a suitable template support or functional doping agent that can be efficiently interfaced with Ag NPs that serve to boost key performance parameters such as catalyst activity, stability and selectivity. Therefore, exploring an effective strategy for constructing efficient metal NPs catalyst remains an active area of research. In particular, a key consideration to afford enhanced catalytic activity of noble metal NPs is selection of an appropriate support or doping agent to create additional reaction sites for the catalyst to enhance the electron transport kinetics. PANI is a potential support for Au and Ag NPs catalysis systems due to its low interfacial reactivity, electrical conductivity[5,6,8], adsorbing surface[24] and electrochemical switchability.[5,6,25] The conductivity of a support material in a catalyst system is important to achieve rapid electron transfer kinetics.[7,19] Herein, it is highly desirable to use the advantage of PANI as a functional support to construct an advanced low cost catalyst with favourable catalytic performance. On the other hand, despite the recent developments[6,25] related to the design of metal/semiconductor catalyst systems, little is known about the interfacial electrical behavior of PANI nanocomposites with noble metal NPs with tunable nanointerface behavior. In order to harness the potential of PANI materials for catalysis when interfaced with noble metal NPs, a comprehensive understanding of their electronic effects and structure-function properties are required. At present, such knowledge is currently lacking in metal NPs/PANI based catalytic systems.

The above knowledge gap provided the motivation to design viable PANI/Ag nanocatalyst systems. PANI serves as a redox-responsive, multifunctional, and powerful template for Ag NPs with high stability and greater catalytic activity via electronic communication and charge injection across the Ag/PANI interface. More importantly, this work also reports on the mechanistic illustration of catalytic function and synergism between two dissimilar materials of Ag NPs and a PANI support. Interface hybridization of compositional and structural properties of Ag and PANI may offer accessible reduction sites by altering electronic structure and creation of nanointerfaces by composite formation. In turn, this would contribute to fast electron transport, enhanced kinetics and extraordinary performance under successive catalytic cycles. The rapid electron transfer across the interface of Ag and a conductive polymer are shown to mediate remarkably high catalytic activity in these systems.

## 3.3. Experimental section

### 3.3.1. Materials

Chitosan of medium molecular weight, aniline (purity 99.5%) and APS (purity 98%) were obtained from Sigma-Aldrich. Silver nitrate ($AgNO_3$), sodium borohydride ($NaBH_4$) (purity 95%) and potassium bromide (KBr) (purity 99.5%) were obtained from BDH Chemicals. Sodium hydroxide (NaOH) and hydrochloric acid (HCl) (12.1N) were obtained from Fischer Chemical. 4-NPh (purity 99%) was obtained from Alfa Aesar and was used after purification by three recrystallization cycles.

### 3.3.2. Synthesis of catalysts

Three types of catalysts were prepared with variable amounts of chitosan and PANI. For AgNPs-CP75, containing 75% of aniline, 0.1 g of chitosan was dissolved in 50 mL of 0.1M HCl

solution by stirring for 1 h. 0.3 mL of aniline was added to the solution and stirred for 10 minutes. Similarly, two more solutions containing 0.2 g chitosan and 0.2 mL aniline for AgNP-CP50 and 0.3 g chitosan containing 0.1 mL aniline for AgNP-CP25 were prepared separately. 1.47 g of APS was dissolved in 20 mL of 0.1 M HCl and added at a rate of ca. 1 drop/s to each of the three solutions containing chitosan and aniline. The resulting solutions were stirred for 24 h. The pH of the final solution was neutralized by using aqueous NaOH and HCl as required. The resulting polymer composites were collected by filtration and washed to remove excess APS by repeated washings using Millipore water. The composites were dispersed in 125 ml of 5 mM $AgNO_3$ solution and kept in an ice-bath with continuous stirring. 375 ml of 10 mM $NaBH_4$ was added at a rate of ca.1 drop/s to the solution. The solution was stirred for 1 h after the complete addition of $NaBH_4$ and the mixture was allowed to settle for overnight 24 h. The solution was centrifuged and the obtained material was ground to a powder form after drying in oven for 24 h. Silver NPs were synthesized in accordance with previously published literature.[26]

### 3.3.3. Catalytic activity of nanocomposites

To investigate the catalytic activity of nanocomposites, the reduction of 4-NPh to 4-APh was used as the model reaction. The catalytic reduction studies were carried out using 10 mL of 1.1 mM 4-NPh solution (pH=8.2). At first, 10 mg of catalyst nanocomposites was added into 10 mL of 4-NPh solution and the solution was sonicated to ensure proper dispersal of the catalyst in the solution. Subsequently 20 mg of $NaBH_4$ were added to the mixture and the reaction started immediately. Aliquots of sample (0.2 mL) were taken at time intervals from the reaction mixture, diluted 15 times and filtered using a 0.2 µm nylon syringe filter to separate catalyst from the solution in order to prevent further reaction prior to UV-vis absorbance analysis of the solution. The concentration of 4-NPh was calculated by measuring the UV-vis absorbance of the solution

(λ=400 nm). Temperature effects on the reaction were studied from 303 K to 323 K at the following conditions: 50 mL of 1.1 mM 4-NPh (pH=8.2), 50 mg of catalyst and 100 mg of $NaBH_4$. To study the recyclability, the relative efficiencies of the catalysts were measured for 6 catalytic cycles using 50 mL of 1.1 mM 4-NPh (pH=8.2), 50 mg of catalyst and 100 mg of $NaBH_4$. The used catalyst was isolated from the solution by centrifugation at the end of each cycle, the catalysts were washed with absolute ethanol and Millipore water followed by drying in an oven for about 15 min after each cycle to investigate the reusability of AgNP-CPs catalysts. The recovered samples were re-dispersed in a fresh reaction solution for the next catalytic cycle. After reaction for 30 min, the solution absorbance was measured using UV-Vis spectroscopy. The following equation (Eq. 3.1) was used to calculate conversion (%) where $C_t$ is the concentration of 4-NPh after 30 min and $C_0$ is the concentration of 4-NPh at time 0.

$$Conversion\% = \frac{C_0 - C_t}{C_0} \quad (3.1)$$

## 3.3.4. Measurements and characterization

Product morphology was characterized using TEM (Hitachi HT-7700 microscope) at accelerating voltage 100 kV. For the sample preparation, samples were dispersed in aqueous ethanol solution using an ultrasonic bath, where a drop of suspension was placed onto the holey carbon coated copper grids, where samples were air-dried before imaging. PXRD profiles were obtained using a PANalytical Empyrean powder diffractometer with Co $K_\alpha$ radiation (λ =1.79 Å) powered at 40 kV and 45 mA. X-ray photoelectron spectroscopy (XPS) measurements were performed in a Kratos AXIS Supra X-ray photoelectron spectrometer (powered at 225 W) using Al Kα radiation (λ = 8.357 Å). C 1*s* (284.8 eV) was used to calibrate the binding energies (BE) of the elements. UV-vis spectra were collected using a Varian Cary 100 Scan spectrophotometer.

DRIFT spectra were recorded with a Bio-RAD FTS-40 spectrophotometer where samples were analyzed in reflectance mode. Samples were mixed with pure spectroscopic grade KBr followed by grinding in a mortar and pestle (sample/KBr=1/10).

## 3.4. Results and discussion

Three different polymer-supported silver NPs (AgNP-CP25, AgNP-CP50 and AgNP-CP75, where the number denotes the wt.% of PANI relative to CHI in a binary composite) prepared by facile *in-situ* reduction of $AgNO_3$ in the presence of aqueous dispersion of the PANI composite outlined in the Section 3.3.2. The chitosan-PANI composite (CP) provides an environment where Ag species can be readily adsorbed and reduced to yield supported Ag(0). The formation of nanocatalysts by reduction of $AgNO_3$ solution was indicated by the concomitant change in the color of the polymer dispersion from dark-black to dark-grey dispersion. Aside from redox-switchable characteristics of PANI, the amine/imine groups, the quinoid (Q) and benzenoid (B) forms of PANI afford sites that have strong affinity for anchoring metals. The PANI binding sites can efficiently stabilize and adsorb NPs, in agreement with variable binding affinity reported for metal ions and by the removal of various cation and anion systems from water.[24] In this regard, the redox-responsiveness of PANI is a suitable option to serve as nucleation sites for growth of Ag NPs, and as a multifunctional electro-active template for enhanced catalysis. PXRD pattern of AgNPs-CPs, shown in Figure 3.1a, comprised several reflections at 2θ values (44.7, 52.2 and 76.8°) that correspond to the typical (111), (200) and (220) planes of face-centered cubic (fcc) silver that indicate the crystalline nature of the Ag NPs. The diameter and size distribution of the Ag NPs and AgNP-CPs were analyzed using transmission electron microscopy. Samples were prepared using ethanol dispersion of catalysts that were drop-cast onto carbon-coated copper grids and allowed to dry at 295 K prior to analysis. The typical TEM images of the catalysts clearly

show the formation of well dispersed and supported Ag NPs within polymer materials (Figures 3.1b-e). Statistical analysis (detailed in Appendix) of NPs shows that there is a slight increase in the mean particle diameter of NPs as the ratio of PANI materials increased (*cf.* Figure A.10 in Appendix).

Typically, the catalytic performance of noble metal catalysts is often evaluated by reduction of 4-NPh to 4-APh as a model dye system in the presence of $NaBH_4$.[27-30] 4-APh initially has a characteristic absorption peak at 317 nm in acidic or neutral medium. However, at pH=10 in $CH_3CO_2Na$ buffer, the solution color changed from light to bright yellow, and the absorption peak shifted to 400 nm due to deprotonation and formation of the 4-nitrophenolate ion.[31,32] The reduction process can be monitored by UV-vis spectroscopy by characteristic absorption band of 4-NPh and 4-APh at ca. 400 and 300 nm, respectively. More importantly, this reaction is of high practical significance as 4-NPh is considered as a priority organic water pollutant, which is persistent and generated from the production of herbicides, pesticides, insecticides. By contrast, the formation of 4-APh is a fine chemical of value relevant to industrial dye production and biomedical applications.[15,16,19] In this study, the catalytic reduction of 4-NPh to 4-APh with $NaBH_4$ in aqueous solution was selected as a model reaction to evaluate the catalytic activity of materials. In the absence of catalyst, kinetically this reaction is limited by the positive activation barrier[14,19,27] between donor and acceptor molecules. The physical mixture of PANI/CHI (PMix) also does not show significant catalytic activity as illustrated by a 4-NPh band, where its intensity at 400 nm remains constant over time (Figure 3.2a, inset). Similarly, for the mixture of $NaBH_4$ and 4-NPh in the presence of Ag NPs (without polymer support), poor performance was observed as reduction was complete within 1h (Figure 3.2a). The use of AgNP-CP25 nanocatalyst results in full reduction of 4-NPh within ca. 30 min, (nearly half the time observed for isolated Ag NPs)

according to the sequential UV-vis monitoring at variable time (Figure 3.2b). By contrast, for AgNP-CP50, completion of the reduction process was reduced to 17 min with complete disappearance of the absorbance band at 400 nm, where new bands assigned to 4-APh appear gradually near 300 and 233 nm.

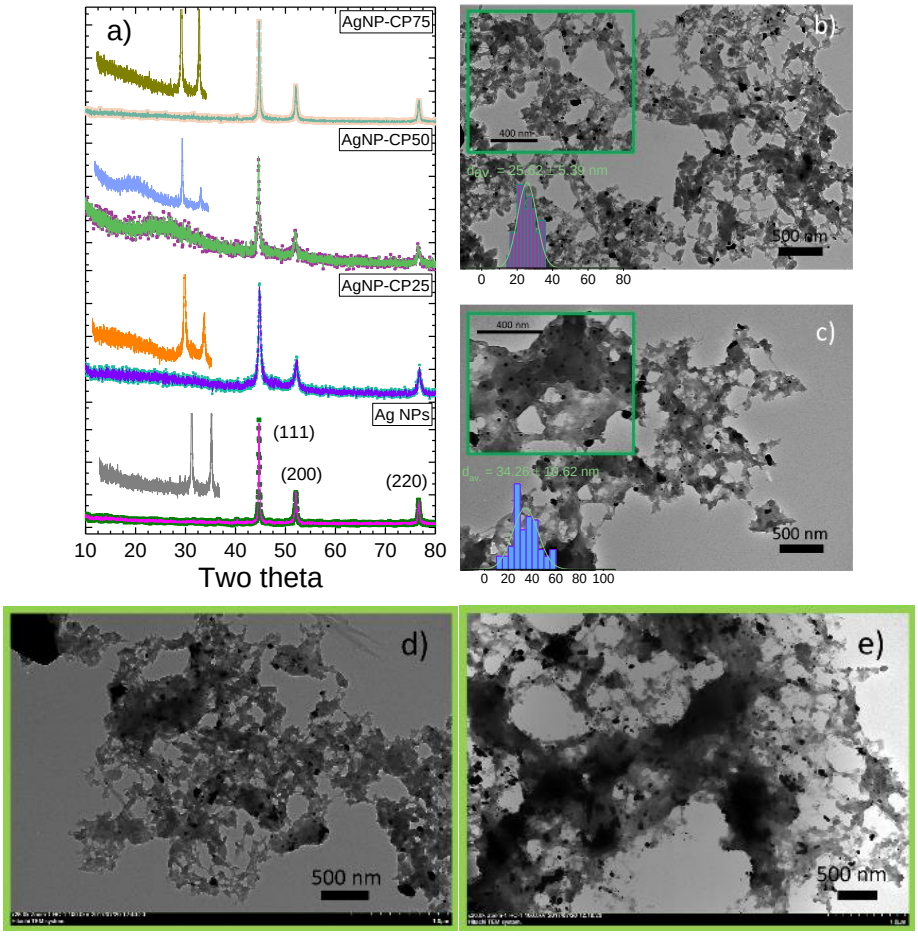


**Figure 3.1.** (a) PXRD spectra of materials. Inset curves are expanded spectra in the range 2θ = (10-55). TEM images of (b, d) AgNP-CP50, (c, e) AgNP-CP75 and; evidence for well dispersed metal NPs on the surface of the active polymer matrix. Insets (b, c): corresponding size distribution of supported Ag NPs based on N=100 NPs.

This transformation and discoloration was evident by visual detection of yellow discoloration of the solution to colorless rapidly, as shown by typical optical images (Figure 3.2c, inset). By the end of the reaction after 26 min, only the band for the product 4-APh (without dilution) obtained

directly from the sample was observed that indicates the formation of a high purity product (*cf.* inset spectra, Figure 3.2c). Unlike AgNPs-CP25 where residual 4-NPh remains after 30 min (*cf.* Figure 3.2b, red arrow). AgNP-CP75 catalyst yields rapid conversion in less than 10 min. Catalytic reduction was tracked by the sequential UV-vis spectra with time (Figure 3.2d) by the appearance of new band for 4-APh near 300 nm. The much shorter time to achieve near completion of reduction by AgNP-CP75 may be due to the electronic properties and reduction mechanism, as detailed in the section below. Although the reduction of 4-NPh to 4-APh is thermodynamically favored ($E_0$|4-NPh/4-APh = -0.76 V, $E_0|H_3BO_3/BH_4^-$ = -1.33 V vs. NHEP), the reaction is not feasible without catalysis (or external inputs) due to a large kinetic barrier for an electronic relay between the donor (D; $BH_4^-$) and the acceptor (A; 4-APh).[14,29]

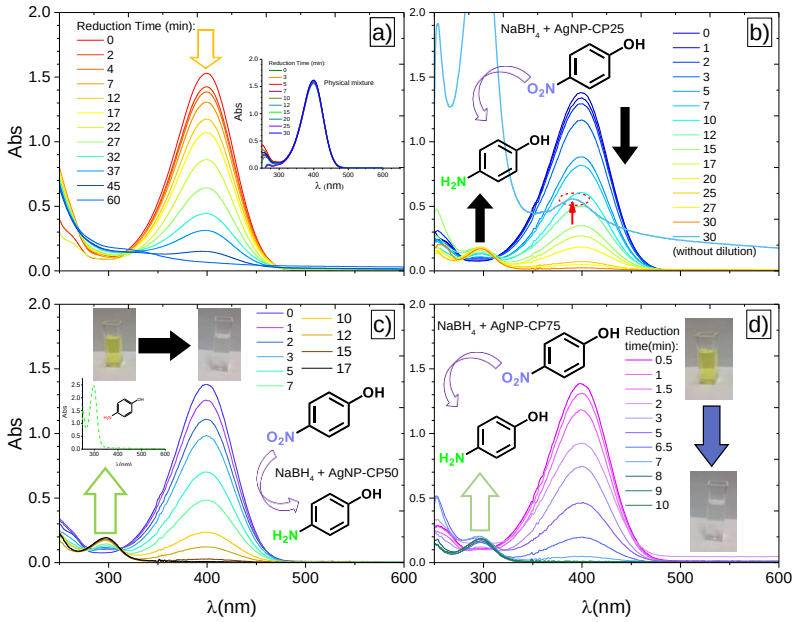


**Figure 3.2**. UV-vis spectra recorded during catalytic reaction which shows gradual reduction of 4-NPh to 4-APh at variable conditions: (a) unsupported Ag NPs (b) AgNP-CP25. Red arrow shows residual 4-NPh after 30 min (c) AgNP-CP50 and (d) AgNP-CP75 at 295 K. Insets: (a) catalytic reaction over PMix, (c) Typical optical images before and after catalysis reduction by AgNP-CP50 and UV-vis spectra of the sample after reduction without dilution, (d) Typical optical images before and after catalysis of the AgNP-CP75; Conditions: [4-NPh] = $1.1\times10^{-3}$ M, 10 mL, [$NaBH_4$]= 0.053M, 20 mg and amount of catalyst: 10 mg.

Metal NPs catalyze the reaction by lowering the kinetic barrier by acting as electronic relay agents and facilitating electron transfer from D→A. Considering that D ($NaBH_4$) is in great excess, the reduction reaction was assumed to follow PFO kinetics for this system. Figure 3.3a shows a linear correlation of $\ln(C_t/C_0)$ versus reaction time in seconds for reduction of 4-NPh using PMix, unsupported Ag NPs and AgNP-CP materials. The relative concentration, $ln(C\,t/C_0)$, decreases linearly with time which supports the use of the PFO kinetic model (Eq. A.1 in Appendix). The results for 4-NPh are in agreement with previous studies using Ag NPs as the catalyst system.[12,14,28,33]

**Table 3.1.** Corresponding apparent rate constants $k_{app}$ ($s^{-1}$) for catalysts. Activity factors, the ratio of rate constant $k_{app}$ to the total mass of the catalyst ($s^{-1}$ $g^{-1}$) were calculated and a comparison of values with literature is presented in Table 6.2. $^{*}k_{app}$ for PMix: $2.6\times10^{-6}$ $s^{-1}$.

| AgNP-CP25 | AgNP-CP50 | AgNP-CP75 | Ag NPs |
|---|---|---|---|
| $17.1\times10^{-4}$ | $33.2\times10^{-4}$ | $15.6\times10^{-3}$ | $4.8\times10^{-4}$ |

The relative concentration, $C_t/C_0$, values for $C_t$ and $C_0$ represent molar concentration ([4-APh]) at variable time intervals and t=0, respectively. The values were estimated from the respective absorbance of band intensities at 400 nm because the concentration of 4-nitophenolate in the medium is proportional to its absorbance intensity (*cf.* calibration curve in Figure A.11). From the linear relationship for $\ln(C_t/C_0)$ and reduction time, the apparent PFO rate constants ($k_{app}$) (Figure 3.3a and Eq. A.1.) and activity factors, the ratio of rate constant $k_{app}$ to the total mass of the catalyst ($s^{-1}$ $g^{-1}$) were estimated and presented in Table 3.1 and Table 6.2 respectively. Enhanced catalytic activity clearly demonstrates the significance of PANI component in the composite. Figure 3.3b shows the conversion rate depicted by $C_t/C_0$ versus reaction time. It is noted here that the catalytic reaction proceeded rapidly at initial stages and slowed down as time went on. The exponential nature of $C_t/C_0$ versus time (s) demonstrates the PFO kinetic model where ~50% reduction of 4-NPh to 4-APh occurred within 1.5 min for AgNPs-CP75. By comparison, reduction of 4-NPh with pure Ag NPs is slower and the decrease observed for 4-NPh with pure silver NPs as the catalyst only reached to less than 50% conversion after 25 min. For the present AgNP-CPs nanocatalysts, if $Ag^0$ crystal surface sites were the only main active centers, pure Ag NPs should be highly active for this conversion (all three AgNP-CPs contain only about 7% wt. Ag, on the basis of atomic absorption spectroscopy, AAS), which would contradict the unsatisfactory results observed for Ag itself in Figure 3.3a,b.

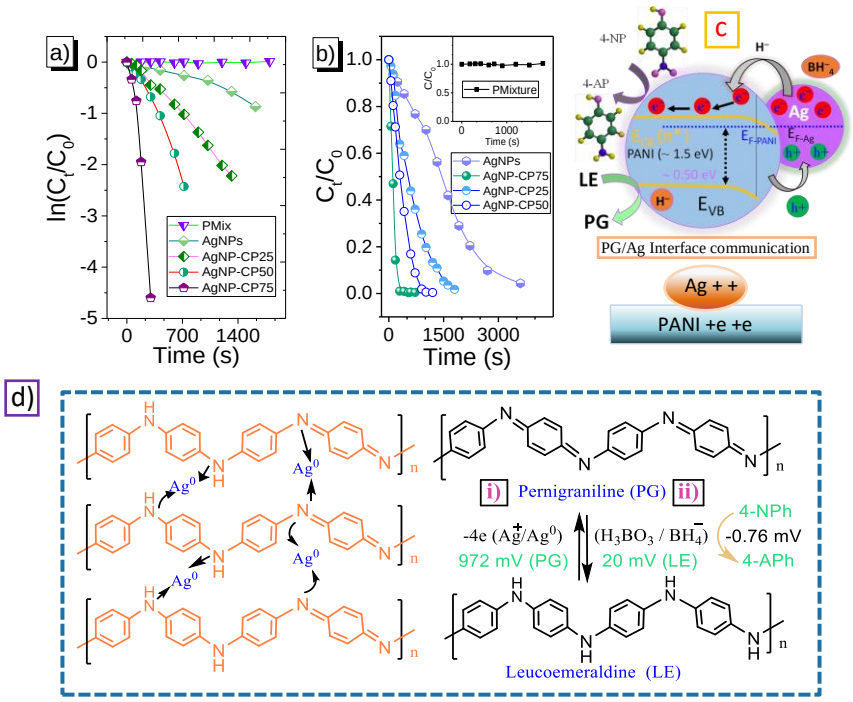


**Figure 3.3.** (a) Plot of $\ln(C_t/C_0)$ versus time for reduction of 4-NPh using PMix, Ag NPs and different catalysts. (b) Residual fraction of 4-NPh in solution *vs.* reaction time upon treatment with unsupported Ag NPs and different catalysts or PMix (inset). (c) Schematic illustration of the Fermi alignment and charge injection at the interface of AgNPs-CP composites. In parallel, the polymer is reduced as electrons are added to the $\pi^*$ band and holes injected into metal NPs contact region, and (d) Schematic illustration of Ag NPs stabilization by PG/LE.

To shed light on the high activity and underlying mechanistic insights for AgNP-CPs, the electronic properties of these systems were studied. Polyaniline is well-recognized as a p-type semiconductor with band gap of around 1.5 eV where its doped state has the highest conductivity.[8,34-37] PG support serves not only to act as a bridge and expressway between the AgNPs surface to accelerate electron transfer from the oxidation sites ($BH_4^-$) to the reduction sites (4-NPh), but may also contribute to high catalytic activity due to the existence of abundant active PG oxidation sites. A major advantage about conductivity of PG is that it creates a nanostructured electronic interface with high surface area when combined with NPs. By contrast, greater PANI content, creates a larger bridging interface area and active reduction sites which mediates the contact between the catalyst and reactant to maintain efficient and fast electron transport. The existence of Ag/PANI interface

provided increased opportunities to tune the interface of the catalyst. $BH_4^-$ ions and 4-NPh co-adsorb onto the Ag NP surface. Part of the injected electrons and $H^-$ ions from $BH_4^-$ to the metal may transfer to the 4-NPh [28] and the neighboring PG, resulting in a region of depletion where there is a surplus electron density on PANI as electrons relay to PG from a depleted interface region. Electron relay from D→A ($BH_4^-$ to 4-NPh) and PG results in an electron enriched PANI region with high surface area ($E_0$|PG/LE = -0.20 V vs. $E_0$|$H_3BO_3/BH_4^-$ = -1.33 V) which results in re-conversion of PG to LE. According to Zhang et al.[38], interfacing metal NPs with a redox-responsive polymer or a semiconductor such as metal oxides would allow for Fermi level alignment where electrons would escape from metal to semiconductor (Figure 3.3c). Alan J. Heeger[36] reported a possible mechanism (*cf*. Eq. 3.2) to account for charge injection which confirms our experimental findings.

$$(\pi\text{-PG})_n + y\ (e^-) \longrightarrow [(\pi\text{-LE})^{-y}]_n \qquad (3.2)$$

Such charge redistribution that occurs between PG ($e^-$ acceptor) and $BH_4^-$ mediated by $Ag^0$ that would result in the creation of a high surface area nanostructured region of electron rich and poor interfaces within the nanocomposite. Semi-conducting polymers have band gaps and PANI serves as a p-type semiconducting polymer, where electrons from $BH_4^-$ can be injected into an empty $\pi^*$-band mediated by metallic contacts.[36] The distribution of electrons generate interfacial electron-hole pairs, where a larger surface area with nanostructured active reduction sites allow more opportunity for electron transfer and reduction of 4-NPh by facilitating electron uptake by reactant molecules.[39] The greater abundance of such PANI regions with surplus $e^-$ contribute to more depleted electrons in Ag. Therefore, faster catalytic reaction occurs as observed herein. A synergistic electron transfer reaction between PANI and Au NPs of this type is unprecedented.[6] However, the direct electron transfer into PG alone does not seem to be plausible without Ag NPs, as confirmed by zero catalytic

activity of PMix without silver (*cf.* Figures 3.2a and 3.3b, inset). This suggests that the reaction rate enhancement under reaction conditions is not due to polymer or isolated Ag NPs by themselves individually even though an increase in the conductive polymer content parallels the enhanced activity of the catalysts. According to Scheme 3.1a, this type of $e^-$ communication is thermodynamically favourable in the presence of silver. The process between $BH_4^-$ and PG is kinetically favoured when the two phases are in direct contact (*cf.* Scheme 3.1b) as silver provides an alternate path to overcome the kinetic barrier for this transfer process by changing the $e^-$ transfer mechanism.

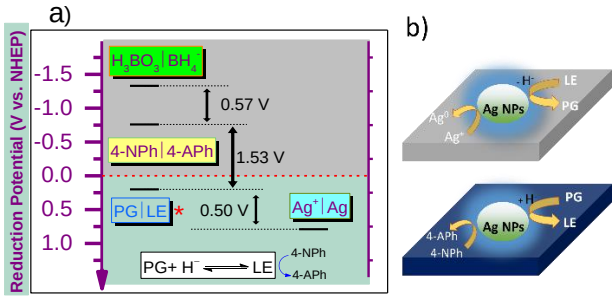


**Scheme 3.1.** a) Scheme showing the relative reduction potential for PANI, Ag, $NaBH_4$ and 4-NPh with respect to NHE, indicating the thermodynamic feasibility of $e^-$ transfer from $BH_4^-$ to both PG and 4-NPh species.*Value converted from data referred to the Ag/AgCl/3M NaCl electrode from ref.[5] b) Top: reduction process during synthesis and Bottom: oxidation process and receiving $H^-$ at interface during catalysis performance.

On the other hand, aside from the existence of plenty of surplus electrons and electron-enriched reduction sites at the Ag/PG interface, enhanced catalytic activity may also relate to a large physisorption of 4-NPh onto the PANI domains due to favorable π-π interactions, ion-dipole and hydrogen bonding. Chemisorption of reactant to the catalysts surface is reported to play an important role for the reduction of 4-NPh and its reaction rate constant.[19] Opportune adsorption and desorption of product/reactant species is a key factor in heterogeneous catalysis. An adsorption process with an appropriate affinity between catalyst and reactant such that it is not too weak, nor too strong, is essential to achieve optimal catalytic properties. Several reports indicate that direct

chemisorption of 4-APh product may block the diffusion of 4-NPh which ends up with reduced catalytic activity after the first cycle, thereby limiting the recyclability of the catalyst.[40,41] The introduction of PANI for AgNPs-CP catalysts (Ag NPs loading of ca. 7% w/w) could regulate the chemisorption of 4-APh. This in turn accelerates desorption of 4-APh and facilitates a faster catalytic reaction and recyclability of catalysts.

In order to further confirm the proposed mechanism, a study was performed using XPS to elucidate the effect of PANI on the electronic structure of Ag. As displayed in Figure 3.4a, a survey of the XPS spectra reveals the presence of N 1*s*, Ag 3*p*, O 1*s*, C 1*s* and Ag 3*d* core levels. Based on high resolution XPS results (*cf.* bottom part of Figure 3.4c), $Ag^0$ is exclusively present in as-prepared Ag NPs. Two bands at 368.1 and 374.1 eV correspond to the two spin-orbit doublets of $3d_{5/2}$ and $3d_{3/2}$ binding energies, respectively, where the splitting of the 6.0 eV is in agreement with standard data for $Ag^0$.[22,42] Multiple peaks of deconvoluted Ag 3*d* spectra for these nanocatalysts provide strong support that more than one silver species is present. The bands at higher binding energy in all catalysts (ca. 370.3 eV) are assigned to Ag satellite peaks which result in asymmetric lineshapes. Furthermore, no band corresponding to Ag (I, II) such as oxide species (367-368 eV) were observed on the surface of particles. The existence of free metallic Ag as major component is clearly observed along with other BE signatures of Ag 3*d* at 368.8 eV (and 369.4 eV for AgNPs-CP50) which is much higher than typical BE of $Ag^0$ that normally found at 368.2 eV. This band with positive shift was assigned to Ag with a higher oxidation state in the structure of the AgNPs-CPs (*cf.* upper part of Figure 3.4c), mainly due to Ag $(0)^{+\delta}$ bound to =N- groups (Ag-N), which results in substantially increased BE of $Ag^0$.[17,43] The slight increase in oxidation state of Ag is due to the interaction with a relatively high electronegative N atom, in agreement with similar types of

Ag(0)-thiol end group interactions.[43] The slight increase in =N- 1*s* BE from 398.9 to 399.2 eV (Figure 3.5a) provides strong support for this type of interaction.

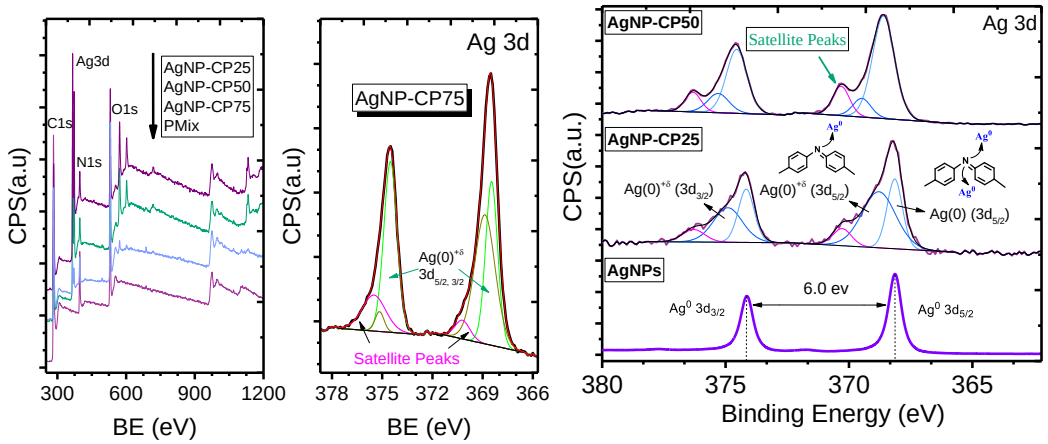


**Figure 3.4.** (a) XPS survey**,** (b, c) High resolution Ag 3*d* XPS spectra obtained from the AgNPs-CP nanocomposites.

Such types of electronic interactions likely alter the electronic structure of Ag and PG with a concomitant boost in the catalytic activity of nanocomposite systems. Similarly, Figure 3.5b shows a high resolution Ag spectrum for AgNPs-CP75, where two types of silver (0) species are present in the material along with an obvious Ag satellite at 370.3 eV. The band at 368.8 eV is higher than typical $Ag^0$ and may indicate a partial oxidation of Ag due to interaction with N atoms. Figure 3.5a shows the N 1*s* spectra for PMix and the catalyst materials. PANI is archetypical conductive polymers that exists in several oxidation states; including leucoemeraldine, emeraldine, and pernigraniline. Each state is characterized by relative compositions of imine (or quinoid, *Q*) and secondary amine (or benzenoid, *B*) structural units. N 1*s* XPS spectrum of the PMix can be further resolved into two bands at 398.9 and 399.9 eV contributed by *Q* and *B* N 1*s* respectively,[4] with almost equal composition (mol. %) signifying that the initial PANI in the composite adopts the E

form (*cf.* Figure 3.5a, bottom). The ratio of the Q/B nitrogen species were quantified (see Table 3.2). With increasing PANI content, the peak corresponding to nitrogen of B greatly reduced in AgNP-CP75 sample and =N- was predominantly present in its oxidized form in this system (*cf.* top part of Figure 3.5a) with a slight shift to higher BE indicating a decreased electron density around the N atom after silver complexation. The slight positive shift for N 1*s* is understood because of changes in electron density after binding =N- with Ag(0). The band for –NAg– is anticipated to appear at BE lower than –NH– and higher than =N– due to replacement of hydrogen with a less electronegative metal atom. The above interpretation parallels an independent report on N atoms coordinated with Co and H atoms.[44]

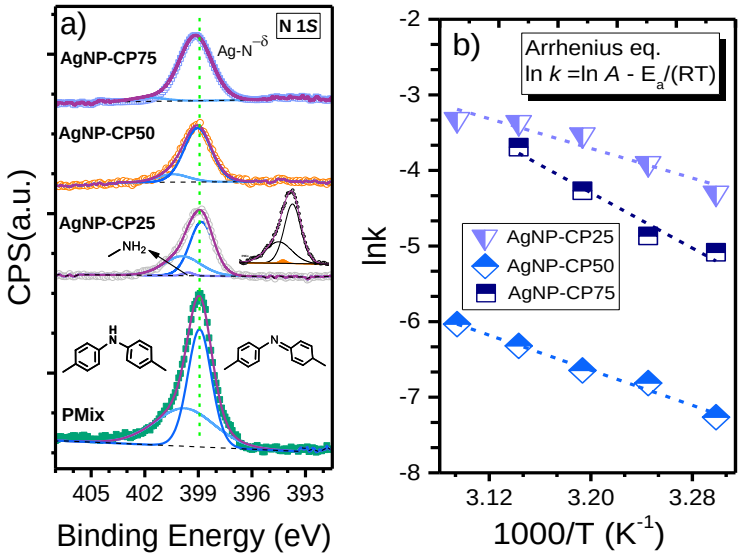


**Figure 3.5**. (a) N 1s XPS spectra of the PMix and catalysts. (b) The Arrhenius plot for the reaction catalyzed by different catalysts.

**Table 3.2.** Proportion (%) of N species in catalysts.

| | PMix | AgNP-P25 | AgNP-CP50 | AgNP-CP75 |
|---|---|---|---|---|
| **(Q)** | 55.2 | 62.7 | 74.9 | 94.1 |
| **(B)** | 44.4 | 35.7 | 25.1 | 5.9 |

The findings of this study suggest that the presence of PANI in nanocomposites strongly influence the catalytic activity and signifies the importance of *in-situ* oxidized PANI (PG) for the electron transfer between $BH_4^-$ and 4-NPh. Notably, PG is considered to be the key active reduction sites. PG improves the catalytic activity by increasing electron capacity of the catalyst via interfacial electron-hole pairs. Therefore, electron delocalization between π-conjugated PG and Ag alters the electronic structure of Ag and imparts high activity and durability to the system. *In-situ* reduction of highly dispersed metal NPs on the support network has been reported elsewhere.[17] These findings are consistent with the work published by Bu et al.,[7] where PANI is inferred to be oxidized in the presence of $Ag^+$ during synthesis of catalyst, thereby affording the loss of electrons for the *in-situ* reduction of $Ag^+$ ions to $Ag^0$. In parallel, this yields a catalyst mainly in its PG form that is oxidized by contributions from $H^-$ from $BH^-_4$ in an aqueous environment where the reduction reaction occurs.[25] The above results are in agreement with reports for other materials that indicate that PANI aides the reduction of $Ag^+$ to $Ag^0$ and –NH– groups are oxidized to =N– due to its redox-switchability associated with the variable valence state of nitrogen.[7]

In cases where an excess amount of electrons are present on the surface of Ag(0) NPs, the electron delocalization between π-conjugated PG electrons and Ag alters the electronic structure of the system by partial transfer of electrons from Ag to PG, as discussed above. This electron flow from Ag to PG-PANI not only creates additional active sites for 4-NPh to accept electrons but also enhances catalysis durability by preventing catalysis breakdown and limiting Ag oxidation by shifting its standard redox potential.[20] To obtain further insights on the activation barrier of

catalysts and the mechanistic route, the catalytic reduction of 4-NPh was studied by determination of $k_{app}$ at variable temperature (30, 35, 40, 45 and 50°C). On the basis of the kinetics plots at variable temperature (*cf*. Table A.3) and the linear fit to the Arrhenius plot (ln $k_{app}$ vs 1000/T), the estimated activation energy ($E_a$; kJ/mol) was estimated as follows in parentheses: AgNPs-CP25 (76.3), AgNPs-CP50 (48.2) and AgNPs-CP75 (40.8). AgNPs-CP75 can significantly reduce the activation energy of this reaction, which accounts for the notable rapid reduction and greater catalytic activity as more electronic sites are available (Figure 3.5b).

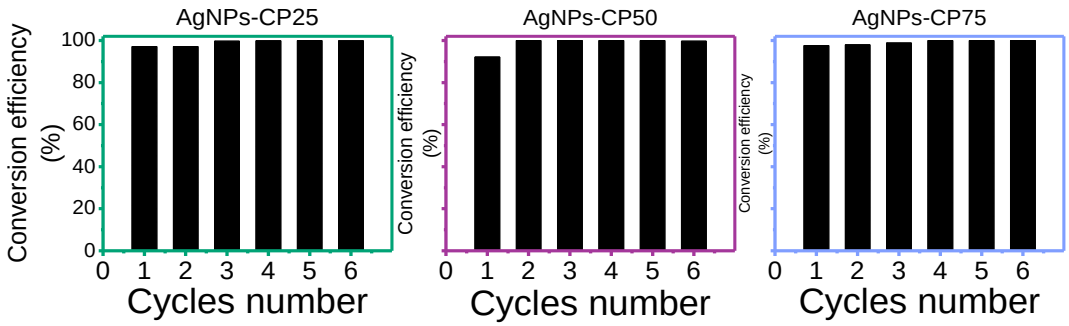


**Figure 3.6.** Reusability of the AgNPs-CP catalysts for the reduction of 4-NPh; Reaction conditions: 50 mL [4-NPh] = $1.1\times10^{-3}$ M, 25 °C, t=30 min, and 50 mg catalyst loading.

The markedly different activation energies signify that the three systems differ in terms of surface catalysis reaction and the mechanistic pathway. In parallel, these values are lower than those for several recently reported metallic NPs catalysts such as tantalum oxide,[29] gold nanoboxes[45], Ag@procyanidin grafted eggshell membrane[14]. Variable activation energies are indicative of a distinct reduction mechanism route for the catalysts in this study, where the lowest activation energy was observed for AgNPs-CP75 that contain higher PANI content.

The recyclability of catalysts as operating stability and reusability of a heterogeneous catalyst since it represents two important parameters for practical applications. A successive series of reduction experiments were performed where a fresh mixture of $NaBH_4$ and 4-NPh was added to

the catalyst and the reaction progress after each cycle. The catalysis was tracked using UV-vis spectroscopy and the reusability of AgNP-CPs are shown in Figure 3.6. After completion of six catalytic cycles, the conversion efficiency (%) was between 91-100% which indicates that composite does not undergo major decomposition or decline in activity under multiple cycles of reuse. After six successive reaction cycles, catalysts presented outstanding reusability. This excellent durable stability of the catalysts may be attributed to high strength of PANI and the existence of various functional groups that favor the immobilization of silver NPs onto the polymer materials. The contribution of ion-dipole, hydrogen bonding, and metal-ligand binding interactions stabilize the structure and integrity of the system. The well-known oxidation of Ag and poisoning by 4-APh after the first cycle is a major challenge in recyclability of Ag catalysts.[6] The electronic properties of the catalyst described herein prevent the oxidation of Ag by increasing the reduction potential of the polymer through the presence of electronegative -N= when coupled with LE. The physisorption of reactants and products on PG and opportune adsorption energy of the product on Ag/PG facilitates its recyclability,[6] since there is a slight amount of Ag present in AgNPs-CPs materials. After all, the systems reported here do not seem to rely solely Ag NPs but reveal a synergistic effect between Ag and PG as a key factor for improved performance of the system. Therefore, poisoning and oxidation of the Ag surface is less likely for such polymer composite materials. Supported NPs have an advantage related to facile isolation from a reaction system via centrifugation. In contrast, the settling and isolation of colloidal unsupported fine pure Ag NPs pose greater challenges in phase separation, re-use and catalytic efficiency.

## 3.5. Conclusion

In summary, PANI serves as a conductive and redox-switchable organic polymer support with versatile multifunctional properties that enhance catalysis of Ag NPs. The interfacial synergism

between highly dispersed Ag and the extensive π-conjugated network structure of PG result in catalysts with improved activity and recyclability. During *in-situ* reduction of $Ag^{+}$, LE is fully converted to PG upon silver reduction. Tuning the π-conjugated structure and interface of the polymer composite provides additional active sites with surplus electrons for transfer to 4-NPh due electronic effects. PG appears to prevent Ag from oxidation when the two phases of the composite are in intimate contact, and this is inferred to play a major role that governs the outstanding catalytic and recycle properties. The high catalytic efficiency and degree of recyclability related to the favourable surface interactions and synergistic effects between PG and Ag favor a reduced activation energy for the catalytic reduction process. This study contributes to the expanded development of highly active and unique interface-mediated metal nanoparticle catalysts for applications that require mild reaction conditions.

# 3.7. References


1. Rivnay, J.; Inal, S.; Collins, B. A.; Sessolo, M.; Stavrinidou, E.; Strakosas, X.; Tassone, C.; Delongchamp, D. M.; Malliaras, G. G. Structural Control of Mixed Ionic and Electronic Transport in Conducting Polymers. *Nat. Commun.* **2016**, *7*, 11287.

2. Kang, K.; Watanabe, S.; Broch, K.; Sepe, A.; Brown, A.; Nasrallah, I.; Nikolka, M.; Fei, Z.; Heeney, M.; Matsumoto, D.; Marumoto, K.; Tanaka, H.; Kuroda, S.-i.; Sirringhaus, H. 2D Coherent Charge Transport in Highly Ordered Conducting Polymers Doped by Solid State Diffusion. *Nat. Mater.* **2016**, *15*, 896-902.

3. Reiss, P.; Couderc, E.; De Girolamo, J.; Pron, A. Conjugated Polymers/Semiconductor Nanocrystals Hybrid Materials-Preparation, Electrical Transport Properties and Applications. *Nanoscale* **2011**, *3*, 446-489.

4. Wei, W.; Wang, G.; Yang, S.; Feng, X.; Müllen, K. Efficient Coupling of Nanoparticles to Electrochemically Exfoliated Graphene. *J. Am. Chem. Soc.* **2015**, *137*, 5576-5581.

5. Pérez-Mitta, G.; Marmisollé, W. A.; Trautmann, C.; Toimil-Molares, M. E.; Azzaroni, O. Nanofluidic Diodes with Dynamic Rectification Properties Stemming from Reversible Electrochemical Conversions in Conducting Polymers. *J. Am. Chem. Soc.* **2015**, *137*, 15382-15385.

6. Jin, C.; Han, J.; Chu, F.; Wang, X.; Guo, R. Fe3O4@PANI Hybrid Shell as a Multifunctional Support for Au Nanocatalysts with a Remarkably Improved Catalytic Performance. *Langmuir* **2017**, *33*, 4520-4527.

7. Bu, Y.; Chen, Z. Role of Polyaniline on the Photocatalytic Degradation and Stability Performance of the Polyaniline/Silver/Silver Phosphate Composite under Visible Light. *ACS Appl. Mater. Interfaces* **2014**, *6*, 17589-17598.

8. Zhang, Y.; Duan, Y.; Liu, J.; Ma, G.; Huang, M. Wormlike Acid-Doped Polyaniline: Controllable Electrical Properties and Theoretical Investigation. *J. Phys. Chem. C* **2018**, *122*, 2032-2040.

9. Liu, X.; Gregurec, D.; Irigoyen, J.; Martinez, A.; Moya, S.; Ciganda, R.; Hermange, P.; Ruiz, J.; Astruc, D. Precise Localization of Metal Nanoparticles in Dendrimer Nanosnakes or Inner Periphery and Consequences in Catalysis. *Nat. Commun.* **2016**, *7*, 13152.

10. Yin, Z.; Wang, Y.; Song, C.; Zheng, L.; Ma, N.; Liu, X.; Li, S.; Lin, L.; Li, M.; Xu, Y.; Li, W.; Hu, G.; Fang, Z.; Ma, D. Hybrid Au–Ag Nanostructures for Enhanced Plasmon-Driven Catalytic Selective Hydrogenation through Visible Light Irradiation and Surface-Enhanced Raman Scattering. *J. Am. Chem. Soc.* **2018**, *140*, 864-867.

11. Li, T.; Vongehr, S.; Tang, S.; Dai, Y.; Huang, X.; Meng, X. Scalable Synthesis of Ag Networks with Optimized Sub-monolayer Au-Pd Nanoparticle Covering for Highly Enhanced SERS Detection and Catalysis. *Sci. Rep.* **2016**, *6*.

12. Baruah, B.; Gabriel, G. J.; Akbashev, M. J.; Booher, M. E. Facile Synthesis of Silver Nanoparticles Stabilized by Cationic Polynorbornenes and Their Catalytic Activity in 4-Nitrophenol Reduction. *Langmuir* **2013**, *29*, 4225-4234.

13. Huang, F.; Gao, Y.; Zhang, Y.; Cheng, T.; Ou, H.; Yang, L.; Liu, J.; Shi, L.; Liu, J. Silver-Decorated Polymeric Micelles Combined with Curcumin for Enhanced Antibacterial Activity. *ACS Appl. Mater. Interfaces* **2017**, *9*, 16880-16889.

14. Liang, M.; Su, R.; Huang, R.; Qi, W.; Yu, Y.; Wang, L.; He, Z. Facile in Situ Synthesis of Silver Nanoparticles on Procyanidin-Grafted Eggshell Membrane and Their Catalytic Properties. *ACS Appl. Mater. Interfaces* **2014**, *6*, 4638-4649.

15. Huang, R.; Zhu, H.; Su, R.; Qi, W.; He, Z. Catalytic Membrane Reactor Immobilized with Alloy Nanoparticle-Loaded Protein Fibrils for Continuous Reduction of 4-Nitrophenol. *Environ. Sci. Technol.* **2016**, *50*, 11263-11273.

16. Lu, S.; Hu, Y.; Wan, S.; McCaffrey, R.; Jin, Y.; Gu, H.; Zhang, W. Synthesis of Ultrafine and Highly Dispersed Metal Nanoparticles Confined in a Thioether-Containing Covalent Organic Framework and Their Catalytic Applications. *J. Am. Chem. Soc.* **2017**, *139*, 17082-17088.

17. Liu, J.; He, K.; Wu, W.; Song, T.-B.; Kanatzidis, M. G. In Situ Synthesis of Highly Dispersed and Ultrafine Metal Nanoparticles from Chalcogels. *J. Am. Chem. Soc.* **2017**, *139*, 2900-2903.

18. Lawrence, R. L.; Scola, B.; Li, Y.; Lim, C.-K.; Liu, Y.; Prasad, P. N.; Swihart, M. T.; Knecht, M. R. Remote Optically Controlled Modulation of Catalytic Properties of Nanoparticles through Reconfiguration of the Inorganic/Organic Interface. *ACS Nano* **2016**, *10*, 9470-9477.

19. Liang, Y.; Chen, Z.; Yao, W.; Wang, P.; Yu, S.; Wang, X. Decorating of Ag and CuO on Cu Nanoparticles for Enhanced High Catalytic Activity to the Degradation of Organic Pollutants. *Langmuir* **2017**, *33*, 7606-7614.

20. Wang, A.-L.; Xu, H.; Feng, J.-X.; Ding, L.-X.; Tong, Y.-X.; Li, G.-R. Design of Pd/PANI/Pd Sandwich-Structured Nanotube Array Catalysts with Special Shape Effects and Synergistic Effects for Ethanol Electrooxidation. *J. Am. Chem. Soc.* **2013**, *135*, 10703-10709.

21. Dolatkhah, A.; Wilson, L. D. Magnetite/Polymer Brush Nanocomposites with Switchable Uptake Behavior Toward Methylene Blue. *ACS Appl. Mater. Interfaces* **2016**, *8*, 5595-5607.

22. Xu, G.; Yu, Y.; He, H. Silver Valence State Determines the Water Tolerance of Ag/Al2O3 for the H2–C3H6–SCR of NOx. *J. Phys. Chem. C* **2017**, *122*, 670-680.

23. Kästner, C.; Thünemann, A. F. Catalytic Reduction of 4-Nitrophenol Using Silver Nanoparticles with Adjustable Activity. *Langmuir* **2016**, *32*, 7383-7391.

24. Dolatkhah, A.; Wilson, L. D. Salt-Responsive Fe3O4 Nanocomposites and Phase Behavior in Water. *Langmuir* **2017**, *34*, 341-350.

25. Ayad, M. M.; Amer, W. A.; Kotp, M. G.; Minisy, I. M.; Rehab, A. F.; Kopecký, D.; Fitl, P. Synthesis of Silver-Anchored Polyaniline–Chitosan Magnetic Nanocomposite: A Smart System for Catalysis. *RSC Adv.* **2017**, *7*, 18553-18560.

26. Mulfinger, L.; Solomon, S. D.; Bahadory, M.; Jeyarajasingam, A. V.; Rutkowsky, S. A.; Boritz, C. Synthesis and Study of Silver Nanoparticles. *J. Chem. Educ.* **2007**, *84*, 322.

27. Bao, Z.; Yuan, Y.; Leng, C.; Li, L.; Zhao, K.; Sun, Z. One-Pot Synthesis of Noble Metal/Zinc Oxide Composites with Controllable Morphology and High Catalytic Performance. *ACS Appl. Mater. Interfaces* **2017**, *9*, 16417-16425.

28. Gangula, A.; Podila, R.; M, R.; Karanam, L.; Janardhana, C.; Rao, A. M. Catalytic Reduction of 4-Nitrophenol using Biogenic Gold and Silver Nanoparticles Derived fromBreynia rhamnoides. *Langmuir* **2011**, *27*, 15268-15274.

29. Su, Y.; Lang, J.; Li, L.; Guan, K.; Du, C.; Peng, L.; Han, D.; Wang, X. Unexpected Catalytic Performance in Silent Tantalum Oxide through Nitridation and Defect Chemistry. *J. Am. Chem. Soc.* **2013**, *135*, 11433-11436.

30. Dou, L.; Zhang, H. Facile Assembly of Nanosheet Array-Like CuMgAl-Layered Double Hydroxide/rGO Nanohybrids for Highly Efficient Reduction of 4-Nitrophenol. *J. Mater. Chem. A* **2016**, *4*, 18990-19002.

31. Fageria, P.; Uppala, S.; Nazir, R.; Gangopadhyay, S.; Chang, C.-H.; Basu, M.; Pande, S. Synthesis of Monometallic (Au and Pd) and Bimetallic (AuPd) Nanoparticles Using Carbon Nitride (C3N4) Quantum Dots via the Photochemical Route for Nitrophenol Reduction. *Langmuir* **2016**, *32*, 10054-10064.

32. Qi, H.; Yu, P.; Wang, Y.; Han, G.; Liu, H.; Yi, Y.; Li, Y.; Mao, L. Graphdiyne Oxides as Excellent Substrate for Electroless Deposition of Pd Clusters with High Catalytic Activity. *J. Am. Chem. Soc.* **2015**, *137*, 5260-5263.

33. Wang, Q.; Liu, S.; Wang, H.; Yang, Y. In Situ Pore-Forming Alginate Hydrogel Beads Loaded with in Situ Formed Nano-Silver and their Catalytic Activity. *Phys. Chem. Chem. Phys.* **2016**, *18*, 12610-12615.

34. Yakuphanoglu, F.; Şenkal, B. F. Electronic and Thermoelectric Properties of Polyaniline Organic Semiconductor and Electrical Characterization of Al/PANI MIS Diode. *J. Phys. Chem. C* **2007**, *111*, 1840-1846.

35. Kwon, O.; McKee, M. L. Calculations of Band Gaps in Polyaniline from Theoretical Studies of Oligomers. *J. Phys. Chem. B* **2000**, *104*, 1686-1694.

36. Heeger, A. J. Semiconducting and Metallic Polymers: The Fourth Generation of Polymeric Materials. *J. Phys. Chem. B* **2001**, *105*, 8475-8491.

37. Dallas, P.; Georgakilas, V. Interfacial Polymerization of Conductive Polymers: Generation of Polymeric Nanostructures in a 2-D Space. *Adv. Colloid Interface Sci.* **2015**, *224*, 46-61.

38. Zhang, P.; Shao, C.; Zhang, Z.; Zhang, M.; Mu, J.; Guo, Z.; Liu, Y. In Situ Assembly of Well-Dispersed Ag Nanoparticles (AgNPs) on Electrospun Carbon Nanofibers (CNFs) for Catalytic Reduction of 4-Nitrophenol. *Nanoscale* **2011**, *3*, 3357.

39. Li, M.; Chen, G. Revisiting Catalytic Model Reaction p-Nitrophenol/$NaBH_4$ Using Metallic Nanoparticles Coated on Polymeric Spheres. *Nanoscale* **2013**, *5*, 11919.

40. Bai, S.; Shen, X.; Zhu, G.; Li, M.; Xi, H.; Chen, K. In situ Growth of $Ni_xCo_{100-x}$ Nanoparticles on Reduced Graphene Oxide Nanosheets and Their Magnetic and Catalytic Properties. *ACS Appl. Mater. Interfaces* **2012**, *4*, 2378-2386.

41. Zhu, C.-H.; Hai, Z.-B.; Cui, C.-H.; Li, H.-H.; Chen, J.-F.; Yu, S.-H. In Situ Controlled Synthesis of Thermosensitive Poly(N-isopropylacrylamide)/Au Nanocomposite Hydrogels by Gamma Radiation for Catalytic Application. *Small* **2012**, *8*, 930-936.

42. Deng, H.; Yu, Y.; Liu, F.; Ma, J.; Zhang, Y.; He, H. Nature of Ag Species on Ag/γ-$Al_2O_3$: A Combined Experimental and Theoretical Study. *ACS Catal.* **2014**, *4*, 2776-2784.

43. Battocchio, C.; Fratoddi, I.; Fontana, L.; Bodo, E.; Porcaro, F.; Meneghini, C.; Pis, I.; Nappini, S.; Mobilio, S.; Russo, M. V.; Polzonetti, G. Silver Nanoparticles Linked by a Pt-Containing Organometallic Dithiol Bridge: Study of Local Structure and Interface by XAFS and SR-XPS. *Phys. Chem. Chem. Phys.* **2014**, *16*, 11719-11728.

44. Wang, L.; Zhang, W.; Zheng, X.; Chen, Y.; Wu, W.; Qiu, J.; Zhao, X.; Zhao, X.; Dai, Y.; Zeng, J. Incorporating Nitrogen Atoms into Cobalt Nanosheets as a Strategy to Boost Catalytic Activity Toward $CO_2$ Hydrogenation. *Nat. Energy* **2017**, *2*, 869-876.

45. Zeng, J.; Zhang, Q.; Chen, J.; Xia, Y. A Comparison Study of the Catalytic Properties of Au-Based Nanocages, Nanoboxes, and Nanoparticles. *Nano Lett.* **2010**, *10*, 30-35.

# CHAPTER 4

# Salt-Responsive $Fe_3O_4$ Nanocomposites and Phase Behavior in Water*

*Reprinted with permission from Dolatkhah, A.; Wilson, L. D. *Langmuir* **2018**, 34, 341-350. © 2017 American Chemical Society. DOI: 10.1021/acs.langmuir.7b03613. A.D. performed all experimental work and wrote the first draft of the manuscript. L.D.W. directed the study and revised the manuscript prior to publication.

## 4.1. Abstract

The ability to achieve exquisite control over polymer building blocks within multi-compartment magnetite nanocomposites to afford predictable and ordered packing hierarchical structures remains a significant challenge for the design of NCs. Thus, there is an urgent need to develop new types of nanodimensional assemblies that undergo responsive shape-shift, size-, phase- and morphological transitions, especially for processes that are triggered by biologically relevant stimuli such as ionic gradients to meet the demand for diverse applications. Accordingly, an unprecedented concept for the preparation of salt-responsive magnetite/polyaniline composite nano-assemblies with chemically distinct dual-compartment structures was reported. The size, shape, and nanodimensional phase separation of the PANI assemblies within NCs were adjusted in a facile manner with incremental changes in salt gradients using NaCl (*aq*). Composition effects bestow desirable diversiform shape, size and phase behavior of the incorporated conductive polymer via dynamic H-bonding. The size, shape and superparamagnetic character of iron oxide nanoparticles are unaffected by a "*salting-in*" process. The mechanism, gradual morphological evolution, interchangeable nano phase-separation and ion-stimulated disassembly of PANI building blocks for these magneto/ion-responsive polymer-composite IONPs at elevated ionic strength are strongly supported by DLS, Raman spectroscopy, TEM and equilibrium dye (MB/MO) recognition studies.

## 4.2. Introduction

Nanofabrication of multifunctional hybrid nano-assemblies by interfacing suitable building blocks with desired morphology and functionality gives rise to new structures with tailored multiple functionalities and advanced features due to the coupling effect of constituent components. Magnetic nanoparticles (NPs), especially superparamagnetic IONPs are among the

most promising materials for biomedical applications and hybrid design.[1] IONPs have been extensively employed in the design of NCs to yield advanced materials for applications in bio-separation,[2] catalyst immobilization,[1] magnetically-targeted delivery of drug/gene systems,[3-5] magnetic sensors,[6,7] contrast agents in magnetic resonance imaging[8-11], advanced water treatment,[12] hyperthermia[13] and magnetofection.[14] In contrast to alternative magnetic nano systems such as cobalt or nickel, IONPs are nontoxic and biocompatible, where assimilation by the body and efficient clearance occurs via regulated iron metabolic processes.[4,15] Substantive numbers of successful reports on magnetite NPs as composite building blocks are known due to their extraordinary multifunctional properties that emerge upon incorporation within structural hybrids. IONPs display size-dependent magneto-responsive behavior (superparamagnetic at < 27 nm) that result in convenient remote magnetic modulation of composites.[16] Various structural NP/polymer nanohybrid model systems with multifunctional complexity including micelle encapsulation,[17] core-shell structures,[18] polymer dispersion matrices[4] have been reported which surpass the inherent structural and functional limitations imposed on magnetite NCs[19,20]. These intimately bound organic-inorganic NCs demonstrate the role of diverse multicomponent functionality with enhanced performance for specific applications.

In spite of significant achievements in structural diversity of magnetite incorporated hierarchical nanomaterials, challenges remain for the specific control of organized coupling of polymer building blocks at multi-size scales to create new multi-functional structures with predictable and programmable architecture in a facile manner. Stimuli-sensitive systems have attracted particular interest, mainly due to their tunable physicochemical properties, along with stimuli-responsiveness to afford control over structural properties in a step-wise fashion.[21,22] In the past decades, such polymers have played a pivotal part in the development of diverse

nanostructures for biomedical applications due to their programmable and directional self-assembly.[23] The hierarchical structure of intelligent stimuli-responsive polymers that undergo self-assembly can be manipulated by the same external stimuli which triggers the process. Rational self-assembly employing noncovalent interactions may enable the design of chemical architectures with defined size and shape. The integration of smart polymers by coupling growth onto magnetite building blocks would allow for more control over size and morphology at the nanoscale regime. H-bonding is a ubiquitous noncovalent interaction in Nature and the ability to impose size/phase shift in binary magnetite hybrid assemblies is advantageous. The ability to impose size/phase shift in hybrid assemblies, using directed H-bonding, triggered by external stimuli makes our approach conceptually unique from other reports and offers a new level of tunability to achieve multi-compartment nanostructures, especially in the case of ion-responsive PANI nanocomposites, which are sparsely reported to date in the literature.

To this end, a new concept on ion-responsive dynamic H-bonding in NCs. In particular, such NCs consist of PANI particles with adjustable size, shape and phase separation from solution was reported. This system was integrated onto magnetite colloids through surface initiated and seeded nucleation polymerization. It was demonstrated that PANI aggregates can be tailored in a facile manner to provide access to a range of multi-size and -shape with diversiform morphology by control of the chitosan and salt fraction. The size, morphology and magnetic behavior of nanoscale magnetite building blocks remain unchanged which endow the advantage of magnetic properties in the system. Using a post-synthetic strategy, an unprecedented salt-responsive property of the PANI within such NCs in aqueous solution was demonstrated. The reversible phase transformation can be externally triggered by salinity gradients as revealed by Raman spectroscopy, TEM, DLS and selective organic dye binding assays. In comparison to dispersed forms of PANI and $Fe_3O_4$

NPs, this facile and modular design strategy exploits the properties of both individual components. It was anticipated that this study will catalyze further research and development in diverse areas related to magnetic resonance imaging, nano-electronics, desalination, and biomedical devices.

# 4.3. Experimental section

## 4.3.1. Materials

$FeCl_2.4H_2O$ (purity ≥99.0 %), aniline, chitosan low molecular weight as powder, acrylic acid, N-Methyl-2-pyrrolidone (NMP) and ammonium persulfate, $(NH_4)_2.S_2O_8$ were obtained from Sigma-Aldrich. $FeCl_3.6H_2O$ (purity ≥ 99.0 %) was supplied by Alfa Aesar, Canada. Acetic acid was obtained from Fisher Scientific. All chemicals used in this study were analytical grade, purchased commercially and used as received without further purification. Milli-Q water (with resistivity of 18.2) obtained from Barnstead (Nanopure Diamond) was used throughout all experiments.

## 4.3.4. Characterization

DRIFT spectra of IONPs, acrylic acid functionalized IONPs (AIONPs) and resultant PANI/Iron oxide nanocomposites (PIONc) were recorded with a Bio-RAD FTS-40 spectrophotometer where samples were analyzed in reflectance mode. All samples were prepared by mixing and grinding materials with pure spectroscopic grade KBr (1:10 wt. ratio) using a mortar and pestle. Multiple scans were acquired in reflectance mode and all spectra were baseline corrected relative to the background of spectroscopic grade KBr. The thermal analysis of nanoparticle (NP) assemblies was carried out using a thermogravimetric analyzer (TA Instruments, TGA Q500). Samples were placed in a platinum pan holder and heated at a scanning rate of 5°C/min with a nitrogen flow (90 mL/min) and heating to 900 °C. PXRD patterns of the IONPs

and NC samples were recorded using a PANalytical Empyrean powder diffractometer using monochromatic Co $K_\alpha$ radiation (1.79 Å) with a 2θ scan rate of 3.2° $min^{-1}$ from 10° to 80° (2θ). UV-vis spectra were collected using a Varian Cary 100 Scan spectrophotometer using 1 cm quartz cuvettes and the spectra of pure solvent was subtracted from the solution spectra to afford baseline corrected data. Transmission electron microscopy (TEM) images and elemental composition of NCs were obtained in Bright-field mode using a Hitachi HT-7700 microscope at accelerating voltage 100 kV, coupled with energy dispersive X-ray (EDX) and selected area electron diffraction (SAED) analysis system. SAED patterns and EDX spectra of samples were obtained by high resolution TEM. For the sample preparation, samples were dispersed in aqueous solution (Mill-Q water) using an ultrasonic bath, where a drop of suspension was placed onto the holey carbon coated copper grids, and then samples were air-dried before imaging. Particle size distributions of the magnetite and NP assemblies were acquired using DLS with a Malvern Zetasizer instrument. Highly dilute aqueous solutions were analyzed at 20 °C and 90° scattering angle using disposable cuvettes. For salt dependent size distributions, NCs were dispersed in aqueous salt solution and adjusted to specific concentrations for DLS measurements. The Raman spectroscopic data for salt-responsive NCs was obtained with a Renishaw Raman Invia instrument using 514.5 nm excitation source with three exposures with a 10 mW laser power, on wet and as-separated samples from dispersion using a magnet. To change between doped and de-doped states, solutions were transferred into a vial, washed exhaustively with Millipore water and centrifuged at 8000 rpm for 30 min, where NCs collected and re-dispersed in aqueous solution were subsequently measured by DLS. This process was repeated for six cycles.

## 4.3.2. Surface functionalized particles

The synthesis process of hybrid nanostructures involves the oxidative surface-initialized polymerization[24-26] of aniline in the presence of surface treated magnetite colloids and CHI as stabilizer. Uniform IONPs initially were prepared, as described previously with a minor modifications.[27,28] In brief, the ferrous ($Fe^{+2}$) chloride and ferric ($Fe^{+3}$) chloride were dissolved in 200 mL Millipore water with a 1:2 mole ratio in a three neck round-bottom flask equipped with a gas flow adapter and rubber septum. The reaction was performed at 80 °C in an oil bath under a nitrogen atmosphere. The temperature raised to 80°C and 100 mL of NaOH solution was added slowly drop-wise to the above mixture. The reaction proceeded for 40 min with stirring, and after completion of the reaction, the black precipitate was isolated with a magnet and washed with Millipore water, at least 5 times, to yield IONPs. Subsequently, AIONPs were prepared by dispersing as-prepared IONPs (1 g) in 100 ml (0.5 % w/w acrylic acid) solution, where the pH was adjusted to pH 6. The suspension was subjected to ultrasonic treatment for 3 h at 70 °C under a $N_2$ gas atmosphere. Then acrylic acid functionalized IONPs was purified by five separation-dispersion cycles in Millipore water and collected using by magnetic separation during each purification step.

## 4.3.3. Assembly of composites

To prepare binary PIONcx, first homogeneous CHI/ANI solutions with variable fraction of monomer, aniline 200 µl and chitosan (0.0, 3.0, 5.0, 7.0 CHI, wt. %) were prepared in 0.5 % acetic acid solution and a fixed amount of (0.25 g) acrylic acid coated IONPs were suspended in 100 ml of the above solutions. The mixture was defined as solution A. The mixture was sonicated for 1 h in order to improve the dispersion of AIONPs in CHI/ANI solution and enrichment of aniline around the surface of NPs. Separately, an aqueous solution of APS with the ratio of equimolar amount compared to aniline was prepared and slowly introduced drop-wise to the mixture of A

under continuous stirring. The solution was degassed using $N_2$ for 30 min prior to adding APS and the polymerization was carried out for 8 h. After the reaction, the product was collected via magnetic separation and dried under vacuum overnight at 60° C after five washing cycles by re-dispersing into Millipore water. The synthesized PIONcs was further washed by collecting and dispersion in water for 5 cycles to remove any salt, monomers and possible oligomers. The obtained PANI/iron oxide NCs with variable composition were designated as PIONcx, (where x = 0.0, 3.0, 5.0 and 7.0) according to a variable weight ratio (%) of CHI.

## 4.3.4. Selective affinity and ionic dye recognition experiments

Molecular selective experiments in batch mode employed 15 ml of a solution containing a mixture of MB and MO with concentration values near 0.013 and 0.037 mM, respectively. 100 mg of PIONc5 was dispersed in the solution mixture and shaken for 5 h.

## 4.3.5. Adsorption isotherms:

The amount of dye adsorbed onto the composite was determined using Eq. 4.1.

$$q_e\,(mmol.g^{-1}) = \frac{(C_0 - C_e) \times V}{m} \tag{4.1}$$

where $C_0$ ($mmol.L^{-1}$) and $C_e$ ($mmol.L^{-1}$) are the initial and the equilibrium dye concentrations. $q_e$ ($mmol.g^{-1}$) is the adsorbed amount of MB per unit mass of adsorbent, V (L) is the volume of the MB solution (ml) and m (g) is the weight of the adsorbent. The Langmuir model describes monolayer uptake of the adsorbate onto the sorbent with identical adsorption sites and no lateral interactions between adsorbates. As the surface adsorption sites of the sorbent become occupied,

no further adsorption will occur at that occupied sites. The Langmuir model is expressed as follows:[29]

$$q_e(mmol.g^{-1}) = \frac{q_m K_L C_e}{1 + K_L C_e} \quad (4.2)$$

$q_e$ is the maximum adsorption at equilibrium, $C_e$ is the equilibrium concentration of the dye in solution and $K_L$ denotes Langmuir constant, which indicates affinity of the binding site. 10 and 20 mg of PIONc5 were dispersed in 3 ml of MB and MO solutions at variable concentration (0.1-1.5 mM). The mixtures were shaken in a horizontal shaker (SCILOGEX SK-O330-Pro) for 24 h contact time. The supernatant solutions were isolated, diluted and analyzed by UV-vis spectroscopy. The data obtained was used to yield adsorption isotherms. The isotherm profiles of the above model for MB and MO and the parameters were obtained from nonlinear fitting

# 4.4. Results and discussion

## 4.4.1. Design and assembly into responsive biphasic hybrid particles

Chemically distinct biphasic hybrid nanostructures containing magnetite colloids and PANI with variable size, shape, and morphology were prepared in a two-step process, as illustrated in Figure 4.1a. The synthesis of heterogeneous particles relies on the surface initiated polymerization method[30-32] to couple PANI onto the surface of IONPs through a seeded nucleation-polymerization. IONFAL2Ps were prepared by a conventional co-precipitation method that affords a high magnetite yield.[27,33] TEM images of the corresponding NPs with a mean hydrodynamic diameter ($D_h$) ca. 72 nm are shown (*cf.* Figure A.13a,b in Appendix). Firstly, the initial IONPs are decorated with acrylic acid in aqueous solution, rendering numerous free vinyl groups on the NP surface.

Dispersion polymerization of PANI was achieved with surface treated IONPs with acrylic acid to afford loci that favor polymerization and surface capture of the growing PANI macromolecules. The covalent bond formed between IONP seeds and radical polymers evolve as nuclei which adsorb growing free polymers onto the surface to yield polymer particles with ordered packing as a NC structure. Furthermore, once nuclei evolve onto the surface, favorable interfacial surface energy allows for PANI to grow heterogeneously at AIONPs surface rather than in bulk solution homogeneously. This leads to formation of dual phase magnetic NCs with self-assembled polymer compartments as building blocks. Surface treatment of IONPs with a grafting agent such as acrylic acid is a key step to promote stability, dispersion quality (see images in Figure 4.1a), and functionality in order to promote the surface capture of growing radical PANI polymers on the inorganic seed surface.[34] The freshly prepared acrylic acid functionalized IONPs were dispersed in acetic acid solution (0.5 %) with a polymer stabilizer (CHI). These pre-treated particles serve as seeds for PANI assemblies where biphasic particle fabrication was accomplished by introducing APS as the radical oxidizing agent[35,36] which affords surface-initiated and seeded polymer formation of aniline onto the IONPs surface, affording assembly of ordered PANI structures onto the surface of magnetite. After introducing APS into the mixed medium, it forms radicals as a function of pH and temperature. Radicals react with aniline monomers and acrylic acid present on the surface of IONPs. Polymerization of PANI can proceed with vinyl groups which are reactive sites that may serve as loci for surface capture of growing radical chains. Ultimately, the nuclei on magnetite surface and in solution coalesce by H-bonding to self-assemble as stable nanospheres through seeded nucleation (Figure 4.1e), where the result is phase separation from solution.[37] It is believed that such hybrid nanostructures of IONPs and PANI offer a unique approach for construction of multi-functional nanohybrids with chemically distinct multi-component polymer

and magnetite phases with promising prospects in imaging, biomedicine, magnetic-directed drug delivery and advanced material modification.[38,39]

## 4.4.2. Structural characterization of NC hetero-structures

The successful conjugation of two phases in a resultant biphasic nanostructure was studied by various characterization techniques. FTIR spectroscopy shows characteristic vibrational features arising from polymerization of aniline and particles associated onto the IONPs. Characteristic spectral features of PANI, at 1580 and 1510 $cm^{-1}$ in Figure 4.1b are assigned to the *v*(C=C) vibrations of the quinoid and benzenoid rings, respectively.[24,40] The signals of C–N, C=N and -N=Q=N- (Q denotes the quinoid ring) stretching modes centered near 1303, 1244 and 1377 $cm^{-1}$ are clearly evident. In-plane deformation features of C-H stretching are noted at 1148 $cm^{-1}$.[41] As expected, the IR spectra reveal characteristic spectral features of magnetite at 580 $cm^{-1}$ and assigned to *v*(Fe-O), as shown in the inset of Figure 4.1b.

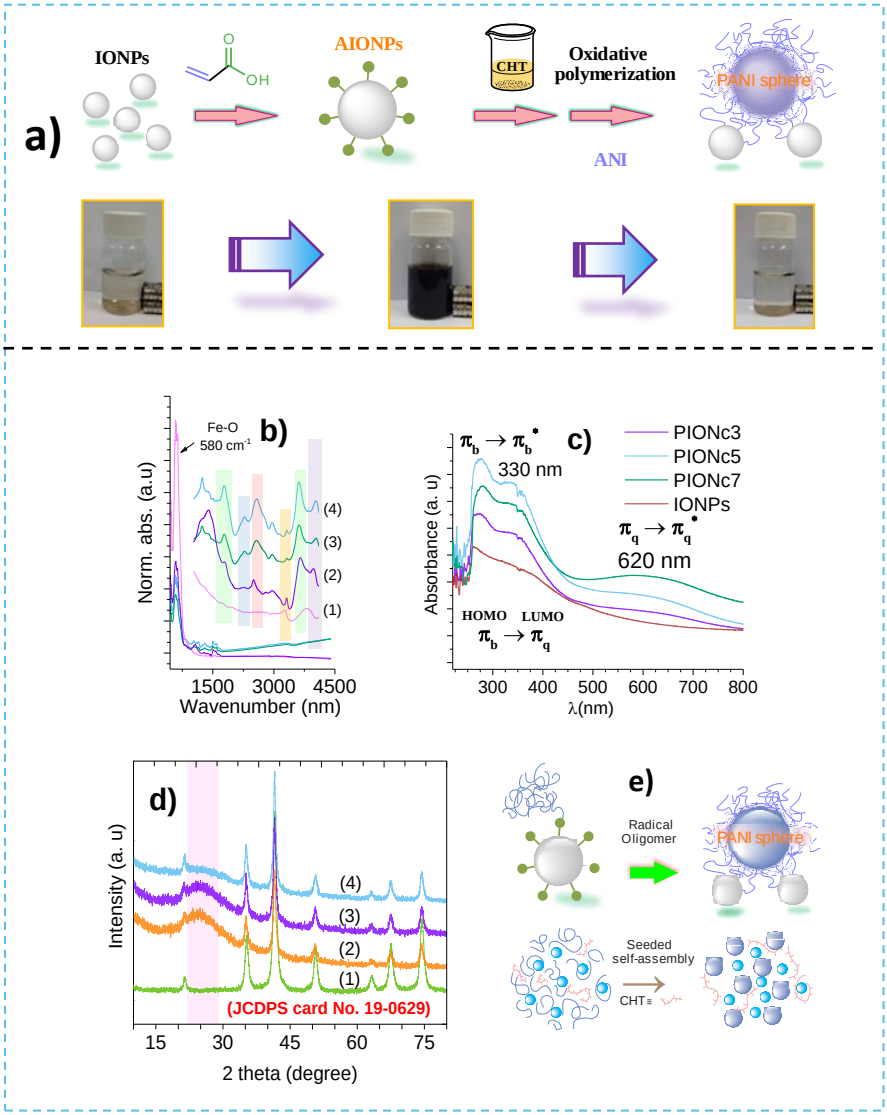


**Figure 4.1.** (a) Schematic representation of the PIONCx synthesis and representative images of samples prepared at each stage. Synthetic preparation involves two steps: *i*. surface treatment of IONPs and self-assembly, and *ii*. Self-assembled polymer particles generated through surface initialized seeded nucleation polymerization. (b) FT-IR spectra of (1) acrylic acid adsorbed IONPs, (2) PIONCc3, (3) IOPNc5, (4) PIONc7 samples. Image (c) shows absorbance spectra of hetero particles ($\lambda_{max}$ = 330 and 620 nm) dispersed in NMP solutions. (d) PXRD patterns for (1) IONPs and PIONCx nanostructures; (2) x=7, (3) x=5, (4) x=3, where the band observed ca. 2θ = 25 relates to PANI domains. (e) Illustration of self-assembly and polymer growth onto the IONPs surface.

In addition, AIONPs, exhibit two features centered at ca. 1550 and 1600 $cm^{-1}$ that are assigned to $\nu_s(CO_2^-)$ and $\nu_a(CO_2^-)$ of carbonyl groups due to carboxylate anion formation. The $\nu_s(CO_2^-)$

signal in NCs is shifted slightly to higher frequencies (1446 $cm^{-1}$) with the growth of PANI polymers onto the composites that provide further support of the proposed Fe-O-R surface-bonding mode (Figure 4.1b).[42] The asymmetric band is difficult to recognize since it is masked by strong aromatic C=C stretching bands. The absorption maxima at 330 nm and 620 nm in Figure 4.1c are attributed to the PANI polymer transitions associated with IONPs colloids. These absorption bands result from the π-π* benzenoid and quinoid excitation transitions and imply the presence of PANI and its association with IONPs.[43]

The crystal structure and composition of species present in resultant NC materials were examined by PXRD. Clearly, the NCs are comprised of two highly crystalline and partially amorphous domains (Figure 4.1d). Regardless of the available weight fraction of CHI, the main PXRD lines can be routinely indexed to well-defined crystalline iron oxide phase (JCPDS No. 19-0629). For NC samples, the location of main PXRD lines are identical to those of IONPs that reveal similar crystalline structure as pure magnetite. However, a lower intensity and broad diffraction peak centered at $2\theta$ =20-24° was observed in the NCs, supporting the existence of amorphous PANI due to (100), and (110) diffractions of the polymer domains. These signatures relate to the periodicity of PANI chains perpendicular and parallel to the PANI chains, respectively.[41,44-47] The partial absence of PANI and monodisperse periodicity of the IOPNc7 composite imply that molecular packing of PANI within the NCs becomes less ordered with decreasing weight fraction of CHI (%).[47]

## 4.4.3. Phase characterization of NCs

The morphological features of NCs were investigated using transmission electron microscopy (TEM), where typical TEM images are shown in Figure 4.2a-c for IOPNc3. In accordance with TEM results, hybrid PANI structures prepared at the lowest CHI content can be divided into two

distinct domains, larger particles with near perfect spherical shape that contain voids (dimple-shape particles, $d_{av}$ ~ 220 nm) and dispersed smaller-sized particles ($d_{av}$ ~ 20 nm) in Figure 4.2d. From phase characterization analysis it was evident that these domains belong to assembled PANI and inorganic seeds. The results suggest that, PANI particles were successfully integrated onto the magnetite seed particle surface. In Figure 4.2d, the size of magnetite particles within the NCs ranged from 10 to 28 nm. This range agrees with the average diameter of the original IONPs (Figure A.13) providing support that the size and morphology of magnetite NPs were unchanged after formation of the PANI NCs. It is likely that solvent was trapped within the hydrophobic polymer aggregates during the self-assembly process which gives rise to the dimple-shaped aggregates (*cf*. Figure 4.2a), especially for solvent with higher viscosity. The structures formed here further support the dimple formation mechanism, as reported elsewhere.[48-50] These peculiar structures are expected to emerge in the rigid hydrophobic polymers such as PANI when chain mobility is low in the presence of CHI leading to increased solvent viscosity.[51] Dimple formation also requires a narrow range of solvent viscosity; low enough to allow coalescence of bubbles and high enough to prevent homogeneous shrinkage of the polymer aggregates.

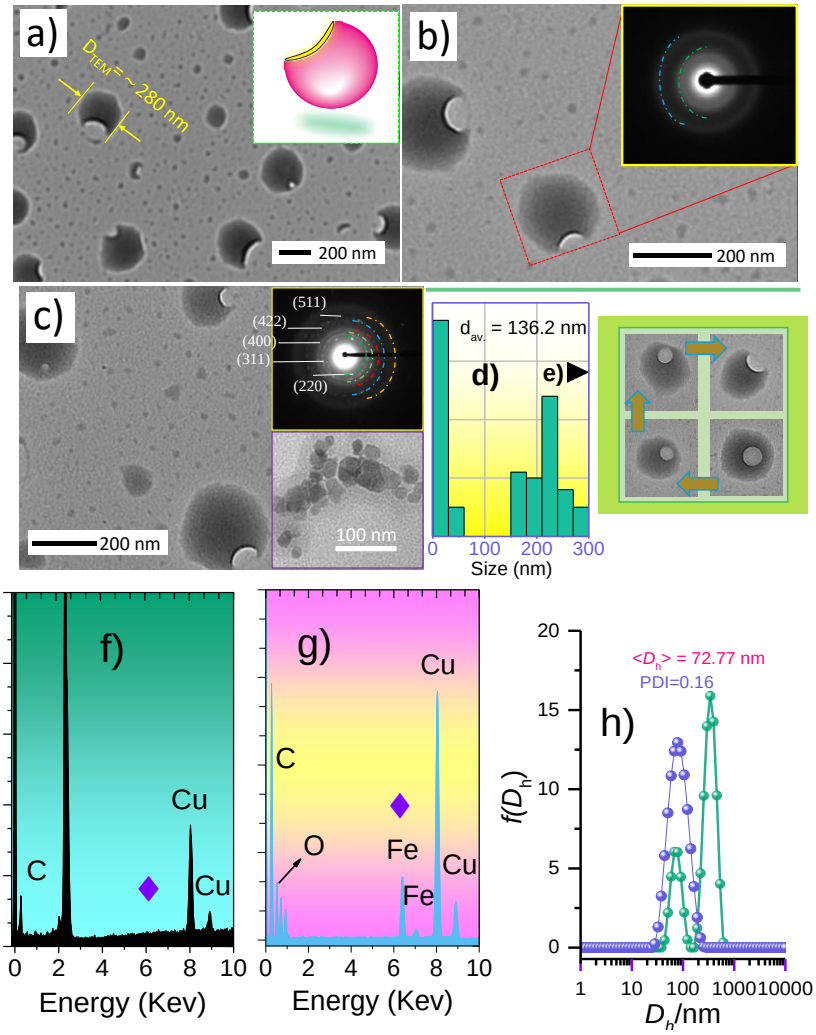


**Figure 4.2.** (a-b-c) show the TEM images of IOPNc3 nanohybrids and inset (a) a schematic representation of dimple-shaped particles formed in NCs. In inset b, the selected area of the electron diffraction pattern where the beam focused on larger particles and inset c the selected area of electron diffraction pattern related to the magnetite phase (from image in inset 2c bottom) in NC materials. (d) Size distribution histograms PIONc3 particles consisting of a bimodal size population ($d_{av.}$ ~ 18 and 220 nm). (e) Proposed four-step formation of dimple-shaped aggregates: seeded-nucleation, formation of porous-like spheres (yellow spheres represent trapped solvent), coalescence, and breaking bubble due to high *surface-to-volume*. (Particles are from different images) and size histogram of PIONc3 composites obtained from TEM. (f) The corresponding EDX mapping lines collected from small-sized domains and (g) larger particles (from different images). (♦) indicates Fe band position. Shown in (h) bimodal intensity-average hydrodynamic diameter distribution $f(D_h)$ of PIONc3 hetero particles measured by DLS compared to *as prepared* parent IONPs.

The initial phase of nucleation and assembly, yield particles that resemble porous spheres. Due to the high interfacial energy of small trapped air bubbles, they tend to coalesce into larger structures within aggregates. In turn, this leads to formation of dimples when a large solvent bubble escapes through the weakest region close to the surface (*cf*. Figure 4.2e).[48-50] In order to investigate compositional distribution, EDX and SAED analysis was carried out on PIONc3 NCs. The SAED pattern from large objects, which exhibit two exocentric diffuse and weak ring patterns with no coherent electron scattering. This supports limited long-range order and the presence of polycrystalline PANI domains based on the PXRD patterns (*cf*. Figure 4.2b, and Figure A.14). For the SAED analysis (Figure 4.2c inset), the beam is focused on small-sized objects (Figure 4.2c inset, bottom) that clearly show five distinguishable exocentric rings composed of discrete diffraction spots indexed to (220), (311), (400), (422), (511) and (440) reflections consistent with the spinel structure of magnetite. These observations are in agreement with PXRD results suggesting that high crystallinity of IONPs domains are preserved.

The detailed structural features of these domains obtained from EDX analysis (Figure 4.2g) and it clearly displays the signals of Fe and O as major elements at values 6.39, 7.05 and 0.53 keV. Cu K signals arise from sample grids. Similarly, Figure 4.2f reveals EDX lines from large objects. Fe and O were not observed; however, distinct lines at values 0.227 keV, denote the characteristic $K_{\alpha}$ energy of carbon, which confirm the presence of organic polymer in this specific phase and provides strong support that these unique dual-compartment distinct biphasic systems are formed with excellent magnetism properties. In solution, PIONc3 was further characterized by dynamic light scattering (*cf*. Figure 4.2h). Interestingly, a comparison with the unimodal IONPs, the NC reveal a new emerging band near 330 nm assigned to coupled growth of PANI aggregates in the system. The size and morphology of PANI particles were found to critically depend on the CHI

content. As the relative amount of CHI (%) in the NC increased during the polymerization. A smaller size distribution that corresponds to polymer conjugates was obtained due to the higher stabilizer efficiency with more accessible interaction sites. In Figure 4.3a, the TEM images of each hybrid nanostructure prepared with fixed CHI (%) are shown. TEM images reveal a distinct mixture of small-sized magnetite NPs and spherical polymer particles. To gain further insight on the size distribution and to interpret the accessible sizes and phases, a histogram was obtained by measurement of 100 NPs of different images for different regions using ImageJ software from TEM micrographs to reveal the size distribution (*cf*. Figure A.13 for statistics). TEM images for NPs with a lower CHI fraction (3.0 %) revealed dimple-shaped particles, and average diameters of nearly 213 nm were noted (*cf*. Figure 4.3a), as discussed above. Increasing the CHI content to 5 % favors formation of spherical PANI domains with smaller average diameter that was reduced to 150 nm, where the PANI NPs became more uniform in shape and size. An increase in the CHI fraction (7 %) led to PANI NPs with a reduced average diameter of 73 nm with an increased particle homogeneity according to the PDI values (*cf*. Figure 4.3b).

Notably, the particle number increased when polymerization occurred with higher stabilizer levels. The stabilizer efficiency (manifests itself by formation of small-sized and large number of polymer particles) increases with greater stabilizer concentration.[52] Stabilizer efficiency of CHI relates to the hydroxyl, carbonyl, and amine functional groups of the polymer backbone which can form hydrogen bonds with PANI spheres. A reduced efficiency at 3.0 % CHI was attributed to the attenuated accessibility of functional groups and its limited adsorption ability, resulting in the formation of fewer and larger size particles.[51] The approach reported here also enables replacement of non-aqueous solvents and other polymer stabilizers such as PVP[53] which are less desired and environmentally friendly for separation and detection in targeted drug delivery and biological

applications.[54] More detailed size information of such PIONcx NPs can be estimated by DLS measurements. A comparison of the intensity size distributions of hetero particles in aqueous solution made at variable CHI content are shown in Figure 4.3b. The results further confirm TEM observations and the hydrodynamic diameter ($D_h$) distributions clearly show bimodal size for PIONc (x = 3, 5, 7) NCs. The bimodal $D_h$ distribution in solution indicate the presence of variably sized particles. The average peak diameter of NCs deduced from DLS vary from 243.6 to 419 nm as CHI varies from 3 to 7 %. In the case of PIONc3, an average particle diameter (419.4 nm) was detected, while lower diameters were observed for PIONc5 (327.3 nm) and PIONc7 (243.6 nm). The DLS-based diameter for larger-sized particles (the prominent peak centered ca. 340 nm) also shifted from higher to lower values. In contrast, the peak assigned to the $Fe_3O_4$ within assemblies was ca. 70 nm for all NCs, with a slight shift to larger $D_h$ values relative to its original TEM value (Figure A.13), in agreement with the shrunk and swollen particles estimated by TEM and DLS, respectively. The $\Delta d_{av.}$ between larger and smaller composite particles by DLS is ca. 176 nm which gives access to variable sizes over this range. Therefore, this method offers a new approach for controlling well-defined polymer building blocks within NC structures. The intensity weighted mean hydrodynamic size, (z-average hydrodynamic diameter, $d_p$, nm) is given by Eq. 4.3.

$$< d_p >= \frac{\sum n_i d_{pi}^6}{\sum n_i d_{pi}^5} \tag{4.3}$$

Where $n_i$ is the number density of particles with a diameter of $d_p$. The DLS technique tends to bias larger particles owing to the greater intensity contribution of larger particles ($I_{sc} \approx R^6$).[55] The intensity of small-sized magnetite particles with $D_h$ = 75 nm in PIONc3 for instance, is $9 \times 10^3$ times lower than that for particles with larger diameter (ca. $D_h$ = 340 nm) in a mixture of particles with large size variation. When intensity-weighted peak is converted to a number-weighted

intensity, it will reveal smaller number for particles with diameter of 340 nm, in comparison to small-sized particles observed by a statistical analysis of self-assembled polymer arrangements.

In an attempt to further rationalize the role of stabilizer, the formation of NCs without stabilizer was investigated. An interesting observation was noted when the size distribution of NCs was estimated by DLS, where no noticeable polymer aggregates were observed for NCs with x = 0.0. As shown in Figure 4.4a (inset), DLS estimates of PIONc0 reveal a unimodal size distribution with the average hydrodynamic diameter of 111 nm (PDI = 0.18). It is inferred that in the absence of CHI, aniline polymerization likely occurred in bulk solution that contains dispersed IONPs rather than the localized phase. DLS measurements clearly exhibit that $D_h$ shifted to higher values in the NC compared to the initial $Fe_3O_4$ NPs. Moreover, TEM and DLS was utilized to evaluate the nanostructures of PIONc0 NPs (*cf.* Figure 4.4a,b), where the size of the NPs varied from 15 to 24 nm with an average diameter of 18.3 nm. The latter corresponds to the size distribution of pristine magnetite and the foregoing concur with the size distribution of the parent IONPs obtained from TEM. Figure 4.4c displays the particle diameter results at variable CHI content of NCs and Figure 4.4d summarizes the overall results of CHI weight fraction with NCs particle diameter measured by both DLS and TEM (see inset in Figure 4.4d). By decreasing the CHI content (7 % to 3 %), the hydrodynamic diameter of NCs decreased sharply (450 to 70 nm). Similarly, TEM results also reveal that the average particle size display a similar trend (250 to 75 nm) with decreasing stabilizer, as shown in the Figure 4.4d, inset. The observations decribed herein and the close correlation of the results obtained from TEM and DLS imply that CHI plays a key role in NC design.

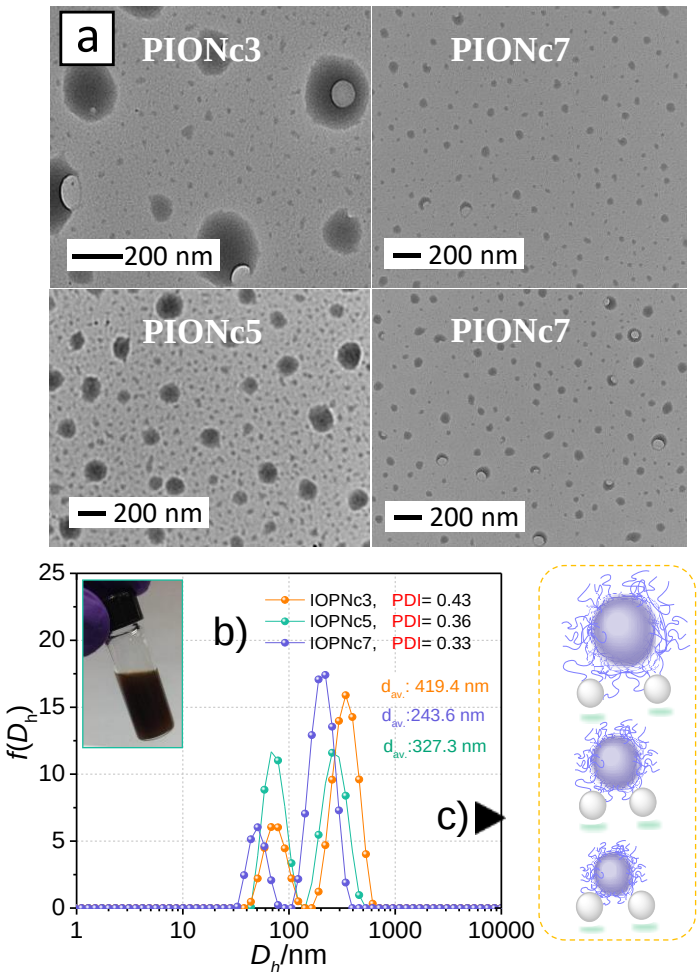


**Figure 4.3.** (a) TEM bright-field micrographs of heteroparticles of the magnetic/PANI domain that are well tuned with variable CHI content (3%, 5%, and 7%). (b) Bimodal intensity size distribution of heteroparticle hybrids with variable CHI content obtained by DLS relate to the TEM images presented above. (c) Schematic size-tuning of PANI domains. The inset in (b) shows the dispersion of aqueous NC (x = 5%). Note the presence of free magnetite particles.

Further insight on the magnetic response of NCs was investigated in an external magnetic field by measuring UV-vis spectra of NCs in NMP solution as a function of time after a permanent magnet was applied from the lower region of the solution. PIONc5 was dispersed in the NMP and the samples were taken at different time intervals for UV-vis measurements. As shown in Figure 4.4e, the absorbance of IOPNc5 rapidly decreased in NMP solution after applying a magnetic field. The results suggest that the magnetite NPs still preserve their magnetic properties similar to the

parent $Fe_3O_4$ NPs within NCs. The separation occurs rapidly and nearly complete within 5 min of the applied magnetic field. For comparison, the spectrum of the sample after free settling without disturbance is shown in Figure 4.4e. This indicates that IONPs subside slower (within 3h) than when a small magnetic field is applied. This is essential and convenient to manipulate suspension of PANI aggregate NCs within minutes.

### 4.4.4. Salt-stimulated disassembly and size/phase transition in solution

Among the noncovalent interactions, H-bonding is the most common one used by nature that contributes to biological diversity. Nanostructured conducting polymers such as PANI are attractive due to their unique chemical, and physical properties and potential applications as building blocks for nanoelectronics. Right now, two different types of pH and redox stimuli are known for PANI.[21,36,56,57] The pH switching of doped/de-doped state of PANI was reported to control the morphological evolution of PANI between nanowire and helical structure states using dynamic hydrogen bonding induced via a chiral acid dopant.[56] Similarly, Lv and co-workers reported that redox-triggered disintegration of the PANI microcapsules occurs with release of self-healing loads as a function of the polymer shell oxidation state.[36] However, salt-responsive materials,[58] especially salt-responsive self-assembly processes has not been reported in the literature for PANI. In contrast, a unique and rare example of stimuli-responsive PANI particles within magnetite NCs that undergo a salt-triggered disassembly via dynamic hydrogen bonding was reported. Direct monitoring the salt-responsive disassembly of molecular assemblies and transformation of polymer aggregates upon salt addition was monitored by DLS measurements. Figure 4.5b,c illustrates the size distribution of PIONc3 particles at variable dosage (0.2 to 1.8 M) of NaCl (*aq*). Evolution of a new size-distribution centered near 36 nm indicates that aggregates evolve into smaller particles when 0.2 M salt stimulus was added to the aqueous dispersion of

PIONc3 composite, while magnetite NPs remain at $<D_h>$ ~ 110 nm (Figure 4.5c). Further dosing of salt reveals a shift of the peak centered ~ 650 nm to smaller size distributions, while the peak centered ca. 30 nm disappears concurrently. At elevated electrolyte concentration up to 0.8 M, larger-sized distribution tends to shift towards ca. 120 nm. On the other hand, the signature near 35 nm completely disappeared. Excess salt concentration above 1 M finally leads to disappearance of all polymer peaks and the resulting unimodal distribution and the diameter size of the NCs return to the average value of the parent IONPs (Figure 4.5b).

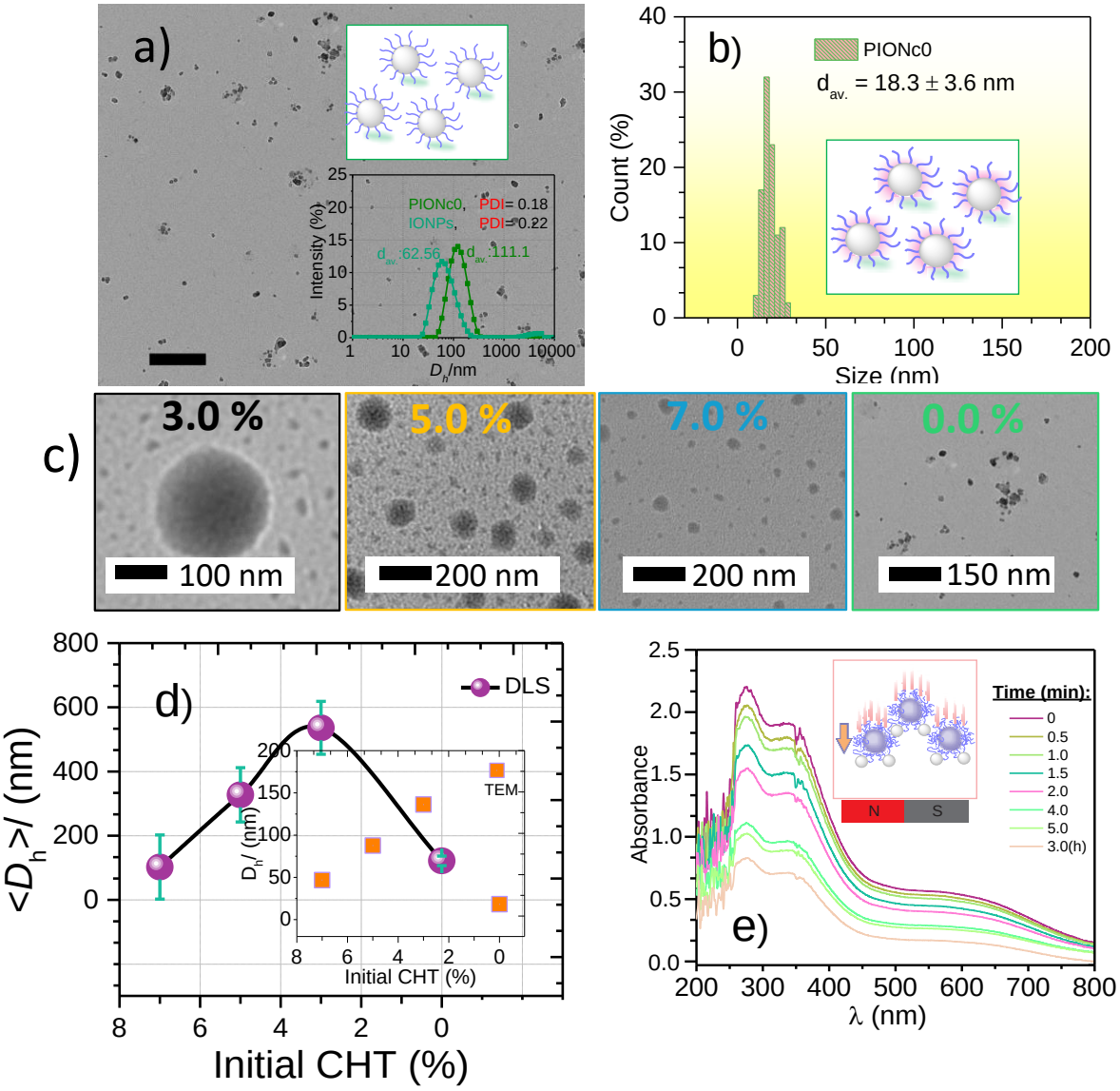


**Figure 4.4.** (a) TEM micrograph of PIONc0 particles synthesized without initial CHI; the scale bar is 100 nm. (Inset) DLS characterization of IONPs and PIONc0 showing the change in size distribution of particles in composite. (b) Histograms of size distribution of PIONc0. (c) Size and phase transitions of PANI components in PIONcx prepared in variable stabilizer %. (d) Size transition of PANI domains in NCs plotted as function of CHI % as measured by DLS and TEM (inset). (e) Magnetic response of PIONc5 as function of time in NMP under magnetic field (non-uniform).

It is of interest to exploit the details of how salt gradients affects these responsive transitions and to see if this behavior relates to NCs reversible tailoring and modulation of polymer compartment. Earlier work by Kim and co-workers revealed that electrical switching of PANI

vesicles under redox cycling arises from disrupted hydrogen bonding upon PANI reduction.[21] This work was extended by Lv and co-workers for controlled cargo delivery under redox responsive release.[36] A number of factors play a role in salt mediated trigger this micro-phase transformation. In neutralized (de-doped) PANI, polymer chains are densely compacted due to strong intermolecular amine-imine hydrogen bonding (Scheme 6.2).[21]

Firstly, the amine-imine intermolecular hydrogen bonding becomes weaker in the salt solution with looser packing of polymer chains due to presence of single bonds. Therefore, polymer chains can readily rotate with reduced rigidity and enhanced mobility in solution (Figure 4.5e and Scheme 6.2). Secondly, PANI has variable wettability and permeability as function of the doping/redox state.[36] PANI in its doped form exhibits more wettability and water permeability than the de-doped state due to a greater hydrophilicity in the acid-doped state.[59] The disassembly and size-shift of PANI compartment is promoted by the combined effect of these factors to yield more flexible chains, enhanced hydrophilicity, and greater permeability of ions into the PANI aggregates. It is noteworthy that the TGA results for the onset of degradation for self-assembled PANI domains in NCs occur at temperatures well above that for samples prepared by physical mixing (Figure 4.5a and A.16, expanded curve). This indicates stronger intramolecular interactions occur for the PANI domains with compact NC structures and tight packing. As the salt concentration rose to ca. 1 M, PANI chains underwent salt doping, where the salt-polymer interactions exceed that of the inter-/intra-chain hydrogen bonding. The cation-N (amide/amine) leads to screening effects by intramolecular π-π and hydrogen bonding. Consequently, the polymer undergoes swelling by salt ("*salting-in*" interactions) effects and the aggregates undergo disassembly, where the size distribution of aggregates coincide with pristine IONPs. The slight shift to a larger size

distributions relative to solid particles relate to interfacial polymer *salting-in* effects and shrinkage of particles after drying.[60]

To gain a further understanding on the role of salt effects, the interactions associated with disintegration of PIONc3 was studied by Raman spectroscopy. The Raman spectra of wet PIONc3 (Figure 4.5d) sample shows a strong band at 1164 $cm^{-1}$ assigned to *in plane* C-H bending of the quinoid ring.[61] The bands at 1220, 1490 and 1595 $cm^{-1}$ are assigned to C-N stretching of the benzenoid ring, C=N stretching for quinoid ring C-C stretching of the benzenoid rings, respectively[47]. It is interesting to note that the intensity of the band at 1333 $cm^{-1}$ characteristic for semi-quinoid ($C\text{-}N^{\bullet+}$) radical stretching[61] was greater for disassembled samples, as compared to the spectra of *as-prepared* PIONc3. This is an obvious characteristic of emeraldine salt form of PANI (doped state).

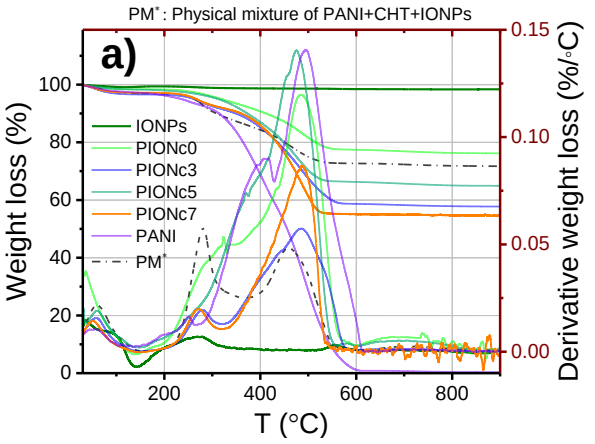


IONPs in DMSO

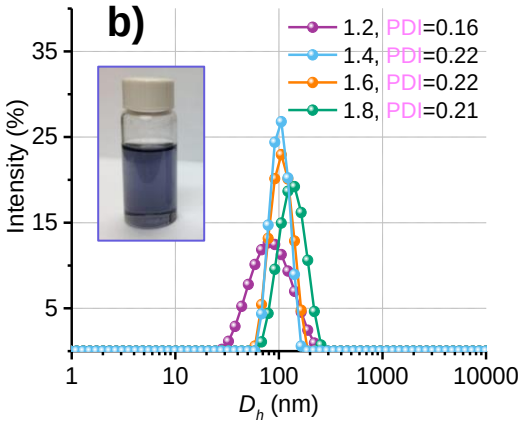


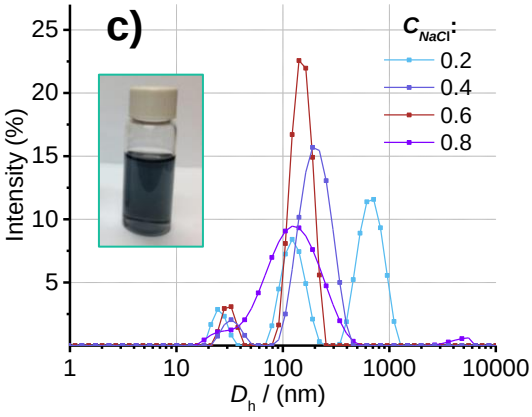

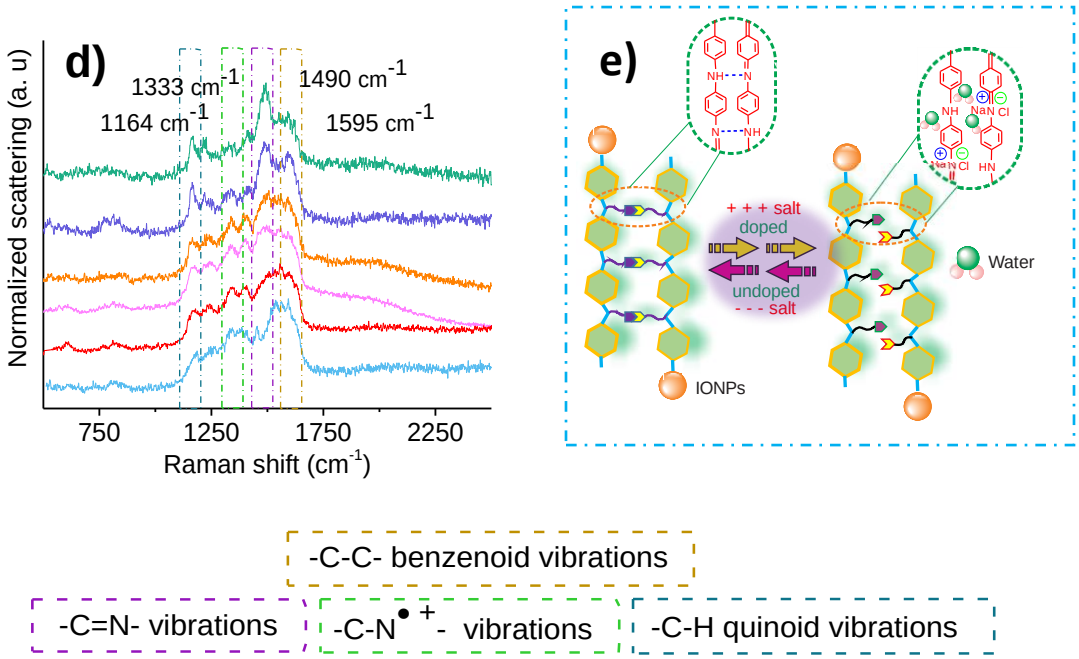


**Figure 4.5.** (a) TGA/DTG profiles of PIONcx NCs measured under nitrogen flow over range of 25-900 ˚C and their comparison with pure PANI and PANI/IONPs with IONPs loading of 20 % prepared by physical mixture at a temperature ramp of 5˚ C $min^{-1}$. (b, c) DLS characterization of the salt-doped PIONc5 NC at variable $C_{NaCl}$ and following micro-phase behavior in water. (d) Following phase transformation and salt effects on the polymer components using Raman spectroscopy (λ = 514.5 nm excitation) for dispersed samples in aqueous dispersion, from top to bottom are from PIONc3 composite and different levels of NaCl with $C_{NaCl}$ = 0.1, 0.5, 0.8, and 1.8 M, respectively. (e) Schematic hydrogen bonding regulated disassembly of PANI aggregates at the magnetite surface and disrupting inter-/intra-chain hydrogen bonding in the presence of ions. Insets (b) and (c) show the images of PIONc5 samples in dimethyl sulfoxide (DMSO) after de-doping and doping with salt (2.0 M).

A similar conclusion was drawn from the peak intensity at 1490 $cm^{-1}$ (due to C=N stretching) which decreases gradually and completely disappears for disassembled species with greater salt dose. The results indicate an interaction between $Na^+$ ions and quinoid nucleophilic nitrogen. Additional changes in band intensity at 1164, 1595 $cm^{-1}$ and the shift in the peak assigned to 1218 $cm^{-1}$ relate to C-H stretching of quinoid rings. The salt-responsive disintegrated system is presumed to be analogous to the doped emeraldine salt, regulated by hydrogen bonding according to mechanism presented in Figure 4.5e. This salt-doped PANI is analogous to the *salting-in* effect

described by the Hofmeister series (counterion binding effects).[62] A similar phase separation from water has been reported for temperature responsive systems with upper critical phase separation in water. Polymer aggregates are solvent induced as the consequence of extensive hydrogen bonded and ordered structure of water. Hofmeister series result in altering the structural properties of aggregated assemblies by destruction or formation of supramolecular architectures which gives rise to ion responsive structures.[63] NaCl is classified as intermediate between kosmotrope (structure maker) and chaotrope (disorder maker) salt (Figure 4.5e and A.15). To further corroborate the DLS findings and identify the structures associated with two self-assembled and disassembled states in the presence of salt, TEM images for the samples prepared at elevated salinity were obtained to track the breakdown of the assembly and the phase transition (Figure A.16). Remarkably, solid aggregates exhibit phase-shift behavior and the size of larger aggregates apparently decreased as function of ionic strength. Therefore, to clarify whether ion-dipole interactions occur between PANI and ionic species, the ion-dye recognition of the NCs was studied using cationic and anionic dyes.

Specifically, MO and MB were chosen because their ionic nature which can likely undergo favorable ion-dipole interactions with such NCs in aqueous solution. The Langmuir isotherm provides a description of monolayer adsorption of MB for such NCs with maximum adsorption of 0.34 mmol.$g^{-1}$ (*cf.* Figure 4.6a). In contrast, MO in its anion form which has lower affinity for the NC. MB likely associates with de-doped PANI in a similar fashion as $Na^+$ ions (*cf.* Figure 4.6a,c). Nevertheless, the effect of weak π-π stacking arrangements in solution cannot be overruled. MB displays a maximum monolayer adsorption of 108.7 mg $g^{-1}$ with a 75.5 % uptake from the dye solution (*cf.* Table A.4). It was concluded that the salt-induced interchange process occurs via a "*salting-in"* process mediated by multiple hydrogen bonding. Figure 4.6b illustrates the DLS

variation in average diameter of NCs. The DLS estimates of the initial diameter of PIONc3 was ca. 500 nm where the average size decreased dramatically. These results indicate a unique and versatile salinity-stimulated transformation, where he initial average diameter of composites are responsive to salt concentration as seen from TEM images above 0.8 M, where the NC is comprised of IONPs without any polymer assembly.

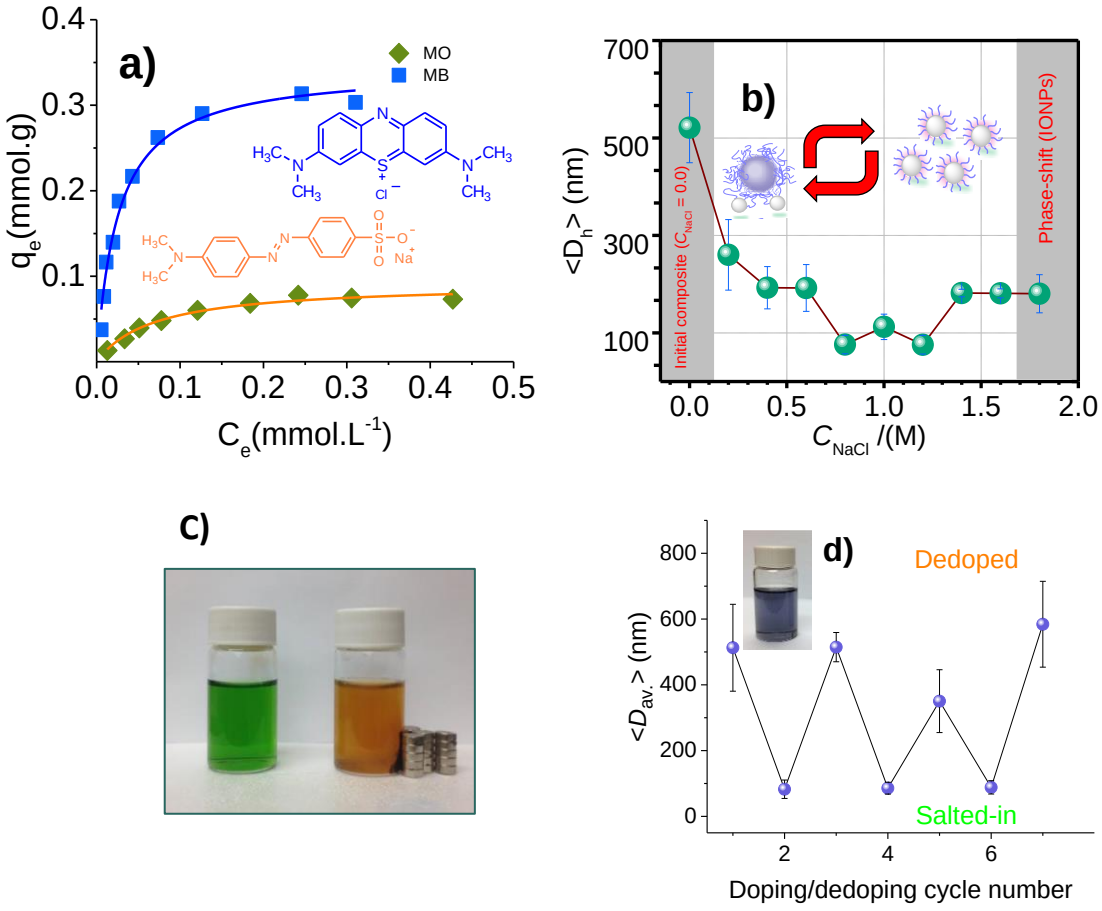


**Figure 4.6.** (a) Langmuir adsorption isotherms (Eq. 4.2) of MB and MO on PIONc5. $C_e$ (mmol/L): equilibrium concentration of dyes. $q_e$ (mmolg$^{-1}$): the amount of dye adsorbed at equilibrium. Insets: the chemical structures of MB and MO (b) DLS measurements monitoring the evolution of PIONc5 average size in the aqueous solution with successive salt addition from $C_{NaCl}$ = 0.1 to 1.8 M (c) Photographs of MB/MO mixture before (left) and after (right) treated with PIONc5. Initial concentrations approximately 0.013 and 0.037 mM respectively (*cf.* Figure A.17). (d) Peak DLS particle <$D_h$> recorded at alternated 1.8 M salt and washing/centrifuging in consecutive doping runs. Photograph images of NaCl doped/de-doped sample in DMSO.

Furthermore, according to DLS measurements, two states are interchangeable by reversible intermolecular hydrogen bonding as PANI was un-doped. The particle size $<D_h>$ varies between 676.6 to 418 nm for the self-assembled state, while $<D_h>$ varies (102.1 to 62.7 nm) for salt induced disassembly when NCs are doped with 1.8 M NaCl solution and de-doped after extensive water washing. After salt is removed, PANI chains become interconnected to form larger aggregates and nano dimensional phase separation which is reversible under alternated doping/de-doping cycles (*cf*. Figure 4.6d).

## 4.5. Conclusion

In this study, a unique dynamic salt-responsive phase separation of PANI NCs from aqueous solution was demonstrated. This study is a first example that reveals such an effect accompanied with magnetism in a chemically distinct dual compartment hierarchical structure. Salt-triggered disassembly leads to an attractive fine-tuning and adjustable polymer matrix with responsive size-, shape-, and phase-transitions in aqueous solution. The salt sensitive phase-shift and chemical interactions in disassembled PANI domains for the NC system was studied by complementary methods (Raman spectroscopy, DLS, and uptake of ionized dye probes). The integrated system exploits features of constituent species with potential multifunctional and dual-responsive character. It is anticipated that this previously unreported dynamic hydrogen bonding process of PANI constructed with salt-responsive modulation will advance the field of multifunctional hybrid nanosystems with unique recognition for controlled-release and magnetically site-directed delivery devices in saline environments.

# 4.7. References


1. Gage, S. H.; Stein, B. D.; Nikoshvili, L. Z.; Matveeva, V. G.; Sulman, M. G.; Sulman, E. M.; Morgan, D. G.; Yuzik-Klimova, E. Y.; Mahmoud, W. E.; Bronstein, L. M., Functionalization of Monodisperse Iron Oxide NPs and Their Properties as Magnetically Recoverable Catalysts. *Langmuir* **2013**, *29*, 466-473.

2. Munaweera, I.; Aliev, A.; Balkus, K. J., Electrospun Cellulose Acetate-Garnet Nanocomposite Magnetic Fibers for Bioseparations. *ACS Appl. Mater. Interfaces* **2014**, *6*, 244-251.

3. Neuberger, T.; Schopf, B.; Hofmann, H.; Hofmann, M.; von Rechenberg, B., Superparamagnetic Nanoparticles for Biomedical Applications: Possibilities and Limitations of a New Drug Delivery System. *J. Magn. Magn. Mater.* **2005**, *293*, 483-496.

4. Ulbrich, K.; Hola, K.; Subr, V.; Bakandritsos, A.; Tucek, J.; Zboril, R., Targeted Drug Delivery with Polymers and Magnetic Nanoparticles: Covalent and Noncovalent Approaches, Release Control, and Clinical Studies. *Chem. Rev.* **2016**, *116*, 5338-5431.

5. Mahmoudi, M.; Sant, S.; Wang, B.; Laurent, S.; Sen, T., Superparamagnetic Iron Oxide Nanoparticles (SPIONs): Development, Surface Modification and Applications in Chemotherapy. *Adv. Drug Deliver. Rev.* **2011**, *63*, 24-46.

6. Fragouli, D.; Torre, B.; Villafiorita-Monteleone, F.; Kostopoulou, A.; Nanni, G.; Falqui, A.; Casu, A.; Lappas, A.; Cingolani, R.; Athanassiou, A., Nanocomposite Pattern-Mediated Magnetic Interactions for Localized Deposition of Nanomaterials. *ACS Appl. Mater. Interfaces* **2013**, *5*, 7253-7257.

7. Leigh, S. J.; Purssell, C. P.; Bowen, J.; Hutchins, D. A.; Covington, J. A.; Billson, D. R., A Miniature Flow Sensor Fabricated by Micro-Stereolithography Employing a Magnetite/Acrylic Nanocomposite Resin. *Sens. Actuators, A* **2011**, *168*, 66-71.

8. Jun, Y. W.; Lee, J. H.; Cheon, J., Chemical Design of Nanoparticle Probes for High-Performance Magnetic Resonance Imaging. *Angew. Chem. Int. Edit.* **2008**, *47*, 5122-5135.

9. Sitthichai, S.; Pilapong, C.; Thongtem, T.; Thongtem, S., CMC-Coated $Fe_3O_4$ Nanoparticles as New MRI Probes for Hepatocellular Carcinoma. *Appl. Surf. Sci.* **2015**, *356*, 972-977.

10. Li, Z.; Wang, S. X.; Sun, Q.; Zhao, H. L.; Lei, H.; Lan, M. B.; Cheng, Z. X.; Wang, X. L.; Dou, S. X.; Lu, G. Q., Ultrasmall Manganese Ferrite Nanoparticles as Positive Contrast Agent for Magnetic Resonance Imaging. *Adv. Healthc Mater.* **2013**, *2*, 958-964.

11. Lee, J. H.; Huh, Y. M.; Jun, Y.; Seo, J.; Jang, J.; Song, H. T.; Kim, S.; Cho, E. J.; Yoon, H. G.; Suh, J. S.; Cheon, J., Artificially Engineered Magnetic Nanoparticles for Ultra-Sensitive Molecular Imaging. *Nat. Med.* **2007**, *13*, 95-99.

12. Xie, Y. J.; Yan, B.; Xu, H. L.; Chen, J.; Liu, Q. X.; Deng, Y. H.; Zeng, H. B., Highly Regenerable Mussel-Inspired Fe3O4@Polydopamine-Ag Core-Shell Microspheres as Catalyst and Adsorbent for Methylene Blue Removal. *ACS Appl. Mater. Interfaces* **2014**, *6*, 8845-8852.

13. Laurent, S.; Dutz, S.; Hafeli, U. O.; Mahmoudi, M., Magnetic Fluid Hyperthermia: Focus on Superparamagnetic Iron Oxide Nanoparticles. *Adv. Colloid Interface Sci.* **2011**, *166*, 8-23.

14. Shi, W.; Liu, X. Y.; Wei, C.; Xu, Z. C. J.; Sim, S. S. W.; Liu, L. B.; Xu, C. J., Micro-Optical Coherence Tomography Tracking of Magnetic Gene Transfection Via Au-$Fe_3O_4$ Dumbbell Nanoparticles. *Nanoscale* **2015**, *7*, 17249-17253.

15. Lartigue, L.; Alloyeau, D.; Kolosnjaj-Tabi, J.; Javed, Y.; Guardia, P.; Riedinger, A.; Pechoux, C.; Pellegrino, T.; Wilhelm, C.; Gazeaut, F., Biodegradation of Iron Oxide Nanocubes: High-Resolution In Situ Monitoring. *ACS Nano* **2013**, *7*, 3939-3952.

16. Dolatkhah, A.; Wilson, L. D., Magnetite/Polymer Brush Nanocomposites with Switchable Uptake Behavior Toward Methylene Blue. *ACS Appl. Mater. Interfaces* **2016**, *8*, 5595-5607.

17. Kim, D. H.; Vitol, E. A.; Liu, J.; Balasubramanian, S.; Gosztola, D. J.; Cohen, E. E.; Novosad, V.; Rozhkova, E. A., Stimuli-Responsive Magnetic Nanomicelles as Multifunctional Heat and Cargo Delivery Vehicles. *Langmuir* **2013**, *29*, 7425-7432.

18. Esmaeilnejad-Ahranjani, P.; Kazemeini, M.; Singh, G.; Arpanaei, A., Study of Molecular Conformation and Activity-Related Properties of Lipase Immobilized onto Core-Shell Structured Polyacrylic Acid-Coated Magnetic Silica Nanocomposite Particles. *Langmuir* **2016**, *32*, 3242-3252.

19. Kao, J.; Xu, T., Nanoparticle Assemblies in Supramolecular Nanocomposite Thin Films: Concentration Dependence. *J. Am. Chem. Soc.* **2015**, *137*, 6356-6365.

20. Zhang, J. Y.; Santos, P. J.; Gabrys, P. A.; Lee, S.; Liu, C.; Macfarlane, R. J., Self-Assembling Nanocomposite Tectons. *J. Am. Chem. Soc.* **2016**, *138*, 16228-16231.

21. Kim, H.; Jeong, S. M.; Park, J. W., Electrical Switching between Vesicles and Micelles via Redox-Responsive Self-Assembly of Amphiphilic Rod-Coils. *J. Am. Chem. Soc.* **2011**, *133*, 5206-5209.

22. Yao, K. J.; Chen, Y.; Zhang, J.; Bunyard, C.; Tang, C. B., Cationic Salt-Responsive Bottle-Brush Polymers. *Macromol. Rapid Commun.* **2013**, *34*, 645-651.

23. Cobo, I.; Li, M.; Sumerlin, B. S.; Perrier, S., Smart Hybrid Materials by Conjugation of Responsive Polymers to Biomacromolecules. *Nat. Mater.* **2015**, *14*, 143-159.

24. Gu, H. B.; Huang, Y. D.; Zhang, X.; Wang, Q.; Zhu, J. H.; Shao, L.; Haldolaarachchige, N.; Young, D. P.; Wei, S. Y.; Guo, Z. H., Magnetoresistive Polyaniline-Magnetite Nanocomposites with Negative Dielectrical Properties. *Polymer* **2012**, *53*, 801-809.

25. Wei, H.; Gu, H.; Guo, J.; Wei, S.; Liu, J.; Guo, Z., Silica Doped Nanopolyaniline with Endured Electrochemical Energy Storage and the Magnetic Field Effects. *J. Phys. Chem. C* **2013**, *117*, 13000-13010.

26. Wang, X.; Lu, Q.; Wang, X.; Joo, J.; Dahl, M.; Liu, B.; Gao, C.; Yin, Y., Photocatalytic Surface-Initiated Polymerization on $TiO_2$ toward Well-Defined Composite Nanostructures. *ACS Appl. Mater. Interfaces* **2015**, 8, 538-546.

27. Zhou, H.; Kim, J. P.; Bahng, J. H.; Kotov, N. A.; Lee, J., Self- Assembly Mechanism of Spiky Magnetoplasmonic Supraparticles. *Adv. Funct. Mater.* **2014**, *24*, 1439-1448.

28. Ling, D.; Hyeon, T., Chemical Design of Biocompatible Iron Oxide Nanoparticles for Medical Applications. *Small* **2013**, *9*, 1450-1466.

29. Ma, L.; Wang, Q.; Islam, S. M.; Liu, Y.; Ma, S.; Kanatzidis, M. G., Highly Selective and Efficient Removal of Heavy Metals by Layered Double Hydroxide Intercalated with the $MoS_4^{2-}$ Ion. *J. Am. Chem. Soc.* **2016**, *138*, 2858-2866.

30. He, J.; Perez, M. T.; Zhang, P.; Liu, Y. J.; Babu, T.; Gong, J. L.; Nie, Z. H., A General Approach to Synthesize Asymmetric Hybrid Nanoparticles by Interfacial Reactions. *J. Am. Chem. Soc.* **2012**, *134*, 3639-3642.

31. Zhu, J. H.; Wei, S. Y.; Zhang, L.; Mao, Y. B.; Ryu, J. E.; Haldolaarachchige, N.; Young, D. P.; Guo, Z. H., Electrical and Dielectric Properties of Polyaniline-$Al_2O_3$ Nanocomposites Derived from Various $Al_2O_3$ Nanostructures. *J. Mater. Chem.* **2011**, *21*, 3952-3959.

32. Wei, H. G.; Gu, H. B.; Guo, J.; Wei, S. Y.; Liu, J. R.; Guo, Z. H., Silica Doped Nanopolyaniline with Endured Electrochemical Energy Storage and the Magnetic Field Effects. *J. Phys. Chem. C* **2013**, *117*, 13000-13010.

33. Chandra, V.; Park, J.; Chun, Y.; Lee, J. W.; Hwang, I. C.; Kim, K. S., Water-Dispersible Magnetite-Reduced Graphene Oxide Composites for Arsenic Removal. *ACS Nano* **2010**, *4*, 3979-3986.

34. He, H. B.; Li, B.; Dong, J. P.; Lei, Y. Y.; Wang, T. L.; Yu, Q. W.; Feng, Y. Q.; Sun, Y. B., Mesostructured Nanomagnetic Polyhedral Oligomeric Silsesquioxanes (POSS) Incorporated with Dithiol Organic Anchors for Multiple Pollutants Capturing in Wastewater. *ACS Appl Mater Interfaces* **2013**, *5*, 8058-8066.

35. Guo, N.; Liang, Y. M.; Lan, S.; Liu, L.; Zhang, J. J.; Ji, G. J.; Gan, S. C., Microscale Hierarchical Three-Dimensional Flowerlike TiO2/PANI Composite: Synthesis, Characterization, and Its Remarkable Photocatalytic Activity on Organic Dyes under UV-Light and Sunlight Irradiation. *J. Phys. Chem. C* **2014**, *118*, 18343-18355.

36. Lv, L. P.; Zhao, Y.; Vilbrandt, N.; Gallei, M.; Vimalanandan, A.; Rohwerder, M.; Landfester, K.; Crespy, D., Redox Responsive Release of Hydrophobic Self-Healing Agents from Polyaniline Capsules. *J. Am. Chem. Soc.* **2013**, *135*, 14198-14205.

37. Zhang, L.; Peng, H.; Kilmartin, P. A.; Soeller, C.; Tilley, R.; Travas-Seidic, J., Self-Assembled Hollow Polyaniline/Au Nanospheres Obtained by a One-Step Synthesis. *Macromol. Rapid Commun.* **2008**, *29*, 598-603.

38. Jang, J. S.; Ja, J.; Lim, B., Synthesis and Characterization of Monodisperse Silica-Polyaniline Core-Shell Nanoparticles. *Chem. Commun.* **2006**, 15, 1622-1624.

39. Zhou, W. D.; Yu, Y. C.; Chen, H.; DiSalvo, F. J.; Abruna, H. D., Yolk-Shell Structure of Polyaniline-Coated Sulfur for Lithium-Sulfur Batteries. *J. Am. Chem. Soc.* **2013**, *135*, 16736-16743.

40. Zhang, Y. J.; Lin, Y. W.; Chang, C. C.; Wu, T. M., Magnetic Properties of Hydrophilic Iron Oxide/Polyaniline Nanocomposites Synthesized by In Situ Chemical Oxidative Polymerization. *Synth. Met.* **2010**, *160*, 1086-1091.

41. Zhang, Z. M.; Wan, M. X.; Wei, Y., Highly Crystalline Polyaniline Nanostructures Doped with Dicarhoxylic Acids. *Adv. Funct. Mater.* **2006**, *16*, 1100-1104.

42. Rana, S.; Jadhav, N. V.; Barick, K. C.; Pandey, B. N.; Hassan, P. A., Polyaniline Shell Cross-Linked $Fe_3O_4$ Magnetic Nanoparticles for Heat Activated Killing of Cancer Cells. *Dalton Trans.* **2014**, *43*, 12263-12271.

43. Shimano, J. Y.; MacDiarmid, A. G., Polyaniline, a Dynamic Block Copolymer: Key to Attaining its Intrinsic Conductivity? *Synth. Met.* **2001**, *123*, 251-262.

44. Pouget, J. P.; Jozefowicz, M. E.; Epstein, A. J.; Tang, X.; Macdiarmid, A. G., X-Ray Structure of Polyaniline. *Macromolecules* **1991**, *24*, 779-789.

45. Park, H. W.; Kim, T.; Huh, J.; Kang, M.; Lee, J. E.; Yoon, H., Anisotropic Growth Control of Polyaniline Nanostructures and Their Morphology-Dependent Electrochemical Characteristics. *ACS Nano* **2012**, *6*, 7624-7633.

46. Hung, W. I.; Chang, C. H.; Chang, Y. H.; Wu, P. S.; Hung, C. B.; Chang, K. C.; Lai, M. C.; Hsu, S. C.; Wei, Y.; Jia, X. R.; Yeh, J. M., Self-Assembly Behavior of Amphiphilic Poly(amidoamine) Dendrimers with a Shell of Aniline Pentamer. *Langmuir* **2013**, *29*, 12075-12083.

47. Yao, Q.; Chen, L. D.; Zhang, W. Q.; Liufu, S. C.; Chen, X. H., Enhanced Thermoelectric Performance of Single-Walled Carbon Nanotubes/Polyaniline Hybrid Nanocomposites. *ACS Nano* **2010**, *4*, 2445-2451.

48. Riegel, I. C.; Eisenberg, A.; Petzhold, C. L.; Samios, D., Novel Bowl-Shaped Morphology of Crew-Cut Aggregates from Amphiphilic Block Copolymers of Styrene and 5-(N,N-Diethylamino)isoprene. *Langmuir* **2002**, *18*, 3358-3363.

49. Wang, J.; Kuang, M.; Duan, H. W.; Chen, D. Y.; Jiang, M., pH-Dependent Multiple Morphologies of Novel Aggregates of Carboxyl-Terminated Polymide in Water. *Eur. Phys. J. E* **2004**, *15*, 211-215.

50. Zhang, M.; Liu, L. Y.; Chang, W. X.; Li, J., Controllable and Reversible Dimple-Shaped Aggregates Induced by Macrocyclic Recognition Effect. *Langmuir* **2015**, *31*, 13581-13589.

51. Cruz-Silva, R.; Arizmendi, L.; Del-Angel, M.; Romero-Garcia, J., pH- and Thermosensitive Polyaniline Colloidal Particles Prepared by Enzymatic Polymerization. *Langmuir* **2007**, *23*, 8-12.

52. Bourgeat-Lami, E.; Guyot, A., Preparation of Monodisperse Polystyrene Particles Using Thiol-Ended Polyethylene Oxide Stabilizer in Dispersion Polymerization. *Poly Bul* **1995**, *35*, 691-696.

53. Huang, J.; Li, Q.; Li, D. N. A.; Wang, Y.; Dong, L. J.; Xie, H. A.; Wang, J.; Xiong, C. X., Fluxible Nanoclusters of Fe3O4 Nanocrystal-Embedded Polyaniline by Macromolecule-Induced Self-Assembly. *Langmuir* **2013**, *29*, 10223-10228.

54. Hao, R.; Xing, R. J.; Xu, Z. C.; Hou, Y. L.; Gao, S.; Sun, S. H., Synthesis, Functionalization, and Biomedical Applications of Multifunctional Magnetic Nanoparticles. *Adv. Mater.* **2010**, *22*, 2729-2742.

55. Kazim, S.; Jager, A.; Steinhart, M.; Pfleger, J.; Vohlidal, J.; Bondarev, D.; Stepanek, P., Morphology and Kinetics of Aggregation of Silver Nanoparticles Induced with Regioregular Cationic Polythiophene. *Langmuir* **2016**, *32*, 2-11.

56. Bell, O. A.; Wu, G. L.; Haataja, J. S.; Brommel, F.; Fey, N.; Seddon, A. M.; Harniman, R. L.; Richardson, R. M.; Ikkala, O.; Zhang, X.; Faul, C. F. J., Self-Assembly of a Functional Oligo(Aniline)-Based Amphiphile into Helical Conductive Nanowires. *J. Am. Chem. Soc.* **2015**, *137*, 14288-14294.

57. Lv, L. P.; Landfester, K.; Crespy, D., Stimuli-Selective Delivery of two Payloads from Dual Responsive Nanocontainers. *Chem. Mater.* **2014**, *26*, 3351-3353.

58. Magnusson, J. P.; Khan, A.; Pasparakis, G.; Saeed, A. O.; Wang, W. X.; Alexander, C., Ion-Sensitive "Isothermal" Responsive Polymers Prepared in Water. *J. Am. Chem. Soc.* **2008**, *130*, 10852-10853.

59. Inzelt, G.; Pineri, M.; Schultze, J. W.; Vorotyntsev, M. A., Electron and Proton Conducting Polymers: Recent Developments and Prospects. *Electrochim. Acta.* **2000**, *45*, 2403-2421.

60. Molla, M. R.; Prasad, P.; Thayumanavan, S., Protein-Induced Supramolecular Disassembly of Amphiphilic Polypeptide Nanoassemblies. *J. Am. Chem. Soc.* **2015**, *137*, 7286-7289.

61. Pandey, K.; Yadav, P.; Mukhopadhyay, I., Elucidating the Effect of Copper as a Redox Additive and Dopant on the Performance of a PANI Based Supercapacitor. *Phys. Chem. Chem. Phys.* **2015**, *17*, 878-887.

62. Ball, P.; Hallsworth, J. E., Water Structure and Chaotropicity: Their Uses, Abuses and Biological Implications. *Phys. Chem. Chem. Phys.* **2015**, *17*, 8297-8305.

63. Gibb, C. L. D.; Gibb, B. C., Anion Binding to Hydrophobic Concavity Is Central to the Salting-in Effects of Hofmeister Chaotropes. *J. Am. Chem. Soc.* **2011**, *133*, 7344-7347.

# CHAPTER 5

# Activated Release of Self-Healing Materials from Hydrogen Bonding-Gated Stimuli-Responsive Polyaniline Microparticles*

* This manuscript is under peer-review. A.D. performed all experimental work and wrote the manuscript. L.D.W. directed the study and revised the manuscript prior to publication.

## 5.1. Abstract

Salt-activated hydrogen bonding chemistry was exploited to develop responsive release systems for self-healing (guest) molecules from capsular polyaniline (PANI) particles. Payloads were physically entrapped within PANI microparticles constructed by an interface-templated polymerization, where responsive payload release was achieved using salt-dependent (sodium chloride) gradients. We propose a co-activation mechanism for release of guest molecules attributed to hydrogen bonding and polymer expansion. The release mechanism relies on a salt activator with cleavage of saline-responsive noncovalent interactions within the mesoporous particles. The responsiveness and materials release is co-activated by changes in polymer shell permeability, expansion and polymer shell hydrophobicity. Anion pair solvation and its concentration (degree of doping) play pivotal role on the ion-responsiveness, where NaCl stimuli offers a versatile method for triggering sustained release for advanced applications of enhanced anti-corrosion protection in harsh saline environments.

## 5.2. Introduction

Stimuli-responsive particles with externally triggerable activity and response constitute a growing research area in the design of smart gating devices for controlled delivery. Responsive materials can alter their chemical and/or physical properties upon external stimuli; therefore, the molecular structure can be tuned to achieve tailored controlled-release properties.[1,2] Core-shell polymer microcapsules with switchable morphology and responsiveness to external stimuli have been a popular theme in research.[1] Polymer capsules of this type have suitable controlled-release properties since the payload can be stabilized for a broad spectrum of guest materials.

Metals are readily undergo corrosion in aggressive environmental conditions such as the presence of moisture and chloride ions, resulting in detrimental effects on metallic surfaces.

Impermeable anti-corrosion coatings that act as a barrier for water and ions offer a straightforward solution. In cases where coatings are susceptible to damage, metal surfaces become exposed to water or salts, resulting in further corrosion. One possible strategy[3] for the design of coating with self-repair and anticorrosion surface properties employs microencapsulation of effective corrosion inhibitors within suitable carriers. Such types of carrier systems are responsive to corrosion environments such as pH, salt, humidity, and redox stimuli.[3-5] Nitrogen containing organic corrosion inhibitors are very effective and less harmful than $Cr^{VI+}$ based pigments or coatings. Furthermore, N-based coatings are not required in high concentration,[5] where self-healing monomers[3,5] are capable of efficient binding to metal and formation of polymerized protective surfaces that suppress corrosion reactions within the exposed domains via self-repair.

As a highly tunable conductive polymer, polyaniline has attracted significant attention due to its low monomer cost, high nitrogen content, unique physicochemical properties and reversibly controlled conversions.[6-8] In a previous study,[9] a *first example* was reported that doping emeraldine base (EB) form of polyaniline (PANI) with NaCl led to the formation of doped emeraldine salt (ES) with versatile salt-responsive PANI assemblies. The key thermodynamic requirement for the doping of PANI by $Na^+$ is the requirement of charge neutrality of amine groups by $Cl^-$ counterions in the final complex that yields complex stability. This new insight on salt-induced phase transitions provided the motivation herein to study the encapsulation of nitrogenous self-healing molecules within PANI particles and trace their release profile upon triggering by the corresponding stimuli. It can be inferred that responsive hollow particles for corrosion protection can be applied to deliver corrosion inhibitors or self-healing agents as a unique design strategy.

Based on the expectation that responsive PANI polymers may be well-suited for development of microparticles with salt-gated release property, PANI microcapsules were prepared herein to

store “self-healing agents” within the shell of such particles that can undergo sustained and environmentally triggerable release. The overall schematic mechanism for particles formation, shell cleavage, and interchangeable polymer structure is illustrated in Scheme 5.1a,b.

# 5.3. Experimental section

## 5.3.1. Materials

All chemicals were purchased from commercial suppliers and used as received. Aniline (ACS reagent, Sigma-Aldrich), Toluene (99.8%, Sigma-Aldrich), ammonium persulfate (98%, Sigma-Aldrich ), Sodium dodecyl sulfate (99%, Alfa Aesar), poly(vinyl alcohol) (98%, Sigma-Aldrich), dimethyl sulfoxide-$d_6$ (Cambridge Isotopes), 2-mercaptobenzothiazole (99.8%, Sigma-Aldrich), 2-mercaptobenzimidazole (99.8%, Sigma-Aldrich), Dimethyl terephthalate (Standard for quantitative NMR, Sigma-Aldrich) and benzotriazole (99.8%, Sigma-Aldrich).

## 5.3.2. Synthesis of particles and materials loading

A mixture of toluene (2.46 mL) and aniline (0.2 mL) was added into a 50 mL round bottom flask charged with 25 mL aqueous solution containing 125 mg Sodium dodecyl sulfate (SDS) and dissolved self-healing agents. In order to achieve efficient encapsulation, we used saturated solutions of materials in water for MBT, MBI and BTA. The concentrations of MBT, MBI and BTA in aqueous solution were 1, 0.43 and 1 mg/mL respectively. The mixture was homogenized at 60 ˚C using ultrasonication for 30 min. After emulsification 1 mL polyvinyl alcohol (10% w/w) was added to the mini-emulsion and the resulting milk-like emulsion was magnetically stirred for 30 min under ice cooling. Then 3.5 mL of ammonium persulfate (APS) (0.75 mg/mL) was prepared and added dropwise to the above mini-emulsion under ice-bath cooling. The color of emulsion

turned dark green gradually as APS added. The resulting capsules were isolated by centrifuge and rinsed three cycles with Millipore water and centrifuge.

### 5.3.3. Release experiments

For studying the release of materials, 40-50 mg of loaded particles were dispersed in 1 mL Millipore water and the dispersion was transferred into dialysis bag. Then the dialysis bag was immersed in 20 mL of 0.5 M sodium chloride solution. The solution was stirred at constant rate at room temperature and after certain time intervals a small volume of (300 µL) release medium was taken and diluted 10-fold in a quartz cuvette. The same amount of fresh water was added back into solution to keep the total volume constant. The concentration of materials at various time points were then measured using UV-Vis spectroscopy (Varian Cary 100 Scan spectrophotometer). Experiments were performed in triplicate.

### 5.3.4. Characterization and general techniques

TEM observations were conducted using a Hitachi HT-7700 electron microscope operating at an acceleration voltage of 80 kV. The sample for TEM observations was prepared by placing 10$\mu$L of diluted nanoparticles dispersions (~0.10% w/w) on copper grids coated with thin films of carbon and air dried before analysis. UV-vis spectra were collected using a Varian Cary 100 Scan spectrophotometer using 1 cm quartz cuvettes and the spectra of pure water or sodium chloride solution was used for baseline correction.

The surface area and pore structure properties of particles were measured in a Micromeritics ASAP 2020 (Norcross, GA) instrument. Briefly, a 1.0 g sample was degassed at an evacuation rate of 5 mmHg/s and at ~100 °C. Alumina (Micromeretics) was used to calibrate the instrumental parameters, where the estimated accuracy in SA was ±5%. The BET SA was determined from the

adsorption isotherm using 0.162 $nm^2$ for gaseous molecular nitrogen. The Barret-Joyner-Halenda method was used to estimate the pore volume/pore diameter and micropore SA.

NMR spectra were acquired on a Bruker 500 MHz NMR spectrometer using a 30° observation pulse, 1k scans and relaxation delay of 60.0 s operated in the Fourier transform mode. DMSO-$d_6$ was used as the solvent. To evaluate the encapsulation efficiency, 6 mg of capsules were dissolved in 1 mL DMSO-$d_6$ for 24 h and 1 mg of internal standard TPH was added. The signals corresponding to the self-healing materials BTA ($2H_{aro}$, $\delta$ =7.91 *ppm*), MBI (-SH, $\delta$ =12.53 *ppm*) and MBT (-SH, $\delta$ =13.80 *ppm*) were integrated and compared to the internal standard PTH signal ($4H_{aro}$, $\delta$ =8.08 *ppm*). The mole ratio of ($n_s/n_i$) of sample (*s*) and internal standard (*i*) are obtained by using their respective integral areas of sample ($I_s$) and internal standard ($I_i$) and considering he number of nuclei (*N*) contributing to the signal (Eq. 5.1):[19, 20]

$$\frac{n_s}{n_i} = \frac{I_s}{I_i} \times \frac{N_i}{N_s} \tag{5.1}$$

The inhibitor loading % was calculated using Eq. 5.2.

$$Loading\ \% = \left[\frac{Weight\ of\ minhibitor\ in\ microcapsules}{weight\ of\ microcapsules}\right] \times 100 \tag{5.2}$$

Percentage of release calculated using Eq. 5.3.

$$Percentage\ of\ release = \left[\frac{Weight\ of\ inhibitor\ released\ into\ solution}{weight\ of\ inhibitor\ in\ microcapsules}\right] \times 100 \tag{5.3}$$

## 5.4. Results and discussion

Polymeric capsules are produced by using o/w miniemulsion[10] which utilizes dispersed liquid droplets and interfaces as template in continues phase that contains excess surfactants. The procedure is depicted in Scheme 5.1a. A liquid pair of aqueous and water-immiscible organic solvent is essential for the development of o/w emulsions. The underlying hypothesis herein asserts that nitrogenous molecular species would be preferentially entrapped in hollow PANI capsules during emulsion-templated encapsulation. In turn, the payload contents would be released in response to the salt (NaCl) dopant when the PANI shell is complexed with the cation ($Na^+$).[9] Polyaniline was polymerized in a dispersed phase containing saturated levels of self-healing materials in aqueous solution. The concentration of guest materials in aqueous solution were 1 mg/mL (MBT), 0.43 mg/mL (MBI) and 1 mg/mL (BTA). Oxidative polymerization of aniline with ammonium persulfate as the oxidant source was utilized to form PANI capsules.[9,11,12] When toluene was added into water solution that is saturated with self-healing guest materials, water-organic two phase system formed where the heavier aqueous phase resided at the bottom and the lighter toluene layer was above. Payloads and aniline preferentially partition in the dispersed organic phase due to their higher miscibility and continues aqueous phase contains a small amount of monomer and organic payload. After emulsification by ultrasonic aided treatment of the mixture, a milky homogeneous emulsion was obtained. Upon addition of APS, monomers present in aqueous phase react first with APS. Then, monomers in the toluene side of the interface diffuse to the o/w interface during the course of the reaction. Monomers and growing chains meet and react at the interface which acts as template, especially for chains growing from the monomers located at the toluene side of the interface.[13-15] As the polymer length reaches a critical size, the polymer is precipitated at the oil/water interface, where the self-healing guests are entrapped in

nanopores inside the PANI shell. Addition of co-surfactant (PVA) is essential to lower the rate of coalescence and the stability of polymer particles since the viscosity of a continuous phase significantly affects the stability of an emulsion droplet by hindering Ostwald ripening of the miniemulsion[13,16,17]

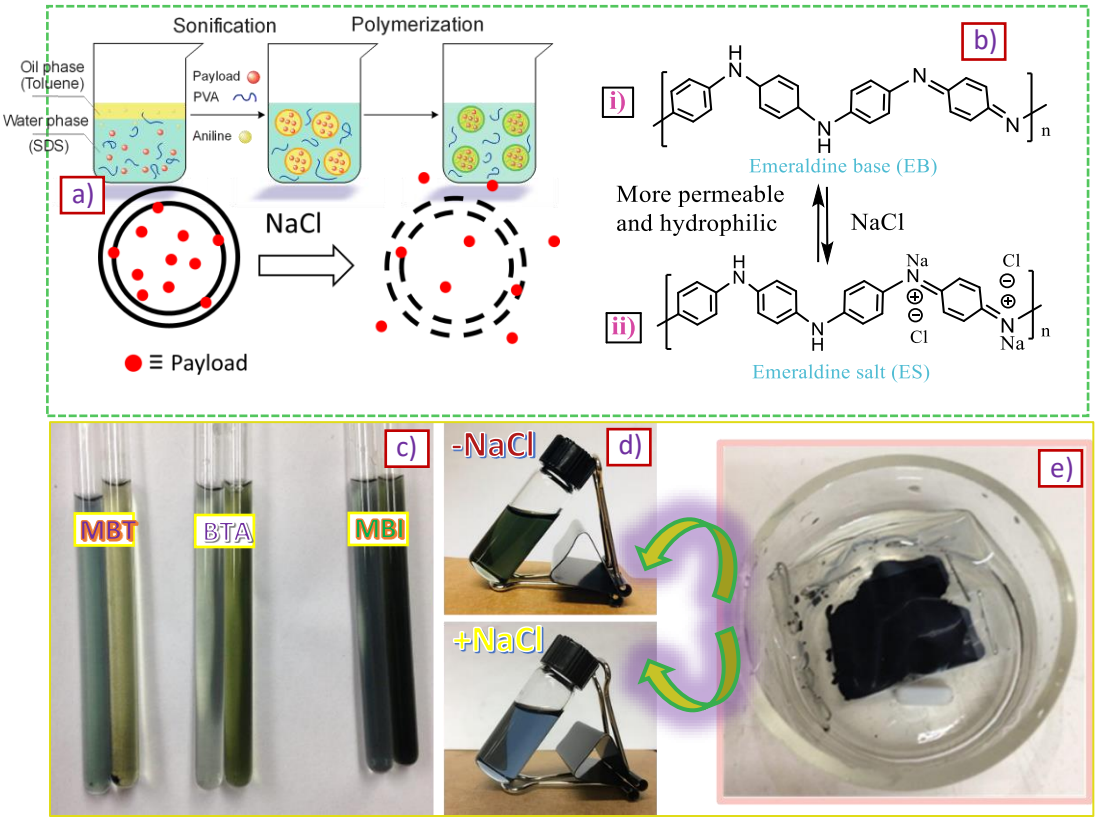


**Scheme 5.1.** a) Polymeric capsules were prepared using o/w miniemulsion and droplets interface as template. Illustration of salt-gated molecular transport through release into aqueous sodium chloride solution dialysis. b) Interchangeable PANI structure and emeraldine salt formation. c) Optical images of polymer particles dispersed in water and the color change, d) Solutions of MBT dissolved in NMP before (green) and after stimuli exposure (blue) in a dialysis bag (e).

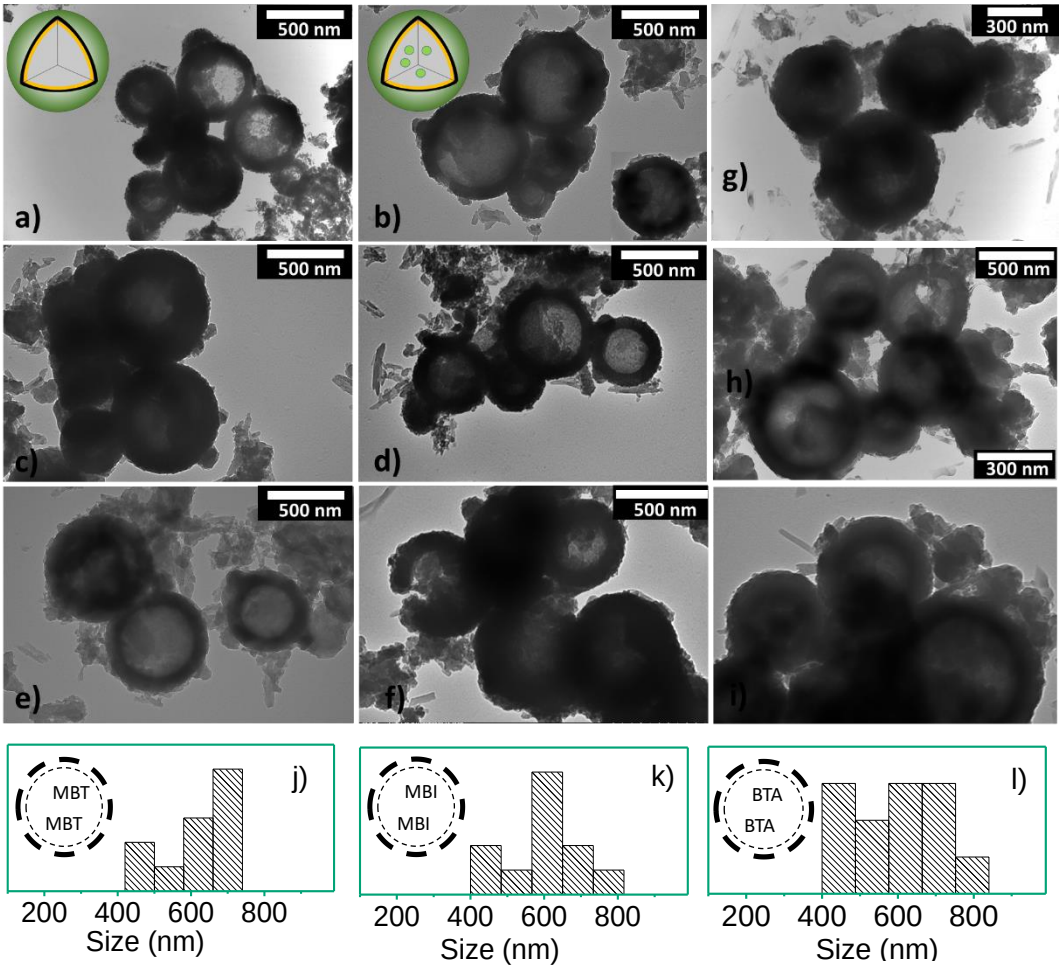


**Figure 5.1.** Nanocontainers consist of distinct core/shell structure and hollow nanocapsules morphology. TEM micrographs of the stimuli-responsive PANI nanocapsules (a) loaded with MBT materials (c,e) MBI (b,d,f) and BTA (g,h,i). The insets in the upper left-hand corners, a schematic depiction of nanocontainer with payload and without payload and schematic of core/shell morphology. (j-l) size histograms of particles.

The morphology of core-shell hollow particles was identified by TEM and the corresponding images are shown in Figure 5.1a-i. The well-defined core with outer shell structure can clearly be observed. The average size of particles was between 400-700 nm. The relatively large size and the size distribution of particles observed in TEM (Figure 5.1j-l) clearly indicate the mini-emulsion became destabilized during the polymerization due to the high ionic strength in the dispersion system. Furthermore, nitrogen adsorption/desorption results confirm that materials have mesoporous structure with relatively high surface area and small pores with can capture self-

healing materials within the small mesopores of PANI, along with gating effects associated with hydrogen bonding that prevent material diffusion after shell formation. The Brunauer-Emmett-Teller specific surface area, pore radius distribution center, and total pore volume are found to be 77.9 $m^2 g^{-1}$ (74.2 $m^2 g^{-1}$ for MBT loaded particle), 1.5 nm, and 0.43 $cm^3 g^{-1}$, respectively for the particles shown in Fig. 2a-c. After exposure to the corresponding stimuli, capsules were dried and dissolved in N-methyl-2-pyrrolidone (NMP) along with particles at ambient conditions in the absence of salt (NaCl). The color of NMP solution of original PANI capsules dialyzed at such ambient conditions were green. Furthermore, upon salt doping, the NMP solution became blue (Scheme 5.1b, and photographs of NMR tubes) which is attributed to the change in electronic transitions of PANI.[18]

To quantify the loading level of guests within particles and encapsulation efficiency, quantitative proton NMR (qNMR) spectroscopy was used with dimethyl terephthalate (TPH) as the internal standard. The qNMR method has been shown to be a reliable, convenient, precise, rapid and reproducible analytical tool for small molecule quantitation.[19-23] $^1$H NMR spectral results (Figure 5.2) of the guest molecules, PANI, and the guest loaded PANI samples were obtained. The guest loading efficiency (PANI/load wt.%) were estimated: 5% (MBT), 6% (BTA) and 8% (MBI). Among these systems, MBI had the highest encapsulation efficiency (see Appendix for calculations).

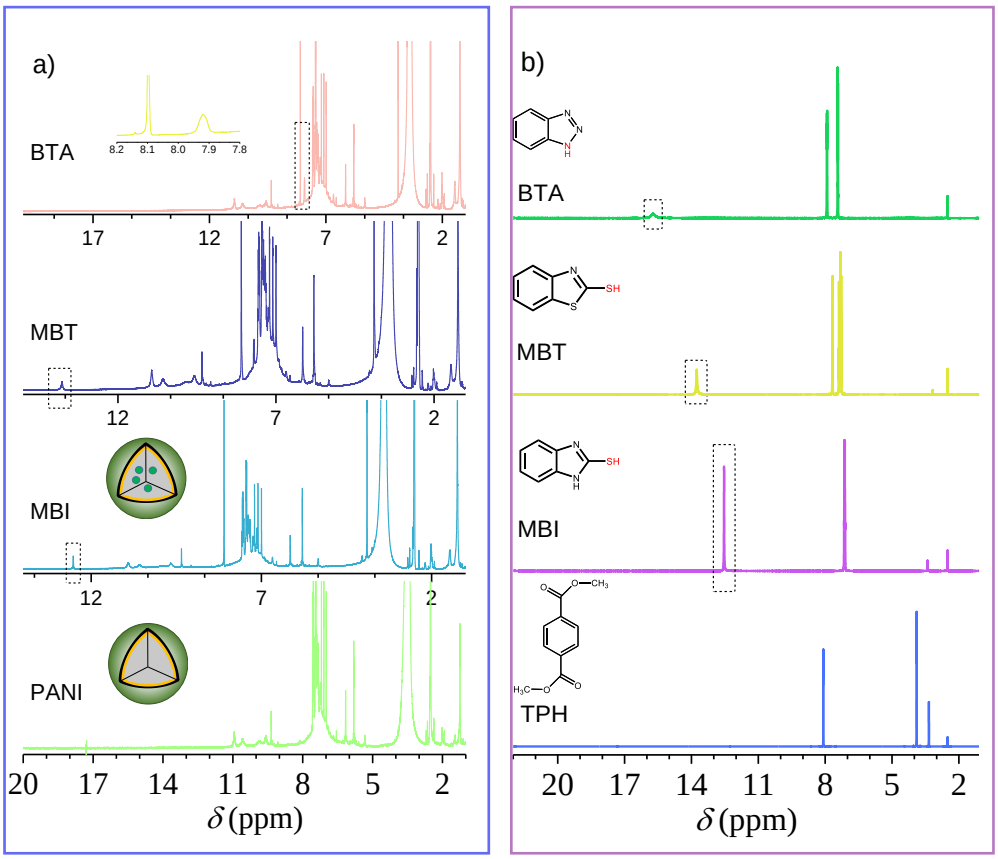


**Figure 5.2.** $^{1}$H NMR spectra recorded (500 MHz, 293 K) for (a) PANI and particles loaded with guest materials (in DMSO-$d_6$) with DMT as internal standard for quantification of payloads (b) Internal standard and load materials (in DMSO-$d_6$).

To assess the feasibility of the proposed release, we carried out controlled sodium chloride-triggered release of the encapsulated self-healing agents. One possible application of the salt responsive PANI capsules with a nanosized shell is the release of self-healing materials for corrosion protection strategies.[4,5] Nanoscale PANI spheres provide a large interfacial area for the interaction of ions. The mechanism of salt activated release is based on cation doping of PANI. For this purpose, the loaded polymer dispersions were dialyzed against 0.5 M NaCl solution (Scheme 5.1b). To evaluate the stimuli-triggered release performance, we chose nitrogen-based oxidation inhibitors as the guest molecules. The optical absorbance of MBT, BTA and MBI is reported to be at various wavelengths ($\lambda_{max}$): 320, 265 and 300 nm, respectively. After centrifugal

separation from Millipore water and drying, the capsules were dialyzed against a sodium chloride medium. Typically, capsules were dispersed in water (ca. 40-50 mg of in 1 mL) and were placed inside a dialysis membrane (Membra-Cel™, MWCO 14000) that was immersed into 20 mL of 0.5 M aqueous NaCl. Periodically, a 300 μL aliquot of external release solution was removed and replaced with fresh NaCl solution of the same volume. Then, the concentration of the released guest was diluted to 3 mL in a quartz cuvette and was traced by measuring the UV-vis absorbance at variable time intervals over a 48 h period against the respective calibration curves at the appropriate $\lambda_{max}$ value (Figure A.21). Figures 5.3a,b and 5.4a show the time-dependent release profiles of the inhibitors. These guest materials were found to be slightly leaky to the BTA in the absence of the corresponding stimuli in pure Millipore water. For the two other guest molecules it can clearly be observed that the PANI containers hold the self-healing materials adequately at ambient conditions (without any doping salt) and a flat baseline, where less than 10% leaching was observed over time. The release rate of the guests from the particles was accelerated after salt exposure with the PANI particles. Materials that were exposed to salt began releasing materials after 4 h when compared with the control system, suggesting that responsive release in aqueous media was achieved successfully.

Evidently, as time interval increased for the dispersion, a greater release efficiency enhanced, where a greater amount of material was released more rapidly into the dialysis solution. Notably, there was no significant release for all three systems within the first 4 h which suggests that no physical surface adsorption occurred during materials loading.[24] The total MBT release reached to 64.1% within 48 h (Figure 5.4a). Similar results were observed for particles containing MBI and BTA which released 40.7% and 56.1% of its contents respectively over the same time period (Figures 5.3a,b). Using appropriate calibration curves it was calculated that the concentration of

materials reached to 2.03 mg/mL (MBT), 2.32 mg/mL (BTA) and 0.70 mg/mL (MBI). These levels were much higher than that for particles without salt exposure, where a summary of these results is given in Figure 5.4b. The sigmoidal-shaped release curves are presumably the result of cooperative release. This effect is attributed to the cleavage of intramolecular hydrogen bonding within the shell and full opening of the mesopores activated by ions. The release kinetics can also be affected by the particle dimensions and the shell wall thickness. The initial induction stage (region I) occurs when salt interacts with the EB form of PANI. Once PANI is salt-doped, greater water diffusion and shell permeability occurs, where more pores become accessible for water diffusion. This process leads to a sharp increase in release rate observed in region II of Figure 5.3a. Thereafter, the release rate decreases in region III after most of the guest molecules have been released into solution from the particles.

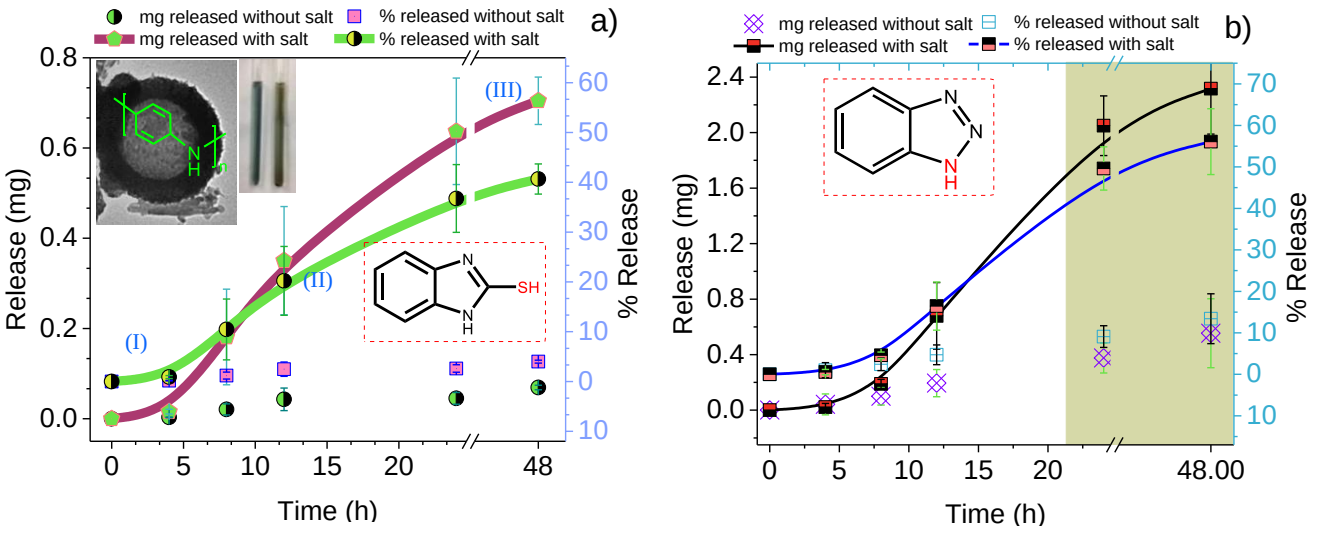


**Figure 5.3.** Salt concentration-activated release profiles and % release of payloads from microcapsule constructs when exposed to 20 mL 0.5 M aqueous NaCl. (a) MBI and (b) BTA. In normal conditions and without salt there is no leakage observed for the materials (control sample); however, materials release is activated upon change in environment. From qNMR measurements, the amount of guest in capsules were 3% wt. for MBT and BTA. The data points represent the average value of 3 measurements and the error bars reflect standard deviations from three experiments.

Thus, it was inferred that sodium chloride regulates the hydrogen bonding within the PANI shell via a salt-gating polymer disassembly process. The increase in the release rate of the materials upon receiving stimuli is most likely the result of a change in permeability, wettability and hydrophilicity of the PANI shells[25,26] of the capsules upon $Na^+$ complexation. The release rates have contributions that arise from several factors. Salt doping of PANI transforms it into more hydrophilic and flexible chain via change in its electronic structure, which aids in greater motional dynamics of the aromatic rings through conversion of double bonds,[18] result in greater permeability toward hydrophilic species.[25] The emeraldine salt PANI (HCl doped) has high permeability towards NaCl compared to the de-doped EB-form of PANI.[25]

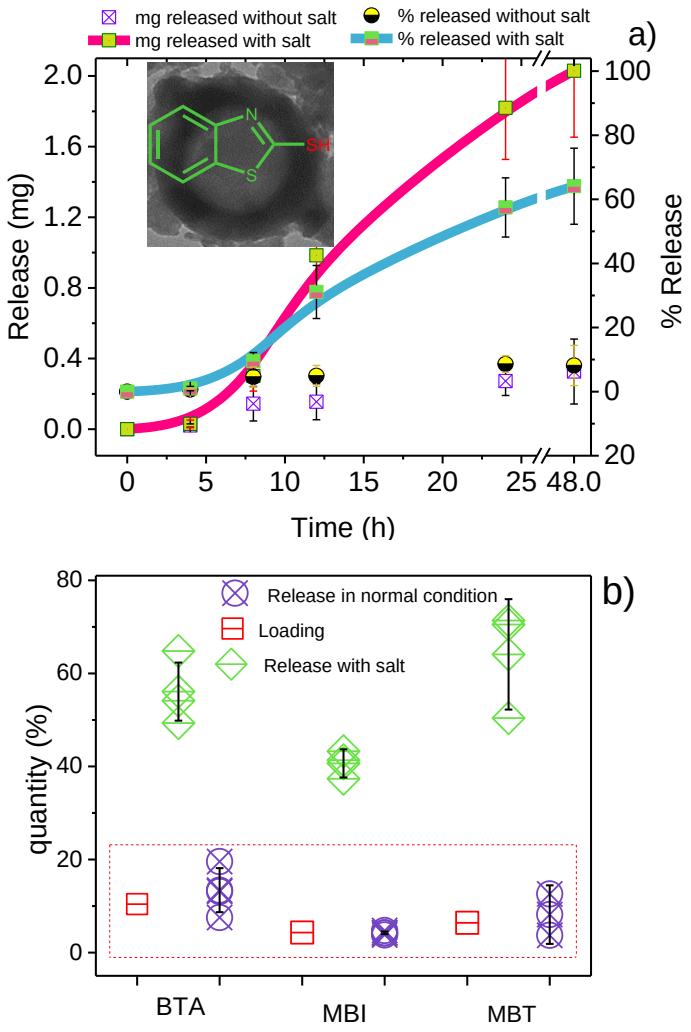


**Figure 5.4.** Stimuli-induced release profiles and % release of payloads from microcapsule constructs with and without salt exposure for (a) MBT. The concentration of guest in capsules was 2% wt. (b) summary and comparison of release with and without salt vs. loading efficiency.

In another respect, PANI capsules exhibited lower MBT release at higher pH values due to a limited ion permeability, where water and negatively charged ions are expelled from the shell structure.[26] This is inferred due to the different ability of anions ($Cl^-$ *vs.* $OH^-$) to form thermodynamically favorable interactions with cation-PANI complexes. $OH^-$ is a kosmotrope (order maker) and is highly hydrated versus a chaotropic anion like $Cl^-$ (disorder maker), where such hydration effects provide an account of the relative stability of the PANI-$Na^+$ complex (*$H_2O$-*

*OH*$^{-}$ int. > *H*$_2$*O-Cl*$^{-}$ int.). Upon doping with $Na^+$, PANI exist in the emeraldine salt form and the minimum requirement for thermodynamic stability of this polyelectrolyte is the presence of $Cl^-$ counter ions within $PANI^+$ to maintain the charge neutrality. Therefore, the interaction of the kosmotrope ($OH^-$) anion with $PANI^+$ at elevated pH is more energetically unfavorable than the chaotropic $Cl^-$ that stabilizes doped PANI.

In doped form, PANI behavior that is similar to polyelectrolytes,[2] where an increased ion concentration gradient creates osmotic pressure that is accompanied by greater water diffusion into the polymer shell with an enormous increase in polymer volume and its shell expansion.[27] The level of water diffusion inside the polymer shell depends on the type on ions according to the Hofmeister solvation, along with the concentration of ions (degree of doping) inside the shells. Presumably, the presence of excess ions within the PANI shell produces greater osmotic pressure[27] that forces water molecules to enter polymer shell that cooperatively enhances guest release.[26-28] The emeraldine base form of PANI is more compact as compared with the leucoemeraldine base form of PANI since strong hydrogen bonding is favoured for the EB-form.[29] Notably, upon cation doping of PANI, it leads to the formation of more single bond (benzenoid) structure for PANI that affords greater motional dynamics. Undoped PANI has been reported to have a very dense and hydrophobic nature as determined by limited salt permeation rates in its undoped state.[25] Cleavage of the H-bonding that constitute the polymeric capsule shell yields greater dynamics of polymer motion. This results in opening of pathways that allow for diffusion of molecules and expelling guest payload out of the mesopores of the capsules. Release of the contents from particles occurs with sigmoidal release profiles that indicates a co-activation interaction process occurs between ions and the polymer shell.[30] PANI containers that are exposed into dialysis solution respond to ions through a cooperative interaction as the polymeric shell undergoes dissociation. Therefore,

we propose that two primary mechanisms contribute to the observed sigmoidal-shaped release curve. Firstly, ions that interact with the polymer shell to weaken the hydrogen bonding interactions.[9,29] Secondly, the osmotic pressure and water diffusion is activated by ions within the polymer shell.[11] These effects provide a plausible explanation that accounts for the salt responsiveness of PANI materials for responsive triggered delivery that is based on a cooperative mechanism, as observed in Figures 5.3a,b and 5.5a.

## 5.5. Conclusion

In summary, we demonstrate the development of a versatile and environmentally-switchable chemical gate for polyaniline in its emeraldine base form. The PANI-salt system can undergo sustained responsive release of self-healing materials as a result of polymer structural changes upon salt exposure. In particular, we report a co-activation type of response for guest release; where salt-dependent cleavage of hydrogen bonding within the PANI shell via an activator fascilitates cooperative release of guest molecules by; *i)* enhanced dynamic motion of polymer; *ii)* increased osmotic pressure within polymer shell, polymer enlargement and increase in hydrophilicity and volume of polymer, *iii)* enhanced permeability and full opening of pores upon polymer expansion. Cations that undergo binding with nitrogen donor groups have greater hydrophiliity, where the counter anions pairs with the bound cation to form energetically favorable co-activator complex  Furthermore, the solvation ability is understood on the basis of the Hofmiester effect for anion solvation, where it plays a critical role on the stabilization of the PANI-cation co-activator system.

Nitrogen containing corrosion inhibitors, even at low concentration, are very effective in corrosion inhibition. Consequently, the cooperative and activatable release reported herein opens

promising alternatives in the exploration of self-healing materials for corrosion protection in aggressive saline environments.

# 5.7. References


1. DiLauro, A. M.; Abbaspourrad, A.; Weitz, D. A.; Phillips, S. T., Stimuli-Responsive Core–Shell Microcapsules with Tunable Rates of Release by Using a Depolymerizable Poly(phthalaldehyde) Membrane. *Macromolecules* **2013**, *46*, 3309-3313.

2. Dolatkhah, A.; Wilson, L. D., Magnetite/Polymer Brush Nanocomposites with Switchable Uptake Behavior Toward Methylene Blue. *ACS Appl. Mater. Interfaces* **2016**, *8*, 5595-5607.

3. Huang, Y.; Deng, L.; Ju, P.; Huang, L.; Qian, H.; Zhang, D.; Li, X.; Terryn, H. A.; Mol, J. M. C., Triple-Action Self-Healing Protective Coatings Based on Shape Memory Polymers Containing Dual-Function Microspheres. *ACS Appl. Mater. Interfaces* **2018**, *10*, 23369-23379.

4. Joshi, A.; Abdullayev, E.; Vasiliev, A.; Volkova, O.; Lvov, Y., Interfacial Modification of Clay Nanotubes for the Sustained Release of Corrosion Inhibitors. *Langmuir* **2012**, *29*, 7439-7448.

5. Abdullayev, E.; Abbasov, V.; Tursunbayeva, A.; Portnov, V.; Ibrahimov, H.; Mukhtarova, G.; Lvov, Y., Self-Healing Coatings Based on Halloysite Clay Polymer Composites for Protection of Copper Alloys. *ACS Appl. Mater. Interfaces* **2013**, *5*, 4464-4471.

6. Gawron, E. L.; Hira, S. M.; Josowicz, M.; Janata, J., Effects of Palladium(II) Chlorocomplex Speciation on the Controlled Interaction with a Polyaniline Film in Acid. *Langmuir* **2017**, *33*, 11930-11935.

7. Dimitriev, O. P., Doping of Polyaniline by Transition-Metal Salts. *Macromolecules* **2004**, *37*, 3388-3395.

8. Dolatkhah, A.; Jani, P.; Wilson, L. D., Redox-Responsive Polymer Template as an Advanced Multifunctional Catalyst Support for Silver Nanoparticles. *Langmuir* **2018**, 34, 10560-10568.

9. Dolatkhah, A.; Wilson, L. D., Salt-Responsive Fe3O4 Nanocomposites and Phase Behavior in Water. *Langmuir* **2017**, 34, 341-350

10. Salaun, F., Microencapsulation by Interfacial Polymerization. *Encapsulation Nanotechnologies*, Mittal, V. Ed, New Jersy, Wiley-Scrivener. **2013**, 137-173.

11. Lv, L.-P.; Zhao, Y.; Vilbrandt, N.; Gallei, M.; Vimalanandan, A.; Rohwerder, M.; Landfester, K.; Crespy, D., Redox Responsive Release of Hydrophobic Self-Healing Agents from Polyaniline Capsules. *J. Am. Chem. Soc.* **2013**, *135*, 14198-14205.

12. Mohamed, M. H.; Dolatkhah, A.; Aboumourad, T.; Dehabadi, L.; Wilson, L. D., Investigation of Templated and Supported Polyaniline Adsorbent Materials. *RSC Adv.* **2015**, *5*, 6976-6984.

13. Gaitzsch, J.; Huang, X.; Voit, B., Engineering Functional Polymer Capsules Toward Smart Nanoreactors. *Chem. Rev.* **2015**, *116*, 1053-1093.

14. Dallas, P.; Georgakilas, V., Interfacial Polymerization of Conductive Polymers: Generation of Polymeric Nanostructures in a 2-D Space. *Adv. Colloid Interface Sci.* **2015**, *224*, 46-61.

15. Tran, H. D.; D'Arcy, J. M.; Wang, Y.; Beltramo, P. J.; Strong, V. A.; Kaner, R. B., The Oxidation of Aniline to Produce "Polyaniline": A Process Yielding Many Different Nanoscale Structures. *J. Mater. Chem.* **2011**, *21*, 3534-3550.

16. Lu, X.; Katz, J. S.; Schmitt, A. K.; Moore, J. S., A Robust Oil-in-Oil Emulsion for the Nonaqueous Encapsulation of Hydrophilic Payloads. *J. Am. Chem. Soc.* **2018**, *140*, 3619-3625.

17. Vimalanandan, A.; Lv, L.-P.; Tran, T. H.; Landfester, K.; Crespy, D.; Rohwerder, M., Redox-Responsive Self-Healing for Corrosion Protection. *Adv. Mater.* **2013**, *25*, 6980-6984.

18. Jang, J.; Ha, J.; Lim, B., Synthesis and Characterization of Monodisperse Silica–Polyaniline Core–Shell Nanoparticles. *Chem. Commun.* **2006**, 1622-1624.

19. Bharti, S. K.; Roy, R., Quantitative $^{1}$H NMR Spectroscopy. *TrAC, Trends Anal. Chem.* **2012**, 35, 5-26.

20. Holzgrabe, U., Quantitative NMR Spectroscopy in Pharmaceutical Applications. *Prog. Nucl. Magn. Reson. Spectrosc.* **2010**, 57, 229-240.

21. Cañueto, D.; Salek, R. M.; Correig, X.; Cañellas, N., Improving Sample Classification by Harnessing the Potential of $^{1}$H-NMR Signal Chemical Shifts. *Sci. Rep.* **2018**, *8*, 11886-11893.

22. Sarpal, A. S.; Silva, S. R.; Silva, P. R. M.; Monteiro, T. V.; Itacolomy, J.; Cunha, V. S.; Daroda, R. J., Direct Method for the Determination of the Iodine Value of Biodiesel by

Quantitative Nuclear Magnetic Resonance (q$^1$H NMR) Spectroscopy. *Energy Fuels* **2015**, *29*, 7956-7968.

23. Simmler, C.; Napolitano, J. G.; McAlpine, J. B.; Chen, S.-N.; Pauli, G. F., Universal Quantitative NMR Analysis of Complex Natural Samples. *Curr. Opin. Biotechnol.* **2014**, *25*, 51-59.

24. Ren, S.; Yang, J.; Ma, L.; Li, X.; Wu, W.; Liu, C.; He, J.; Miao, L., Ternary-Responsive Drug Delivery with Activatable Dual Mode Contrast-Enhanced in Vivo Imaging. *ACS Appl. Mater. Interfaces* **2018**, 10, 31947-31958.

25. Deligöz, H., Preparation of Self-standing Polyaniline-Based Membranes: Doping Effect on the Selective Ion Separation and Reverse Osmosis Properties. *J. Appl. Polym. Sci.* **2007**, *105*, 2640-2645.

26. Pirhady Tavandashti, N.; Ghorbani, M.; Shojaei, A.; Mol, J. M. C.; Terryn, H.; Baert, K.; Gonzalez-Garcia, Y., Inhibitor-loaded conducting polymer capsules for active corrosion protection of coating defects. *Corros. Sci.* **2016**, *112*, 138-149.

27. Roemer, M.; Kurzenknabe, T.; Oesterschulze, E.; Nicoloso, N., Microactuators Based on Conducting Polymers. *Anal. Bioanal.Chem.* **2014**, *373*, 754-757.

28. Bay, L.; Jacobsen, T.; Skaarup, S.; West, K., Mechanism of Actuation in Conducting Polymers: Osmotic Expansion. *J. Phys. Chem. B* **2001**, *105*, 8492-8497.

29. Kim, H.; Jeong, S.-M.; Park, J.-W., Electrical Switching between Vesicles and Micelles via Redox-Responsive Self-Assembly of Amphiphilic Rod−Coils. *J. Am. Chem. Soc.* **2011**, *133*, 5206-5209.

30. Tang, S.; Tang, L.; Lu, X.; Liu, H.; Moore, J. S., Programmable Payload Release from Transient Polymer Microcapsules Triggered by a Specific Ion Coactivation Effect. *J. Am. Chem. Soc.* **2017**, *140*, 94-97.

# CHAPTER 6

## 6.1. Integrated discussion of manuscript chapters

Water pollution and discharge of textile dyes have become a major environmental pollution.[1] To solve this issue, effective and fast dye removal from effluents prior to discharge is necessary. The overall objective of this thesis research was to design of nanocomposites based on stimuli-responsive polymers for the physical/chemical removal of organic dye pollutants from aqueous solution. This integrated discussion section links four thesis chapters and explains how these chapters address the general objectives of the thesis, as listed in section 1.6.1 in the introduction chapter. The manuscript chapters cover four areas of research (Figure 6.1) which are related to the design and fabrication of stimuli-responsive nanocomposites for treatment of two types of organic dyes MB, and 4-NPh under four main themes as described below (*cf.* Scheme 6.1):

1. ***Theme 1*****:** adsorptive removal of MB and MO through modification of chitosan and design of adsorbents based on chitosan and PANI (Chapters 2 , 4).
2. ***Theme 2:*** catalytic reduction of 4-NPh by hybridization of Ag NPs with PANI (Chapter 3).
3. ***Theme 3:*** mechanistic understanding of catalytic reduction of 4-NPh by PANI/Ag nanocatalysts (Chapter 3).
4. ***Theme 4:*** mechanistic study of MB/MO adsorption on chitosan- and PANI-based nanocomposite adsorbents (Chapters 4 , 5).

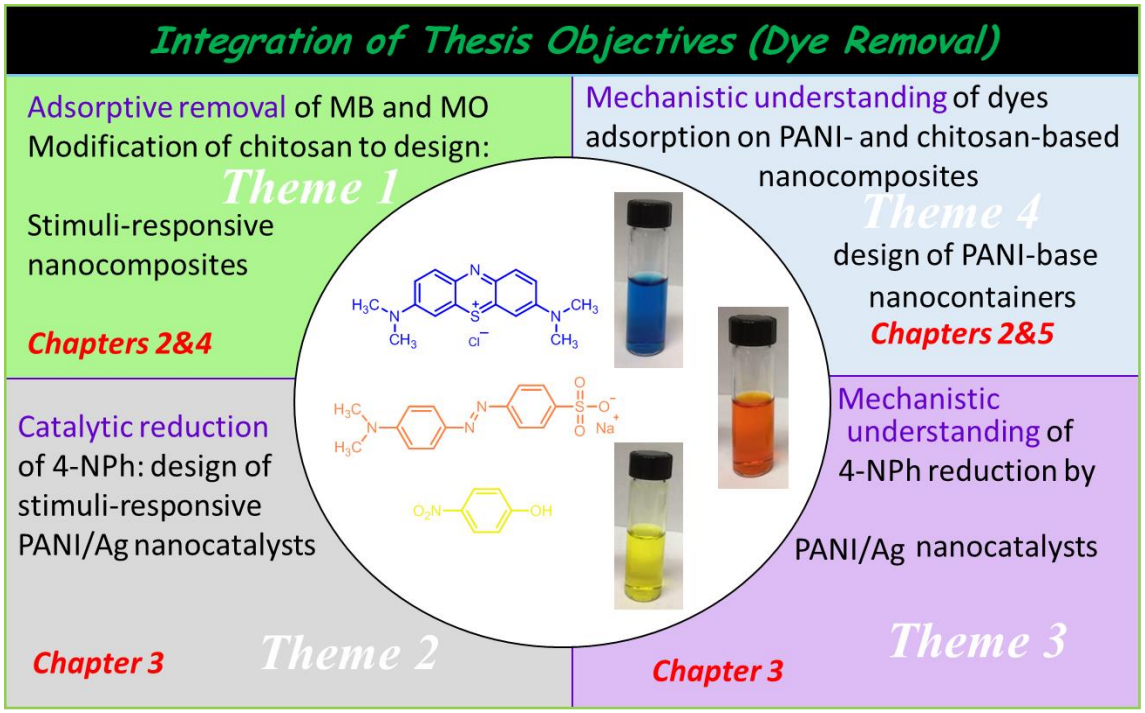


**Scheme 6.1.** Organization of the PhD Thesis objectives into four research themes and four chapters.

In the first approach, enhanced adsorption capacity of chitosan for MB removal from aqueous solution and an understanding the adsorption mechanism (Theme 1, 4) was addressed by rational design of polymer brush nanocomposites as outlined in section 2.4 (Chapter 2). To achieve this goal, polymer brushes containing a chitosan with PIA/PAA side chains were prepared. In order to further enhance MB adsorption on polymer brushes, materials were integrated onto the surface of MNPs. As a result, nano-adsorbent materials were fabricated and their detailed adsorption mechanism was studied, which relates to Theme 1 and 4 of this thesis (*cf*. Scheme 6.1). Prior to this work, a study by Ghorai et al.[2] revealed that grafting polyacrylamide onto xanthan gum and their composites with nanosilica yield adsorbents with excellent adsorption affinity for MB due to enhanced surface area and introduction of electrostatic interactions between MB and hydrolyzed polyacrylamide side chains.

In chapter 3, in order to address theme 2 and 3 of thesis objective, stimuli-responsive nanocatalyst systems were developed by hybridization of Ag NPs with PANI as support for reduction of 4-NPh to 4-APh in the presence of sodium borohydride. Results presented in section 3.4 affirmed that interfacing Ag NPs with redox-responsive PANI led to creation of electron pathways and charge transfer across PANI/Ag boundaries which is desirable for catalytic reduction reactions in the presence of borohydride. The results in section 3.4 revealed that for catalysts with higher PANI content (75% PANI relative to CHI, AgNP-CP75) rate constant per unit mass of catalyst reached 1.6 ($s^{-1}$ $g^{-1}$). This value is higher than that for pure silver NPs and other similar Ag nanocatalysts reported in literature (*cf.* table 6.2). Results from XPS spectroscopy (Section 3.4) revealed that enhancement in catalytic reduction activity of AgNP-CP75 is mainly due to increased charge ($H^-$) transfer across interface of Ag/PANI and electronic structure of AgNP-CP75 where PANI exists dominantly in PG form. Therefore, the results presented in chapter 3 address themes 2 and 3 of thesis by developing high performance catalysts (high activity and stability under consecutive regeneration cycles) and elaborating mechanism of reduction for the reductive removal of 4-NPh. In chapter 4, the work on MB adsorption was extended by designing PANI/MNP nanocomposites adsorbent materials. Mohamed et al.[3] previously reported PANI materials which are synthesized under various conditions to yield templated forms of PANI with variable morphology for the adsorption of MB. According to this report,[3] PANI nanostructure showed adsorption capacity of 85.4 mg $g^{-1}$ for MB in aqueous solution. To facilitate separation of adsorbents from aqueous solution, further enhance surface area of PANI adsorbents and understand mechanistic details on MB adsorption on PANI under theme 1 and 4, PANI/MNP nanocomposites were prepared. In order to increase stability and hydrodynamic volume in PANI adsorbents nanostructures, variable fractions of chitosan were added to nanocomposites.[4] Results

in chapter 4 (Section 4.4.4) concluded that PANI/MNP nanocomposites showed higher adsorption capacity for MB (108.7 mg $g^{-1}$) compared to PANI nanostructures reported previously.[3] Furthermore, PIONcx materials reported in chapter 4 have the advantage of selective MB adsorption over MO in a mixture of MO/MB solution (Section 4.4.4). To understand the mechanistic details of MB adsorption on PANI under theme 1 and 4 of thesis, it was demonstrated that PANI displays salt (NaCl)-responsive behavior (Section 4.4.4). This finding contributed to the MB adsorption mechanism and affirmed that MB interacts with PANI in a similar fashion to $Na^+$ in doped state (*cf.* Scheme 6.2). Above results presented in chapter 4 address theme 1 of thesis and partially address theme 4 on the understanding of MB adsorption by PANI adsorbent materials. However, DLS measurements revealed that interaction with salt leads to disruption of intermolecular hydrogen bonding within PANI adsorbents. From previous reports it has been demonstrated that PANI is a responsive polymer that has variable physicochemical properties depending on surrounding environment (pH, acid/base etc.).[4-6] However, unlike pH/redox-responsiveness[4,5] and acid-doping,[6] salt-responsive behavior in PANI had not been reported at the time of publication of this research (*Langmuir* **2018**, 34, 341. DOI: 10.1021/acs.langmuir.7b03613).[7] Therefore, the results from chapter 4 partially addressed theme 4 of thesis and led to the research project in chapter 5 to fully address theme 4 of thesis on mechanistic details of MB adsorption on PANI adsorbents. Chapter 5 was developed upon results from chapter 4 to complete the knowledge gap in theme 4 on understanding of adsorption mechanism of MB on PANI adsorbent materials. This knowledge gap was partially addressed in chapter 3, however, further understanding was required to fully understand the mechanism of MB and PANI interaction. Therefore, in chapter 5, in order to investigate disruption of hydrogen bonding in PANI, self-healing materials were loaded into PANI capsules and the effect of cation species on their release into solution was studied to

obtain a broader understanding of PANI adsorbents and their behavior upon interaction with NaCl in aqueous media as the second part of fourth theme of thesis objectives (Section 5.4).

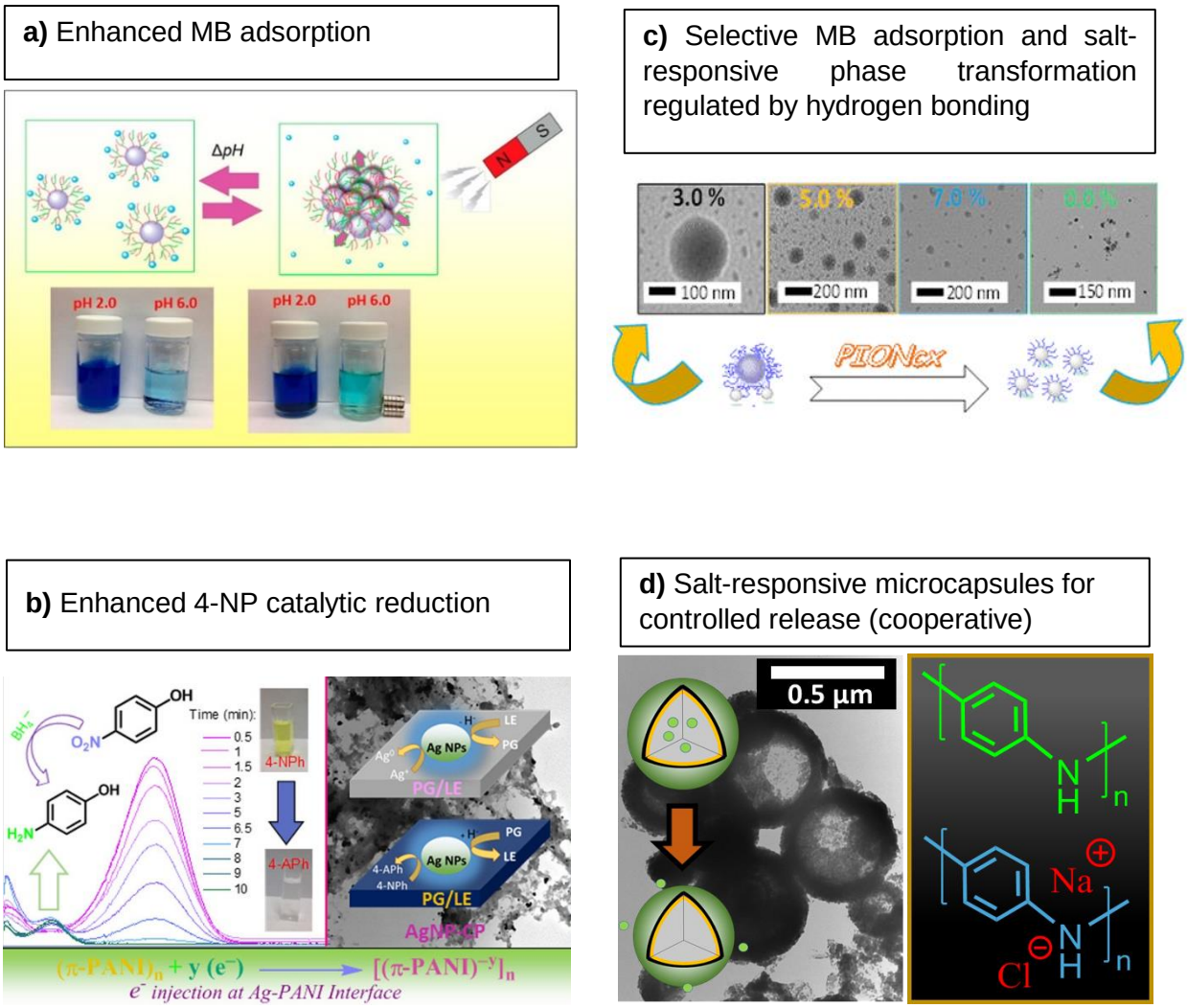


**Figure 6.1.** Outline of four projects in this thesis for chemical and physical MB and 4-NPh dyes treatment in aqueous solution by fabrication of stimuli-responsive nanocomposites. a) Design of magnetite/chitosan polymer brush nanocomposites ($Fe_3O_4$-PAAgCHI and $Fe_3O_4$-PAIgCHI) for MB adsorption. Reprinted with permission from reference[8] © 2016 American Chemical Society. b) 4-NPh catalytic reduction in the presence of $NaBH_4$ by designing PANI/Ag nanocomposites (AgNP-CP75). Reprinted with permission from reference[9] © 2018 American Chemical Society. c) Design of PANI/MNP nanocomposites (PIONc3) with higher surface area and easy manipulation for selective MB adsorption. Reprinted with permission from reference[7] © 2017 American Chemical Society. d) Mechanistic understanding of MB adsorption on PANI and its interaction with salt by designing PANI containers for salt triggered release of MBT, MBI and BTA guest molecules as function of salt and interaction with cation.

## 6.2. Summary

This thesis investigated various approaches to remove dyes from aqueous solution by fabricating inexpensive stimuli-responsive nanocomposites with overall high performance in dye removal from aqueous solutions. In this thesis, two approaches of adsorption and catalytic reduction were applied for the removal of MB and 4-NPh from aqueous solution. The studies presented in this dissertation contribute to structural modification of PANI and CHI polymers for MB and MO adsorption.

First, to overcome the low adsorption capacity and low surface area of chitosan, PIA and PAA were grafted onto the backbone of chitosan. In order to further enhance the surface area and dispersion of adsorbents, polymer brushes were coated onto the surface sites of magnetite via stable bridging bidentate interactions of the carboxylate groups of PIA and PAA. Therefore, pH-/magneto-responsive adsorption of MB using chitosan nanocomposites was achieved. Utilizing the two advantages of stimuli responsiveness and enhanced dye binding affinity of brushes, along with rapid magnetic separation of magnetite nanocrystals, the materials developed herein showed enhanced adsorption performance with MB. For example, in the case of $Fe_3O_4$-PAAgCHI nanocomposites, adsorption capacity enhanced by a nearly 122-fold, in comparison to unmodified chitosan (Table 2.1). A literature comparison for adsorption capacities of nanocomposites prepared in chapter 2 are presented in Table 6.1. The adsorption capacities of MB onto MNCs reported in chapter 2 are notably higher than many other reported values for other adsorbents and have comparative advantages over other PANI and chitosan sorbent materials in terms of lower cost, facile separation, recyclability, and green synthesis.

**Table 6.1.** Literature comparison of adsorption capacities of various adsorbent materials toward MB in aqueous solution.

| Adsorbent | Adsorption capacity (mg/g) | Limitations and Comments | Reference |
|---|---|---|---|
| Carbon nanotube ponytails (CNPs) | 150 | Facile regeneration/High cost/Low adsorption capacity/ lack of magnetic property | 10 |
| Graphene oxide | 389.8 | good adsorption capacity/facile separation/ lack of magnetic properties | 11 |
| Poly(L-dopa)-Based Polyelectrolyte Complexes | 467.1 | Good adsorption capacity/lack of magnetic property/High cost and expensive materials/non-renewable materials | 12 |
| Humic acid-modified perlite (HA/EP) | 82.8 | Low cost /low adsorption capacity/dificult to separate and regerenration | 13 |
| Carbon nanotubes (CNTs) | 35.4 | Low adsortpion capacity/difficult to separate and regeneration | 14 |
| Graphene | 153.9 | Easy preparation/low adsorption capacity/difficult to separate and regeneration | 15 |
| Natural rubber /Chitosan blends | 0.89 | Low adsorption capacity/difficult to separate and regeneration | 16 |
| PANI/α-ZrP Nanocomposites | 156.3 | Low cost/facile synthesis/relatively low adsorption capacity/lack of magnetic property and difficult to regeneration | 17 |
| Multiwalled Carbon | 399 | Good sorption capacity/High cost lack of magnetic properties | 18 |
| (EDTAD)-modified magnetic chitosan (EMC) | 113.3 | Low sorption capacity | 19 |
| Polyacrylamide Grafted Xanthan Gum/nanosilica | 497.5 | Good sorption capacity/low cost/lack of magnetic property/difficult regeneration | 20 |
| Polyaniline hydrogel | 71.2 | Low cost/Low sorption capacity/lack of magnetic properties | 21 |
| Iron sludge | 99.4 | Magnetic properties/low cost/ Low sorption capacity | 22 |
| Magnetic chitosan composite | 45.1 | Magnetic properties/low cost/Low sorption capacity | 23 |
| Magnetite/polymer brush nanocomposites | **470.2** | High adsorption capacity/facile and green synthesis/low cost/easy recoverability/magnetic properties/pH-responsive | This study |

In chapter 3, catalytic reductive conversion was utilized to reduce 4-NPh in the presence of silver nanoparticles (Ag NPs). Therefore, polyaniline/Ag nanocomposites were prepared and studied to evaluate the conversion of 4-NPh to 4-APh. Due to its extraordinary catalytic reduction properties, PANI was used as a template to support Ag NPs, surface adsorption sites, low interfacial reactivity, electrical conductivity, and electrochemical switchability. Chitosan has functional groups similar to PANI which can bind to PANI to form stable composite materials. The mass-based mixing ratio of chitosan/PANI was varied while the silver content was kept

constant. In addition, high catalytic stability was observed for PANI-supported catalysts (*cf*. Figure 3.6) under six consecutive reduction cycles. With a greater increase in the PANI fraction to 75% in ternary composite, reduction reactions showed higher kinetic rates of conversions (*ca.* 32 times enhancement in AgNP-CP75 relative to Ag NPs, *cf.* Table 3.1). The results revealed that the enhancement in the rate of reduction reaction mainly is due to the possibility of charge transfer within interface of conductive Ag and semiconducting polymer. Such a hybridization of Ag and PANI facilitated fast electron transfer across metal/conducting polymer interface and subsequently higher reduction conversion was achieved. The catalytic activity of nanocomposite systems was substantially beyond the activity observed for single component Ag NPs, PANI and CHI in bulk solution, respectively. The results clearly demonstrate that nanocomposites systems with even a small content of Ag NPs can be designed for efficient reductive transformation of 4-NPh to 4-APh. These systems contribute to the overall objective of the thesis by introducing chitosan/PANI nanocatalyst composites for reductive transformation of dyes such as 4-NPh to 4-APh in aqueous media. The catalysts reported in Chapter 3 showed comparative performances over similar nanocatalyst systems reported in the literature in terms catalytic activities (Table 6.2). These results strongly support the hypothesis that PANI can be used as an effective support to design silver nanocatalyst systems with improved catalyst properties.

**Table 6.2.** Comparison of the catalytic activity of the related Ag nanocomposite catalysts reported in literature for the reduction of 4-NPh by $NaBH_4$.

| Catalyst | Activity factor ($s^{-1}g^{-1}$)§ | Reference |
|---|---|---|
| AgNPs-CP75 | 1.6 | This work |
| AgNPs-CP25 | 0.17 | This work |
| AgNPs-CP50 | 0.33 | This work |
| Ag@PANI-CS-$Fe_3O_4$ | 1.0 | 24 |
| Ag-NP/C composite | 1.69 | 25 |
| AgNP@halloysite nanotubes | 0.087 | 26 |
| $SiO_2$@AgNPs | 0.248 | 27 |
| Ag@egg shell membrane | 0.41 | 28 |
| TSC-Ag-1.0* | 0.09 | 29 |
| TAC-Ag-1.4* | 0.41 | 29 |
| TAC-Ag-1.0 | 1.30 | 29 |
| $Fe_3O_4$@$SiO_2$–Ag | $7.67\times10^{-3}$ | 30 |

§ Activity factor denotes the ratio of apparent rate constant $k_{app}$ to the total mass of the catalyst.
*** TSC:** Trisodium citrate dihydrate, **TAC:** Triammonium citrate.

Chapter 4 continued with research on MB adsorption using PANI and magnetite nanostructures. PANI/magnetite nanostructures were developed via surface-initiated polymerization. Using chitosan with variable composition, PANI aggregates with variable sizes was achieved. These types of nanocomposite materials displayed molecularly selective adsorption behavior towards binary dye mixtures that contain MB and MO. To elucidate the binding mode and how PANI nanostructures adsorb MB, their interaction with NaCl was investigated and their size distribution was measured in salt solution. The finding revealed that NaCl interacts in a similar manner to that of MB. Therefore, nanocomposites with salt-responsive properties was demonstrated and contributed to new insights on the mechanism of dye adsorption. It was concluded that adsorption occurs via dipole-ion interaction between the cationic center of MB with the dipole moments of =N- and –NH- groups. However, the details about salt interaction in this study are unresolved as to how the salt fraction interacts with PANI to disassemble the nanostructure via responsive hydrogen bonding interactions.

In chapter 5, mechanistic details of MB adsorption were extended and the nature of the PANI-cation interactions were further studied through an investigation of the salt-responsive hydrogen bonding in PANI-based carriers. Such types of polymer-based carriers were utilized to develop responsive release systems by physical loading of self-healing materials inside a polymer shell (*cf.* Scheme 5.1). Release of three self-healing materials (MBT, MBI, BTA) from PANI capsules was monitored on exposure to salt (NaCl) as the external stimuli. The release profiles revealed that salt interacts with the PANI shell in a co-activated fashion. The interaction of salt with PANI is related to a combination of factors, such as counter ion solvation and its ability to stabilize the PANI-$Na^+$ complex (*cf.* Scheme 6.2). Water diffusion and permeability undergo change upon complexation with salt, and creation of osmotic pressure due to ion concentration gradients, are activated by cation binding which consequently enhances the opening of pores sites and release of entrapped materials into the bulk solution.

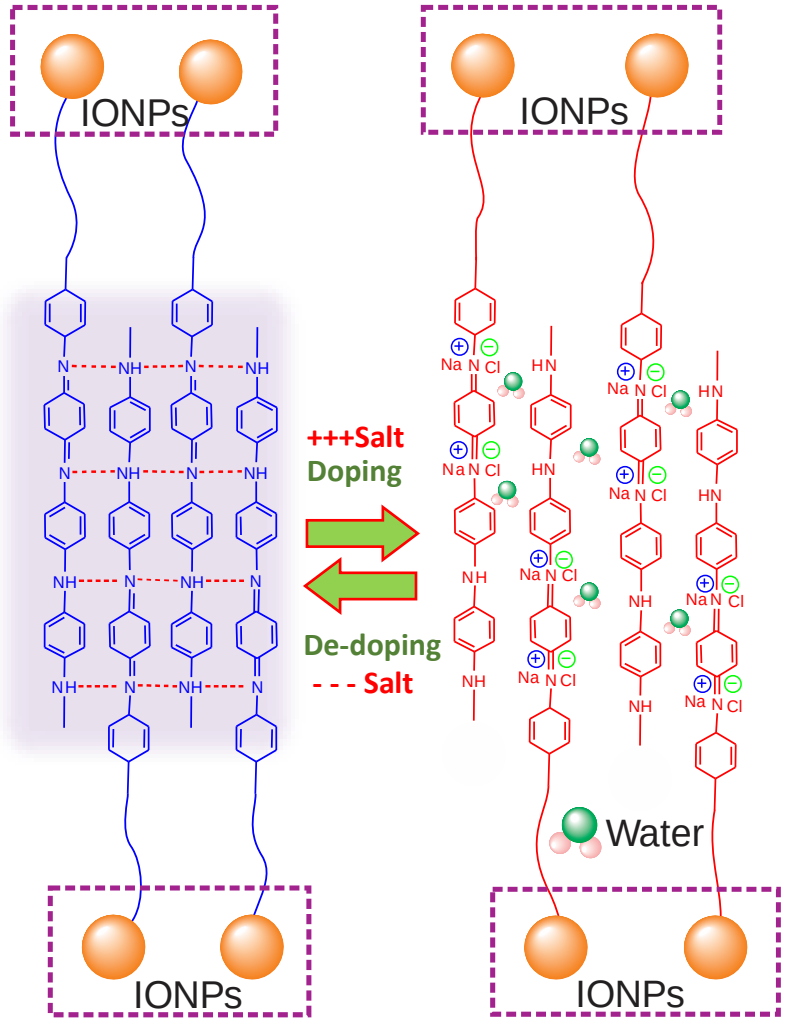


**Scheme 6.2.** Illustration of salt-sensitive transformation and *salting-in* interactions in PANI domains leads to intensified screening of intermolecular hydrogen bonding in an aggregate-like arrangement (right) and intramolecular hydrogen bonding induced assembly (left). Reprinted with permission from reference[7] © 2017 American Chemical Society.

Finally, this dissertation presented the structural fabrication and application of stimuli responsive nanocomposites for dye removal via adsorption and/or catalytic reduction. Several major findings are as follows: chapter 2 and 4 presents the development of improved adsorbents for MB, while chapter 3 investigates the catalytic reduction of 4-NPh. In chapter 5, salt/PANI

interactions were utilized to develop salt-responsive release systems as a means to further understand MB adsorption by PANI. Therefore, several major findings of this thesis are as follows:

***i)*** Chitosan is a poor adsorbent for a model cationic dye (MB). Upon incorporation of polyacids and magnetite with chitosan yields pH-responsive nanocomposites with greater surface area, where facile regeneration and increased adsorption capacity towards MB was achieved. The incorporation of PIA and PAA not only bestows enhanced adsorption capacity, as compared with unmodified chitosan. The presence of polyacid functional groups onto chitosan also creates osmotic pressure within the *brush-like* structures upon deprotonation. This effect is accompanied by electrostatic interactions to yield materials with high affinity for MB at pH conditions above the $pK_a$ of the acids (ca. pH= 3.5. *cf.* Appendix).

***ii)*** Interfacial hybridization of Ag NPs with PANI resulted in creation of abundant active sites for catalytic reduction of 4-NPh to 4-APh. PANI was demonstrated to serve as a conductive and redox-switchable organic polymer support for Ag NPs to achieve interfacial electronic communication across PANI/Ag interface which is responsible for catalytic enhancement for borohydride-based reduction processes.

***iii)*** Polyaniline/magnetite nanostructures were fabricated and utilized to remove MB from aqueous solution. Investigation on mechanism of selective cationic dye adsorption led to demonstration salt (NaCl)-responsive behavior in PANI assemblies, where salt activated dynamic hydrogen bonding for PANI was demonstrated. Salt-responsive behavior of this type led to a conclusion that cationic dye adsorption occurs by a similar mechanism, similar to the NaCl doping for PANI, where the dipole moment interactions contribute to active sites for dye

adsorption. Such a salt doping interaction leads to screening effects by hydrogen bonding. Consequently, the polymer undergoes swelling by salt ("salting-in" interactions) effects and the aggregates undergo disassembly, which finds additional support by complementary results obtained from DLS and Raman spectroscopy.

***iv)*** Salt-responsive behavior was utilized to develop responsive release systems for self-healing materials. The mechanism of salt-responsive release was investigated in detail and was used to reveal further details on the nature of the salt interaction. Finally, it was determined that cation-PANI interaction is combination of various factors that mostly depend on anion pair solvation and its ability to stabilize PANI-cation complexes.

The materials developed herein possess several notable merits: high activity for chemical/physical dye removal, stimuli-responsive behavior and low cost of the materials preparation. These factors contribute to the overall objectives of this dissertation and the development of materials for applications related to advanced dye removal in aqueous media.

## 6.3. Future work

The future work proposed in the next sections aim to further contribute to the overall objectives that lay outside the scope of research presented in this thesis, dye removal through catalytic reduction and adsorption processes.

## 6.3.1. 4-NPh removal

In this section future directions on the removal of 4-NPh will be discussed.

### 6.3.1.1. 4-NPh adsorption

Understanding the role of adsorption for the catalytic reduction in the case of PANI/Ag nanocatalysts still requires further study to be fully addressed. The role of adsorption can be decisive for the catalytic conversion reactions as the electron transfer from donor ($BH_4^-$) to the acceptor (4-NPh) largely depends on the adsorption of reagents both $BH_4^-$ and 4-NPh to the surface of catalysts.[31-33] Therefore, in order to rationally distinguish the role of adsorbing PANI/CHI polymer support from catalytic activity of Ag in the overall conversion reaction, a systematic adsorption isotherm study for 4-NPh is required. This will allow to ascertain the adsorptive role of PANI/CHI versus catalytic role of Ag. This will also help to build a correlation between adsorption phenomena on the surface of polymer support and overall catalytic activity of catalyst for conversion of 4-NPh. Although the objective of chapter 3 is the development of catalyst systems for conversion of 4-NPh, a detailed understanding of the surface adsorption of 4-NPh onto the catalyst remains somewhat unclear. An investigation of the equilibrium adsorption isotherms would allow for rational correlation between adsorption performance and catalytic performance that would give insight on the mechanism of surface interactions that occur during the reduction process on the nanocatalyst surface. With increasing PANI content for the nanocatalysts, higher conversion rates were observed which is attributed to creation of larger interfacial area for electron transfer and creation of additional PANI reduction sites. As part of the ongoing future work, a comprehensive equilibrium adsorption study on nanocomposites needs to be conducted to clarify the role of adsorption at equilibrium conditions.[34] Equilibrium adsorption experiments of 4-NPh on PANI/Ag nanocatalysts can provide insight on the role of physisorption related to the overall

kinetics of the catalytic reduction process. These results can offer possible strategies for additional enhancement on catalysis application and specifically 4-NPh conversion.

### 6.3.1.2. Preliminary results on 4-NPh adsorption

As discussed in section 6.2.1, it is significant to study adsorption isotherms to determine the contributors to the catalytic activity. In addition to the catalytic activity of nanocatalysts, another interesting feature of nanocatalysts that contain PANI concerns the ability to adsorb 4-NPh. UV-vis spectroscopy was applied to monitor the concentration of 4-NPh before and after adsorption and the procedure can be adopted from sections 2.3.5 and 3.3.3 in chapters 2 & 3. Figure 6.2 shows the equilibrium adsorption isotherm for adsorption of 4-NPh on a nanocatalyst with 75% PANI. As evidenced from Figure 6.2, the equilibrium adsorption parameters were analyzed by use of the Sips isotherm model. Initial adsorption isotherm results show that the nanocatalyst with 75% PANI content reached a maximum adsorption capacity of 1.40 mmol/g for 4-NPh. The adsorption isotherms for the two other catalysts will be further studied in order to make a rational comparison and conclusion on the role of adsorption on catalytic performance.

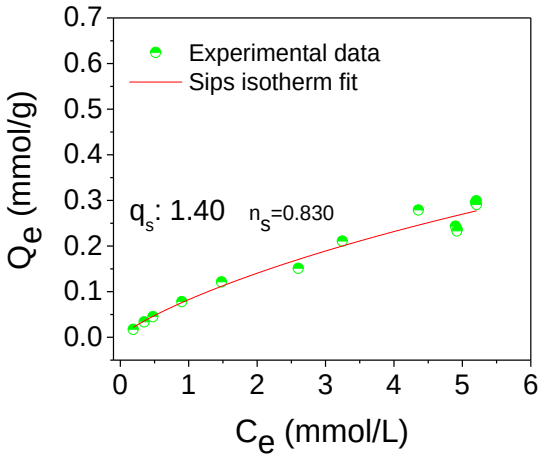


**Figure 6.2.** Equilibrium adsorption isotherms of 4-NPh on PANI/Ag nanocatalysts, where the solid lines are the best-fits according to the Sips and Langmuir adsorption isotherms.

## 6.3.2. MB removal

This section is devoted to the future direction of this thesis on the catalytic reduction of MB.

### 6.3.2.1. MB reduction

As discussed in section 1.1, organic dyes are pervasive chemicals which present potential problems to the environment due to their toxicity.[35-37] Reduction of dyes is another alternative approach to remove or reduce their toxic effects in aquatic environments.[38]

Ag NPs are well known for their unique physical and chemical properties and excellent catalytic activity on many reduction reactions.[39-41] Due to their high catalytic activity,[39, 42] noble metal NPs are widely used to facilitate the catalytic reduction of MB which is a common dye in the paint industry.[31] The bright color of MB can block photosynthesis activity in aquatic environments and adversely affect the growth of plants due to reduced sunlight penetration. However, in the reduced form of LMB, where the blue color rapidly disappears ($\lambda_{max}$ = 256 nm). Furthermore, the reduction of MB to LMB (*cf.* Scheme 6.3) is a useful process in many industrial applications. For example, reduction and oxidation of MB have found applications in colorimetric oxygen indicators that involves accepting or donating hydronium ions.[43]

Therefore, as an extension of the present work, catalytic reduction of aqueous MB to LMB by PANI/Ag nanocatalysts is proposed. Methylene blue reduction experiments will be carried out according to protocols described in section 3.3.3 of chapter 3 for 4-NPh. The reaction can be monitored according to change in color of solution and gradual decrease in maximum spectral absorbance using UV-vis spectroscopy.

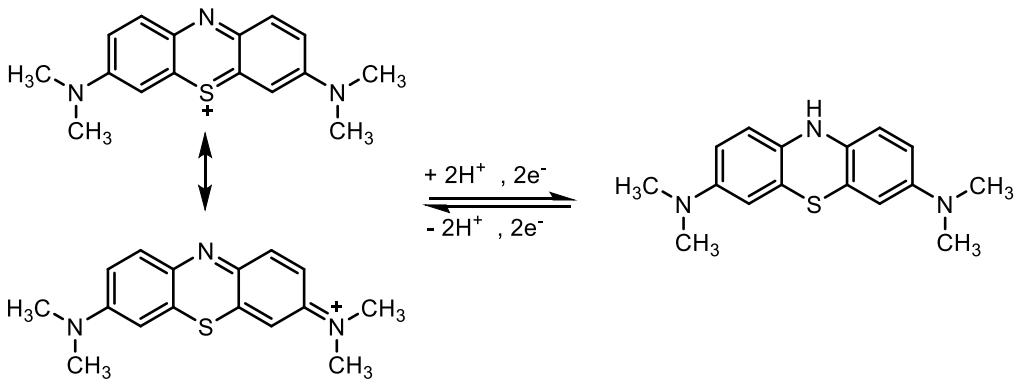


**Scheme 6.3.** Oxidized and reduced forms of MB

## 6.3.2.2. Preliminary results on MB reduction

Some preliminary experiments on MB reduction in the presence of catalysts, as described in chapter 3 have been performed for the reduction of MB (results not shown), where the catalytic activities of the PANI/Ag that contain 75% PANI was evaluated. Similar to the results reported in the study of 4-NPh reduction (*cf.* section 3.3.3), time-dependent UV-vis absorption spectra were recorded during the catalytic reduction and a successive decrease in the intensity of the absorbance band at 640 nm was observed, as illustrated in Figure 6.3. The results show that the maximum absorbance value of MB at $\lambda_{max}$= 664 nm decreases with an increase in the reaction time, and indicates that PANI/Ag nanocatalysts can similarly catalyze the reduction of MB. The catalytic reaction for the catalyst that contains 75% PANI was completed within 21 min.

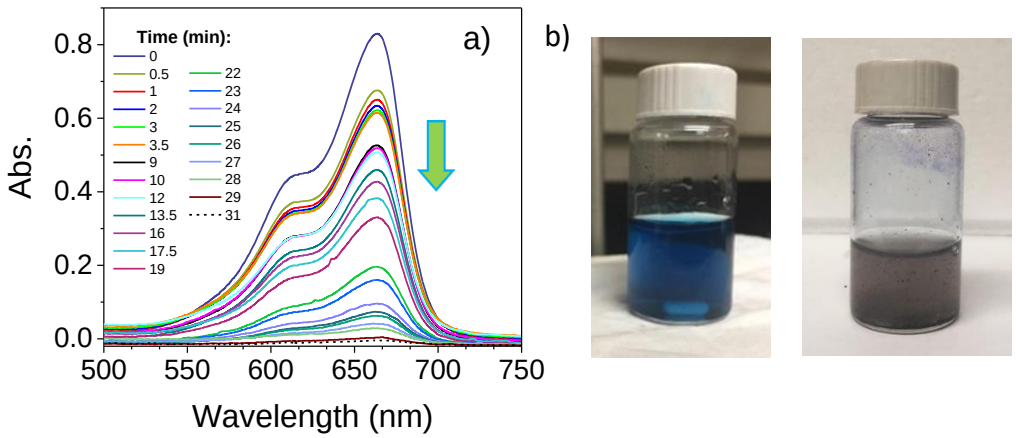


**Figure 6.3.** a) Successive UV-vis spectra of MB aqueous solution containing $NaBH_4$ and PANI/Ag nanocatalysts as a function of reaction time. [MB] = 0.1mM, [$BH_4^-$] = 40 mg in 500 µL water, catalyst solution = 10 mg in 1 ml. b) corresponding color changes of MB before and after reduction.

# 6.4. References


1. Qiu, W.-Z.; Yang, H.-C.; Wan, L.-S.; Xu, Z.-K., Co-Deposition of Catechol/polyethyleneimine on Porous Membranes for Efficient Decolorization of Dye Water. *J. Mater. Chem. A* **2015**, *3*, 14438-14444.

2. Ghorai, S.; Sarkar, A.; Raoufi, M.; Panda, A. B.; Schönherr, H.; Pal, S., Enhanced Removal of Methylene Blue and Methyl Violet Dyes from Aqueous Solution Using a Nanocomposite of Hydrolyzed Polyacrylamide Grafted Xanthan Gum and Incorporated Nanosilica. *ACS Appl. Mater. Interfaces* **2014**, *6*, 4766-4777.

3. Mohamed, M. H.; Dolatkhah, A.; Aboumourad, T.; Dehabadi, L.; Wilson, L. D., Investigation of Templated and Supported Polyaniline Adsorbent Materials. *RSC Adv.* **2015**, *5*, 6976-6984.

4. Cruz-Silva, R.; Arizmendi, L.; Del-Angel, M.; Romero-Garcia, J., pH- and Thermosensitive Polyaniline Colloidal Particles Prepared by Enzymatic Polymerization. *Langmuir* **2007**, *23*, 8-12.

5. Qazi, T. H.; Rai, R.; Boccaccini, A. R., Tissue Engineering of Electrically Responsive Tissues Using Polyaniline Based Polymers: A review. *Biomaterials* **2014**, *35*, 9068-9086.

6. Jang, J.; Ha, J.; Lim, B., Synthesis and Characterization of Monodisperse Silica–Polyaniline Core–Shell Nanoparticles. *Chem. Commun.* **2006,** 1622-1624.

7. Dolatkhah, A.; Wilson, L. D., Salt-Responsive $Fe_3O_4$ Nanocomposites and Phase Behavior in Water. *Langmuir* **2018,** *34*, 341-350.

8. Dolatkhah, A.; Wilson, L. D., Magnetite/Polymer Brush Nanocomposites with Switchable Uptake Behavior Toward Methylene Blue. *ACS Appl. Mater. Interfaces* **2016**, *8*, 5595-5607.

9. Dolatkhah, A.; Jani, P.; Wilson, L. D., Redox-Responsive Polymer Template as an Advanced Multifunctional Catalyst Support for silver Nanoparticles. *Langmuir* **2018**, *34*, 10560-10568

10. Wang, H. T.; Ma, H. Y.; Zheng, W.; An, D. D.; Na, C. Z. Multifunctional and Recollectable Carbon Nanotube Ponytails for Water Purification. *ACS Appl. Mater. Interfaces* **2014**, *6*, 9426-9434.

11. Liu, F.; Chung, S.; Oh, G.; Seo, T. S. Three-Dimensional Graphene Oxide Nanostructure for Fast and Efficient Water-Soluble Dye Removal. *ACS Appl. Mater. Interfaces* **2012**, *4*, 922-927.

12. Yu, L.; Liu, X. K.; Yuan, W. C.; Brown, L. J.; Wang, D. Y. Confined Flocculation of Ionic Pollutants by Poly(L-dopa)-Based Polyelectrolyte Complexes in Hydrogel Beads for Three-Dimensional, Quantitative, Efficient Water Decontamination. *Langmuir* **2015**, *31*, 6351-6366.

13. Luo, W. J.; Gao, Q.; Wu, X. L.; Zhou, C. G. Removal of Cationic Dye (Methylene Blue) from Aqueous Solution by Humic Acid-Modified Expanded Perlite: Experiment and Theory. *Sep. Sci. Technol.* **2014**, 49, 2400-2411.

14. Yao, Y. J.; Xu, F. F.; Chen, M.; Xu, Z. X.; Zhu, Z. W. Adsorption Behavior of Methylene Blue on Carbon Nanotubes. *Bioresour. Technol.* **2010**, *101*, 3040-3046.

15. Liu, T. H.; Li, Y. H.; Du, Q. J.; Sun, J. K.; Jiao, Y. Q.; Yang, G. M.; Wang, Z. H.; Xia, Y. Z.; Zhang, W.; Wang, K. L.; Zhu, H. W.; Wu, D. H. Adsorption of Methylene Blue from Aqueous Solution by Graphene. *Colloids Surf. B* **2012**, *90*, 197-203.

16. Johns, J.; Rao, V. Adsorption of Methylene Blue onto Natural Rubber/Chitosan Blends. *Int. J. Polym. Mater.* **2011**, *60*, 766-775.

17. Wang, L.; Wu, X. L.; Xu, W. H.; Huang, X. J.; Liu, J. H.; Xu, A. W. Stable Organic-Inorganic Hybrid of Polyaniline/alpha-Zirconium Phosphate for Efficient Removal of Organic Pollutants in Water Environment. *ACS Appl. Mater. Interfaces* **2012**, *4*, 2686-2692.

18. Ma, J.; Yu, F.; Zhou, L.; Jin, L.; Yang, M. X.; Luan, J. S.; Tang, Y. H.; Fan, H. B.; Yuan, Z. W.; Chen, J. H. Enhanced Adsorptive Removal of Methyl Orange and Methylene Blue from Aqueous Solution by Alkali-Activated Multiwalled Carbon Nanotubes. *ACS Appl. Mater. Interfaces* **2012**, *4*, 5749-5760.

19. Xia, Y. X.; Dai, X. X.; Huang, S. T.; Tian, X. M.; Yang, H. Y.; Li, Y. C.; Liu, Y.; Zhao, M. J. Fast and Highly Efficient Removal of Methylene Blue by a Novel EDTAD-Modified Magnetic Chitosan Material. *Desalin. Water Treat.* **2013**, *51*, 7586-7595.

20. Ghorai, S.; Sarkar, A.; Raoufi, M.; Panda, A. B.; Schonherr, H.; Pal, S. Enhanced Removal of Methylene Blue and Methyl Violet Dyes from Aqueous Solution Using a Nanocomposite of Hydrolyzed Polyacrylamide Grafted Xanthan Gum and Incorporated Nanosilica. *ACS Appl. Mater. Interfaces* **2014**, *6*, 4766-4777.

21. Yan, B.; Chen, Z.; Cai, L.; Chen, Z.; Fu, J.; Xu, Q. Fabrication of Polyaniline Hydrogel: Synthesis, Characterization and Adsorption of Methylene Blue. *Appl. Surf. Sci.* **2015**, *356*, 39-47.

22. Zhu, S.; Fang, S.; Huo, M.; Yu, Y.; Chen, Y.; Yang, X.; Geng, Z.; Wang, Y.; Bian, D.; Huo, H. A Novel Conversion of the Groundwater Treatment Sludge to Magnetic Particles for the Adsorption of Methylene Blue. *J. Hazard. Mater.* **2015**, *292*, 173-179.

23. Cho, D.-W.; Jeon, B.-H.; Chon, C.-M.; Schwartz, F. W.; Jeong, Y.; Song, H. Magnetic Chitosan Composite for Adsorption of Cationic and Anionic Dyes in Aqueous Solution. *J. Ind. Eng. Chem.* **2015**, *28*, 60-66.

24. Ayad, M. M.; Amer, W. A.; Kotp, M. G.; Minisy, I. M.; Rehab, A. F.; Kopecký, D.; Fitl, P. Synthesis of Silver-Anchored Polyaniline–Chitosan Magnetic Nanocomposite: A Smart System for Catalysis. *RSC Adv.* **2017**, *7*, 18553-18560.

25. Tang, S.; Vongehr, S.; Meng, X. Carbon Spheres with Controllable Silver Nanoparticle Doping. *J. Phys. Chem. C* **2009**, *114*, 977-982.

26. Liu, P.; Zhao, M. Silver Nanoparticle Supported on Halloysite Nanotubes Catalyzed Reduction of 4-Nitrophenol (4-NP). *Appl. Surf. Sci.* **2009**, *255*, 3989-3993.

27. Wang, M.; Tian, D.; Tian, P.; Yuan, L. Synthesis of Micron-$SiO_2$@nano-Ag Particles and their Catalytic Performance in 4-Nitrophenol Reduction. *Appl. Surf. Sci.* **2013**, *283*, 389-395.

28. Liang, M.; Su, R.; Qi, W.; Yu, Y.; Wang, L.; He, Z. Synthesis of Well-Dispersed Ag Nanoparticles on Eggshell Membrane for Catalytic Reduction of 4-Nitrophenol. *J. Mater. Sci.* **2013**, *49*, 1639-1647.

29. Rashid, M. H.; Mandal, T. K. Synthesis and Catalytic Application of Nanostructured Silver Dendrites. *J. Phys. Chem. C* **2007**, *111*, 16750-16760.

30. Chi, Y.; Yuan, Q.; Li, Y.; Tu, J.; Zhao, L.; Li, N.; Li, X. Synthesis of $Fe_3O_4$@$SiO_2$–Ag Magnetic Nanocomposite Based on Small-Sized and Highly Dispersed Silver Nanoparticles for Catalytic Reduction of 4-Nitrophenol. *J. Colloid Interf. Sci.* **2012**, *383*, 96-102.

31. Cao, H. L.; Huang, H. B.; Chen, Z.; Karadeniz, B.; Lu, J.; Cao, R., Ultrafine Silver Nanoparticles Supported on a Conjugated Microporous Polymer as High-Performance Nanocatalysts for Nitrophenol Reduction. *ACS Appl. Mater. Interfaces* **2017,** *9*, 5231-5236.

32. Lu, J.; Perez-Krap, C.; Suyetin, M.; Alsmail, N. H.; Yan, Y.; Yang, S. H.; Lewis, W.; Bichoutskaia, E.; Tang, C. C.; Blake, A. J.; Cao, R.; Schroder, M., A Robust Binary Supramolecular Organic Framework (SOF) with High $CO_2$ Adsorption and Selectivity. *J. Am. Chem. Soc.* **2014,** *136*, 12828-12831.

33. Xu, D.; Diao, P.; Jun, T.; Wu, Q. Y.; Liu, X. F.; Guo, X.; Gong, H. Y.; Li, F.; Xiang, M.; Yu, R. H., Iridium Oxide Nanoparticles and Iridium/Iridium Oxide Nanocomposites: Photochemical Fabrication and Application in Catalytic Reduction of 4-Nitrophenol. *ACS Appl. Mater. Interfaces* **2015,** *7*, 16738-16749.

34. Yang, X. Y.; Li, Y.; Zhang, P.; Zhou, R. M.; Peng, H. L.; Liu, D.; Gui, J. Z., Photoinduced in Situ Deposition of Uniform and Well-Dispersed PtO2 Nanoparticles on ZnO Nanorods for Efficient Catalytic Reduction of 4-Nitrophenol. *ACS Appl. Mater. Interfaces* **2018,** *10*, 23154-23162.

35. Kumar, S.; Khanchandani, S.; Thirumal, M.; Ganguli, A. K., Achieving Enhanced Visible-Light-Driven Photocatalysis Using Type-II NaNbO3/CdS Core/Shell Heterostructures. *ACS Appl. Mater. Interfaces* **2014,** *6*, 13221-13233.

36. Stylidi, M.; Kondarides, D. I.; Verykios, X. E., Pathways of Solar Light-Induced Photocatalytic Degradation of Azo Dyes in Aqueous $TiO_2$ Suspensions. *Appl. Catal. B-Environ.* **2003,** *40*, 271-286.

37. Konstantinou, I. K.; Albanis, T. A., $TiO_2$-Assisted Photocatalytic Degradation of Azo Dyes in Aqueous Solution: Kinetic and Mechanistic Investigations - A review. *Appl. Catal. B-Environ.* **2004,** *49*, 1-14.

38. Xie, Y. J.; Yan, B.; Xu, H. L.; Chen, J.; Liu, Q. X.; Deng, Y. H.; Zeng, H. B., Highly Regenerable Mussel-Inspired $Fe_3O_4$@Polydopamine-Ag Core-Shell Microspheres as Catalyst and Adsorbent for Methylene Blue Removal. *ACS Appl. Mater. Interfaces* **2014,** *6*, 8845-8852.

39. Liu, R. X.; Guo, J. H.; Ma, G.; Jiang, P.; Zhang, D. H.; Li, D. X.; Chen, L.; Guo, Y. T.; Ge, G. L., Alloyed Crystalline Au-Ag Hollow Nanostructures with High Chemical Stability and Catalytic Performance. *ACS Appl. Mater. Interfaces* **2016,** *8*, 16833-16844.

40. Liang, Y.; Chen, Z.; Yao, W.; Wang, P. Y.; Yu, S. J.; Wang, X. K., Decorating of Ag and CuO on Cu Nanoparticles for Enhanced High Catalytic Activity to the Degradation of Organic Pollutants. *Langmuir* **2017,** *33*, 7606-7614.

41. Silva, F. B.; Vieira, S. N.; Goulart, L. R.; Boodts, J. F. C.; Brito-Madurro, A. G.; Madurro, J. M., Electrochemical Investigation of Oligonucleotide-DNA Hybridization on Poly(4-Methoxyphenethylamine). *Int. J. Mol. Sci.* **2008,** *9*, 1173-1187.

42. Sohrabnezhad, S., Study of Catalytic Reduction and Photodegradation of Methylene Blue by Heterogeneous Catalyst. *Spectrochim. Acta, Part A* **2011,** *81*, 228-235.

43. Ganapuram, B. R.; Alle, M.; Dadigala, R.; Dasari, A.; Maragoni, V.; Guttena, V. Catalytic Reduction of Methylene Blue and Congo Red Dyes using Green Synthesized Gold Nanoparticles Capped by Salmalia Malabarica Gum. *Int. Nano Lett.* **2015**, 5, 215-222.

# Appendix: Supporting Tables and Figures

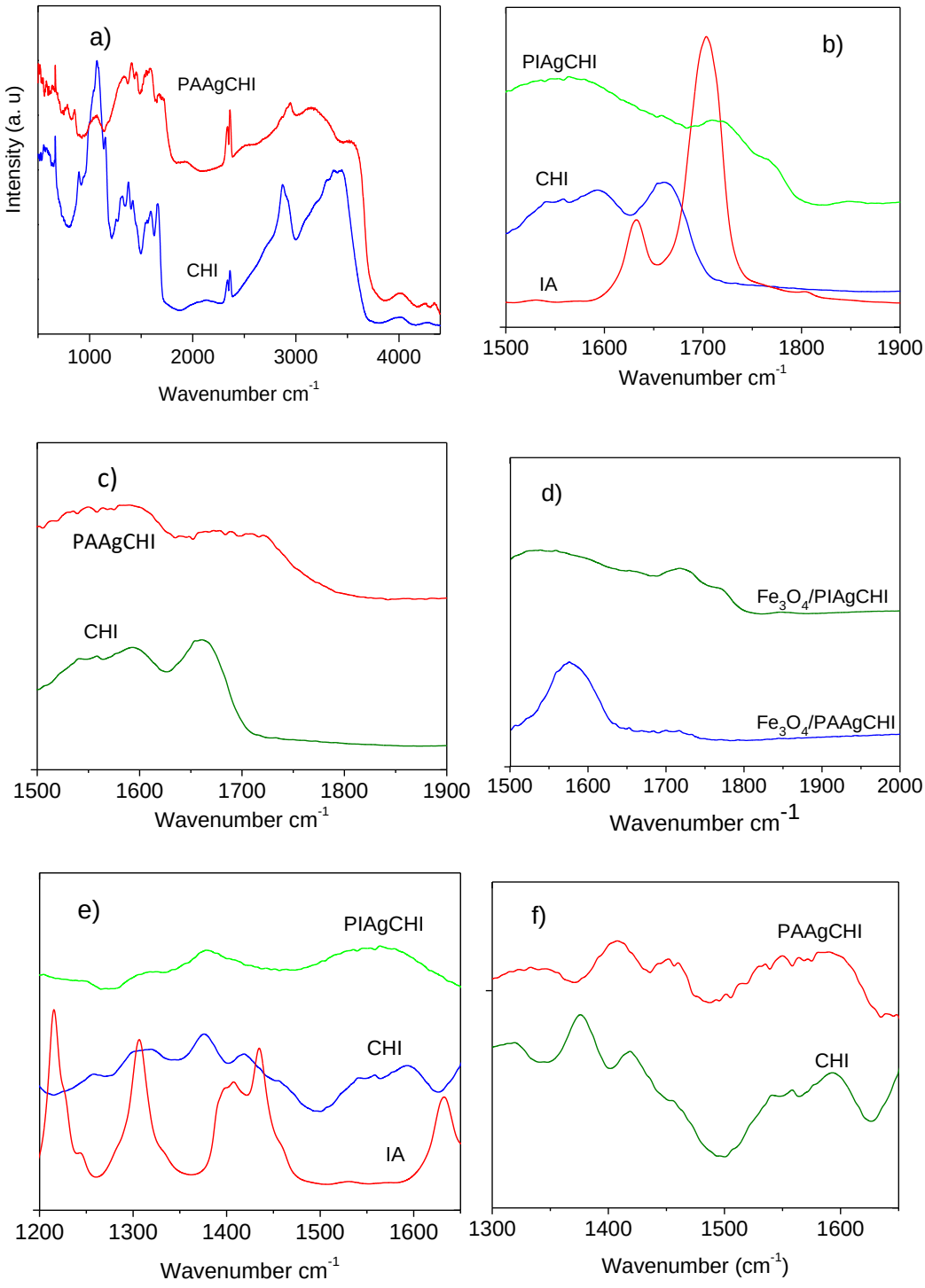
a)
PAAgCHI
CHI
Intensity (a. u)
1000
2000
3000
4000
Wavenumber cm-1
b)
PIAgCHI
CHI
IA
1500
1600
1700
1800
1900
Wavenumber cm-1
c)
PAAgCHI
CHI
1500
1600
1700
1800
1900
Wavenumber cm-1
d)
Fe3O4/PIAgCHI
Fe3O4/PAAgCHI
1500
1600
1700
1800
1900
2000
Wavenumber cm-1
e)
PIAgCHI
CHI
IA
1200
1300
1400
1500
1600
Wavenumber cm-1
f)
PAAgCHI
CHI
1300
1400
1500
1600
Wavenumber (cm-1)

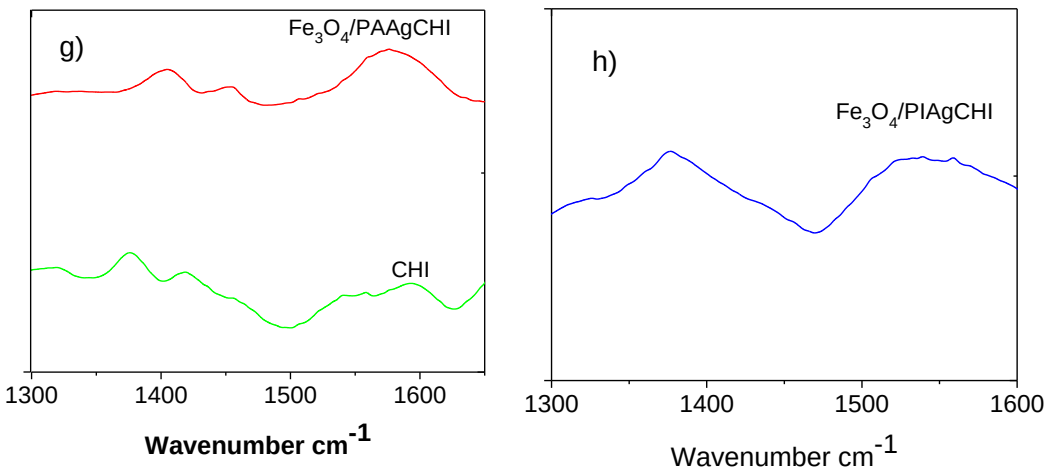


**Figure A.1.** FT-IR spectra of the PAAgCHI polymer brush (i) and pristine chitosan (ii) (a), CHI, PAAgCHI, PIAgCHI, $Fe_3O_4$-PIAgCHI and $Fe_3O_4$-PAAgCHI in the range of carbonyl groups (b,c,d) and symmetric/asymmetric stretching vibrations for $COO^-$ groups (e,f,g,h).

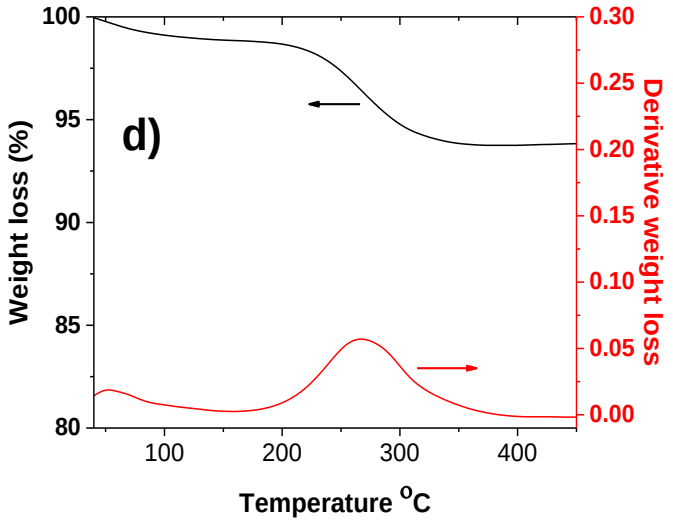


**Figure A.2.** TGA and DTG profile of $Fe_3O_4$-PIAgCHI assemblies.

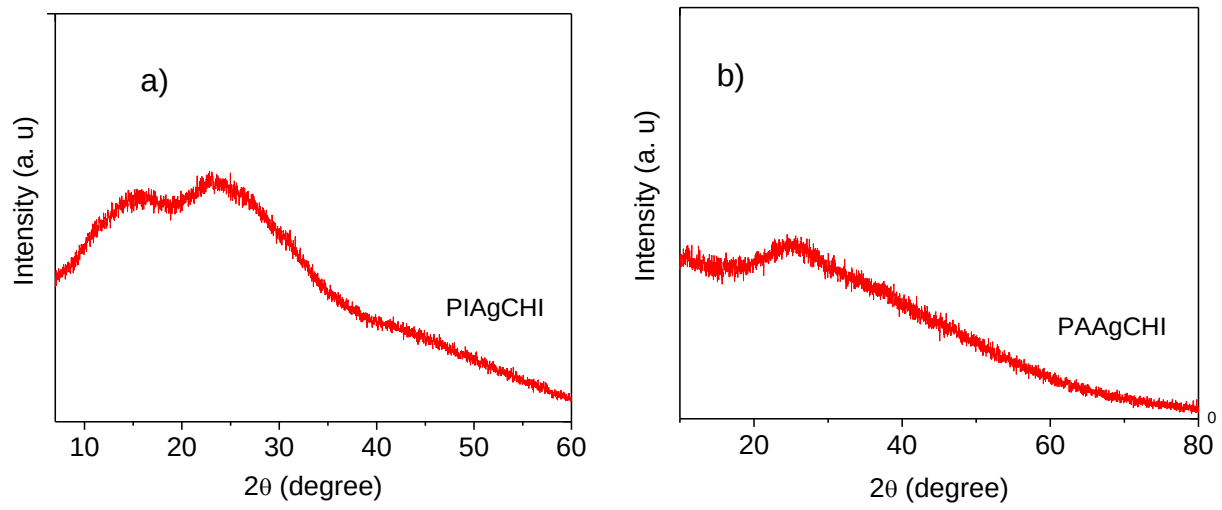


**Figure A.3.** PXRD patterns for PIAgCHI (a), and PAAgCHI (b) brushes.

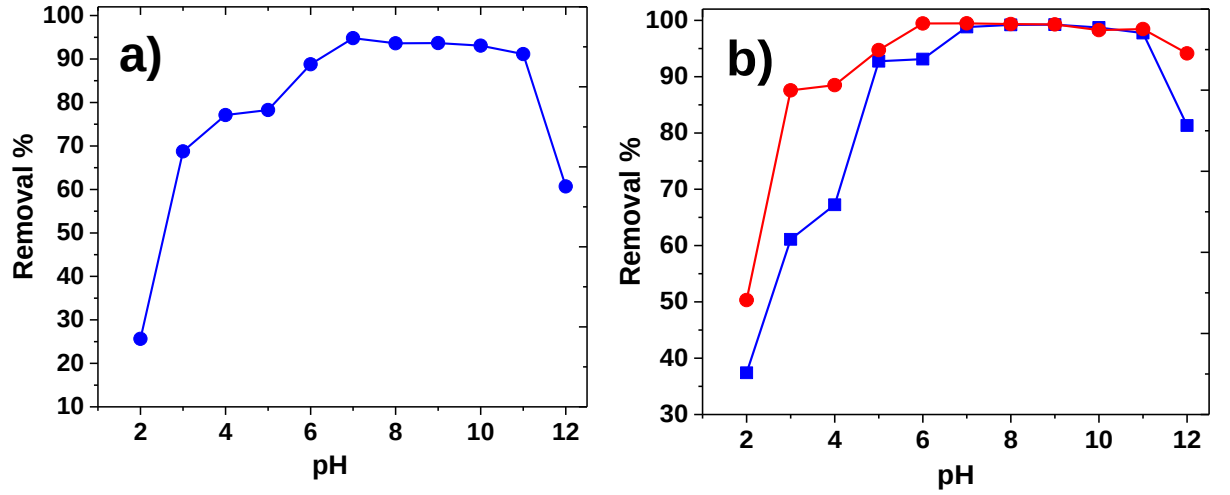


**Figure A.4.** Effect of pH of solution on MB adsorption at 298 K: (a) PIAgCHI; (b) $Fe_3O_4$-PIAgCHI (●) and $Fe_3O_4$-PAAgCHI (■). Experiment conditions: graph (a): m = 10 mg, t = 20 min, $C_0$ (MB) = 0.01 mM, V = 3 ml. graph (b): m = 10 mg, t = 20 min, $C_0$ (MB) =0.06 mM, V= 3 ml.

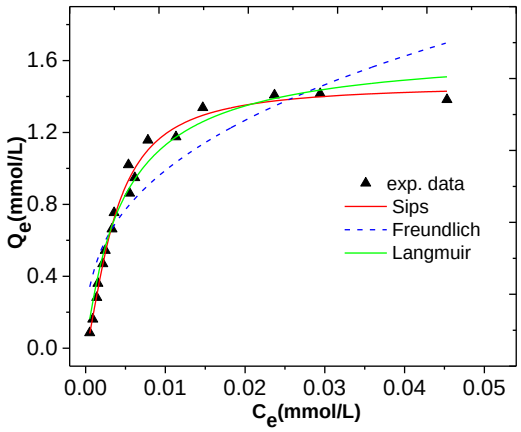


**Figure A.5.** Isotherm sorption results for $Fe_3O_4$-PIAgCHI composite system with MB.

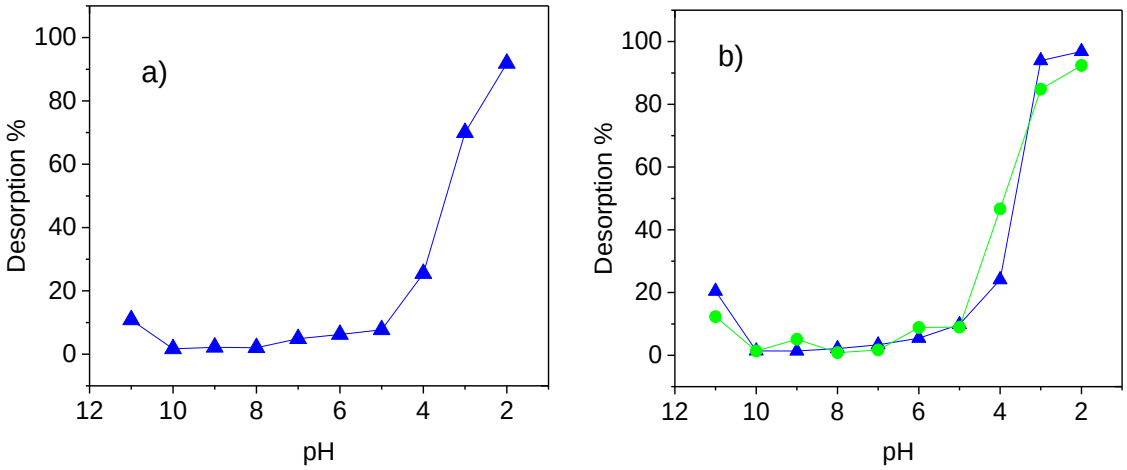


**Figure A.6.** Dependence of MB desorption from PIAgCHI brush (a) and PIAgCHI polymer brush-containing nano hybrids (●) and PAAgCHI polymer brush nano hybrid at variable pH conditions (▲) (b).

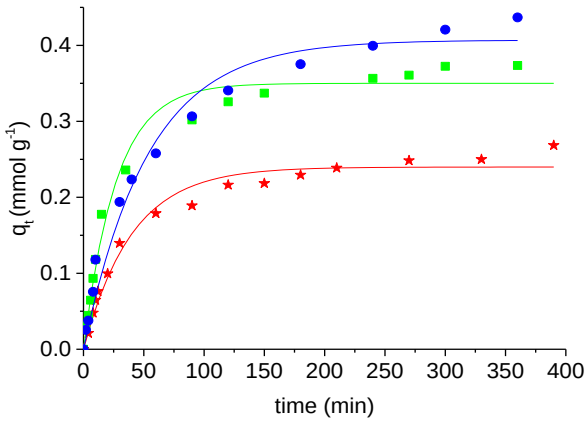


**Figure A.7.** Adsorption kinetics of MB on PIAgCHI (●) $Fe_3O_4$-PAAgCHI (■) and $Fe_3O_4$-PIAgCHI (*) MNCs. The solid line is the PSO best-fit to the experiment data.

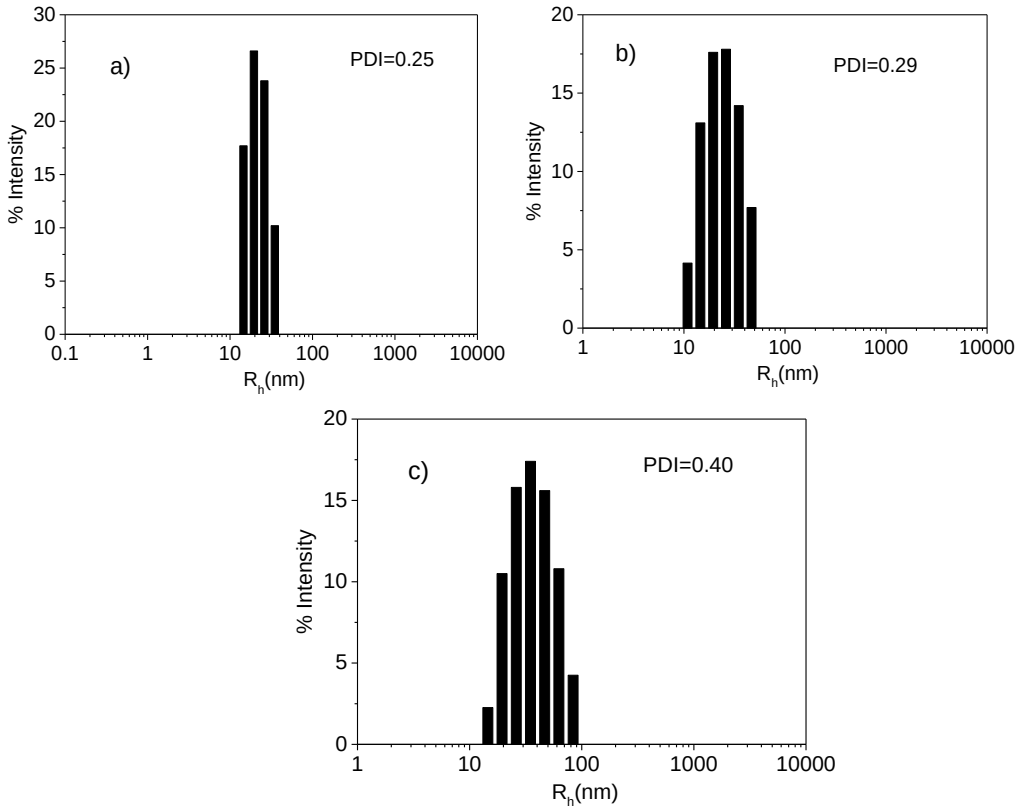


**Figure A.8.** The mean hydrodynamic diameter distributions of $Fe_3O_4$-PIAgCHI particles at pH of 8 (a); $Fe_3O_4$-PAAgCHI at pH 10 (b), and pH 8 (c).

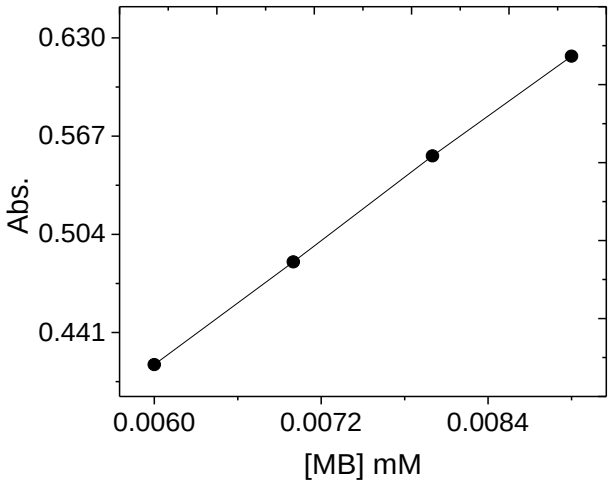


**Figure A.9.** Calibration curve for optical absorbance of MB (λ=664 nm) versus concentration.

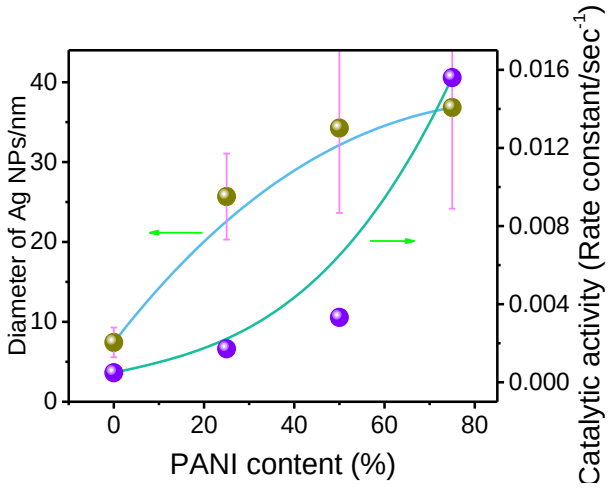


**Figure A.10.** Size and catalytic activity as a function of PANI fraction.

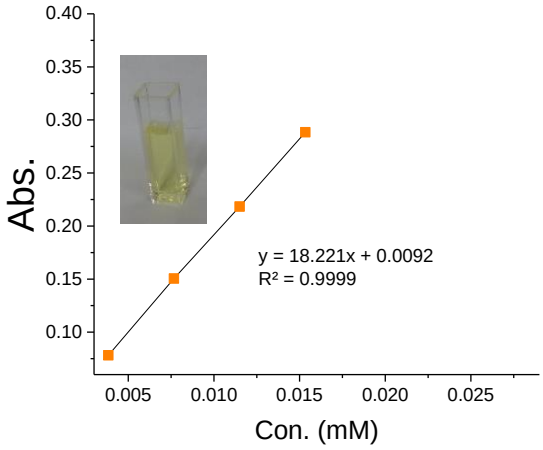


**Figure A.11.** Calibration curve for 4-NPh, optical absorbance (λ=400 nm) versus dye concentration.

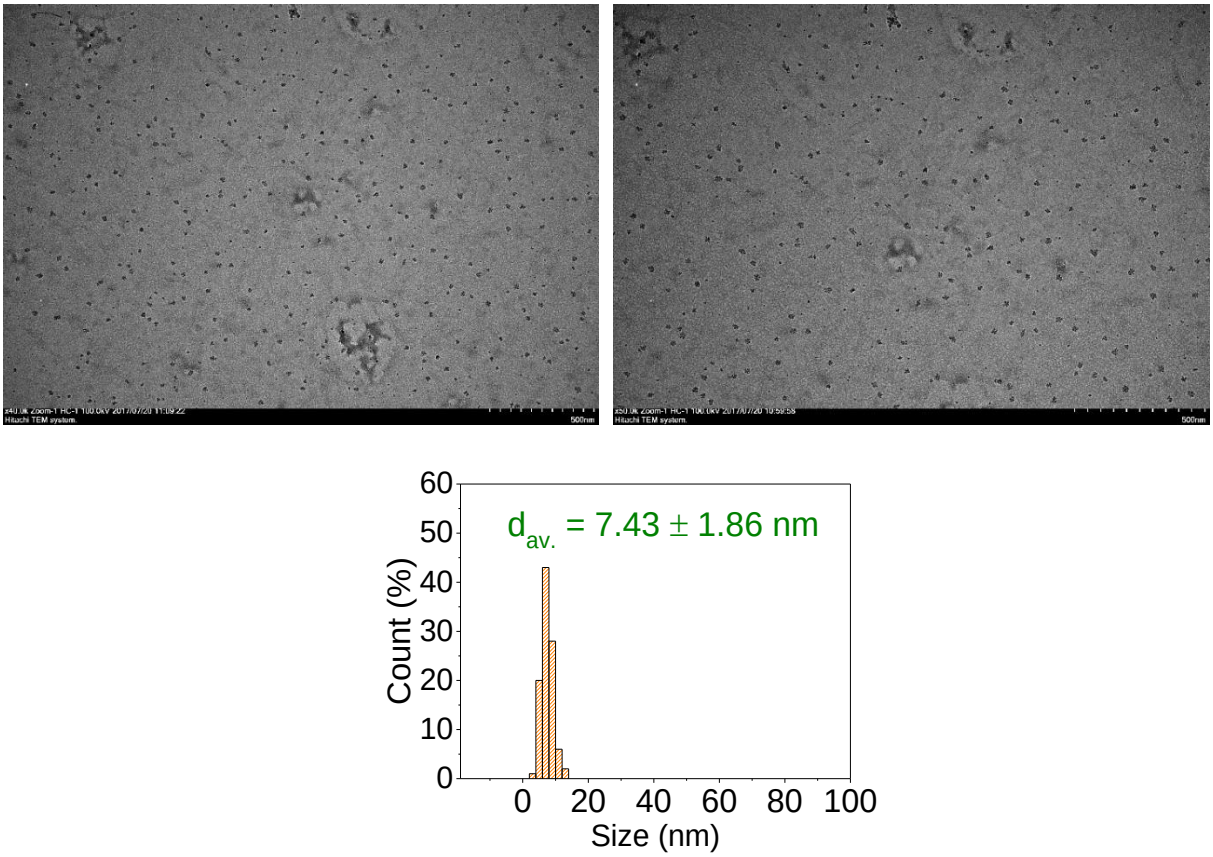


**Figure A.12.** TEM image of *as-prepared* Ag-NPs and particle size histogram.

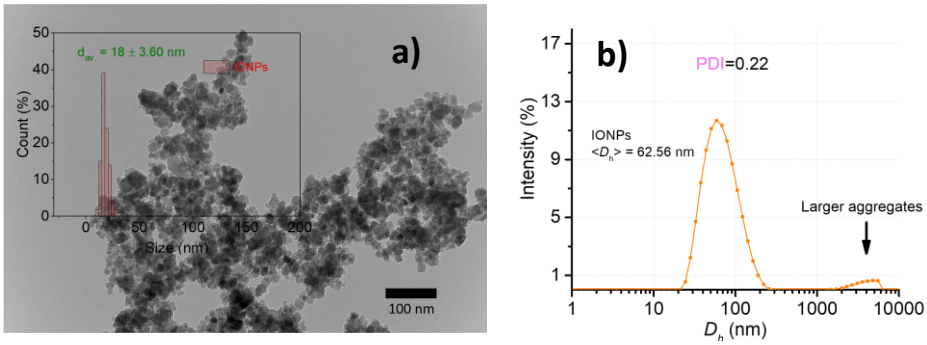


**Figure A.13.** (a) TEM micrograph of as-prepared IONPs and (inset) size distribution obtained from counting 100 particles in the TEM image using the ImageJ software. (b) DLS hydrodynamic diameter distribution of IONPs.

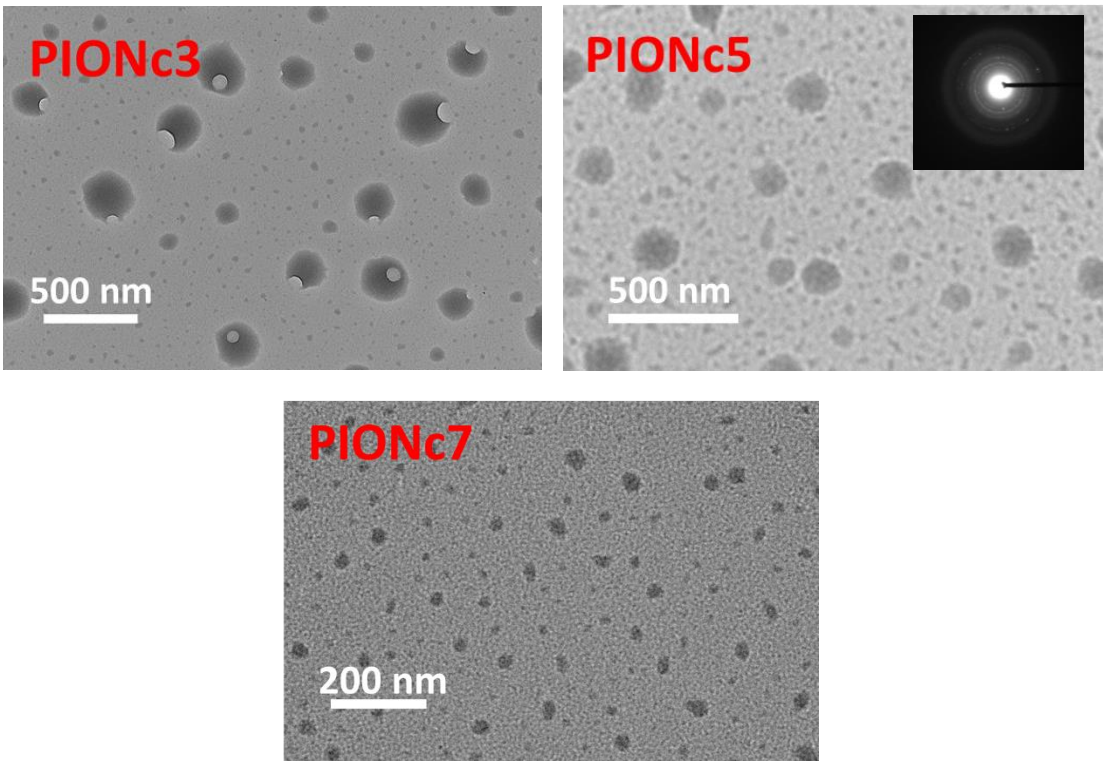


**Figure A.14.** Additional TEM micrographs of the PIONcx structures.

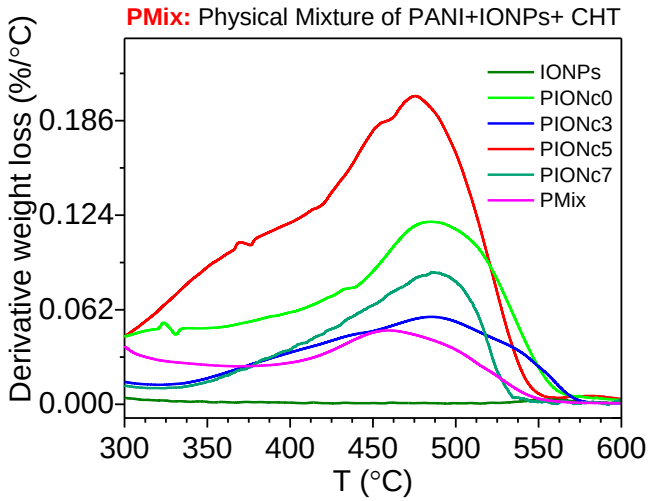


**Figure A.15.** Expanded TGA profiles of PIONcx nanocomposites, IONPs and PMix measured under nitrogen flow.

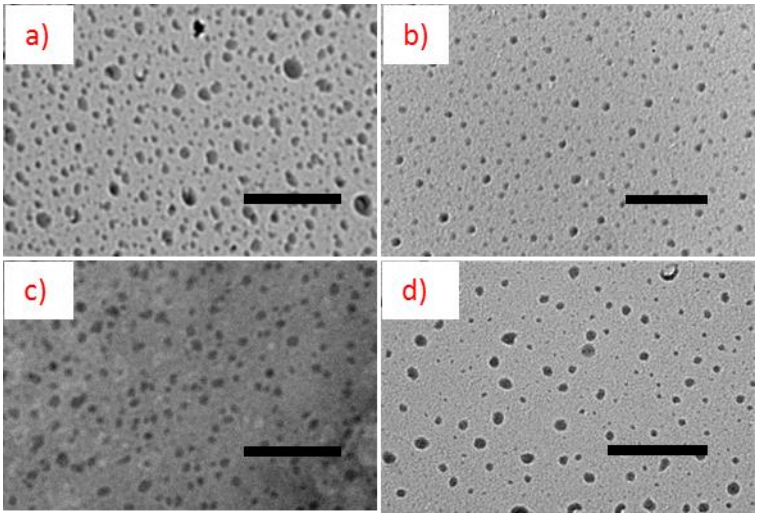


**Figure A.16.** TEM characterization of PIONc3 samples prepared after addition of salt and their phase transition behavior: a) 1.4 M , b) 1.6 M, c) 1.8 M, d) 1 M (bars: a,b,d = 500 nm, c = 100 nm).

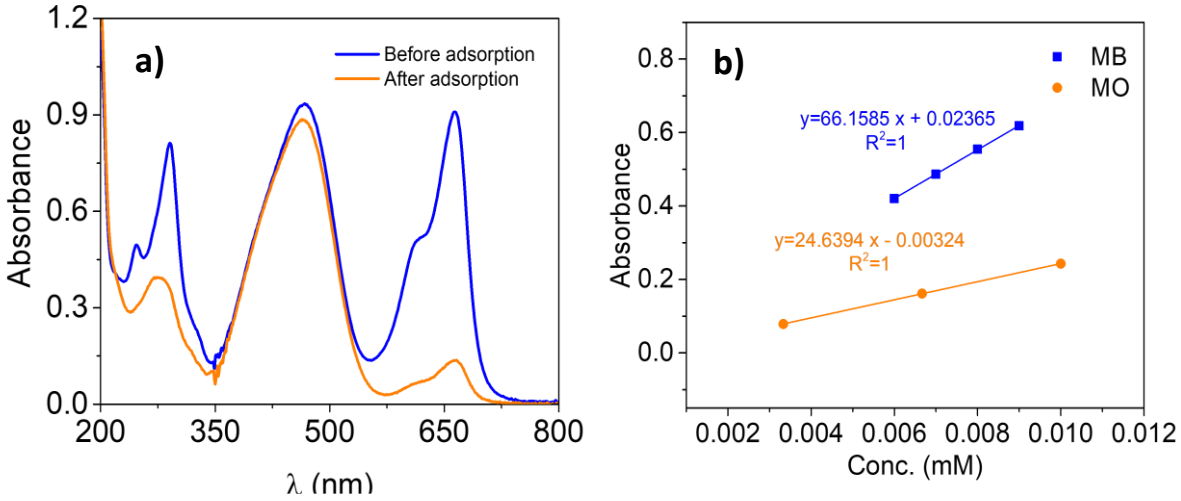


**Figure A.17.** (a) UV-vis spectra of MO/MB mixture before and after adsorption by PIONc5; MB ($\lambda_{max}$ = 664 nm) and MO ($\lambda_{max}$ = 462 nm); V = 15 mL, t = 5 h, m= 150 mg. (b) Calibration curve for MB ($\lambda_{max}$ = 664 nm) and MO ($\lambda_{max}$ = 462 nm). The experiment was carried out to further investigate ion recognition ability of the NCs.

**qNMR calculations was used to estimate the weight of inhibitors in microcapsules using equation 1:**

$n_{BTA}/n_i$ =2.10/4.00 x 4/2 =1.05
$M_w$ DMT=194.19 g/mole
$M_w$ BTA= 119.13 g/mole
1 mg standard=0.005 mmole
0.0058 mmole BTA= 0.62 mg BTA
6 mg loaded PANI capsules in 1 ml DMSO-d6
BTA loading %= 0.62/6 = 10.42 %
Aniline: 0.2 mL, 2.19 mmol
BTA 25 mL *2 mg/mL= 50 mg=0.29 mmoles
BTA/Aniline %=50/200=25%

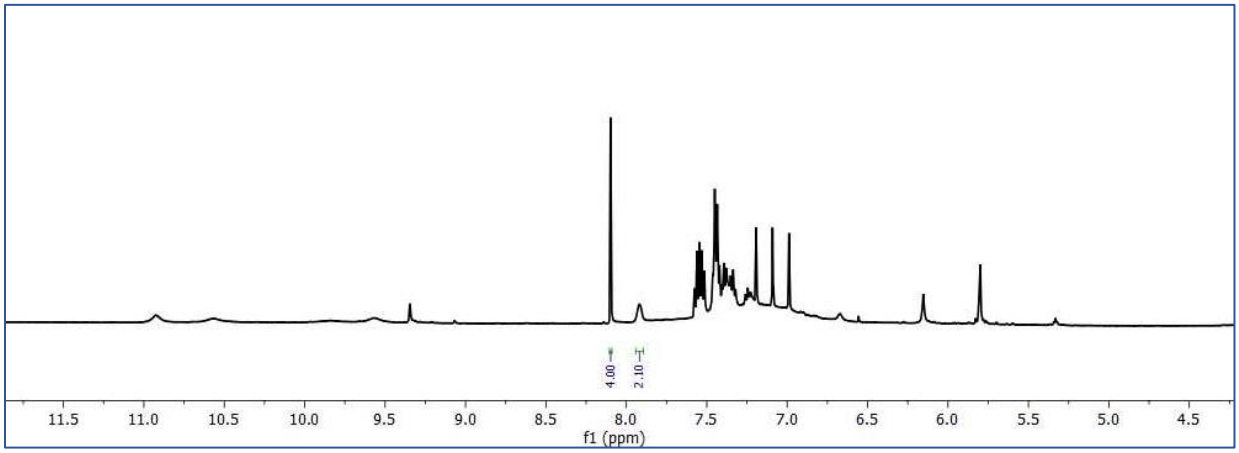


**Figure A.18.** [1]HNMR spectra of BTA loaded in capsules vs. DMT.

$n_{MBT}/n_i$ =0.46/4.00 x 4/1 = 0.46
$M_w$ DMT=194.19 g/mole
$M_w$ MBT= 167.25 g/mole
1 mg standard=0.005 mmole MBI= 0.38 mg MBT
6 mg loaded PANI capsules in 1 ml DMSO-d6
MBT loading %= 0.38/6 = 6.4 %
Aniline: 0.2 mL, 2.19 mmol
MBT 25 mL *1.5 mg/mL= 37.5 mg=0.22 mmoles
MBT/Aniline %=37.5/200=19%

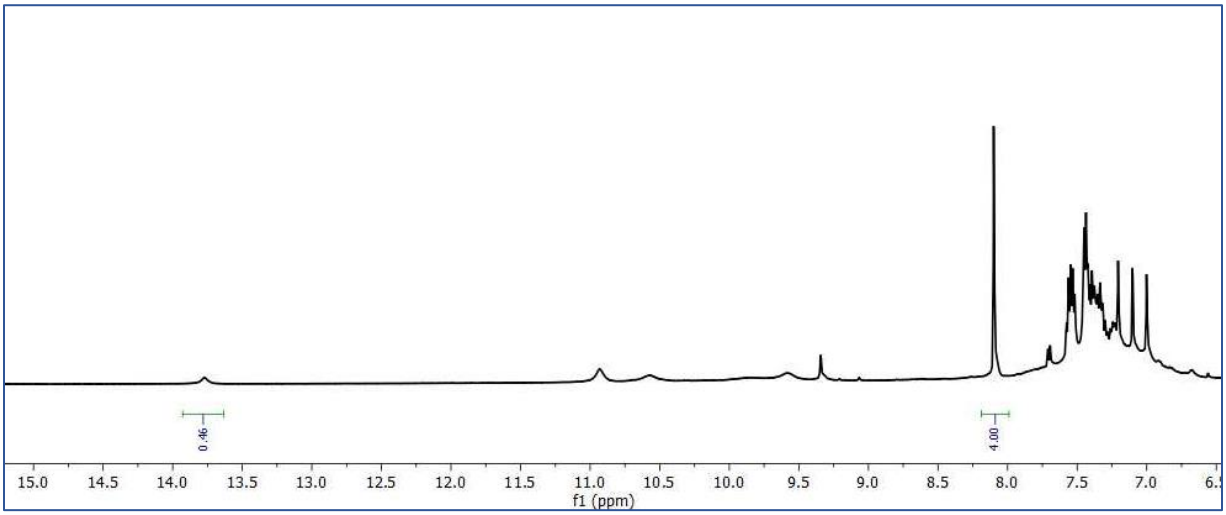


**Figure A.19.** [1]HNMR spectra of MBT loaded in capsules vs. DMT.

$n_{MBI}/n_i$ =0.34/4.00 x 4/1 =0.34
$M_w$ DMT=194.19 g/mole
$M_w$ MBI= 150.20 g/mole
1 mg standard=0.005 mmole
0.0015 mmole MBI= 0.26 mg MBI
6 mg loaded PANI capsules in 1 ml DMSO-d6
MBI loading %= 0.26/6 = 4.3 %
Aniline: 0.2 mL, 2.19 mmol
MBI 25 mL *0.43 mg/mL= 10.7 mg=0.07 mmoles
MBI/Aniline %=10.7/200=5.3%

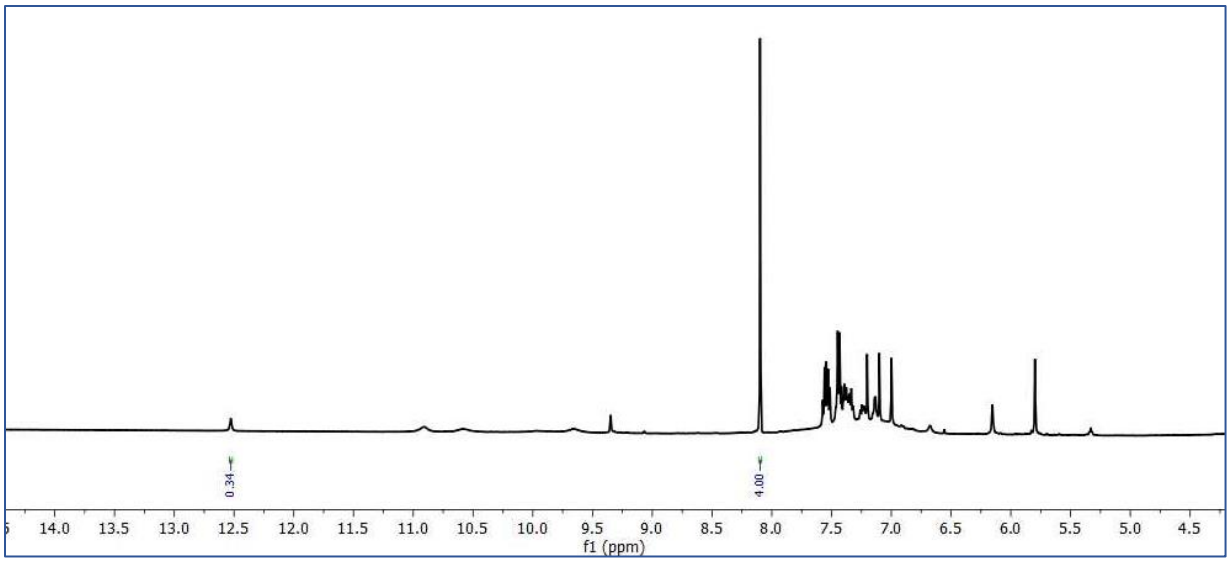


**Figure A.20.** [1]HNMR spectra of MBI loaded in capsules vs. DMT.

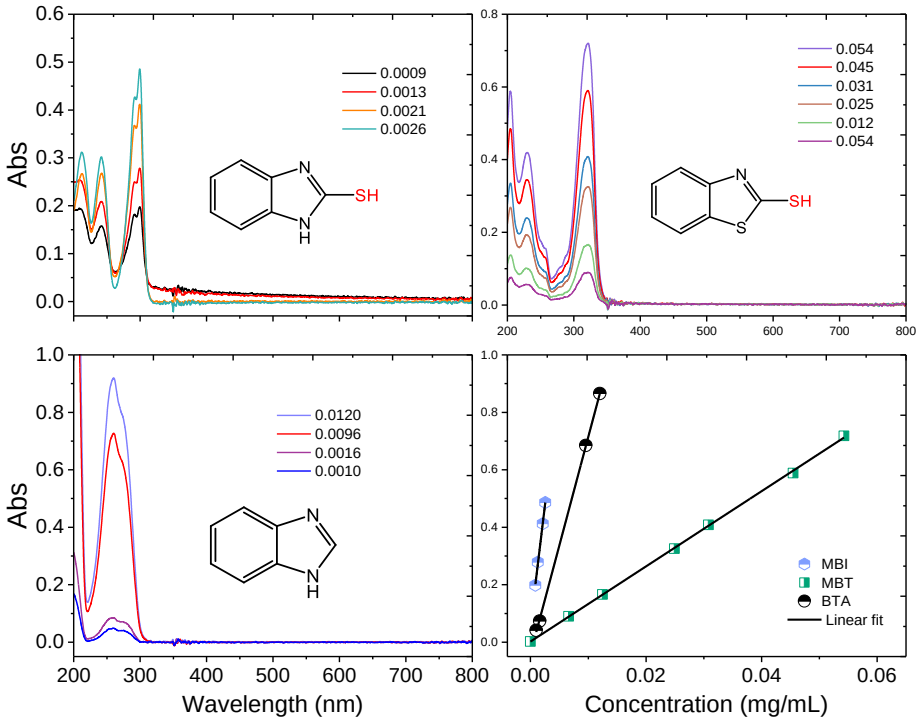


**Figure A.21.** Standard UV-vis curves used to quantify released self-healing agents.

**Table A.1.** PFO and PSO adsorption kinetics.

PFO kinetics :

$$\frac{dC}{dt} = -k_1 C \text{ or } C_t = C_o e^{-k_1 t} \quad \text{(A.1)}$$

$$\frac{dq}{dt} = k_1(q_e - q_t) \text{ or } q_t = q_e(1 - e^{-k_1 t}) \quad \text{(A.2)}$$

$$\ln(q_e - q_t) = \ln q_e - k_1 t \quad \text{(A.3)}$$

Where $k_1$ ($min^{-1}$) = the rate constant
$q_e$= the amounts of dye adsorbed at equilibrium
$q_t$= the amounts of dye adsorbed at a given time

PSO kinetics:

$$\frac{dC}{dt} = -k_2 C^2 \text{ or } \frac{dq}{dt} = k_2(q_e - q_t)^2 \quad \text{(A.4)}$$

$$\frac{t}{q_t} = \frac{1}{k_2 {q_e}^2} + \frac{t}{q_e} \quad \text{(A.5)}$$

$$q_t = \frac{q_e^2 k_2 t}{1 + k_2 q_e t} \quad \text{(A.6)}$$

Where $k_2$ (g $mg^{-1}$ $min^{-1}$) is the PSO rate constant.

**Table A.2.** Summary of TGA results of polymer brushes and the corresponding MNCs.

| | First weight loss | | Second weight loss | | Third weight loss | | |
|---|---|---|---|---|---|---|---|
| Sample | Derivative peak (°C) | Weight loss (%) | Derivative peak (°C) | Weight loss (%) | Derivative peak (°C) | Weight loss (%) | Total weight loss (%) |
| PIAgCHI | 79 | 5.6 | 253 | overlap | 309 | 51.6 | 57.2 |
| $Fe_3O_4$-PIAgCHI | 55 | 1.4 | 267 | 5.2 | - | - | 6.6 |
| $Fe_3O_4$-AAgCHI | 70 | 2.5 | 259 | 5.5 | 422 | 4.6 | 12.7 |

**Table A.3.** Rate constant values as a function of variable temperature.

| | Catalytic rate constant. ($s^{-1}$) | | |
|---|---|---|---|
| Temp ($^0$C) | AgNP-CP25 | AgNP-CP50 | AgNP-CP75 |
| 30 | 0.0062 | 0.0007 | 0.0136 |
| 35 | 0.0077 | 0.0011 | 0.0201 |
| 40 | 0.0140 | 0.0013 | 0.0294 |
| 45 | 0.0249 | 0.0017 | 0.0346 |
| 50 | - | 0.0024 | 0.0360 |

**Table A.4.** Langmuir adsorption isotherm parameters (pH= 6.5, T= 296.15).

| **Dye** | $q_{max}$ **(mmol/g)** | $R^2$ | $K_L$ |
|---|---|---|---|
| **MB** | 0.34 | 0.98 | 38.71 |
| **MO** | 0.09 | 0.98 | 14.58 |

$$\ln\left[C_t / C_0\right] = kt \qquad \text{(Eq. A.1)}$$

$C_t$ is the concentration of 4-NPh at time t
$C_0$ is the concentration of 4-NPh at time 0
k is the first-order rate constant

$$\ln k = \ln A - \frac{E_a}{RT} \qquad \text{(Eq. A.2)}$$

*k* is the first-order rate constant
*A* is the pre-exponential factor
$E_a$ is the activation energy
*R* is the universal gas constant
*T* is the reaction temperature